EUSKAL HERRIKO UNIBERTSITATEA
UNIVERSITY OF THE BASQUE COUNTRY

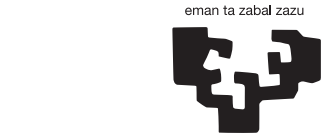

Anharmonic effects in two-dimensional systems: charge density wave transitions and their mechanical stability

Thesis by

Josu Diego López

Supervised by

Ion Errea Lope

and

Raffaello Bianco

Donostia-San Sebastián, October 2024

Contents

Introduction

Atoms in materials fluctuate and oscillate around their equilibrium positions at any temperature, even at absolute zero due to quantum zero-point motion. These vibrations determine many physical and chemical properties of materials, such as their thermodynamic and transport characteristics. Specifically, the temperature dependence of a material's thermodynamic properties is primarily governed by the atomic vibrations, as they are excited at much lower temperatures than electrons. As a result, atomic fluctuations significantly influence various key phenomena, including phase transitions, specific heats and thermal expansion. On the other side, electrical and thermal transport in materials cannot be understood without considering the interaction of electrons with the quanta of atomic vibrations, known as phonons, nor neglecting the interaction between phonons themselves. Even superconductivity, one of the most intriguing phenomena that emerges in materials, is often the result of the electron-phonon interaction. Additionally, the vibrational dynamics leaves different spectroscopic signatures, observable in infrared, Raman, and inelastic x-ray or neutron scattering experiments.

Nowadays, the vibrational properties of materials are typically calculated from first principles within the harmonic approximation. In this framework, the Born-Oppenheimer potential, which describes the dynamics of atoms, is expanded to second order as a function of atomic displacements. However, this approximation leads to several unphysical consequences, for example, the prediction that phonons are well-defined quasiparticles with temperature-independent energies. In reality, phonons have finite lifetimes due to various factors, including anharmonic interactions, as evidenced by the measurable widths of phonon peaks in inelastic scattering experiments. Furthermore, phonon energies do depend on temperature, as exemplified by the softening and collapse of certain modes near second-order phase transitions. Regarding second-order phase transitions, the harmonic approximation also struggles to explain the dynamical stability of the high-temperature undistorted phases. This failure is evident from the presence of imaginary phonon frequencies in the harmonic phonon spectra of the high-temperature phase, which suggest that certain atomic displacements can trigger spontaneous distortions. To effectively capture all these phenomena, it is necessary to move beyond the standard harmonic approximation and incorporate anharmonic terms to the theoretical description.

One way to include anharmonic effects is through perturbation theory applied on top of the harmonic results. Although perturbative approaches can effectively capture important phenomena like the temperature dependence of phonons and their finite lifetimes, they completely collapse when the anharmonic terms in the potential become comparable to or larger than the harmonic terms within the range of the atomic fluctuations. This breakdown frequently occurs in systems with significant atomic displacements, particularly those involving light ions, as well as in materials approaching displacive phase transitions such as charge density waves (CDW), and in low-dimensional materials where atoms have greater freedom to fluctuate. In all these scenarios, anharmonic effects dominate the system's behaviour and properties, requiring non-perturbative approaches for an accurate analysis.

Precisely, this thesis focuses on analysing the impact of non-perturbative anharmonic effects in the ionic dynamics of diverse physical systems. In this context, the self-consistent harmonic approximation (SCHA) [1] emerges as the most effective method for incorporating these anharmonic effects at a non-perturbative level while also accounting for quantum effects. Consequently, the SCHA serves as the core *ab initio* method employed throughout this work. Although this thesis examines a range of systems where anharmonicity plays a crucial role, they are all interconnected by a common theme: reduced dimensionality, particularly in two-dimensional (2D) and quasi-2D systems. Even if each chapter focuses on a different system and includes its own introduction, this general introduction aims to provide an overview of the theoretical challenges we face and highlight their key aspects.

The **first problem** deals with the prediction of charge density wave instabilities and their understanding through *ab initio* calculations. Nowadays, the correct theoretical characterization of this phenomenon based on first principles calculations is limited for systems undergoing CDW transitions due to the breakdown of the standard harmonic approximation for atomic dynamics, which cannot explain the stability of the high-temperature undistorted phases. These limitations hinder the study of both the origin and the melting of the charge modulated state, complicating the comprehensive understanding of the CDW formation. In the first part of this thesis, we address these challenges by incorporating non-perturbative anharmonic effects. In the text that follows, we provide an overview of the CDW phenomenon, a key concept that is ubiquitous throughout the first part of this manuscript and that requires careful examination.

A charge density wave is a many-body state of matter characterized by the static modulation of the conduction electron density, which is accompanied by the corresponding crystal lattice distortion. Phase transitions to this electronic charge ordering state have been reported indeed in low dimensional materials [2, 3], high-temperature superconductors [4–8], as well as many other compounds at low temperatures. While numerous compounds can exhibit CDW transitions, the origin and stabilization of this phenomenon remain topics of ongoing debate, especially in systems with dimensions higher than 1D or quasi-1D.

The concept of a CDW was first proposed by Rudolf Peierls in the 1930s [9], who predicted the electronic instability of a one-dimensional metallic chain with equally spaced atoms. In such a chain, where each metallic ion contributes one valence electron, the valence band is half-filled, and the electron density remains constant in space. These features are illustrated in Fig. 1 (a).

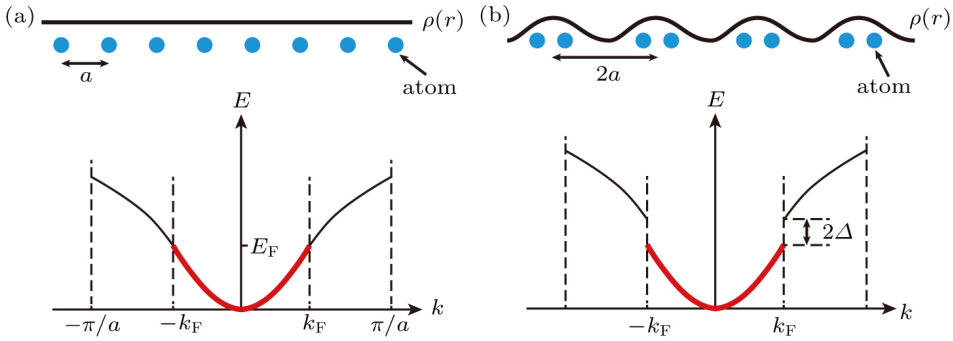

Figure 1: A 1D system in: (a) High temperature metallic state. A lattice with a period of a exhibits a constant $\rho(r)$ charge density and the electron states are filled up to the Fermi level. (b) Peierls distorted insulating lattice: CDW state. Due to electron-phonon interaction, the lattice period changes while the charge density is periodically modulated in a wave-like pattern. The new periodicity opens a gap at the Fermi level, lowering the electronic energy and at the same time resulting in a transition to an insulating state. Figure taken from Refs. [10, 11].

Peierls proposed that this metallic state is energetically unstable, as the system's electronic energy can be reduced by opening a gap at the Fermi wavevector, as displayed in Fig. 1 (b). This transition to an insulating behaviour is achieved by changing the periodicity of the chain. In the half-filled valence band scenario Peierls proposed, this modification occurs through a process known as dimerization: the new period becomes twice the original, resulting in a new unit cell that contains two atoms. This periodic lattice displacement, characterized by a wavevector of $2\mathbf{k}_F$, induces a corresponding modulation in the charge density, forming a charge density wave with the same periodicity. The stability of the CDW phase depends on two factors: first, the reduction of electronic energy outweighing the increase in elastic energy required to displace the atoms, and second, the competition between the minimization of the total energy and the maximization of entropy. That is, as the temperature rises, increased thermal fluctuations can disrupt the ordered charge density state, leading to the temperature-dependent nature of CDW transitions. Consequently, this model predicts a second-order phase transition, known as the Peierls transition, from a high-symmetry metallic state at high temperatures to a reduced symmetry insulating ground state at the transition temperature, $\mathrm{T_{CDW}}$.

Within linear response framework, the rearrangement of the conduction electron density $\rho(\mathbf{q})$ can be related to the periodic modulation of the starting potential $\Phi(\mathbf{q})$ through the so-called Lindhard response function: $\rho(\mathbf{q}) = \chi(\mathbf{q})\Phi(\mathbf{q})$, which is given by:

$$\chi(\mathbf{q}) = \frac{1}{L^D} \sum_{nn'} \sum_{\mathbf{k}}^{1BZ} \frac{f_{n\mathbf{k}} - f_{n'\mathbf{k}+\mathbf{q}}}{\epsilon_{n\mathbf{k}} - \epsilon_{n'\mathbf{k}+\mathbf{q}}} \,. \tag{1}$$

where $\epsilon_{n\mathbf{k}}$ and $\epsilon_{n'\mathbf{k}+\mathbf{q}}$ represent the energies associated with the electronic bands n and n', and wavevectors $\mathbf{k}$ and $\mathbf{k}+\mathbf{q}$, respectively. The corresponding Fermi distribution functions, $f_{n\mathbf{k}}$ and $f_{n'\mathbf{k}+\mathbf{q}}$, describe the occupation of these electronic states. D is the dimensionality of the system, which significantly influences the electronic susceptibility. This dependence on dimensionality is shown in Fig. 2, where the response function is evaluated at different wavevector values for the 1D, 2D and 3D free electron gas. In 1D systems, the response function diverges at $\mathbf{q} = 2\mathbf{k}_F$, leading in the real space to a charge density wave with the same wavevector. In contrast, this peak becomes less pronounced in higher-dimensional systems.

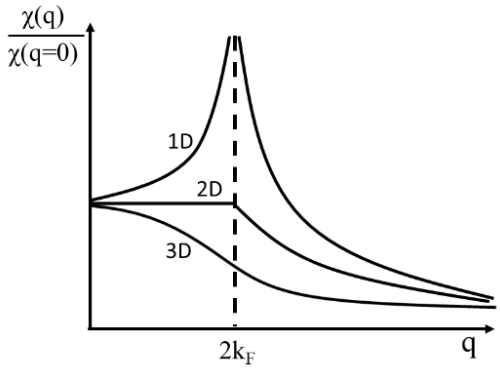

Figure 2: Lindhard response function for the free electron gas in 1D, 2D, and 3D at T = 0 K. The figure illustrates the distinct behaviour of the response function across dimensions, highlighting the divergence observed in 1D systems at $\mathbf{q} = 2\mathbf{k}_F$. Figure taken from Ref. [12].

The behaviour of the Lindhard response function is closely linked to specific topologies of the Fermi surface, which is defined as the set of constant-energy surfaces in reciprocal space that separates occupied from unoccupied states. Fermi surface nesting refers to a configuration where parallel regions of the Fermi surface are connected by a specific wavevector $\mathbf{q}$, known as the nesting vector. According to the Eq. (1), the larger contribution to the electronic susceptibility $\chi(\mathbf{q})$ comes from the electron-hole pair of states (one full, one empty) differing in $\mathbf{q}$ and with similar energies. Hence, in the case of having many $\mathbf{q}$-coupled $\mathbf{k}$ electronic states, $\chi(\mathbf{q})$ will diverge at this specific nesting vector.

In the case of a one-dimensional metal embedded in 3D space, the Fermi surface consists of two parallel planes separated by the wavevector $2\mathbf{k}_F$, as shown in Fig. 3 (a). This configuration enables numerous possible electron-hole excitations near the Fermi surface, a phenomenon known as perfect nesting that is manifested in the divergence of the electronic susceptibility $\chi(\mathbf{q})$ at $\mathbf{q} = 2\mathbf{k}_F$. In higher dimensions, free electron-like systems typically lack nested surfaces. For instance, 2D free electron systems exhibit cylindrical Fermi surfaces, while 3D systems have spherical Fermi surfaces in the free electron limit. Both configurations prevent the existence of nested regions, resulting in the absence of peaks in $\chi(\mathbf{q})$. In contrast, quasi-1D systems often present parallel Fermi surfaces arranged in a one-dimensional manner that allow for better nesting, as illustrated in Fig. 3 (c).

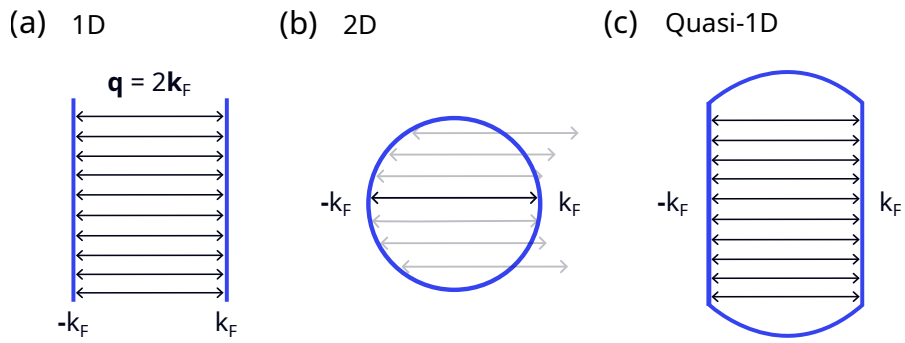

Figure 3: Fermi surface nesting across different dimensions. (a) In a 1D system embedded in 3D space, the Fermi surface consists of two parallel sheets at $\pm\mathbf{k}_F$. A wavevector $\mathbf{q} = 2\mathbf{k}_F$ can connect the entire Fermi surface, resulting in perfect nesting. (b) In a 2D free electron system with a cylindrical Fermi surface, only a very small portion of the surface can be connected by $\mathbf{q} = 2\mathbf{k}_F$, leading to poor nesting. (c) In a quasi-1D system with an elliptical Fermi surface, large parallel regions allow for better nesting.

Walter Kohn predicted in 1959 [13] that any divergence in the electronic susceptibility affect not only the charge density distribution but also phonon spectra. He proposed that electron-hole excitations near the Fermi surface are driven by phonons with the nesting wavevector $\mathbf{q} = 2\mathbf{k}_F$, and as the result of this electron-phonon interaction, the associated phonon mode is softened. The periodic modulation of the lattice would be precisely the macroscopic manifestation of the phonon softening. In fact, above the CDW transition temperature, low-energy acoustic phonon branches can exhibit singularities at the nesting vector, resulting in significant frequency softening, a phenomenon known as the Kohn anomaly effect. As the temperature decreases, the frequency of these phonons continues to drop until it becomes imaginary below the transition temperature, indicating a structural instability and a subsequent phase transition to a different lattice configuration. As a result, CDWs can be identified through the Kohn anomaly effect, using both inelastic scattering experimental techniques and theoretical calculations that in-

clude non-perturbative anharmonic phonon effects. Moreover, phonon softening effects have been observed in materials where the nesting scenario does not apply, highlighting the broader relevance of this phenomenon [14].

Definitely, the Fermi surface nesting explanation is primarily effective in explaining CDW in 1D or quasi-1D systems [15, 16] and therefore, it can be concluded that not all charge density waves are driven exclusively by Fermi surface nesting. Some theories suggest that CDW originate from a strong electron-phonon interaction, with no need of singularities in the electronic susceptibility. The electron-phonon scenario, which will be further developed in Chapter 4, shares similarities with the nesting mechanism in that the corresponding phonon self-energy of a mode $\Pi_\mu(\mathbf{q},\omega)$ in its static limit ($\omega \to 0$) follows a formula analogous to that in Eq. (1), but modulated by the electron-phonon matrix elements:

$$\Pi_\mu(\mathbf{q},\omega=0) = \frac{1}{N_\mathbf{k}} \sum_{nn'} \sum_{\mathbf{k}}^{1BZ} |g^\mu_{n'\mathbf{k}+\mathbf{q},n\mathbf{k}}|^2 \frac{f_{n\mathbf{k}} - f_{n'\mathbf{k}+\mathbf{q}}}{\epsilon_{n\mathbf{k}} - \epsilon_{n'\mathbf{k}+\mathbf{q}}} \,. \tag{2}$$

Although both mechanisms are based on electron-lattice interactions leading to electron-hole excitations, they differ fundamentally: Fermi surface nesting involves elastic scattering, whereas electron-phonon interaction entails inelastic scattering from the lattice.

Among the solids exhibiting charge density wave transitions, transition metal dichalcogenides (TMDs) are particularly interesting due to their layered structure, which potentially features parallel Fermi surfaces like those in Fig. 3 (c) that promote electronic instabilities. However, it has been suggested that the Fermi surface nesting scenario may significantly break down in TMDs, highlighting the role of electron-phonon interactions in their origin and stabilization [16]. Certainly, TMDs, with their relatively simple crystalline structure, provide an ideal platform for studying the competition between Fermi surface nesting and electron-phonon interaction as mechanisms driving the formation of CDWs. Furthermore, TMDs represent the first crystalline structures where three-dimensional (3D) charge density patterns have been observed [2]. In these 3D-CDWs, the propagation vector $\mathbf{q}_{\mathrm{CDW}}$ possesses an out-of-plane component, indicating that the charge density modulation extends beyond the quasi-2D nature of the system and could potentially influence the interlayer distances. A final aspect worth highlighting is that the quasi-2D structure of TMDs provides an excellent opportunity to explore how reducing dimensionality [17] influences the transition to the charge modulated state. A more comprehensive overview of transition metal dichalcogenides can be found in the introduction to Part II of the thesis.

In particular, in this part of the thesis, we focus on a metallic member of the TMD family, 1T-VSe_2. Chapter 5 addresses the charge density wave transition in the bulk form of this compound. We specifically examine whether phonon softening occurs as the temperature decreases towards the transition, employing *ab initio* non-perturbative anharmonic phonon calculations and complementing our

findings with inelastic x-ray scattering data from Dr. Santiago Blanco-Canosa's group. We then analyse and compare the potential mechanisms that could lead to the emergence of the charge modulated state. Finally, we explore the pressure dependence of the CDW transition and the anomalous enhancement of the charge modulated state with increasing pressure. In Chapter 6, we extend our analysis to the monolayer limit of $1\,T$-VSe_2, since the effect of dimensional reduction on the CDWs remains a subject of ongoing debate. A significant challenge is the lack of consensus on the nature of the CDW reconstruction in the monolayer, with different experimental results reporting distinct orders and varying transition temperatures. Aiming to resolve these experimental contradictions, we theoretically analyse the strain dependence of the CDW orders in monolayer $1\,T$-VSe_2, while also studying the mechanisms responsible for the CDW formation.

The **second problem** tackled in this thesis is of a more historical nature, as it addresses the mechanical stability of strictly two-dimensional materials. Despite the evidence presented in the previous paragraph regarding the existence of monolayer materials, historically, the possibility of having two-dimensional crystalline order was considered unlikely [18–20]. However, the discovery of graphene in 2004 [17, 21, 22] challenged these longstanding theoretical predictions. Even today, the exact mechanism behind the stability of these materials remains a topic of intense debate. Although the state-of-the-art on the stability of 2D systems and their connection with phenomenological theories of thermal fluctuations in elastic membranes is explained in detail in the introduction to Part III of the manuscript, we will proceed with a brief summary to facilitate understanding and highlight the most relevant points.

Much of the theoretical difficulty on this problem arises from the strong thermal fluctuations predicted for 2D systems, since reduced dimensionality allows atoms to fluctuate out of the plane. These fluctuations are closely related to the quadratic dispersion of the out-of-plane acoustic mode obtained within the harmonic approximation, which implies that these phonon modes are quickly occupied as the temperature increases. In fact, harmonic theory predicts that the out-of-plane displacements in real space are comparable to the size of the material flake, preventing any crystalline order. Standard theories propose that the anharmonic coupling between in-plane and out-of-plane phonon modes renormalizes the dispersion of the ZA phonon modes, providing it with a linear term at small momenta that somewhat cures the pathologies [23–30]. Along similar lines, it has long been assumed that the out-of-plane vibrational frequency of any continuous membrane acquires a linear term at small wavevectors once anharmonic interactions are included [31]. The linear term stiffens the membrane and consequently suppresses the amplitude of its ripples, which is usually studied from the height correlation function in momentum space, $\langle |h(\mathbf{q})|^2 \rangle$. In the harmonic approximation it scales as $\langle |h(\mathbf{q})|^2 \rangle \sim q^{-4}$ and it is corrected to $q^{-4+\eta}$, with $\eta \sim 0.80 - 0.85$, when the ZA modes is linearized [32, 33]. Since the bending rigidity scales as $\langle |h(\mathbf{q})|^2 \rangle q^4$ [31, 32, 34] in the classical limit, this interpretation implies that the bending stiffness of all membranes and 2D materials diverges in the long wavelength limit, yielding the dubious interpretation that the larger the membrane, the stiffer it becomes.

The experimental confirmation of these ideas is challenging due to both the difficulties in measuring the bending rigidity of graphene [35, 36] and the substrate effects on the dispersion of the ZA modes measured with helium diffraction [37–40].

The quadratic dispersion expected for the ZA mode in the harmonic approximation is imposed by the symmetries intrinsic to strictly 2D systems. In this case phonon frequencies are obtained diagonalizing the $\phi_{ab}/\sqrt{M_a M_b}$ dynamical matrix, where a and b represent both atom and Cartesian indices. Then, M_a is the mass of atom a, and $\phi_{ab} = \left[\frac{\partial V}{\partial R_a \partial R_b}\right]_{\mathbf{R}^0}$ are the second-order force constants obtained as the second-order derivatives of the Born-Oppenheimer potential V with respect to atomic positions $\boldsymbol{R}$ calculated at the positions that minimize V. Rotational symmetry, together with the fact that in a strictly two-dimensional system force constants involving an in-plane and an out-of-plane displacement vanish, makes the ZA mode acquire a quadratic dispersion close to zone center [26]. However, phonons observed experimentally should be derived from the imaginary part of the phonon Green's function that includes anharmonic effects [41]. For low energy modes, such as the ZA mode, dynamical effects can be safely neglected. In this limit the phonon peaks coincide with the eigenvalues of the free energy Hessian $[\frac{\partial F}{\partial \mathcal{R}_a \partial \mathcal{R}_b}]_{\boldsymbol{\mathcal{R}}_{eq}}/\sqrt{M_a M_b}$, where F is the anharmonic free energy, $\mathcal{R}_a$ the average atomic positions, and the derivative is taken at the positions that minimize F [41]. This raises a formidable remark that has remained unnoticed thus far: as both F and V are rotationally invariant, a quadratic dispersion should be expected for the ZA mode not only in the harmonic limit but also when anharmonic interactions are considered.

In any case, the substantial height fluctuations predicted for 2D systems suggest that the problem lies in the regime where anharmonic terms in the potential become comparable to, or even exceed, the harmonic terms. Consequently, the most rigorous approach to address the mechanical stability of 2D systems is to employ a non-perturbative method to include anharmonic effects, just as the SCHA does. In the second part of this thesis, we perform non-perturbative anharmonic calculations on graphene using a membrane model. In this way, we convincingly show that a quadratic dispersion of the ZA mode in unstrained graphene, and any other 2D membrane, is actually expected. We also show that the bending stiffness of graphene is barely affected by phonon-phonon interactions. Our results are in stark contrast to the previously assumed behaviour of membranes because we fully preserve rotational invariance. Precisely, to compare and align our hypothesis with the current standard theory, we compute the Fourier transform of the height-height correlation function, enabling a comprehensive comparison with existing results in the literature.

In summary, this thesis explores anharmonic effects in two-dimensional materials, specifically in contexts where the harmonic approximation and the inclusion of anharmonic effects at perturbative level are no longer adequate. In Part I, which includes Chapters 1 to 4, we establish the theoretical framework necessary for studying the electronic, vibrational, and electron-phonon properties of these

materials. Part II is dedicated to analysing charge density wave transitions in transition metal dichalcogenides, focusing specifically on $1T$-VSe_2. Chapter 5 examines the CDW transition in the bulk form, while Chapter 6 addresses the behaviour of the monolayer case. Finally, in Part III, we examine the anharmonic effects on the atomic vibrations in strictly two-dimensional systems, specifically in graphene, as presented in Chapter 7.

Part I

Theoretical background

1

The Born-Oppenheimer approximation

Matter is composed of atoms, and these, by interacting electrons and nuclei. Electrons, carrying a negative charge, surround the nucleus, which consists of positively charged protons and neutrons. In condensed matter physics, the focus is typically on the outermost valence electrons and ions, defined as the nucleus plus the core electrons, since these inner electrons play a negligible role in chemical bonding and the macroscopic properties of materials. In this context, (valence) electrons and ions can be understood as positive and negative charges interacting through Coulomb forces, while also being influenced by their spin degree of freedom. These microscopic interactions give raise to a great variability of macroscopic behaviours observed in daily materials, such as conductivity, magnetism, and elasticity. Then, by studying these fundamental interactions, we can gain insights into how these simple particles combine to produce the diverse and complex physical properties that characterize the different states of matter.

Whichever the state of matter is, the behaviour and properties of the constituent particles are governed by the principles of quantum mechanics. At the core of this framework lies the Schrödinger equation, which provides all the key information about a system, including its energy levels, wavefunctions, and the probability distributions of its particles. The equation is expressed as:

$$\hat{\mathrm{H}} \left|\Psi_A\right\rangle = E_A \left|\Psi_A\right\rangle \ , \tag{1.1}$$

where $\hat{\mathrm{H}}$ is the Hamiltonian of the system, which contains both the kinetic and potential energy contributions from all the particles. E_A is the eigenvalue corresponding to the quantum state labeled by A and $|\Psi_A\rangle$ the associated eigenvector. The corresponding eigenfunction is given by:

$$\langle \boldsymbol{r}, \mathbf{R} | \Psi_A \rangle = \Psi_A(\boldsymbol{r}, \mathbf{R}) = \Psi_A(\mathbf{r}_1, ..., \mathbf{r}_N, \mathbf{R}_1, ..., \mathbf{R}_M) \tag{1.2}$$

where $\boldsymbol{r} \equiv \{\mathbf{r}_1, ..., \mathbf{r}_N\}$ and $\mathbf{R} \equiv \{\mathbf{R}_1, ..., \mathbf{R}_M\}$ are the position vectors for the N electrons and M ions in the system, respectively. Hence, as the components of the introduced system interact via the Coulomb interaction, the corresponding Hamiltonian takes the following form[1]:

$$\begin{aligned}\hat{\mathrm{H}} = &\sum_{i=1}^{N} -\frac{1}{2}\hat{\nabla}_i^2 - \sum_{I=1}^{M} \frac{1}{2M_I}\hat{\nabla}_I^2 - \sum_{i=1}^{N}\sum_{I=1}^{M} \frac{Z_I}{|\hat{\mathbf{r}}_i - \hat{\mathbf{R}}_I|} \\ &+ \frac{1}{2}\sum_{i=1}^{N}\sum_{\substack{j=1 \\ j\neq i}}^{N} \frac{1}{|\hat{\mathbf{r}}_i - \hat{\mathbf{r}}_j|} + \frac{1}{2}\sum_{I=1}^{M}\sum_{\substack{J=1 \\ J\neq I}}^{M} \frac{Z_I Z_J}{|\hat{\mathbf{R}}_I - \hat{\mathbf{R}}_J|} \\ &= \hat{\mathrm{T}}_e + \hat{\mathrm{T}}_{ion} + \hat{\mathrm{V}}_{e,ion} + \hat{\mathrm{V}}_{e,e} + \hat{\mathrm{V}}_{ion,ion} \ , \end{aligned} \tag{1.3}$$

where lower case indexes correspond to the electrons while the upper case ones to the ions. In this way, M_I and Z_I are the mass and charge of each ion, respectively.

Examining each term of the Hamiltonian reveals that the first two terms represent the kinetic energy operators for electrons and ions. The remaining three terms account for the Coulomb interactions between charged particles: the electron-ion, electron-electron, and ion-ion interaction operators. These electrostatic interaction terms are responsible for coupling the $3(N + M)$ degrees of freedom of our $N + M$ particle system, making the Hamiltonian extremely complex. The magnitude of this complexity is apparent in macroscopic systems, where the number of particles is of the order of Avogadro's number, $\mathrm{N}_A = 6.022{\times}10^{23}$. Consequently, obtaining an exact analytical solution for such systems is virtually impossible, and approximations have to be assumed to make the eigenvalue problem tractable.

In this context, the standard approach to addressing the problem is through the Born-Oppenheimer approximation. As far as the electrons and nuclei are in the same environment, the order of magnitude of the forces over them is similar and, in principle, so is their linear momentum. However, being electrons much lighter than ions, average electronic velocities are much greater than ionic ones and, therefore, electronic wavefunctions can be assumed to adapt instantaneously to the nuclear motion.

Considering this in mathematical terms, the Born-Oppenheimer approximation uncouples the electronic and ionic degrees of freedom in the total wavefunction, which is going to allow us to split the Hamiltonian into electronic and ionic parts. Namely,

$$\Psi(\boldsymbol{r}, \mathbf{R}) = \Psi^e(\boldsymbol{r}; \mathbf{R})\Psi^{ion}(\mathbf{R}) \tag{1.4}$$

where $\Psi^e(\boldsymbol{r}; \mathbf{R})$ is the electronic wavefunction and $\Psi^{ion}(\mathbf{R})$ the ionic one. Following the reasoning above, as from the point of view of the electrons ions are still,

[1]Here and from now on, Hartree atomic units will be used: $\hbar = m_e = e = 4\pi\varepsilon_0 = 1$. In such system of units, the energy unit is the Hartree (1 Ha = 27.2 eV), while the unit of length is the Bohr radius a_0 ($a_0 = 0.529$ Å).

the ionic positions $\mathbf{R}$ are treated as parameters, not as variables, in the electronic wavefunction. In the same way, their kinetic energy can be ignored when dealing with the electronic problem.

Thus, the electronic problem for a set of fixed ionic positions $\mathbf{R}$ is the following:

$$\hat{\mathrm{H}}^{e}\Psi_n^e(\boldsymbol{r};\mathbf{R}) = E_n^e(\mathbf{R})\Psi_n^e(\boldsymbol{r};\mathbf{R}) \ , \tag{1.5}$$

where

$$\hat{\mathrm{H}}^{e} = \hat{\mathrm{T}}_e + \hat{\mathrm{V}}_{e,ion} + \hat{\mathrm{V}}_{e,e} + \mathrm{V}_{ion,ion} \ . \tag{1.6}$$

Once the electronic problem is solved, the ionic one can be faced. Within the the Born-Oppenheimer approximation, the eigenvalue of the ionic problem corresponds to the total energy of the original Hamiltonian in Eq. (1.3):

$$\hat{\mathrm{H}}_n^{ion}\Psi_{nm}^{ion}(\mathbf{R}) = E_{nm}\Psi_{nm}^{ion}(\mathbf{R}) \ , \tag{1.7}$$

where

$$\hat{\mathrm{H}}_n^{ion} = \hat{\mathrm{T}}_{ion} + E_n^e(\mathbf{R}) + \Delta\hat{\mathrm{H}}_n \tag{1.8}$$

and

$$\begin{aligned}\Delta\hat{\mathrm{H}}_n = &-\sum_{I=1}^{M}\frac{1}{2M_I}\int d\boldsymbol{r}\ \Psi_n^{e*}(\boldsymbol{r};\mathbf{R})\hat{\nabla}_I^2\Psi_n^e(\boldsymbol{r};\mathbf{R}) \\ &-\sum_{I=1}^{M}\frac{1}{M_I}\int d\boldsymbol{r}\ \Psi_n^{e*}(\boldsymbol{r};\mathbf{R})\hat{\nabla}_I\Psi_n^e(\boldsymbol{r};\mathbf{R})\hat{\nabla}_I \ .\end{aligned} \tag{1.9}$$

However, electronic and ionic Hamiltonians are still coupled, as far as the electronic energy level n enters in two terms of the ionic Hamiltonian. To deal with this, many times the adiabatic approximation[2] is assumed: the slow ionic motion does not cause any electronic excitations, since such a slow perturbation does not change the electronic eigenstates. This means that $\Delta\hat{\mathrm{H}}_n$ can be neglected and therefore, the ionic potential is just the electronic energy E_n^e obtained in the electronic problem, which is usually named as the Born-Oppenheimer Energy Surface (BOES).

Although the BOES changes for each electronic energy state n, we will just focus on solving the ionic problem corresponding to the ground state one ($n = 0$), which does not cause problems for most crystals at normal and low temperatures. According to the adiabatic approximation, the nuclear motion will not cause any electronic excitations so that the system will stay in its electronic ground state. Namely,

$$V(\mathbf{R}) \equiv E_{n=0}^e(\mathbf{R}) \ . \tag{1.10}$$

[2]In fact, Born-Oppenheimer approximation and adiabatic approximation terms are often used interchangeably, although they are not intrinsically the same. The adiabatic name comes from the absence of energy change among electrons and nuclei.

In this way, the electronic index n is dropped from the nuclear problem, successfully splitting the electronic and nuclear problems. All in all, the Hamiltonian that rules the ionic motion within the adiabatic approximation is:

$$\hat{\mathrm{H}}^{ion} = \hat{\mathrm{T}}_{ion} + \hat{V}(\mathbf{R}) \; . \tag{1.11}$$

The main features analysed throughout the project are related to the motion of ions and therefore, a deep understanding of the electronic problem lies beyond its scope. However, if the ionic motion is going to be analysed, handling previously with the electronic problem is mandatory in order to determine the BOES. In this sense, providing at least a brief introduction to the electronic problem is justified.

2

The electronic problem

The Born-Oppenheimer approximation has provided a crucial simplification by allowing us to decouple the electronic and ionic problems. However, even after this separation, the electronic problem remains challenging due to the coupling of electronic degrees of freedom through the electron-electron interaction term. This chapter focuses on density functional theory (DFT), the most widely used *ab initio* method nowadays for accurately describing the electronic structure of matter. For clarity and simplicity, we will omit the explicit dependence on ionic positions $\mathbf{R}$ from the discussion. Additionally, since the term $V_{ion,ion}$ is constant for a fixed ionic configuration in the electronic problem, it will be excluded from the following explanations.

2.1 Density Functional Theory

DFT was developed by Pierre Hohenberg, Walter Kohn, and Lu Sham in the mid-1960s as a novel approach to understanding the electronic structure of many-body systems. Although its practical application was initially limited by the computational power available at the time, the rapid increase in computational capabilities over the following decades made DFT an essential method in solid-state physics and chemistry. Its ability to provide accurate results with relatively low computational cost has led to a widespread use, leading Walter Kohn to the Nobel Prize in Chemistry in 1998.

As its name suggests, DFT relies on the electronic density $n(\mathbf{r})$ as a fundamental quantity, offering an alternative to the complex wavefunction $\Psi^e(\mathbf{r}_1, ..., \mathbf{r}_N)$ to obtain the properties of a system. In this way, the spatial variables of the problem are notably reduced from $3N$ to 3. The electronic density is defined as the number of electrons per unit volume at a given position $\mathbf{r}$. Formally, this can be expressed

as:

$$n(\mathbf{r}) = \langle \Psi^e | \sum_i^N \delta(\mathbf{r} - \mathbf{r}_i) | \Psi^e \rangle = N \int d^3\mathbf{r}_2 ... d^3\mathbf{r}_N |\Psi^e(\mathbf{r}, \mathbf{r}_2, ..., \mathbf{r}_N)|^2 \ . \tag{2.1}$$

In this definition the antisymmetry of the ground state wavefunction $\Psi^e(\mathbf{r}_1, ..., \mathbf{r}_N)$ with respect to the interchange of electronic coordinates has been incorporated, as we are dealing with a system formed by fermions. Besides, as this wavefunction is normalized, the condition $\int d^3\mathbf{r}\ n(\mathbf{r}) = N$ is fulfilled. Not only that, as in Hartree units the electronic charge is the unity, the function $n(\mathbf{r})$ describes both the electronic and the charge distribution.

2.1.1 Hohenberg-Kohn theorems

DFT is based on two fundamental theorems, proposed and proved by Hohenberg and Kohn in 1964 [42]:

- $\mathbf{1}^{st}$ **Theorem**: For any system of interacting particles in an external potential $V_{ext}(\mathbf{r})$, the potential $V_{ext}(\mathbf{r})$ is uniquely determined, except for a constant, by the ground state particle density $n(\mathbf{r})$.

  $\mathbf{1}^{st}$ **Corollary**: Since the Hamiltonian of the whole system (up to a constant shift in energy) is determined, in principle, so are the wavefunctions for all states. Thus, given $n(\mathbf{r})$, all the properties of the system are completely determined.

- $\mathbf{2}^{nd}$ **Theorem**: There exists a functional of the electronic density for the energy of the system $E[n]$ for any external potential $V_{ext}(\mathbf{r})$. The ground state energy of the system is the global minimum of this functional, being the density that minimizes it the ground state one $n_0(\mathbf{r})$. The mentioned functional can be written in the following way:

  $$E[n] = T[n] + V_{ee}[n] + V_{ext}[n] = F[n] + V_{ext}[n] = F[n] + \int d^3\mathbf{r}\ V_{ext}(\mathbf{r}) n(\mathbf{r}) \ . \tag{2.2}$$

  Here $F[n]$ is a universal functional, independent of the external potential and the specific system under study. It includes contributions from the kinetic energy of the electrons and the electron-electron interaction energy.

  $\mathbf{2}^{nd}$ **Corollary**: $E[n]$ alone is enough to determine the ground state energy and density.

In our specific problem of the electronic structure of a solid the external potential is the electron-ion interaction:

$$\hat{V}_{ext}(\mathbf{r}) = -\sum_{I=1}^{M} \frac{Z_I}{|\hat{\mathbf{r}} - \mathbf{R}_I|} \ . \tag{2.3}$$

2.1.2 The Kohn-Sham equations

The Hohenberg-Kohn theorems suggest solving the electronic problem by minimizing the functional $E[n]$, but they do not provide a specific formula for it. In this situation, Kohn and Sham introduced a new approach that made implementing DFT feasible. Precisely, they suggested replacing the actual interacting electronic system with a fictitious non-interacting system that yields the same ground state density as the original one. In this auxiliary system an effective potential $V_{KS}(\mathbf{r})$ acts on a set of independent electrons, so that the Hamiltonian for the non-interacting system can be expressed as:

$$\hat{\mathrm{H}} = \sum_{i=1}^{N_e} \hat{\mathrm{H}}_{KS}(\mathbf{r}_i) = \sum_{i=1}^{N_e} \left(-\frac{1}{2}\hat{\nabla}_i^2 + \hat{V}_{KS}(\mathbf{r}_i) \right) . \tag{2.4}$$

Thus, each Kohn-Sham orbital $\phi_i(\mathbf{r})$ is obtained by solving the single-particle Schrödinger equation:

$$\left(-\frac{1}{2}\hat{\nabla}^2 + \hat{V}_{KS}(\mathbf{r}) \right) \phi_i(\mathbf{r}) = \epsilon_i \phi_i(\mathbf{r}) . \tag{2.5}$$

Since electrons are fermions, the total electronic wavefunction must be constructed as a Slater determinant to ensure antisymmetry with respect to the interchange of any two electrons:

$$\Psi^e(\mathbf{r}_1, ..., \mathbf{r}_N) = \frac{1}{\sqrt{N!}} \begin{vmatrix} \phi_1(\mathbf{r}_1) & \phi_1(\mathbf{r}_2) & ... & \phi_1(\mathbf{r}_N) \\ \phi_2(\mathbf{r}_1) & \phi_2(\mathbf{r}_2) & ... & \phi_2(\mathbf{r}_N) \\ . & . & ... & . \\ . & . & ... & . \\ \phi_N(\mathbf{r}_1) & \phi_N(\mathbf{r}_2) & ... & \phi_N(\mathbf{r}_N) \end{vmatrix} .$$

It can be shown that the electron density of Eq. (2.1) can be expressed in terms of the single-particle wavefunctions as:

$$n(\mathbf{r}) = \sum_{i=1}^{N_e} |\phi_i(\mathbf{r})|^2 , \tag{2.6}$$

where the sum runs over the occupied states $\phi_i(\mathbf{r})$, with each orbital being doubly occupied due to spin degeneracy in accordance with Pauli's exclusion principle.

The initial step in deriving an expression for the effective potential in Eq. (2.5) involves defining the total energy of the system through the following functional:

$$E_{KS}[n] = T_s[n] + E_{Hartree}[n] + E_{xc}[n] + V_{ext}[n] . \tag{2.7}$$

The first term in this expression is the total kinetic energy, obtained by adding up the kinetic energy of each electron, treated as if they were independent as determined by the KS problem:

$$T_s(\{\phi_i[n]\}) = -\frac{1}{2} \sum_{i=1}^{N_e} \int d^3\mathbf{r}\ \phi_i^*(\mathbf{r}) \nabla_i^2 \phi_i(\mathbf{r}) . \tag{2.8}$$

The second term, the Hartree energy functional, is the classical electrostatic repulsion energy for charge distribution:

$$E_{Hartree}[n] = \frac{1}{2}\int d^3\mathbf{r}_1 d^3\mathbf{r}_2 \frac{n(\mathbf{r}_1)n(\mathbf{r}_2)}{|\mathbf{r}_1 - \mathbf{r}_2|} \,. \tag{2.9}$$

The third term is known as the exchange-correlation energy, which is composed by two elements. On the one hand, the exchange term has a purely quantum origin; the antisymmetry of the wavefunction. It can be understood as a repulsion between electrons due to Pauli's exclusion principle. On the other hand, the correlation term contains all the contributions associated to the fact that the total wavefunction cannot be written as a Slater determinant of single particle wavefunctions, and thus, contains a kinetic and potential part. Finally, the last term in Eq. (2.7) collects the interaction between the electronic density and the external potential, as in Eq. (2.2).

Minimizing this energy functional with respect to the orbital $\phi_i(\mathbf{r}_i)$ using Lagrange multipliers, a single-particle Schrödinger equation of type (2.5) describing the ground state is obtained:

$$\left(-\frac{1}{2}\hat{\nabla}^2 + \hat{V}_{Hartree}(\mathbf{r}) + \hat{V}_{xc}(\mathbf{r}) + \hat{V}_{ext}(\mathbf{r})\right)\phi_i(\mathbf{r}) = \epsilon_i\phi_i(\mathbf{r}) \,. \tag{2.10}$$

This set of equations, known as Kohn-Sham equations, allows to replace the problem of minimizing $E[n]$ by that of solving a non-interacting single-particle Schrödinger equation. The ground state density is constructed with the solutions of the Kohn-Sham equations following Eq. (2.6). Compared to Eq. (2.5), it is evident that the effective potential to choose in the auxiliary problem is

$$\hat{V}_{KS}(\mathbf{r}) = \hat{V}_{Hartree}(\mathbf{r}) + \hat{V}_{xc}(\mathbf{r}) + \hat{V}_{ext}(\mathbf{r}) \,, \tag{2.11}$$

with

$$\hat{V}_{Hartree}(\mathbf{r}) = \int d^3\mathbf{r}' \frac{n(\mathbf{r}')}{|\hat{\mathbf{r}} - \mathbf{r}'|} \tag{2.12}$$

$$\hat{V}_{xc}(\mathbf{r}) = \frac{\delta E_{xc}[n]}{\delta n(\mathbf{r})} \,. \tag{2.13}$$

In conclusion, the Kohn-Sham equations simplify the complex many-body problem to a set of equations for non-interacting electrons in an effective potential V_{KS}. These equations are coupled because the effective potential depends on the electronic density, which, in turn, depends on the Kohn-Sham orbitals, as described in Eq. (2.6). Consequently, they must be solved self-consistently. The primary limitation of this approach is the inability to describe the effective potential exactly, as there is no explicit analytical expression for the exchange-correlation term, requiring approximations. Among these, the local density approximation (LDA) and the generalized gradient approximation (GGA) are the most commonly used and will be briefly discussed.

2.1.3 LDA and GGA functionals

The local density approximation (LDA) assumes that the electronic density is locally uniform, even if the electron distribution is inhomogeneous. In the LDA, the exchange-correlation energy per particle at a point $\mathbf{r}$ with density $n(\mathbf{r})$ is approximated by that of a uniform electron gas with the same density:

$$E_{xc}^{LDA}[n] = \int d^3\mathbf{r}\; n(\mathbf{r})\; \epsilon_{xc}^{unif}[n(\mathbf{r})] \;. \tag{2.14}$$

Here, $\epsilon_{xc}^{\text{unif}}[n(\mathbf{r})]$ represents the exchange-correlation energy per particle of a uniform electron gas with local density $n(\mathbf{r})$. This exchange-correlation energy can be decomposed into two components:

$$\epsilon_{xc}^{unif}[n(\mathbf{r})] = \epsilon_{x}^{unif}[n(\mathbf{r})] + \epsilon_{c}^{unif}[n(\mathbf{r})]\,. \tag{2.15}$$

Being the exchange energy ϵ_x^{unif} the one obtained in the Hartree-Fock approximation for the uniform electron gas:

$$\epsilon_{x}^{unif}[n(\mathbf{r})] = -\frac{3}{4}\left(\frac{3}{\pi}\right)^{\frac{1}{3}} n^{\frac{1}{3}}. \tag{2.16}$$

While there is no exact analytic formula for the correlation energy ϵ_c^{unif}, this term has been calculated numerically for a range of electron densities using Monte Carlo methods [43]. These results have been fitted to a parametrized function $\epsilon_c(r_s)$, where r_s is the average electron distance defined as: $r_s = \left(\frac{3}{4\pi n}\right)^{\frac{1}{3}}$. The parametrized function $\epsilon_c(r_s)$ has to satisfy the known limits for both high and low electron densities. A widely used parametrization is provided by Perdew and Zunger [44], and is given by:

$$\epsilon_c(r_s) = \begin{cases} -0.0480 + 0.031\ln r_s - 0.0116 r_s + 0.0020 r_s \ln r_s & \text{if } r_s < 1 \\ -0.1423/(1 + 1.9529\sqrt{r_s} + 0.3334 r_s) & \text{if } r_s \geq 1. \end{cases} \tag{2.17}$$

Although this approximation may seem overly simplistic, it performs reasonably well for many systems, except for inhomogeneous systems such as isolated atoms or molecules. The correlation energy is typically overestimated, while the exchange energy is underestimated, leading to partially compensating errors [45]. Generally, LDA calculations are effective for predicting structural, elastic, and vibrational properties, though they fail to capture van der Waals forces due to their local nature.

Taking advantage of the good results obtained by the LDA scheme, semilocal approximations were developed in order to take into account the inhomogeneities of the electronic density. Semilocal functionals depend not only on the density at point $\mathbf{r}$, but also on neighbouring ones. In this sense, the gradient of the electronic density can be considered, as the generalized gradient approximation (GGA) does:

$$E_{xc}^{GGA}[n] = \int d^3\mathbf{r}\; f\left(n(\mathbf{r}), \nabla n(\mathbf{r})\right) \;. \tag{2.18}$$

There is no universal formula for the function $f\left(n(\mathbf{r}), \nabla n(\mathbf{r})\right)$, and a variety of models have been developed to approximate the exchange-correlation energy within the GGA framework. Among these, the PBE parametrization proposed by Perdew, Burke, and Ernzerhof [46] is particularly well-regarded and widely used for a broad range of applications.

2.1.4 Van der Waals interactions in DFT

LDA and GGA functionals have turned out successful in predicting structural, elastic and vibrational properties of materials with metallic, ionic or covalent bonds. However, due to their local or semilocal nature, these functionals only consider the electron density around a single point in space. This limitation is particularly problematic when dealing with van der Waals interactions, which are inherently non-local, arising from long-range interactions between fluctuating dipoles. As a result, conventional DFT functionals struggle to accurately describe these dispersive forces.

A straightforward way to account for van der Waals interactions is through the addition of empirical potential to conventional functionals. Specifically, the DFT-D approach involves adding a semi-empirical dispersion correction on top of a converged Kohn-Sham energy:

$$E_{DFT-D} = E_{DFT} + E_{disp} \ . \tag{2.19}$$

The DFT-D2 method of Grimme [47] proposes a semiempirical GGA−type density functional representing van der Waals interactions via a long-range pairwise force field:

$$E_{disp} = -s_6 \sum_{i=1}^{M-1} \sum_{j=i+1}^{M} \frac{C_6^{ij}}{R_{ij}^6} f_{damp}(R_{ij}) \ , \tag{2.20}$$

where s_6 is a global scaling factor that depends on the exchange-correlation functional used, having been optimized for the PBE functional. C_6^{ij} denotes the dispersion coefficient for the atom pair ij and R_{ij} the interatomic distance. To avoid divergences at small distances, this function is damped at short range via

$$f_{damp}(R_{ij}) = \frac{1}{1 + \exp^{-d(\frac{R_{ij}}{R_r} - 1)}} \ . \tag{2.21}$$

Here R_r is the sum of the van der Waals radii for atoms i and j, and d is an additional parameter. Default values for both R_r and C_6^{ij} are proposed in Grimme's original paper [47]. This empirical approach effectively balances accuracy and computational efficiency, making it a popular choice in practical DFT calculations.

Beyond these empirical methods, many efforts in recent years have focused on developing truly non-local exchange-correlation functionals that can effectively incorporate van der Waals dispersive interactions within DFT. One notable example is the vdW-DF functional proposed by Dion et al. in 2004 [48], which is particularly attractive as it is fundamentally based on the electron density.

The overall exchange-correlation energy is divided into two components: a GGA-type exchange-correlation part and a truly non-local correlation part $E_c^{nl}[n]$:

$$E_{xc}[n] = E_{xc}^{GGA}[n] + E_c^{nl}[n], \tag{2.22}$$

where the non-local part accounts for the van der Waals forces. This non-local component is expressed in a computationally tractable form involving a universal kernel $\Phi(\mathbf{r}, \mathbf{r}')$:

$$E_c^{nl}[n] = \frac{1}{2} \int d\mathbf{r}\, d\mathbf{r}'\, n(\mathbf{r})\Phi(\mathbf{r}, \mathbf{r}')n(\mathbf{r}'). \tag{2.23}$$

The kernel depends on the distance $|\mathbf{r}-\mathbf{r}'|$, as well as on the electronic density $n(\mathbf{r})$ and its gradient $\nabla n(\mathbf{r})$. Due to the double integration inherent in this formulation, non-local functionals tend to be quite computationally demanding . However, significant computational efficiency can be achieved by expressing the kernel in terms of cubic splines, allowing the two spatial integrals to be replaced by a single integral over Fourier-transformed quantities, which results in a considerable speedup [49].

2.2 Crystal periodicity

A crystalline solid is composed of periodic repetitions of its unit cell. Due to this inherent periodicity, the effective potential experienced by the electrons within the independent electron approximation (denoted in our DFT calculations as $V_{KS}(\mathbf{r})$) will also exhibit the periodicity of the Bravais lattice. Consequently, for any vector $\mathbf{T}$ belonging to the Bravais lattice:

$$V_{KS}(\mathbf{r}) = V_{KS}(\mathbf{r} + \mathbf{T}). \tag{2.24}$$

Bloch's theorem proves [50] that the eigenstates of a single electron Hamiltonian with a periodic potential can be expressed as plane waves modulated by a function with the periodicity of the lattice:

$$\phi_{n\mathbf{k}}(\mathbf{r}) = e^{i\mathbf{k}\cdot\mathbf{r}} u_{n\mathbf{k}}(\mathbf{r}), \tag{2.25}$$

where $u_{n\mathbf{k}}(\mathbf{r}) = u_{n\mathbf{k}}(\mathbf{r}+\mathbf{T})$ is the periodic part of the Kohn-Sham state. Note that now the eigenstates and eigenvalues of the Kohn-Sham Hamiltonian can be identified with the band index n and the wavevector $\mathbf{k}$ instead of the quantum number i that has been used so far: $\phi_i \to \phi_{n\mathbf{k}}$ and $\epsilon_i \to \epsilon_{n\mathbf{k}}$.

An equivalent formulation of Bloch's theorem is given by:

$$\phi_{n\mathbf{k}}(\mathbf{r} + \mathbf{T}) = e^{i\mathbf{k}\cdot\mathbf{T}} \phi_{n\mathbf{k}}(\mathbf{r}). \tag{2.26}$$

This formula demonstrates that if Bloch's theorem holds for a wavevector $\mathbf{k}$ within the first Brillouin zone (1BZ), it also holds for the wavevector $\mathbf{k'} = \mathbf{k} + \mathbf{G}$, where $\mathbf{G}$ is a reciprocal lattice vector. Since $e^{i\mathbf{G}\cdot\mathbf{T}} = 1$ by definition of reciprocal lattice vectors, the eigenstates and eigenvalues are periodic with respect to the reciprocal lattice vectors:

$$\phi_{n\mathbf{k}+\mathbf{G}}(\mathbf{r}) = \phi_{n\mathbf{k}}(\mathbf{r}), \qquad \epsilon_{n,\mathbf{k}+\mathbf{G}} = \epsilon_{n,\mathbf{k}}. \tag{2.27}$$

Thus, the entire electronic structure can be determined by calculating the eigenvalues and eigenstates only for wavevectors within the first Brillouin zone, avoiding redundancy. This information defines the electronic band structure of the solid.

It is important to note that the wavevectors $\mathbf{k}$ cannot take arbitrary values. Due to the Born–von Karman (BvK) periodic boundary conditions, which impose periodicity over the entire crystal by treating it as if it was infinitely repeating in all directions, the wavevectors $\mathbf{k}$ are quantized. Specifically, these boundary conditions restrict the number of allowed $\mathbf{k}$ vectors to be equal to the number of primitive cells N_{cell} in the crystal:

$$\mathbf{k} = \sum_{i=1}^{3} \frac{n_i}{N_i} \mathbf{b}_i \quad ; \quad n_i \in (0, N_i - 1) \tag{2.28}$$

where $\mathbf{b}_i$, $i = 1, 2, 3$ are the primitive reciprocal lattice vectors, and N_i is the number of primitive cells in the direction of $\mathbf{b}_i$. Consequently, the total number of primitive cells in the crystal is given by $N_{cell} = N_1 N_2 N_3$.

2.2.1 The plane-wave basis

As it is well-established, a Hamiltonian operator can be expressed in any orthonormal basis. For periodic systems, a plane-wave basis, denoted as $|\mathbf{k}\rangle$, is particularly appropriate because it naturally aligns with the translational symmetry of the crystal lattice. The plane-wavefunctions are defined as:

$$\langle \mathbf{r}|\mathbf{k}\rangle = \frac{1}{\sqrt{\Omega}} e^{i\mathbf{k}\cdot\mathbf{r}}, \tag{2.29}$$

where Ω denotes the volume of the entire crystal.

Due to the periodicity of the crystal potential, the Kohn-Sham Hamiltonian takes the following form in the plane-wave basis:

$$\langle \mathbf{k}+\mathbf{G}|\hat{\mathrm{H}}_{KS}|\mathbf{k}+\mathbf{G}'\rangle = \frac{1}{2}|\mathbf{k}+\mathbf{G}|^2 \delta_{\mathbf{G},\mathbf{G}'} + V_{KS}(\mathbf{G}-\mathbf{G'}). \tag{2.30}$$

Here the kinetic energy is diagonal. The periodicity of the crystal potential results in coupling only those plane waves whose wavevectors differ by a reciprocal lattice vector $\mathbf{G}$. The strength of this coupling is characterized by $V_{KS}(\mathbf{G}-\mathbf{G'})$, which represents the Fourier component of the Kohn-Sham potential.

Then, the Hamiltonian in the plane-wave basis is block-diagonal, with each block characterized by a specific crystal momentum $\mathbf{k}$. Consequently, each block can be independently diagonalized by solving the Kohn-Sham Hamiltonian at every $\mathbf{k}$-point allowed by the Born–von Karman boundary conditions within the 1BZ. The eigenvalues obtained at each $\mathbf{k}$-point correspond to the band energies $\epsilon_{n\mathbf{k}}$. For a given band index n, the eigenvectors are formed by the coefficients $C^n_{\mathbf{k}+\mathbf{G}}$. These

coefficients are the essential components needed to construct the Kohn-Sham states from the plane-wave expansion:

$$|\phi_{n\mathbf{k}}\rangle = \sum_{\mathbf{G}} C^n_{\mathbf{k}+\mathbf{G}} \, |\mathbf{k}+\mathbf{G}\rangle \,, \tag{2.31}$$

$$\phi_{n\mathbf{k}}(\mathbf{r}) = \langle \mathbf{r}|\phi_{n\mathbf{k}}\rangle = \frac{1}{\sqrt{\Omega}} \sum_{\mathbf{G}} C^n_{\mathbf{k}+\mathbf{G}} e^{i(\mathbf{k}+\mathbf{G})\cdot\mathbf{r}} = e^{i\mathbf{k}\cdot\mathbf{r}} \left(\frac{1}{\sqrt{\Omega}} \sum_{\mathbf{G}} C^n_{\mathbf{k}+\mathbf{G}} e^{i\mathbf{G}\cdot\mathbf{r}} \right). \tag{2.32}$$

It is therefore evident that the resulting eigenfunctions are indeed Bloch functions.

Although each wavevector $\mathbf{k}$ can, in principle, couple with any reciprocal lattice vector, resulting in theoretically infinite block sizes, this is impractical for actual computations and approximations have to be made. Thus, for practical calculations, we restrict the blocks to a finite size by defining a cutoff energy, E_{cut}, such that only plane waves with energies below this cutoff are included in the expansion:

$$\frac{1}{2}|\mathbf{k}+\mathbf{G}|^2 \leq E_{cut}. \tag{2.33}$$

This criterion may sometimes be insufficient. As discussed in the next section, localized electron wavefunctions might require a significantly larger number of $\mathbf{G}$ vectors for an accurate description.

Finally, the electron density can be computed from the Kohn-Sham states using the following expression:

$$n(\mathbf{r}) = \sum_{n} \sum_{\mathbf{k}}^{\text{1BZ}} f_{n\mathbf{k}} |\phi_{n\mathbf{k}}(\mathbf{r})|^2, \tag{2.34}$$

where the summation is performed over the 1BZ, and the occupation number $f_{n\mathbf{k}}$ is given by the Fermi-Dirac distribution:

$$f_{n\mathbf{k}} = \frac{2}{e^{\beta(\epsilon_{n\mathbf{k}}-\epsilon_F)}+1}. \tag{2.35}$$

Here, the factor of 2 accounts for the spin degeneracy of the Kohn-Sham states. $\beta = 1/k_B T$, where k_B is Boltzmann's constant and T the temperature. The Fermi energy ϵ_F represents the highest occupied energy level.

In principle, the Kohn-Sham Hamiltonian in Eq. (2.30) should be diagonalized at every $\mathbf{k}$-point within the first Brillouin zone allowed by the Born-von Karman boundary conditions. However, since the number of allowed $\mathbf{k}$-points is of the order of $N_{cell} \sim 10^{23}$, sampling the entire Brillouin zone is computationally infeasible. Instead, the zone is divided into a finite grid of $\mathbf{k}$-points using the Monkhorst-Pack algorithm [51], which must be optimized. The Monkhorst-Pack mesh should be fine enough to ensure convergence of the $\mathbf{k}$-point sum in Eq. (2.34) and produce an accurate electronic density.

Moreover, in metals, the discretization of the reciprocal space is specially critical, as at T = 0 K the **k**-points that are occupied or unoccupied change abruptly. As a consequence, the electronic density changes considerably between iterations of the self-consistent cycle, which slows down the convergence drastically. To mitigate this issue without using a denser **k**-point grid, the Fermi-Dirac step function is substituted by a smoother one, the so-called smearing function, introducing effectively a fake temperature. For this purpose, we have employed the Methfessel-Paxton smearing method [52], in which the broadening of the smearing function is an additional parameter to optimize. The ultimate goal is to obtain converged values using the smallest possible **k**-point grid, approaching the limits of zero smearing and an infinite number of **k**-points.

2.3 The pseudopotential approximation

In a solid, core and valence electrons play fundamentally different roles. Core electrons are tightly bound to the nucleus, experiencing minimal influence from other atoms. As a result, their wavefunctions are highly localized. In contrast, valence electrons, which reside in the outer layers, have broader wavefunctions and are more likely to interact with those of neighbouring atoms. These valence electrons are primarily responsible for bonds between atoms and chemical reactions, while core electrons largely remain uninvolved in such processes.

The localized and highly oscillatory wavefunctions of core electrons are difficult to describe accurately in a plane-wave basis without using a large number of such functions. This scenario implies a large cutoff energy E_{cut} and results in large matrices for diagonalization, requiring a great computational effort. On the contrary, valence electrons, being less tightly bound, require fewer plane waves for an accurate representation. In this situation, pseudopotentials are used to replace the core electrons and the nucleus with an effective potential that acts on the valence electrons. By focusing only on the valence electrons, the computational load is reduced, while still accurately capturing the essential physics of the material.

The process of constructing a pseudopotential begins with the calculation of the electronic configuration of an isolated atom, typically using DFT. The valence electrons are then selected and used to construct the pseudopotential. The goal is to create a potential that reproduces the scattering properties of the actual ion, but with a much smoother, less oscillatory wavefunction for the valence electrons within a certain cutoff radius around the nucleus. Inside this cutoff radius, the true oscillatory wavefunction is replaced by a smoother function, while outside the radius, the true wavefunction is used. The cutoff radius is chosen such that this replacement does not affect the material's overall description.

By inverting the Schrödinger equation, one eventually obtains the pseudopotential that produces the corresponding smooth wavefunction for each valence electron:

$$\left(-\frac{1}{2}\nabla_i^2 + V_i^{ps}(\mathbf{r})\right)\phi_i^{ps}(\mathbf{r}) = \epsilon_i \phi_i^{ps}(\mathbf{r}). \tag{2.36}$$

The pseudopotential $V_i^{ps}(\mathbf{r})$ replaces the full electron-ion potential $V_{ext(\mathbf{r})}$ in the Kohn-Sham equations. As a result, the equations only need to be solved for the valence electrons, which significantly simplifies the computational workload.

There are various types of pseudopotentials, each with its own method of construction and application. In this work we have employed both norm-conserving [53] and ultrasoft [54] pseudopotentials. Norm-conserving pseudopotentials are designed to ensure that the pseudowavefunction preserves the total charge within the core radius, consistent with the all-electron wavefunction. Still, the norm-conserving constrain often requires a high plane-wave cutoff to properly describe the core region, which can be counterproductive and computationally expensive. To address this issue, ultrasoft pseudopotentials were developed. By removing the norm-conservation constraint, ultrasoft pseudopotentials allow for a softer potential that approximates the effect of core electrons with a reduced plane-wave cutoff. However, because norm-conservation is not enforced, there is a deficit of valence charge in the core region. The price to be paid is a more complicated expression for the charge density, where augmentation charges are introduced to compensate for the missing valence charge.

3

The ionic problem

The adiabatic Born-Oppenheimer approximation discussed in Chapter 1 has allowed us to decouple the electronic and ionic problems. In Chapter 2, we have addressed the electronic problem assuming a fixed ionic configuration. Many properties of solids are fairly good described within this static lattice model; for instance, this is the case of metallic transport properties. However, many others, like specific heats and thermal expansion, arise due to lattice dynamics. Even the electron-phonon coupling in superconductivity cannot be well characterized without taking into account the ionic degrees of freedom. In order to know about the notable ionic motion, the ionic problem in Eq. (1.11) has to be solved. In this problem, the ions move in a potential defined by the previously calculated electronic total ground state energy, which is commonly referred to as the Born-Oppenheimer Energy Surface (BOES).

In the ionic problem the positions of the nuclei are not fixed parameters any more. That is to say, ions in a crystal oscillate around their equilibrium lattice sites $\mathbf{R}^0$, which correspond to the ionic configuration that minimizes the BOES. Precisely, the position of the s^{th} ion in the n^{th} unit cell is

$$\mathbf{R}_{ns} = \mathbf{T}_n + \mathbf{d}_s + \mathbf{u}_s(\mathbf{T}_n) = \mathbf{R}^0_{ns} + \mathbf{u}_s(\mathbf{T}_n) \,, \tag{3.1}$$

where $\mathbf{T}_n$ is the Bravais lattice vector pointing to the origin of the corresponding primitive cell and $\mathbf{d}_s$ is the position vector of the s^{th} ion inside the cell. The sum of these two vectors results in the position vector $\mathbf{R}^0_{ns}$ that indicates the equilibrium lattice site of the s^{th} ion in the n^{th} cell. Finally, the vector $\mathbf{u}_s(\mathbf{T}_n)$ denotes the displacement of the corresponding atom from its equilibrium position.

The BOES is an extremely complex energy landscape, since it contains an enormous number of degrees of freedom, around $\sim 10^{23}$, corresponding to the vast number of atoms in a typical solid. In this situation, as a first assumption it is considered that the ionic displacements $\mathbf{u}_s(\mathbf{T}_n)$ are much smaller than the

interatomic distances. This premise of small oscillations seems reasonable in the case of most solids that are at temperatures well below their melting point. In this way, a Taylor expansion of the BOES can be developed around the $\mathbf{R}^0$ ionic positions that minimize the energy:

$$V(\mathbf{R}) = V(\mathbf{R}^0) + \sum_{n=2}^{\infty} V_n,$$

$$V_n = \frac{1}{n!} \sum_{\substack{s_1,\dots,s_n \\ \alpha_1,\dots,\alpha_n \\ \mathbf{T}_1,\dots,\mathbf{T}_n}} \phi_{s_1\dots s_n}^{\alpha_1\dots\alpha_n}(\mathbf{T}_1,\dots,\mathbf{T}_n)\, u_{s_1}^{\alpha_1}(\mathbf{T}_1)\dots u_{s_n}^{\alpha_n}(\mathbf{T}_n), \tag{3.2}$$

with $\phi_{s_1\dots s_n}^{\alpha_1\dots\alpha_n}(\mathbf{T}_1,\dots,\mathbf{T}_n)$ being the n-th order force constants defined as:

$$\phi_{s_1\dots s_n}^{\alpha_1\dots\alpha_n}(\mathbf{T}_1,\dots,\mathbf{T}_n) = \left[\frac{\partial^n V(\mathbf{R})}{\partial u_{s_1}^{\alpha_1}(\mathbf{T}_1)\dots\partial u_{s_n}^{\alpha_n}(\mathbf{T}_n)}\right]_{\mathbf{R}=\mathbf{R}^0}. \tag{3.3}$$

The number of possible lattice vectors $\mathbf{T}$ is equal to the number of unit cells. The atom index s ranges from 1 to p, which is the number of atoms per unit cell, while α corresponds to the Cartesian coordinates x, y and z. The first term in Eq. (3.2) represents the energy at equilibrium. Moreover, since we are at a local minimum of the BOES, the first-order term in the expansion V_1 is zero by definition. Namely, each linear term is proportional to the forces acting on individual ions, and at equilibrium all forces must be zero. Therefore, V_1 does not contribute to the energy expansion and is omitted from the formula.

In standard computational methods, understanding this energy landscape is crucial for analysing the material's response to variations in its lattice vectors $\{\mathbf{a}_i\}$. These variations are described by the strain tensor ϵ, which transforms the lattice parameters as follows:

$$a'_{i\alpha} = \sum_{\beta} (\delta_{\alpha\beta} + \epsilon_{\alpha\beta}) a_{i\beta}, \tag{3.4}$$

where α, β are the Cartesian coordinates. When using standard computational approaches for lattice relaxation, the Born-Oppenheimer stress tensor is calculated to quantify how changes in the lattice parameters affect the electronic energy of the system. This stress tensor is defined as:

$$P_{\alpha\beta}^{(\mathrm{BO})} = -\frac{1}{\Omega}\left[\frac{\partial V(\mathbf{R})}{\partial \epsilon_{\alpha\beta}}\right]_{\epsilon=0}, \tag{3.5}$$

where Ω is the volume of the simulation box. It is important to note that at this level of approximation the contribution of the ions to the energy is neglected and therefore, the Born-Oppenheimer stress tensor does not account for the thermal or quantum fluctuations of the ions.

3.1 The harmonic approximation

The harmonic approximation assumes that the properties of a system are accurately described when the expansion of the BOES about its minimum is truncated at the second order. This is the lowest-order approximation that accounts for ionic displacements, as the linear term vanishes when the expansion is performed around the minimum of the BOES. Therefore, the harmonic expansion of the ionic potential takes the following form:

$$V^{harm}(\mathbf{R}) = V(\mathbf{R}^0) + \frac{1}{2}\sum_{\substack{s,s'\\ \alpha,\alpha'\\ n,n'}} \Phi_{ss'}^{\alpha\alpha'}(\mathbf{T}_n, \mathbf{T}_{n'}) u_s^{\alpha}(\mathbf{T}_n) u_{s'}^{\alpha'}(\mathbf{T}_{n'}) \ . \tag{3.6}$$

Before calculating the eigenvalues of the harmonic Hamiltonian, it is convenient to introduce the analysis of the classical normal modes of the ions. In the case of a crystal formed by the repetition of N_{cell} unit cells, each containing a polyatomic basis of p ions, there are $3pN_{cell}$ Newtonian equations of motion; one for each of the three Cartesian components of the displacement of the total pN_{cell} ions. These equations can be expressed as:

$$M_s \ddot{u}_s^{\alpha}(\mathbf{T}_n) = -\frac{\partial V^{harm}(\mathbf{R})}{\partial u_s^{\alpha}(\mathbf{T}_n)} = -\sum_{n's'\alpha'} \Phi_{ss'}^{\alpha\alpha'}(\mathbf{T}_n, \mathbf{T}_{n'}) u_{s'}^{\alpha'}(\mathbf{T}_{n'}) \ . \tag{3.7}$$

It is desirable to solve these equations for the normal modes of the crystal, namely, those in which all ions oscillate at a common frequency w. With this aim, using a wave ansatz, we seek solutions of the form:

$$u_s^{\alpha}(\mathbf{T}_n, t) = \epsilon_s^{\alpha}(\mathbf{q}) e^{i(\mathbf{q}\cdot\mathbf{T}_n - w(\mathbf{q})t))} \ . \tag{3.8}$$

Due to the well-known Born-Von Karman boundary conditions, the possible values of $\mathbf{q}$ that yield different displacements reduce to the number of unit cells N_{cell}. Substituting Eq. (3.8) into (3.7), the Fourier transform of the interatomic force constants appears:

$$\Phi_{ss'}^{\alpha\alpha'}(\mathbf{q}, \mathbf{q}') = \frac{1}{N_{cell}} \sum_{n,n'} \Phi_{ss'}^{\alpha\alpha'}(\mathbf{T}_n, \mathbf{T}_{n'}) e^{-i(\mathbf{q}\cdot\mathbf{T}_n + \mathbf{q}'\cdot\mathbf{T}_{n'})}. \tag{3.9}$$

Due to the translational symmetry of the Bravais lattice, the force constants only depend on the relative position between two sites: $\mathbf{T}_n - \mathbf{T}_{n'}$. As a result, only the terms with $\mathbf{q}' = -\mathbf{q}$ are non-zero, simplifying Eq. (3.9) to:

$$\Phi_{ss'}^{\alpha\alpha'}(\mathbf{q}) = \Phi_{ss'}^{\alpha\alpha'}(\mathbf{q}, -\mathbf{q}) = \sum_{n} \Phi_{ss'}^{\alpha\alpha'}(\mathbf{T}_n) e^{-i\mathbf{q}\cdot\mathbf{T}_n} \ . \tag{3.10}$$

Here, we have used the translational symmetry of the Bravais lattice: $\Phi_{ss'}^{\alpha\alpha'}(\mathbf{T}_n, \mathbf{T}_{n'}) = \Phi_{ss'}^{\alpha\alpha'}(\mathbf{T}_n - \mathbf{T}_{n'}, 0) \equiv \Phi_{ss'}^{\alpha\alpha'}(\mathbf{T}_n - \mathbf{T}_{n'})$. Later on the index of the summatory has been redefined.

The problem is then reduced to the diagonalization of the dynamical matrix, defined as:

$$D_{ss'}^{\alpha\alpha'}(\mathbf{q}) = \frac{\Phi_{ss'}^{\alpha\alpha'}(\mathbf{q})}{\sqrt{M_s M_{s'}}}, \tag{3.11}$$

which is a $3p \times 3p$ tensor. The eigenvalue problem for this matrix can be expressed as:

$$\sum_{s'\alpha'} D_{ss'}^{\alpha\alpha'}(\mathbf{q})\epsilon_{s'\mu}^{\alpha'}(\mathbf{q}) = w_\mu^2(\mathbf{q})\epsilon_{s\mu}^{\alpha}(\mathbf{q}). \tag{3.12}$$

In this equation, the frequencies of the normal modes $w_\mu^2(\mathbf{q})$ are the eigenvalues, while the polarization vectors $\epsilon_{s'\mu}^{\alpha'}(\mathbf{q})$ are the corresponding eigenvectors. The index μ ($\mu = 1, ..., 3p$) represents the branch index, and $\mathbf{q}$ is a wavevector located within the first Brillouin zone.

Remarkably, for a crystal with a basis containing p ions, the number of normal modes for each value of $\mathbf{q}$ is $3p$, which matches the number of degrees of freedom in a unit cell. Additionally, since there are as many distinct $\mathbf{q}$ vectors as there are unit cells in the crystal, the total number of normal modes amounts to $3pN_{cell}$. This coincides with the total number of degrees of freedom in the entire crystal, underscoring the consistency of the vibrational modes with the system's structural properties.

In classical mechanics, the diagonalization of the dynamical matrix yields the normal modes of the harmonic crystal, corresponding each of them to an independent harmonic oscillator. Within quantum theory of the harmonic crystal, it can be shown [50] through a procedure involving the bosonic creation and annihilation operators, $\hat{b}_{\mu\mathbf{q}}^\dagger$ and $\hat{b}_{\mu\mathbf{q}}$ respectively, that the ionic Hamiltonian can be written as

$$\hat{\mathrm{H}}^{ion} = \hat{V}_0 + \sum_\mu \sum_{\mathbf{q}}^{1BZ} w_\mu(\mathbf{q}) \left(\hat{b}_{\mu\mathbf{q}}^\dagger \hat{b}_{\mu\mathbf{q}} + \frac{1}{2} \right) . \tag{3.13}$$

The second term is just the sum of $3pN_{cell}$ independent quantum harmonic oscillators, corresponding each addend to a classical normal mode in Eq. (3.12). It is well known from quantum mechanics that the energy spectrum of a quantum harmonic oscillator is discrete, being the energy step between two adjacent energy levels constant. Specifically, the contribution to the total energy of the normal mode with frequency $w_\mu(\mathbf{q})$ is:

$$E_{\mu\mathbf{q}} = \left(n_{\mu\mathbf{q}} + \frac{1}{2} \right) w_\mu(\mathbf{q}) \, , \tag{3.14}$$

where $n_{\mu\mathbf{q}}$ is the quantum number of excitation of the corresponding mode, which is restricted to zero and integer values. However, it is usual not to speak about excitation numbers, but about equivalent quasiparticles called phonons. In this complementary nomenclature, when a certain normal mode is excited to its $n_{\mu\mathbf{q}}^{th}$ level, it is said that there are $n_{\mu\mathbf{q}}$ phonons of type μ and momentum $\mathbf{q}$. Definitely, phonons are the energy quanta $w_\mu(\mathbf{q})$ in lattice vibrations. As phonons must be

bosons, their distribution function obeys Bose-Einstein statistics:

$$n_B(w_\mu(\mathbf{q})) = \frac{1}{e^{\frac{w_\mu(\mathbf{q})}{k_B T}} - 1} , \tag{3.15}$$

where $w_\mu(\mathbf{q})$ is the energy of the corresponding phonon.

Thus, the total energy of the Hamiltonian of the system at a given temperature within the harmonic approximation is determined by $3pN_{cell}$ quantum numbers $n_{\mu\mathbf{q}}$:

$$E = V_0 + \sum_\mu \sum_{\mathbf{q}}^{1BZ} \left(n_{\mu\mathbf{q}} + \frac{1}{2} \right) w_\mu(\mathbf{q}) . \tag{3.16}$$

If one wishes to study the phonons of a crystalline solid, the harmonic phonon dispersion relation has to be plotted in the first Brillouin zone, which is more commonly known as the harmonic phonon spectrum.

3.2 Density Functional Perturbation Theory

To solve the ionic problem within the harmonic approximation, it is imperative to calculate the second derivatives of the ionic potential $V(\mathbf{R})$, as these allow us to obtain the dynamical matrices needed to describe the vibrational properties of a system. Unfortunately, calculating *ab initio* these derivatives can be extremely cumbersome. A common approach is the finite displacement method, where atoms are displaced from their equilibrium positions, and the resulting energies and/or forces are calculated using DFT. This method allows for a direct and intuitive way to derive the force constants by taking numerical derivatives of the forces with respect to the atomic displacements. However, this procedure has significant limitations. Not only are calculations involving supercells in DFT computationally expensive, but accurate phonon calculations are also restricted to **q**-points that are commensurate with the supercell size, thereby limiting the exploration of the phonon dispersion across the Brillouin zone.

As an alternative, perturbative methods such as density functional perturbation theory (DFPT) can be employed, which allow for the direct calculation of dynamical matrices and phonon frequencies at arbitrary **q**-points without the need for a supercell. In particular, these approaches leverage quantum mechanical perturbation theory to evaluate how ionic displacements affect electronic properties, enabling accurate phonon calculations across the Brillouin zone.

The first derivatives of the potential with respect to atomic displacements are relatively straightforward to compute, thanks to the Hellmann-Feynman theorem [55, 56]. According to this theorem, the force on an atom can be expressed as:

$$\frac{\partial V(\mathbf{R})}{\partial u_a} = \frac{\partial E^e(\mathbf{R})}{\partial u_a} = \langle \Psi^e | \frac{\partial \hat{\mathrm{H}}^e}{\partial u_a} | \Psi^e \rangle = \frac{\partial V_{ion,ion}}{\partial u_a} + \int d\mathbf{r} n(\mathbf{r}) \frac{\partial V_{ext}(\mathbf{r})}{\partial u_a} . \tag{3.17}$$

Here and from now on, we use the single index $a \equiv (\mathbf{T}_n, s, \alpha)$ to represent both atoms and Cartesian coordinates. The relation in the previous equation holds because the only explicit dependence on the ionic coordinates in the electronic Hamiltonian comes from the ion-ion electrostatic interaction term and the external potential. The second derivatives at equilibrium, which are necessary for calculating the force constants, are then given by:

$$\Phi_{ab} = \left[\frac{\partial^2 V}{\partial u_a \partial u_b}\right]_{\mathbf{R}^0} = \left[\frac{\partial^2 V_{ion,ion}}{\partial u_a \partial u_b}\right]_{\mathbf{R}^0} + \\ + \int d\mathbf{r} \left[\frac{\partial n(\mathbf{r})}{\partial u_a}\right]_{\mathbf{R}^0} \left[\frac{\partial V_{ext}(\mathbf{r})}{\partial u_b}\right]_{\mathbf{R}^0} + \int d\mathbf{r}\, n(\mathbf{r}) \left[\frac{\partial^2 V_{ext}(\mathbf{r})}{\partial u_a \partial u_b}\right]_{\mathbf{R}^0} . \tag{3.18}$$

This equation illustrates how the phonon properties are linked to the electronic structure. Specifically, calculating the second derivatives of the ionic potential requires not only the electron density $n(\mathbf{r})$ but also its variation with respect to ionic displacements. This dependency remarks why such calculations can be complex and computationally demanding. By employing DFPT, these challenging derivatives are handled more efficiently.

The essence of density functional perturbation theory (DFPT) [57–59] is to apply first order perturbation theory to calculate the variation of the Kohn-Sham levels and orbitals when the ions are displaced from their equilibrium position. The Kohn-Sham problem was established in Eq. (2.5) and the electronic density given in Eq. (2.6). With this in mind, it is useful to define the first order term of the Taylor expansion of a general function f in the ionic displacements as

$$\Delta f(\mathbf{r}) = \sum_a \left[\frac{\partial f(\mathbf{r})}{\partial u_a}\right]_{\mathbf{R}^0} u_a \, , \tag{3.19}$$

and making this first order expansion in the Kohn-Sham effective Hamiltonian, the eigenvalues, the eigenfunctions, and the density:

$$\begin{aligned} \hat{\mathrm{H}}_{KS} &\to \hat{\mathrm{H}}_{KS} + \Delta\hat{\mathrm{H}}_{KS} \\ \epsilon_{n\mathbf{k}} &\to \epsilon_{n\mathbf{k}} + \Delta\epsilon_{n\mathbf{k}} \\ |\phi_{n\mathbf{k}}\rangle &\to |\phi_{n\mathbf{k}}\rangle + |\Delta\phi_{n\mathbf{k}}\rangle \\ n(\mathbf{r}) &\to n(\mathbf{r}) + \Delta n(\mathbf{r}), \end{aligned}$$

where the eigenvalues and eigenvectors of the Kohn-Sham Hamiltonian are identified by the band index n and the wavevector $\mathbf{k}$, while $\langle \mathbf{r} | \Delta\phi_{n\mathbf{k}} \rangle = \Delta\phi_{n\mathbf{k}}(\mathbf{r})$. Then the eigenvalue problem at linear order is

$$\left(\hat{\mathrm{H}}_{KS} - \epsilon_{n\mathbf{k}}\right) |\Delta\phi_{n\mathbf{k}}\rangle = -\left(\Delta\hat{\mathrm{H}}_{KS} - \Delta\epsilon_{n\mathbf{k}}\right) |\phi_{n\mathbf{k}}\rangle \tag{3.20}$$

and the linear variation of the electronic density:

$$\Delta n(\mathbf{r}) = 2\ \mathrm{Re}\left[\sum_n \sum_{\mathbf{k}}^{1BZ} f_{n\mathbf{k}} \phi^*_{n\mathbf{k}}(\mathbf{r}) \Delta\phi_{n\mathbf{k}}(\mathbf{r})\right], \tag{3.21}$$

where the occupation of the Kohn-Sham states is ruled by the Fermi-Dirac distribution $f_{n\mathbf{k}}$.

Eq. (3.20) is known as the Sternheimer equation [60] and is the perturbed version of the Kohn-Sham equation settled in Eq. (2.5). Finally, the expression for the linear change of the Hamiltonian, ΔH_{KS}, can be derived by means of functional derivatives:

$$\Delta H_{KS} = \Delta V_{ext}(\mathbf{r}) + \int d\mathbf{r}' \left(\frac{1}{|\mathbf{r} - \mathbf{r}'|} + f^{xc}(\mathbf{r}, \mathbf{r}', w = 0) \right) \Delta n(\mathbf{r}') \, . \tag{3.22}$$

Remarkably, Eqs. (3.20)–(3.22) form a set of self-consistent equations for the perturbed system that can be solved following an analogous loop to the one introduced in the Kohn-Sham problem. Equivalently, we could have defined the problem in terms of $\left[\frac{\partial n(\mathbf{r})}{\partial u_s^\alpha}\right]_{\mathbf{R}^0}$ instead of $\Delta n(\mathbf{r})$, as the set of self-consistent equations must hold for each coefficient in the linear expansion (3.19). In conclusion, the DFPT formalism introduced above gives the derivatives of the density required to obtain the dynamical matrices.

In this work, harmonic dynamical matrices have been obtained within DFPT using the *ph.x* package from the Quantum Espresso software [61, 62]. Ideally, dynamical matrices should be computed for all **q**-points in the first Brillouin zone, corresponding to the number of cells in the crystal. However, due to the computational expense of DFPT, a more feasible approach is to sample the first Brillouin zone with a small uniform grid of **q**-points, for which dynamical matrices are subsequently calculated. Then, a discrete Fourier transform is performed to obtain the interatomic force constants matrix for the real-space supercell. In this sense, basic properties of discrete Fourier analysis reveal that longer-ranged real-space force constants require finer **q**-point grids for convergence. Finally, Fourier interpolation estimates phonon modes and frequencies at arbitrary wavevectors using the interatomic force constants. These final steps are carried out using the *q2r.x* and *matdyn.x* packages in Quantum Espresso.

3.3 Beyond the harmonic approximation

Thus far, the resolution of the ionic problem has relied on two key assumptions. First, we have assumed that the ionic displacements from their equilibrium positions are much smaller than the interatomic distances. Second, we have assumed that the properties of solids can be adequately described by truncating the expansion of the ionic potential at second order around its minimum. The first assumption, known as the small oscillations approximation, is generally valid for most solids at temperatures below their melting point. However, the second assumption, referred to as the harmonic approximation, is more restrictive, as many important physical phenomena arise from the anharmonic terms that are neglected in this approach.

The harmonic approximation predicts that phonons are well-defined quasiparticles with an infinite lifetime and whose energy does not depend on temperature. These two characteristics represent inherent failures of the harmonic approximation. In reality, phonons have finite lifetimes due to anharmonic interactions with other phonons (and other interactions, such as the electron–phonon coupling), as evidenced by the measurable width of phonon peaks in inelastic x-ray or neutron scattering experiments. Additionally, experimental observations show that phonon energies do depend on temperature, as exemplified by the softening and eventual collapse of certain phonon modes near second-order phase transitions. In fact, one of the primary objectives of this thesis is to theoretically characterize this phenomenon through *ab initio* calculations in charge density wave systems. This task is even more challenging considering that the harmonic approximation also fails to explain the stability of the corresponding high-temperature undistorted phase, as evinced by imaginary phonon frequencies that indicate that certain atomic displacements can lead to spontaneous distortions. Finally, the harmonic approximation can sometimes even fail to predict the correct equilibrium positions of the ions, as the experimentally observed positions may not correspond to the minimum of the potential. Therefore, to accurately address all such phenomena, it is necessary to move beyond the standard harmonic approximation and incorporate anharmonic terms into the description.

A common method for introducing anharmonic effects is through perturbation theory, where the higher-order terms in the expansion of the BOES are treated as perturbations. These terms describe interactions between phonons, giving rise to processes such as phonon creation, annihilation, and scattering. Although perturbative approaches can effectively capture important phenomena like the temperature dependence of phonons and their finite lifetimes, they completely collapse when the anharmonic terms in the potential become comparable to or larger than the harmonic terms within the range of the ionic fluctuations. This situation typically arises when ionic displacements are large, particularly in systems containing light ions or when the material approaches a displacive phase transition, such as the previously mentioned charge density wave instabilities. In all such cases the anharmonic effects are no longer small corrections but rather dominate the system's behaviour, requiring non-perturbative approaches for an accurate description.

Therefore, to effectively address strong anharmonic effects, as we aim to do in this thesis, employing a non-perturbative approach is essential. Anharmonic effects at a non-perturbative level are typically addressed using molecular dynamics simulations [63]. However, these methods are computationally intensive and do not account for quantum fluctuations. Path-integral molecular dynamics [64] do incorporate the quantum nature of atomic vibrations, but it involves an even greater computational cost. In this thesis, we will employ instead a stochastic implementation of the Self-Consistent Harmonic Approximation (SCHA) [1]. Despite its computational demands, this method provides a more efficient alternative to path integral molecular dynamics while still accurately capturing quantum effects.

3.3.1 The Self-Consistent Harmonic Approximation (SCHA)

The Self-Consistent Harmonic Approximation (SCHA), introduced by Hooton in 1955 [1], provides a non-perturbative treatment of anharmonicity that incorporates both thermal and quantum effects on the ionic vibrations. The non-perturbative nature entails that the Born-Oppenheimer energy surface is not approximated at any stage. Instead, the SCHA establishes a variational method based on the free energy of the ionic Hamiltonian, making it suitable at any temperature.

Namely, at a fixed temperature T, the free energy of the ionic Hamiltonian in Eq. (1.11), denoted as $H \equiv H^{ion}$ in this section, is determined by the sum of the internal energy and the entropic contribution:

$$F_H = \mathrm{tr}(\rho_H H) + \frac{1}{\beta}\mathrm{tr}(\rho_H \ln \rho_H) = -\frac{1}{\beta}\ln Z_H \ , \tag{3.23}$$

where the partition function is $Z_H = \mathrm{tr}(e^{-\beta H})$, the density matrix $\rho_H = e^{-\beta H}/Z_H$ and $\beta = 1/(k_B T)$.

Given the complexity of the many-body system, directly calculating the exact free energy is not feasible. Instead, a quantum variational principle in the free energy can be formulated by replacing the actual density matrix by any other $\rho_{\mathcal{H}}$ defined by a trial Hamiltonian $\mathcal{H} = T_{ion} + \mathcal{V}$. The resulting free energy functional is then expressed as:

$$F_H(\mathcal{H}) = \mathrm{tr}(\rho_{\mathcal{H}} H) + \frac{1}{\beta}\mathrm{tr}(\rho_{\mathcal{H}} \ln \rho_{\mathcal{H}}) \ , \tag{3.24}$$

which satisfies the so-called Gibbs-Bogoliubov inequality:

$$F_H \leq \mathcal{F}_H(\mathcal{H}) \ . \tag{3.25}$$

Adding and subtracting $\mathrm{tr}(\rho_{\mathcal{H}}\mathcal{H})$ in equation (3.24) leads to:

$$F_H(\mathcal{H}) = F_{\mathcal{H}} + \mathrm{tr}[\rho_{\mathcal{H}}(V - \mathcal{V})] \ . \tag{3.26}$$

The equality in equation (3.25) is evidently satisfied when $\mathcal{H} = H$. Therefore, minimizing $F_H(\mathcal{H})$ with respect to the trial Hamiltonian $\mathcal{H}$ establishes a quantum variational principle for the free energy valid at any temperature.

Even if the variational principle is valid for any trial potential $\mathcal{V}$, the SCHA method restricts it to a harmonic one. As a result, the trial Hamiltonian takes the well-known general form:

$$\mathcal{H} = T_{ion} + \mathcal{V} = \sum_{a=1}^{3M} \frac{{P_a}^2}{2M_a} + \frac{1}{2}\sum_{ab}^{3M}(R_a - \mathcal{R}_a)\Phi_{ab}(R_b - \mathcal{R}_b) \ . \tag{3.27}$$

The trial Hamiltonian $\mathcal{H}$ is then determined by two groups of parameters: the ionic equilibrium positions $\boldsymbol{\mathcal{R}}$ and the auxiliary second-order force constants matrix $\boldsymbol{\Phi}$. Here and henceforth, we will use bold symbols to denote vectors or tensors in component free notation.

The assumption of a harmonic trial potential simplifies the minimization process, as the probability density to find the system in a general ionic configuration $\mathbf{R} \equiv \{\mathbf{R}_1, ..., \mathbf{R}_M\}$ can be expressed in an analytic form in terms of the parameters of the auxiliary Hamiltonian $\mathcal{H}$. Specifically, the SCHA probability distribution function itself is expressed as a product of Gaussians:

$$\rho_{\mathcal{H}}(\mathbf{R}) = \langle \mathbf{R} | \rho_{\mathcal{H}} | \mathbf{R} \rangle = \sqrt{\det(\boldsymbol{\Psi}^{-1}/2\pi)} \exp\left(-\sum_{ab} \frac{1}{2} \Psi^{-1}_{ab} (R_a - \mathcal{R}_a)(R_b - \mathcal{R}_b) \right) . \tag{3.28}$$

Here, det represents the determinant. At this point, it is important to emphasize that what we have referred to as "ionic equilibrium positions" are, in fact, the expected values of the position operator:

$$\langle \mathbf{R} \rangle_{\rho_{\mathcal{H}}} = \boldsymbol{\mathcal{R}}, \tag{3.29}$$

which in turn correspond to the centroids of the trial Gaussian probability distribution function. In this sense the centroid positions are not necessarily equivalent to the ionic positions at the minimum of the BOES. On the other hand, the variance of the Gaussians is represented by $\boldsymbol{\Psi}$, which is the displacement–displacement correlation matrix, defined as:

$$\Psi_{ab} = \langle u_a u_b \rangle_{\rho_{\mathcal{H}}} = \frac{1}{\sqrt{M_a M_b}} \sum_{\mu} \frac{(1 + 2n_B(\omega_{\mu\mathcal{H}}))}{2\omega_{\mu\mathcal{H}}} \varepsilon^a_{\mu\mathcal{H}} \varepsilon^b_{\mu\mathcal{H}}, \tag{3.30}$$

where $u_a = R_a - \mathcal{R}_a$ indicates the displacement from the average atomic position. This analytic form depends on the phonon frequencies $\omega_{\mu\mathcal{H}}$ and polarization vectors $\varepsilon^a_{\mu\mathcal{H}}$ that are obtained by diagonalizing the dynamical matrix associated with the auxiliary force constants matrix $\boldsymbol{\Phi}$:

$$\sum_b \frac{\Phi_{ab}}{\sqrt{M_a M_b}} \varepsilon^b_{\mu\mathcal{H}} = \omega^2_{\mu\mathcal{H}} \varepsilon^a_{\mu\mathcal{H}}. \tag{3.31}$$

On the other hand, $n_B(\omega)$ in Eq. (3.30) is the bosonic average occupation number. To ensure that the distribution function $\rho_{\mathcal{H}}(\mathbf{R})$ is normalizable, it is essential for $\boldsymbol{\Psi}$ and thus $\boldsymbol{\Phi}$ to be positive-definite matrices.

Considering this probability density, the quantum statistical average of any observable $O(\mathbf{R})$ that is exclusively function of the ionic positions is given by

$$\langle O \rangle_{\rho_{\mathcal{H}}} = \mathrm{tr}(\rho_{\mathcal{H}} O) = \int d\mathbf{R}\, \rho_{\mathcal{H}}(\mathbf{R}) O(\mathbf{R}) \, . \tag{3.32}$$

Making use of this last expression, the free energy in the equality (3.26) can be rewritten through the simple formula:

$$F_H(\mathcal{H}) = F_{\mathcal{H}} + \int d\mathbf{R}[V(\mathbf{R}) - \mathcal{V}(\mathbf{R})]\rho_{\mathcal{H}}(\mathbf{R}) \,, \tag{3.33}$$

where $F_{\mathcal{H}}$ is the harmonic free energy given by

$$F_{\mathcal{H}} = \sum_{\mu=1}^{3M} \left\{ \frac{1}{2}\omega_{\mu\mathcal{H}} - \frac{1}{\beta} \ln\left[1 + n_B(\omega_{\mu\mathcal{H}})\right] \right\}, \tag{3.34}$$

$V(\mathbf{R})$ the BOES of ionic configuration $\mathbf{R}$ and $\mathcal{V}(\mathbf{R})$ is the trial harmonic energy for the same configuration.

The quantum variational principle for free energy involves minimizing the functional $F_H(\mathcal{H})$ with respect to the trial harmonic Hamiltonian $\mathcal{H}$. This minimization process depends on knowing the gradient of the free energy with respect to its independent coefficients. Given that the harmonic free energy and the probability density have analytic forms, these gradients can be computed analytically as follows:

$$\frac{\partial F_H(\mathcal{H})}{\partial \mathcal{R}_a} = -\left\langle f^a(\mathbf{R}) - f^a_{\mathcal{H}}(\mathbf{R}) \right\rangle_{\rho_{\mathcal{H}}} , \tag{3.35}$$

$$\frac{\partial F_H(\mathcal{H})}{\partial \Phi_{ab}} = \frac{1}{2} \sum_{cd} \frac{\partial \Psi_{cd}}{\partial \Phi_{ab}} \left\langle \left(f^d(\mathbf{R}) - f^d_{\mathcal{H}}(\mathbf{R})\right) \sum_e \Psi^{-1}_{ce}(R_e - \mathcal{R}_e) \right\rangle_{\rho_{\mathcal{H}}} , \tag{3.36}$$

where $\frac{\partial F_H(\mathcal{H})}{\partial \mathcal{R}_a}$ is the gradient with respect to the centroid positions and $\frac{\partial F_H(\mathcal{H})}{\partial \Phi_{ab}}$ with respect to the force constants. Here, $\mathbf{f}(\mathbf{R})$ represents the atomic forces for the ionic configuration $\mathbf{R}$, and $\mathbf{f}_{\mathcal{H}}(\mathbf{R})$ denotes the forces derived from the auxiliary potential $\mathcal{V}$:

$$f^a_{\mathcal{H}}(\mathbf{R}) = -\frac{\partial \mathcal{V}(\mathbf{R})}{\partial R_a} = -\sum_b \Phi_{ab}(R_b - \mathcal{R}_b). \tag{3.37}$$

The main challenge in calculating the free energy and its gradient arises from the integrals in Eqs. (3.33)-(3.36), due to the unknown explicit formulas for the potential $V(\mathbf{R})$ and by extension, for the atomic forces $\mathbf{f}(\mathbf{R})$. The usual approach in this situation is assuming a Taylor expansion of the potential [65], but computing higher-order force constants can be a complex and time-consuming task. Instead, the stochastic implementation of the SCHA method proposes using a random sampling method to estimate these integrals, taking advantage of the analytic nature of the ionic probability density $\rho_{\mathcal{H}}(\mathbf{R})$, as detailed in the next section.

3.3.2 The Stochastic Self-Consistent Harmonic Approximation (SSCHA)

The stochastic implementation of the Self-Consistent Harmonic Approximation (SSCHA) was introduced to address the challenges of computing the integrals in the gradient of the free energy analytically [66]. In this method, these integrals are substituted by finite sums using a set of stochastic ionic configurations $\{\mathbf{R}_I\}_{I=1,\dots,N_c}$ generated in a supercell from the harmonic distribution $\rho_{\mathcal{H}}(\mathbf{R})$ in Eq. (3.28). The calculation of quantum statistical averages for operators dependent only on the ionic positions is then simplified as:

$$\int d\mathbf{R} O(\mathbf{R}) \rho_{\mathcal{H}}(\mathbf{R}) \simeq \frac{1}{N_c} \sum_{I}^{N_c} O(\mathbf{R}_I). \tag{3.38}$$

Here N_c are the number of created ionic configurations, while $O(\mathbf{R}_I)$ is the value of the operator $O(\mathbf{R})$ at a certain ionic configuration $\mathbf{R}_I$. Evidently, the sum recovers the value of the integral in the limit $N_c \to \infty$, where the stochastic error vanishes. Therefore, the free energy gradients in Eqs. (3.35)-(3.36) can be determined through this stochastic procedure by calculating the energies and atomic forces on each of the $\mathbf{R}_I$ configurations.

The SSCHA minimization is conducted using a conjugate gradient (CG) algorithm, and it takes place within a subspace of parameters that preserves the crystal symmetries. The whole minimization process is sketched in the flowchart of Fig. 3.1. The minimization of the free energy is started from an arbitrary initial harmonic Hamiltonian $\mathcal{H}_0$ (in the initial step j = 0). The usual procedure is to start from the real harmonic Hamiltonian of the system obtained through a previous DFPT calculation. However, it is essential to adjust any imaginary frequencies to ensure stability in the harmonic approximation. Then, based on the corresponding density matrix $\rho_{\mathcal{H}_0}$, N_c ionic configurations are generated. The energy and atomic forces for each configuration are then computed within supercells, which allows to perform the stochastic calculation of the free energy gradients. Subsequently, a conjugate gradient step is performed to update both the equilibrium positions $\boldsymbol{\mathcal{R}}$ and the force constants $\boldsymbol{\Phi}$, leading to a new auxiliary Hamiltonian $\mathcal{H}_j$.

In principle, in order to obtain the gradient in the next step of the CG minimization, Born-Oppenheimer energies and atomic forces should be recalculated using a new set of configurations generated with the updated distribution $\rho_{\mathcal{H}_j}(\mathbf{R})$. However, from experience is known that generally hundreds of steps are needed to reach the minimum of the free energy, so that, undoubtedly, calculating total energies and forces every CG step using an *ab initio* engine would be exorbitantly time-demanding. To address this problem, a reweighting technique is introduced, which consists of introducing the factor $\rho_{\mathcal{H}_j}(\mathbf{R})/\rho_{\mathcal{H}_{j_0}}(\mathbf{R})$ in the integral evaluation at step j of the CG minimization:

$$\langle O \rangle_{\rho_{\mathcal{H}_j}} = \int d\mathbf{R} O(\mathbf{R}) \rho_{\mathcal{H}_j}(\mathbf{R}) \simeq \frac{1}{N_c} \sum_{I=1}^{N_c} O(\mathbf{R}_I) \frac{\rho_{\mathcal{H}_j}(\mathbf{R}_I)}{\rho_{\mathcal{H}_{j_0}}(\mathbf{R}_I)} , \tag{3.39}$$

where j_0 is the step of the minimization at which the configurations where generated. This reweighting technique is valid as far as the normalization condition of $\rho_{\mathcal{H}_j}$, given by $\langle \rho_{\mathcal{H}_j} / \rho_{\mathcal{H}_{j_0}} \rangle$, does not deviate significantly from the unity. Actually, the Kong-Liu effective sample size is a more reliable statistical parameter to check [67] :

$$N_j^{\text{eff}} = \frac{\sum_{I=1}^{N_c} \rho_j^2(I)}{\left(\sum_{I=1}^{N_c} \rho_j(I)\right)^2}, \tag{3.40}$$

where $\rho_j(I) = \frac{\rho_{\mathcal{H}_j}(\mathbf{R}_I)}{\rho_{\mathcal{H}_{j_0}}(\mathbf{R}_I)}$. The Kong-Liu ratio quantifies how much of the weighted samples contribute to the averages, helping to determine whether the sample set is diverse or dominated by a few high-weight configurations. If the effective sample size N_j^{eff} remains sufficiently large, it suggests that the reweighting process is effective and that the weighted samples provide a reliable estimate. In this case the CG step is performed, updating the auxiliary Hamiltonian $\mathcal{H}_j$ and allowing the minimization loop to proceed. On the contrary, if at any step j the following condition is met:

$$\frac{N_j^{\text{eff}}}{N_c} < \eta, \tag{3.41}$$

where η is input parameter around 0.5, it signals a potential problem. Specifically, the set of configurations $\mathbf{R}_I$ created out of $\mathcal{H}_{j_0}$ does not represent accurately the updated distribution $\rho_{\mathcal{H}_j}$, and the minimization is stopped due to poor statistics. In this case, the minimization is restarted with new configurations generated from $\mathcal{H}_j$. Each of these sets of ionic configurations is formally referred to as a "population". Multiple populations may be needed before reaching the free energy minimum, depending primarily on the starting point of the minimization process.

In principle, the minimization loop has to go on until the gradient goes to zero. Since achieving a true vanishing gradient is nearly impossible, it is accepted that the minimum of the free energy is reached when all components of the gradient are below a specified threshold value. In practice, different threshold values may be required for each of the gradients, and these should be chosen to ensure proper convergence of the SCHA frequencies and equilibrium positions. Once the convergence is reached, one can always add extra configurations to the penultimate population, reducing the statistical error and obtaining more accurate results.

The centroid positions at the free energy minimum $\boldsymbol{\mathcal{R}}_{eq}$ are the average ionic positions fully accounting for quantum, thermal and anharmonic effects, following Eq. (3.29). The dynamical matrix based on the final force constants $\boldsymbol{\Phi}$,

$$\mathrm{D}_{ab}^{(\mathrm{S})} = \frac{1}{\sqrt{M_a M_b}} \Phi_{ab}(\boldsymbol{\mathcal{R}}_{eq}), \tag{3.42}$$

determines the amplitude of the vibrations around these equilibrium positions, and is, thus, positive definite by construction; as explained, the harmonic density matrix would diverge otherwise. In this sense, the positive phonon frequencies

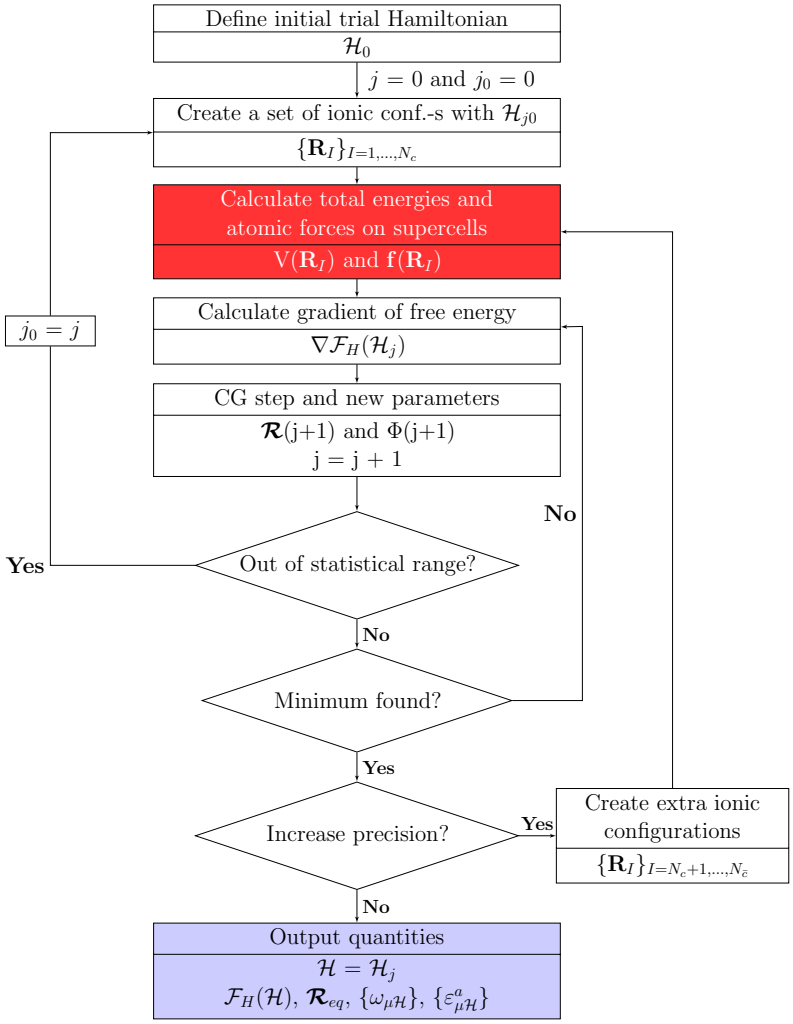

Figure 3.1: Flowchart of the SSCHA minimization process. The block in red, which corresponds to the calculation of the total energies and atomic forces on supercells, is where nearly all the computation time goes when an *ab initio* method is used.

derived from this dynamical matrix do not represent the true renormalized anharmonic phonon spectra, as they fail to account for second-order phase transitions where frequencies can collapse to zero. As it is explained in Section 3.3.4, these auxiliary phonon frequencies should just be considered as components of the variational problem, and only acquire physical meaning beyond this mean-field approximation.

3.3.3 The stress tensor in the SSCHA

At the conclusion of the SSCHA minimization, it is also possible to obtain the anharmonic stress tensor $\mathbf{P}$, which incorporates the effects of both quantum and thermal ionic fluctuations. This stress tensor is calculated by evaluating the derivatives of the free energy with respect to the strain tensor ϵ as follows [67]:

$$P_{\alpha\beta} = -\frac{1}{\Omega}\left[\frac{\partial \mathcal{F}_H(\mathcal{H})}{\partial \epsilon_{\alpha\beta}}\right]_{\epsilon=0} = \left\langle P^{(\mathrm{BO})}_{\alpha\beta}(\mathbf{R})\right\rangle_{\rho_{\mathcal{H}}} - \frac{1}{2\Omega}\sum_{s=1}^{M}\left\langle u_s^{\alpha}(\mathbf{R}) f_s^{\beta}(\mathbf{R}) + u_s^{\beta}(\mathbf{R}) f_s^{\alpha}(\mathbf{R})\right\rangle_{\rho_{\mathcal{H}}}. \tag{3.43}$$

In this formula, we explicitly distinguish the Cartesian coordinates α, β and the atomic index s. For atomic displacements $\mathbf{u}(\mathbf{R})$ and forces $\mathbf{f}(\mathbf{R})$, the lower index refers to the atomic index, while the upper index denotes the Cartesian coordinate. On the other side, Ω is the volume of the simulation box, and $\mathbf{P}^{(\mathrm{BO})}(\mathbf{R})$ is the classical stress tensor for the configuration with the ions displaced to $\mathbf{R}$, as defined in Eq. (3.5). Thus, to numerically compute the SCHA stress tensor within the stochastic framework of Eq. (3.38), it is necessary to calculate both the forces and the classical stress tensor for each structure in the ensemble.

Additionally, the knowledge of the anharmonic stress tensor $\mathbf{P}$ allows for the relaxation of the lattice parameters during the SSCHA minimization. To update the lattice, the stress tensor is computed when the free energy minimization with respect to $\boldsymbol{\mathcal{R}}$ and $\boldsymbol{\Phi}$ at constant volume has stopped, whether due to poor statistics or because the free energy minimum has been reached. Then, the following strain is applied:

$$\epsilon_{\alpha\beta} = \Omega\left(P_{\alpha\beta} - P^{*}\delta_{\alpha\beta}\right). \tag{3.44}$$

where P^{*} is the target pressure of the relaxation, and $\delta_{\alpha\beta}$ is the Kronecker delta. With this strain, the lattice vectors $\{\mathbf{a}_i\}$ are updated for the next population as follows:

$$a'_{i\alpha} = a_{i\alpha} + \lambda_{\{\mathbf{a}_i\}}\sum_{\beta}\epsilon_{\alpha\beta}a_{i\beta}, \tag{3.45}$$

where $\lambda_{\{\mathbf{a}_i\}}$ is the update step. The best $\lambda_{\{a_i\}}$ step is obtained with $\lambda_{\{a_i\}} = \frac{1}{3\Omega B_0}$, with B_0 being the bulk modulus.

3.3.4 Second-order structural phase transitions in the SSCHA

Ehrenfest's classification scheme, proposed in 1933 [68], was the initial attempt to categorize phase transitions based on thermodynamic properties. In this scheme, second-order phase transitions are characterized by a discontinuity in the second derivative of the free energy with respect to a thermodynamic variable, while the first derivative remains continuous across the transition. This implies that quantities like entropy and magnetization change smoothly, without any abrupt jumps, while response functions like the heat capacity or the magnetic susceptibility show sudden changes at the transition point.

Landau's theory, formulated in 1937 [19, 69], refined the understanding of second-order phase transitions by introducing the concept of an order parameter, a scalar or vectorial magnitude that distinguishes between different phases. In this framework, at high temperatures, the system exhibits higher symmetry, and the order parameter is typically zero. As the temperature drops below the critical temperature T_c, the order parameter changes continuously from zero to a non-zero value, signalling the emergence of a new phase with lower symmetry. This gradual evolution, characteristic of second-order phase transitions, contrasts with the abrupt jumps in the order parameter observed in first-order transitions. The different behaviour of the order parameter in first and second-order phase transitions is illustrated in Fig. 3.2. This distinction emphasizes that Landau's theory specifically applies to second-order phase transitions, making the order parameter a crucial variable for characterizing their nature. In the case of displacive phase transitions, such as ferroelectric and charge density wave transitions, the order parameters are the average atomic positions measured in diffraction experiments, which correspond to the centroid positions that the SSCHA minimization specifically optimizes.

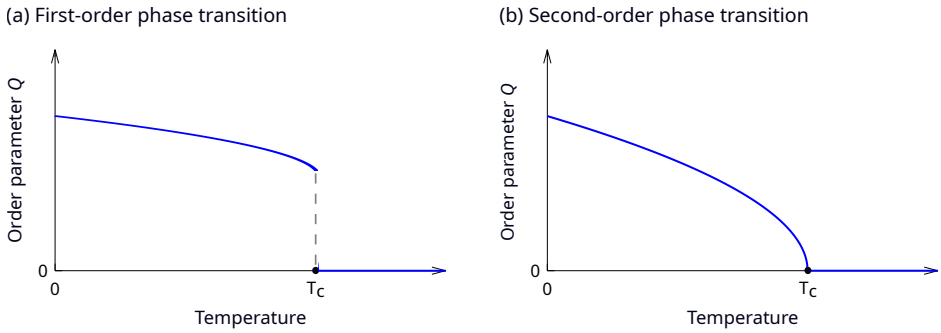

Figure 3.2: Comparison of the order parameter behaviour in (a) first-order and (b) second-order phase transitions. (a) In a first-order transition, the order parameter exhibits a discontinuous jump at T_c, indicating a sudden phase change. (b) In a second-order transition, the order parameter evolves smoothly and continuously from zero to a finite value as the temperature decreases below T_c.

A key aspect of Landau's framework for second-order phase transitions is that the free energy of a system near the transition can be expressed as an expansion in terms of the order parameter. Since a system at equilibrium will always minimize its free energy, above the critical temperature T_c, this minimum corresponds to the high-symmetry phase where the order parameter is zero. As the temperature approaches the critical temperature, this free energy minimum becomes shallower, ultimately turning into a saddle point at T_c. At lower temperatures, the system transitions to a lower-symmetry configuration with non-zero order parameter, for which the free energy minimum is lower. This behaviour is plotted in Fig. 3.3. In displacive phase transitions, this change of curvature can be characterized through the second derivative of the free energy with respect to the centroids in the high-symmetry configuration. Namely, the free energy Hessian is positive-definite at high temperatures, but lowering the temperature it develops at least a null eigenvalue right at the critical temperature. Lowering further the temperature, this eigenvalue finally becomes negative, indicating a distortion that decreases the free energy. Definitely, the knowledge of the temperature evolution of the free energy curvature with respect to the centroids in a high-symmetry configuration allows the identification of second-order displacive phase transitions, including charge density waves. However, it should be remarked that not all charge density waves are associated with second-order transitions [70], and therefore, this theory may not fully address those scenarios.

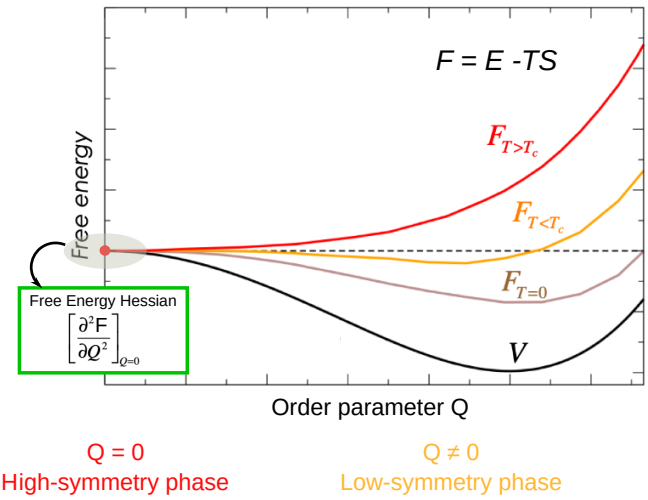

Figure 3.3: Free energy landscape in a second-order phase transition. As the temperature decreases towards the critical temperature, the free energy minimum shifts from a high-symmetry state, flattens at the critical temperature, and transitions into a lower-symmetry phase. The temperature-dependent evolution of the free energy curvature, particularly with respect to the order parameters in a high-symmetry configuration, is crucial for identifying and characterizing second-order phase transitions.

Using the SSCHA code, one could compute the free energy for a set of distorted atomic configurations, which then enables the numerical calculation of the mentioned curvature at each temperature using finite differences, as described in Ref. [71]. However, this numerical approach is computationally intensive due to the large number of configurations in the ensemble required by the finite differences method to reduce the stochastic error. Moreover, it involves performing SCHA minimizations in the low-symmetry distorted phase, which is more challenging because the reduced symmetry increases the number of free parameters in the trial Hamiltonian.

To address this issue, Bianco et al. [41] presented a specific analytic formula for the SCHA free energy curvature with respect to centroid positions, which avoids the departure from the high-symmetry configuration to calculate derivatives of the free energy and estimate the occurrence of second-order phase transitions. In component-free notation the curvature is given by:

$$\frac{\partial^2 F}{\partial \boldsymbol{\mathcal{R}} \partial \boldsymbol{\mathcal{R}}} = \boldsymbol{\Phi} + \overset{(3)}{\boldsymbol{\Phi}} \boldsymbol{\Lambda}(0) [\mathbf{1} - \overset{(4)}{\boldsymbol{\Phi}} \boldsymbol{\Lambda}(0)]^{-1} \overset{(3)}{\boldsymbol{\Phi}} , \tag{3.46}$$

where $\overset{(n)}{\boldsymbol{\Phi}}$ are the n-th order anharmonic force constants, which are calculated as quantum averages taken with the SSCHA density matrix: $\overset{(n)}{\boldsymbol{\Phi}} = \left\langle \frac{\partial^n V}{\partial \mathbf{R}^n} \right\rangle_{\rho_{\mathcal{H}}}$. The negative-definite fourth-order tensor $\boldsymbol{\Lambda}(0)$ is the static limit of the dynamical tensor $\boldsymbol{\Lambda}(z)$. For a generic complex number z, the components of the latter tensor are defined as:

$$\Lambda^{abcd}(z) = -\frac{\hbar^2}{8} \sum_{\mu\nu} \frac{F(z, \omega_\mu, \omega_\nu)}{\omega_\mu \omega_\nu} \varepsilon_\mu^a \varepsilon_\nu^b \varepsilon_\mu^c \varepsilon_\nu^d , \tag{3.47}$$

where ω_μ^2 and ε_μ^a are the eigenvalues and corresponding eigenvectors of the auxiliary SSCHA dynamical matrix $\mathbf{D}^{(\mathrm{S})}$ in Eq. (3.42), and

$$F(z, \omega_\mu, \omega_\nu) = \frac{2}{\hbar} \left[\frac{(\omega_\mu + \omega_\nu)[1 + n_B(\omega_\mu) + n_B(\omega_\nu)]}{(\omega_\mu + \omega_\nu)^2 - z^2} - \frac{(\omega_\mu - \omega_\nu)[n_B(\omega_\mu) - n_B(\omega_\nu)]}{(\omega_\mu - \omega_\nu)^2 - z^2} \right] . \tag{3.48}$$

Then, the free energy Hessian based dynamical matrix can be considered a temperature-dependent generalization of the harmonic dynamical matrix, in which quantum, thermal and anharmonic effects are included. Namely:

$$\mathbf{D}^{(\mathrm{F})} = \frac{1}{\sqrt{\mathbf{M}}} \frac{\partial^2 F}{\partial \boldsymbol{\mathcal{R}} \partial \boldsymbol{\mathcal{R}}} \frac{1}{\sqrt{\mathbf{M}}} = \mathbf{D}^{(\mathrm{S})} + \overset{(3)}{\mathbf{D}} \boldsymbol{\Lambda}(0) [\mathbf{1} - \overset{(4)}{\mathbf{D}} \boldsymbol{\Lambda}(0)]^{-1} \overset{(3)}{\mathbf{D}}. \tag{3.49}$$

Here, $M_{ab} = \delta_{ab} M_a$ is the mass matrix, $\mathbf{D}^{(\mathrm{S})}$ is the auxiliary dynamical matrix in

Eq. (3.42), and $\overset{(n)}{\mathbf{D}}$ are the dynamical matrices associated with the n-th order anharmonic force constants:

$$\overset{(3)}{\mathrm{D}}_{abc} = \frac{\overset{(3)}{\Phi}_{abc}}{\sqrt{M_a M_b M_c}} = \frac{1}{\sqrt{M_a M_b M_c}} \left\langle \frac{\partial^3 V}{\partial R_a \, \partial R_b \, \partial R_c} \right\rangle_{\rho_{\mathcal{H}}}, \tag{3.50}$$

$$\overset{(4)}{\mathrm{D}}_{abcd} = \frac{\overset{(4)}{\Phi}_{abcd}}{\sqrt{M_a M_b M_c M_d}} = \frac{1}{\sqrt{M_a M_b M_c M_d}} \left\langle \frac{\partial^3 V}{\partial R_a \, \partial R_b \, \partial R_c \, \partial R_d} \right\rangle_{\rho_{\mathcal{H}}}. \tag{3.51}$$

Then, the temperature-dependent anharmonic phonons are obtained by diagonalizing this matrix through the equation:

$$\sum_b \mathrm{D}^{(\mathrm{F})}_{ab} \epsilon^b_\mu = \Omega^2_\mu \epsilon^a_\mu. \tag{3.52}$$

Negative values of the anharmonic phonon frequencies Ω_μ indicate a structural distortion that decreases the free energy. This information can be used to determine CDW transition temperatures, since the CDW will appear when $\mathbf{D}^{(\mathrm{F})}$ develops a negative eigenvalue in the high-symmetry phase upon lowering the temperature. This technique has been successful in the characterization of displacive structural phase transitions in a large variety of strongly anharmonic systems, such as superconducting hydrides [72, 73], thermoelectric compounds [74, 75], and materials hosting CDWs [76–78].

3.3.5 Dynamical theory of the SSCHA

The theory introduced in the latter section is static in the sense that it is not based on time-dependent properties, but on the variation of the free energy with respect to a static variation of the centroid positions. In order to build a quantum anharmonic dynamical theory, Bianco et al. [41] formulated an *ansatz* for the interacting phonon Green function $\mathbf{G}(i\Omega_n)$ for the variable $\sqrt{M_a}(R^a - \mathcal{R}^a_{eq})$. In this formulation, $\Omega_n = 2\pi n/\beta$ is the nth bosonic Matsubara frequency [79]. Later, Monacelli et al. [80] and Lihm et al. [81] simultaneously proved this *ansatz* to be correct. The interacting SCHA phonon propagator can be calculated from the Dyson-type relation:

$$\mathbf{G}(i\Omega_n) = \mathbf{G}^{(0)}(i\Omega_n) + \mathbf{G}^{(0)}(i\Omega_n)\mathbf{\Pi}(i\Omega_n)\mathbf{G}(i\Omega_n), \tag{3.53}$$

as illustrated in the Feynman diagram representation shown in Fig. 3.4 (a). Here $\mathbf{G}^{(0)}(i\Omega_n)$ is the non-interacting SCHA auxiliary phonon propagator, described by the dynamical matrix of the SSCHA effective harmonic Hamiltonian:

$$[\mathbf{G}^{(0)}]^{-1}(i\Omega_n) = (i\Omega_n)^2 \mathbf{1} - \mathbf{D}^{(\mathrm{S})}. \tag{3.54}$$

By combining these equations, one arrives to:

$$\mathbf{G}^{-1}(i\Omega_n) = (i\Omega_n)^2 \mathbf{1} - (\mathbf{D}^{(\mathrm{S})} + \mathbf{\Pi}(i\Omega_n)). \tag{3.55}$$

In these equations $\mathbf{\Pi}(i\Omega_n)$ is the SCHA dynamical self-energy, and it is defined as:

$$\mathbf{\Pi}(i\Omega_n) = \overset{(3)}{\mathbf{D}}\mathbf{\Lambda}(i\Omega_n)[\mathbf{1} - \overset{(4)}{\mathbf{D}}\mathbf{\Lambda}(i\Omega_n)]^{-1}\overset{(3)}{\mathbf{D}} \,. \tag{3.56}$$

where the n-th order anharmonic dynamical matrices $\overset{(n)}{\mathbf{D}}$ are defined in Eqs. (3.50) and (3.51). The fourth-order tensor $\mathbf{\Lambda}(i\Omega_n)$ is defined in Eq. (3.47) for a general complex number z; in the last equation, z specifically denotes a Matsubara frequency. Figure 3.4 (b) provides the diagrammatic representation of this self-energy. For future applications, it is useful to express the SCHA self-energy in the basis of the SCHA auxiliary modes, after performing a Fourier transform. This gives:

$$\Pi_{\mu\nu}(\mathbf{q}, i\Omega_n) = \sum_{ab} \Pi_{ab}(\mathbf{q}, i\Omega_n)\varepsilon^a_\mu(-\mathbf{q})\varepsilon^b_\nu(\mathbf{q}), \tag{3.57}$$

where $\varepsilon^a_\mu(\mathbf{q})$ are the eigenvectors of the SCHA auxiliary dynamical matrix in the reciprocal space, $\mathbf{D}^{(\mathrm{S})}(\mathbf{q})$.

In the static limit ($i\Omega_n = 0$), the quasiparticle energies correspond to the frequencies of the free energy Hessian, aligning with the static theory discussed in the previous section:

$$\mathbf{G}^{-1}(0) = -(\mathbf{D}^{(\mathrm{S})} + \mathbf{\Pi}(0)) = -\mathbf{D}^{(\mathrm{F})}. \tag{3.58}$$

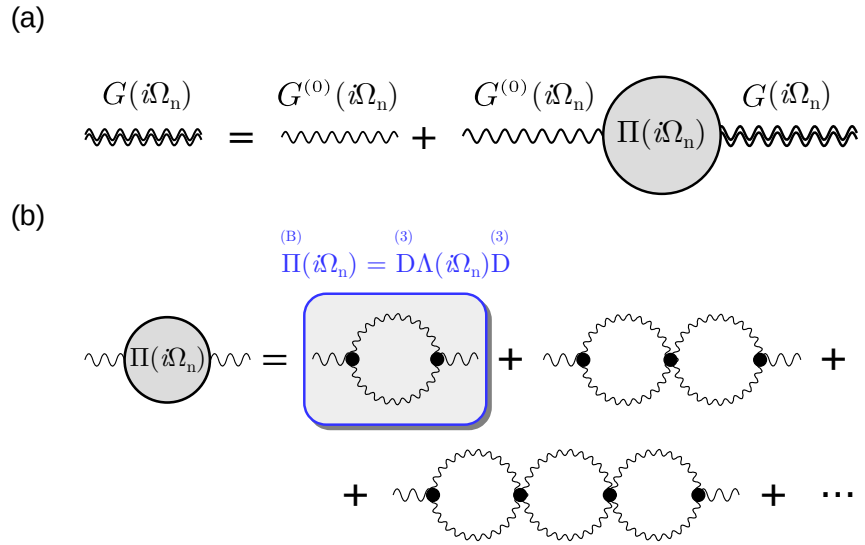

Figure 3.4: (a) Diagrammatic representation of the Dyson equation for the SCHA phonon propagator, as given in Eq. (3.53). (b) Diagrammatic representation of the SCHA self-energy in Eq. (3.56). The bubble approximation, highlighted in blue, consists of retaining only the first term in the expansion.

The bubble approximation

The bubble approximation consists on retaining only the first term in the Taylor expansion of the SCHA dynamical self-energy in Eq. (3.56), neglecting in this way the terms containing fourth-order force constants $\overset{(4)}{\mathbf{D}}$. This simplification, which often yields good results, effectively reduces the calculation to just the bubble term in the corresponding Feynman diagram, as highlighted in blue in Fig. 3.4 (b). The so-called bubble self-energy is then given by:

$$\overset{(B)}{\mathbf{\Pi}}(i\Omega_n) = \overset{(3)}{\mathbf{D}}\mathbf{\Lambda}(i\Omega_n)\overset{(3)}{\mathbf{D}}\,. \tag{3.59}$$

The spectral function

The physical phonons measured in experiments, such as inelastic scattering, are not the eigenvalues of $\mathbf{D}^{(\mathrm{S})}$ nor $\mathbf{D}^{(\mathrm{F})}$, but the spectral functions associated to the displacement-displacement correlation functions. By performing an analytic continuation of the Green function defined in Eq. (3.55) to the real frequency domain, with the substitution $i\Omega_n \to \omega + i\delta^+$, the spectral function $\sigma(\omega)$ can be expressed as [72]:

$$\sigma(\omega) = -2\ \mathrm{Im}\left(\mathrm{Tr}\left[\boldsymbol{G}(\omega + i\delta^+)\right]\right), \tag{3.60}$$

where ω is the energy (frequency) and δ^+ an infinitesimally small positive real number. Peaks in the spectral function as a function of the frequency ω indicate phonon quasiparticles having certain frequencies after anharmonic renormalization. Precisely, the lifetime of these collective vibrational excitations is inversely proportional to the peaks' width. Therefore, sharp peaks indicate long-lived and stable quasiparticles, while a broad spectrum suggests that anharmonicity has removed the existence of well-defined particles.

By exploiting lattice translational symmetry, the quantities can be Fourier transformed, so that the spectral function for a given point $\mathbf{q}$ of the BZ is given by:

$$\sigma(\mathbf{q},\omega) = -\frac{\omega}{\pi}\ \mathrm{Im}\left(\mathrm{Tr}\left[\boldsymbol{G}(\mathbf{q},\omega + i\delta^+)\right]\right), \tag{3.61}$$

or alternatively:

$$\sigma(\mathbf{q},\omega) = -\frac{\omega}{\pi}\ \mathrm{Im}\left(\mathrm{Tr}\left[(\omega + i\delta^+)^2\mathbf{1} - \mathbf{D}^{(\mathrm{S})}(\mathbf{q}) - \mathbf{\Pi}(\mathbf{q},\omega + i\delta^+)\right]^{-1}\right). \tag{3.62}$$

The non-interacting solution is obtained by neglecting the SCHA self-energy, resulting in the expression:

$$\begin{aligned}\sigma^{(0)}(\mathbf{q},\omega) &= -\frac{\omega}{\pi}\ \mathrm{Im}\left(\mathrm{Tr}\left[\boldsymbol{G}^{(0)}(\mathbf{q},\omega + i\delta^+)\right]\right) \\ &= -\frac{\omega}{\pi}\ \mathrm{Im}\left(\mathrm{Tr}\left[(\omega + i\delta^+)^2\mathbf{1} - \mathbf{D}^{(\mathrm{S})}(\mathbf{q})\right]^{-1}\right).\end{aligned} \tag{3.63}$$

Each mode contributes to the energy spectrum with a Dirac delta peak, centered around the frequencies $\omega_\mu(\mathbf{q})$ that are obtained by diagonalizing $\mathbf{D}^{(\mathrm{S})}(\mathbf{q})$, the reciprocal space version of the SSCHA auxiliary dynamical matrix in Eq. (3.42). That is:

$$\sigma^{(0)}(\mathbf{q},\omega) = \sum_\mu \sigma_\mu^{(0)}(\mathbf{q},\omega) = \frac{1}{2}\sum_\mu \left[\delta(\omega-\omega_\mu(\mathbf{q})) + \delta(\omega+\omega_\mu(\mathbf{q}))\right]. \tag{3.64}$$

Within an interacting picture, the simplest solution is provided by the so-called static approximation, which consists of replacing the full dynamical SCHA self-energy $\mathbf{\Pi}(\mathbf{q},\omega)$ with its static value $\mathbf{\Pi}(\mathbf{q},\omega=0)$. Consequently, the spectral function is:

$$\begin{aligned}\overset{(stat)}{\sigma}(\mathbf{q},\omega) &= -\frac{\omega}{\pi}\,\mathrm{Im}\left(\mathrm{Tr}\left[(\omega+i\delta^+)^2\mathbf{1} - \mathbf{D}^{(\mathrm{S})}(\mathbf{q}) - \mathbf{\Pi}(\mathbf{q},0)\right]^{-1}\right)\\ &= -\frac{\omega}{\pi}\,\mathrm{Im}\left(\mathrm{Tr}\left[(\omega+i\delta^+)^2\mathbf{1} - \mathbf{D}^{(\mathrm{F})}(\mathbf{q})\right]^{-1}\right).\end{aligned} \tag{3.65}$$

In this static approximation, the quasiparticle spectrum remains non-interacting, where there is no mode mixing or broadening due to anharmonic interactions. Indeed, each mode contributes a sharp Dirac delta peak to the energy spectrum, but in this case centered at the frequencies $\Omega_\mu(\mathbf{q})$, which are derived from the reciprocal space dynamical matrix based on the free energy Hessian $\mathbf{D}^{(\mathrm{F})}(\mathbf{q})$. The corresponding eigenvalue problem in real space is defined in Eq. (3.52). Then:

$$\overset{(stat)}{\sigma}(\mathbf{q},\omega) = \sum_\mu \overset{(stat)}{\sigma_\mu}(\mathbf{q},\omega) = \frac{1}{2}\sum_\mu \left[\delta(\omega-\Omega_\mu(\mathbf{q})) + \delta(\omega+\Omega_\mu(\mathbf{q}))\right]. \tag{3.66}$$

The full dynamical SCHA self-energy ($i\Omega_n \neq 0$) can only be computed in the current SSCHA code within the bubble approximation introduced in Eq. (3.59). In the mode basis defined in Eq. (3.57), the bubble term at any $\mathbf{q}$-point is obtained through the formula:

$$\begin{aligned}\overset{(B)}{\Pi}{}_{\mu\nu}(\mathbf{q},\omega+i\delta_{\mathrm{se}}) = -\frac{\hbar^2}{8N_{\mathbf{q}}}\sum_{\substack{\mathbf{q}_1\mathbf{q}_2\\ \rho_1\rho_2}}\sum_{\mathbf{G}}\delta_{\mathbf{G},\mathbf{q}+\mathbf{q}_1+\mathbf{q}_2}\frac{F(\omega+i\delta_{\mathrm{se}},\omega_{\rho_1}(\mathbf{q}_1),\omega_{\rho_2}(\mathbf{q}_2))}{\omega_{\rho_1}(\mathbf{q}_1)\omega_{\rho_2}(\mathbf{q}_2)}\\ \times \overset{(3)}{\mathrm{D}}{}_{\mu\rho_1\rho_2}(-\mathbf{q},-\mathbf{q}_1,-\mathbf{q}_2)\overset{(3)}{\mathrm{D}}{}_{\rho_1\rho_2\nu}(\mathbf{q}_1,\mathbf{q}_2,\mathbf{q}).\end{aligned} \tag{3.67}$$

The meaning of the different variables remains consistent with previous definitions, where δ_{se} represents an infinitesimally small positive number, similar to the δ^+ used above. The $\mathbf{q}_i$ sums are performed on a mesh of $N_{\mathbf{q}}$ $\mathbf{q}$-points within the Brillouin zone. The reciprocal lattice vectors are denoted by $\mathbf{G}$, and the function

F is defined in Eq. (3.48). Besides, $\overset{(3)}{\mathrm{D}}_{\mu\rho_1\rho_2}(\mathbf{q},\mathbf{q}_1,\mathbf{q}_2)$ are the SCHA normal components of $\overset{(3)}{\mathbf{D}}(\mathbf{q},\mathbf{q}_1,\mathbf{q}_2)$, which is the Fourier transform of $\overset{(3)}{\mathbf{D}}(\mathbf{T}_1,\mathbf{T}_2,\mathbf{T}_3)$. Finally, $\omega_\rho(\mathbf{q})$ are the frequencies obtained from $\mathbf{D}^{(\mathrm{S})}(\mathbf{q})$.

Note that, as long as the real-space dynamical matrices $\mathbf{D}^{(\mathrm{S})}(\mathbf{T}_1,\mathbf{T}_2)$ and $\overset{(3)}{\mathbf{D}}(\mathbf{T}_1,\mathbf{T}_2,\mathbf{T}_3)$ decay faster with distance than the supercell size, they can be Fourier interpolated at any point in reciprocal space. Consequently, in Eq. (3.67), neither $\mathbf{q}$ nor $\mathbf{q}_i$ are restricted to the commensurate grid of the supercell used in the SSCHA minimization, which allows us to compute the dynamical SSCHA self-energy at any $\mathbf{q}$-point. The self energy must be converged with respect to the $\mathbf{q}_i$ grids in which the summation is performed, which can be arbitrarily increased up, and the infinitesimally small smearing value δ_{se}.

No-mode mixing approximation

Computing the full spectral function in Eq. (3.59) for a given wavevector value $\mathbf{q}$ can involve significant computational effort, as it requires inverting a large matrix for each frequency value ω. The no-mode mixing approximation simplifies this process by assuming that the self-energy $\mathbf{\Pi}(\mathbf{q},\omega+i\delta^+)$ is diagonal in the mode basis:

$$\Pi_{\mu\nu}(\mathbf{q},\omega+i\delta^+) \simeq \delta_{\mu\nu}\Pi_{\nu\nu}(\mathbf{q},\omega+i\delta^+). \tag{3.68}$$

This approach, which is often highly accurate, not only reduces the computational cost but also entails that the total spectral function is given by the sum of individual mode spectral functions:

$$\sigma(\mathbf{q},\omega) = \sum_\mu \sigma_\mu(\mathbf{q},\omega). \tag{3.69}$$

The contribution to the spectral function from each phonon mode ($\mathbf{q}$,μ) is given by:

$$\begin{aligned}\sigma_\mu(\mathbf{q},\omega) = \frac{1}{2\pi}\Bigg[&\frac{-\mathrm{Im}\mathcal{Z}_\mu(\mathbf{q},\omega)}{[\omega-\mathrm{Re}\mathcal{Z}_\mu(\mathbf{q},\omega)]^2+[\mathrm{Im}\mathcal{Z}_\mu(\mathbf{q},\omega)]^2}\\ &+\frac{\mathrm{Im}\mathcal{Z}_\mu(\mathbf{q},\omega)}{[\omega+\mathrm{Re}\mathcal{Z}_\mu(\mathbf{q},\omega)]^2+[\mathrm{Im}\mathcal{Z}_\mu(\mathbf{q},\omega)]^2}\Bigg],\end{aligned} \tag{3.70}$$

where

$$\mathcal{Z}_\mu(\mathbf{q},\omega) = \sqrt{\omega_\mu^2(\mathbf{q})+\Pi_{\mu\mu}(\mathbf{q},\omega+i\delta_{\mathrm{se}})}, \tag{3.71}$$

with $\Pi_{\mu\mu}(\mathbf{q},\omega+i\delta_{\mathrm{se}})$ being the diagonal part of the self-energy in the mode basis.

Lorentzian approximation

The shape of the contribution of each phonon mode to the spectral function $\sigma_\mu(\mathbf{q},\omega)$ in Eq. (3.70) resembles that of a Lorentzian function, but with frequency-dependent centers and widths. As a result, the overall spectral function $\sigma(\mathbf{q},\omega)$ generally differs from a simple superposition of real Lorentzians. However, in certain cases $\sigma_\mu(\mathbf{q},\omega)$ can be approximated with a true Lorentzian, indicating that the quasiparticle picture is still valid after the inclusion of anharmonicity. In such cases the individual spectral functions can indeed be expressed as:

$$\sigma_\mu(\mathbf{q},\omega) = \frac{1}{2\pi}\left[\frac{\Gamma_\mu(\mathbf{q})}{[\omega-\Theta_\mu(\mathbf{q})]^2+[\Gamma_\mu(\mathbf{q})]^2}+\frac{\Gamma_\mu(\mathbf{q})}{[\omega+\Theta_\mu(\mathbf{q})]^2+[\Gamma_\mu(\mathbf{q})]^2}\right], \tag{3.72}$$

where the center of the Lorentzian $\Theta_\mu(\mathbf{q})$ is the quasiparticle energy and $\Gamma_\mu(\mathbf{q})$ is the half width at half maximum (HWHM) anharmonic linewidth of the μ mode with momentum $\mathbf{q}$, respectively. All in all, the Lorentzian approximation implies that each mode corresponds to an anharmonic phonon with a specific energy, shifted from the SSCHA auxiliary frequencies by $\Delta_\mu(\mathbf{q}) = \Theta_\mu(\mathbf{q}) - \omega_\mu(\mathbf{q})$, and a finite lifetime $\tau_\mu(\mathbf{q})$, given by $\tau_\mu(\mathbf{q}) = 1/(2\Gamma_\mu(\mathbf{q}))$. These features are illustrated in Fig. 3.5.

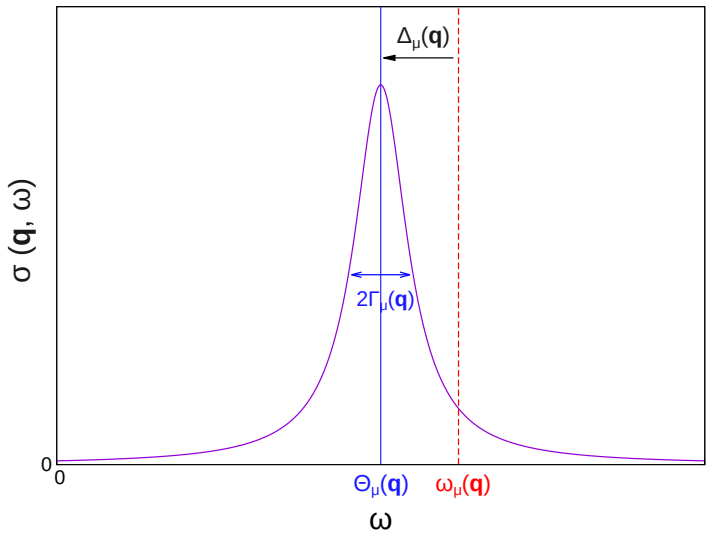

Figure 3.5: Red dashed vertical lines indicate the Dirac delta-shaped spectral function of non-interacting SSCHA auxiliary particles from Eq. (3.64) at a fixed point $\mathbf{q}$. In contrast, the blue lines represent the spectral function within the no-mode mixing approximation, in the particular case where the contribution of mode μ is Lorentzian-shaped. The vertical blue lines mark the anharmonic phonon frequencies within the quasiparticle picture, $\Theta_\mu(\mathbf{q})$. The double-headed blue arrow denotes the full width at half maximum (FWHM), highlighting the spectral broadening due to anharmonic effects. The horizontal black arrow remarks the frequency shift, $\Delta_\mu(\mathbf{q})$, between the two approaches.

Within the Lorentzian approximation, the SSCHA code offers several methods to estimate quasiparticle frequencies and linewidths. The most accurate approach involves solving the self-consistent equation:

$$\Theta_\mu(\mathbf{q}) = \mathrm{Re}\, \mathcal{Z}_\mu(\mathbf{q}, \Theta_\mu(\mathbf{q})), \tag{3.73a}$$

which provides an estimate for $\Theta_\mu(\mathbf{q})$ and subsequently yields the linewidth:

$$\Gamma_\mu(\mathbf{q}) = -\mathrm{Im}\, \mathcal{Z}_\mu(\mathbf{q}, \Theta_\mu(\mathbf{q})). \tag{3.73b}$$

Alternatively, one can avoid solving this equation by evaluating the expression with auxiliary phonon frequencies within the so-called "one-shot" approximation:

$$\overset{(os)}{\Theta}_\mu(\mathbf{q}) = \quad \mathrm{Re}\, \mathcal{Z}_\mu(\mathbf{q}, \omega_\mu(\mathbf{q})) \tag{3.74a}$$

$$\overset{(os)}{\Gamma}_\mu(\mathbf{q}) = -\mathrm{Im}\, \mathcal{Z}_\mu(\mathbf{q}, \omega_\mu(\mathbf{q})). \tag{3.74b}$$

When the SCHA self-energy is a small perturbation of the SCHA free propagator ($\Pi_{\mu\mu} << \omega_\mu^2$), a further approximation can be taken by truncating the Taylor expansion of Eq. (3.71) at first order:

$$\overset{(pert)}{\Theta}_\mu(\mathbf{q}) = \quad \tfrac{1}{2\omega_\mu(\mathbf{q})} \mathrm{Re}\, \Pi_{\mu\mu}(\mathbf{q}, \omega_\mu(\mathbf{q})), \tag{3.75a}$$

$$\overset{(pert)}{\Gamma}_\mu(\mathbf{q}) = -\tfrac{1}{2\omega_\mu(\mathbf{q})} \mathrm{Im}\, \Pi_{\mu\mu}(\mathbf{q}, \omega_\mu(\mathbf{q})). \tag{3.75b}$$

The Lorentzian approximation is not always valid and must be evaluated at each specific case. In systems with strong anharmonicity the ideal Lorentzian peak shape associated with well-defined phonon modes can become disrupted. As a result, the phonon quasiparticle picture breaks down, and parameters like $\Theta_\mu(\mathbf{q})$ and $\Gamma_\mu(\mathbf{q})$ become inadequate for describing the system's vibrational properties. Figure 3.6 illustrates a scenario where this approximation fails due to the appearance of a shoulder, an extra bump next to the main phonon peak. Another signatures of strong anharmonicity in spectral functions include peak broadening, mode mixing, and extra peaks (satellites). These anomalies complicate the interpretation of experimental data and can easily lead to misinterpretations. The appearance of extra peaks, for example, might be wrongly attributed to phase transitions.

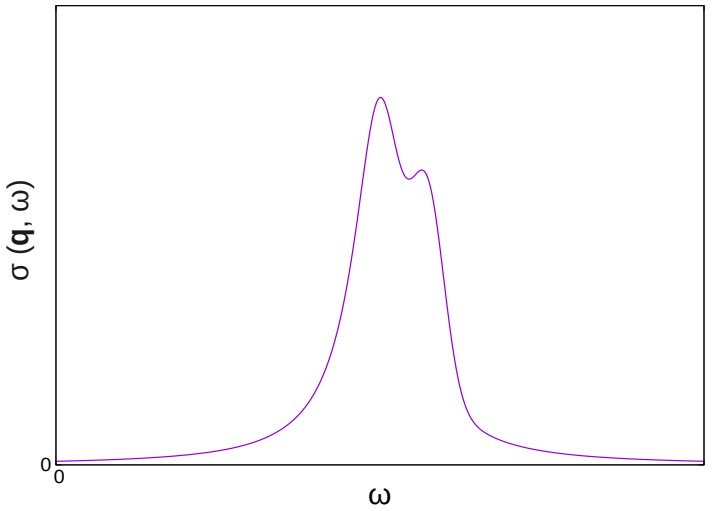

Figure 3.6: Spectral function at point $\mathbf{q}$ showing a shoulder, an additional, less pronounced bump next to the main peak. This feature indicates deviations from the ideal Lorentzian shape and suggests the presence of strong anharmonicity and mode interactions.

In summary, the SSCHA code calculates several types of frequencies for a phonon mode. The auxiliary phonon frequencies $\omega_\mu(\mathbf{q})$ coming from the variational problem do not have actual physical meaning since they are positive definite and simple parameters of the variational minimization. However, they are crucial for defining the density matrix that minimizes the free energy and therefore, for computing averages. The static frequencies $\Omega_\mu(\mathbf{q})$ obtained from the free energy Hessian $\mathrm{D}^{(\mathrm{F})}(\mathbf{q})$ are physically significant quantities that can be used to identify second-order phase transitions, as a collapse to zero frequency indicates a structural instability. Finally, although inelastic scattering experiments measure the full spectral function, the phonon frequencies $\Theta_\mu(\mathbf{q})$ extracted through the Lorentzian approximation offer the most accurate representation of a true physical quantity, as long as the quasiparticle picture is preserved.

4

The electron-phonon interaction

Until now, our study has relied on the adiabatic approximation, enabling us to address the electronic and nuclear problems separately, without accounting for any interactions between electrons and phonons. However, the assumption that the ionic motion has no influence on the electronic states is not always valid. In fact, the interaction between electrons and phonons is fundamental to significant physical phenomena, such as superconductivity and the formation and stabilization of charge density waves. To explain these physical phenomena, one has to go beyond the adiabatic approximation by incorporating the previously neglected electron-phonon interaction term, $\Delta\hat{\mathrm{H}}_n$, in Eq. (1.9).

Regarding the $\Delta\hat{\mathrm{H}}_n$ term, the first addend involves second order derivatives of the electronic wave function with respect to nuclear positions while the second one involves first order derivatives. Hence, only the latter component contributes at linear order in displacement, making it the dominant term. At this linear order, the electron-phonon Hamiltonian can be simplified to:

$$\hat{\mathrm{H}}_{e-ph} = \sum_I \frac{1}{M_I} \left[\hat{\mathbf{P}}_I\right]_e \hat{\mathbf{P}}_I \ , \tag{4.1}$$

where $\left[\hat{\mathbf{P}}_I\right]_e$ means that the ionic momentum operator is applied over the electronic states. This operator can be rewritten in second quantization using the standard fermionic creation and annihilation operators:

$$\left[\hat{\mathbf{P}}_I\right]_e = \sum_{nn'} \sum_{\mathbf{kk'}}^{1BZ} \hat{c}^\dagger_{n'\mathbf{k'}}, \hat{c}_{n\mathbf{k}} \left\langle \phi_{n'\mathbf{k'}} \right| \hat{\mathbf{P}}_I \left| \phi_{n\mathbf{k}} \right\rangle \ , \tag{4.2}$$

where $\hat{c}^\dagger_{n'\mathbf{k'}}$, creates and $\hat{c}_{n\mathbf{k}}$ annihilates a Kohn-Sham state.

Following a procedure involving the expansion of Kohn-Sham electronic states to linear order as in Section 3.2, $|\phi_{n\mathbf{k}}\rangle \rightarrow |\phi_{n\mathbf{k}}\rangle + |\Delta\phi_{n\mathbf{k}}\rangle$, within quantum perturbation theory and the transformation of the ionic momentum operator into bosonic ladder operators, the electron-phonon Hamiltonian can be rewritten in the Fröhlich way:

$$\hat{\mathrm{H}}_{e-ph} = \frac{1}{\sqrt{N_{\mathbf{q}}}} \sum_{\mu} \sum_{nn'} \sum_{\mathbf{kq}}^{1BZ} g^{\mu}_{n'\mathbf{k}+\mathbf{q},n\mathbf{k}}\, \hat{c}^{\dagger}_{n'\mathbf{k}+\mathbf{q}}\, \hat{c}_{n\mathbf{k}} \left(\hat{b}_{\mu\mathbf{q}} + \hat{b}^{\dagger}_{\mu-\mathbf{q}}\right) , \tag{4.3}$$

where the electron-phonon matrix elements are given by

$$g^{\mu}_{n'\mathbf{k}+\mathbf{q},n\mathbf{k}} = \sum_{m} \sum_{s} e^{i\mathbf{q}\cdot\mathbf{T}_m} \frac{1}{\sqrt{2M_s w_{\mu}(\mathbf{q})}} \langle\phi_{n'\mathbf{k}+\mathbf{q}}| \sum_{\alpha} \left[\frac{\partial \hat{\mathrm{H}}_{KS}}{\partial u^{\alpha}_{s}(\mathbf{T}_m)}\right]_{\mathbf{R}^0} \epsilon^{\alpha}_{s\mu}(\mathbf{q}) \, |\phi_{n\mathbf{k}}\rangle \ . \tag{4.4}$$

The Fröhlich Hamiltonian given in Eq. (4.3) describes processes in which an electron in the band n and with momentum $\mathbf{k}$ either absorbs a phonon of mode μ with momentum $\mathbf{q}$ or emits a phonon of mode μ with momentum -$\mathbf{q}$, changing its state to one in the band n' and with momentum $\mathbf{k}$+$\mathbf{q}$. The electron-phonon matrix element $g^{\mu}_{n'\mathbf{k}+\mathbf{q},n\mathbf{k}}$ quantifies the probability amplitude for these transitions. Remarkably, the electronic ground state and harmonic phonon spectra DFPT calculations provide all the necessary information to construct H_{e-ph}.

Once the electron-phonon Hamiltonian is properly established, the Green's function method is the suitable formalism for addressing the electron-phonon many-body problem. The Green's functions are derived from the Dyson equations [79], which, in this context, are expressed as follows:

$$G_n(\mathbf{k}, i\omega_m) = G^0_n(\mathbf{k}, i\omega_m) + G^0_n(\mathbf{k}, i\omega_m)\Sigma_n(\mathbf{k}, i\omega_m)G_n(\mathbf{k}, i\omega_m) \tag{4.5}$$

for the electron Green function $G_n(\mathbf{k}, i\omega_m)$ and

$$D_{\nu}(\mathbf{q}, i\Omega_m) = D^0_{\nu}(\mathbf{q}, i\Omega_m) + D^0_{\nu}(\mathbf{q}, i\Omega_m)\Pi_{\nu}(\mathbf{q}, i\Omega_m)D_{\nu}(\mathbf{q}, i\Omega_m) \tag{4.6}$$

for the phonon Green function. In the equations above, $G^0_n(\mathbf{k}, i\omega_m)$ and $D^0_{\nu}(\mathbf{q}, i\Omega_m)$ are the non-interacting phonon Green functions, and $\Sigma_n(\mathbf{k}, i\omega_m)$ and $\Pi_{\nu}(\mathbf{q}, i\Omega_m)$ are the electron and phonon self-energies, respectively, due to the electron-phonon interaction.

In principle, one would need to consider an infinite series of diagrams to fully address the electron-phonon many-body problem. However, according to Migdal's theorem, all vertex corrections are of order $\sqrt{m_e/M_I}$ [82]. Consequently, the lowest-order diagram is typically the most significant and provides a good approximation for the self-energies. After summing over Matsubara frequencies and analytically continuing the functions to real frequencies, the self-energies can

be expressed as follows:

$$\Sigma_n(\mathbf{k},\omega) = \frac{1}{N_\mathbf{q}} \sum_{\nu,\mathbf{q},n'} \left| g^\nu_{n'\mathbf{k}+\mathbf{q},n\mathbf{k}} \right|^2 \left[\frac{n_B(\omega_\nu(\mathbf{q})) + \frac{1}{2} f_{n'\mathbf{k}+\mathbf{q}}}{\omega + i\delta + \omega_\nu(\mathbf{q}) - \epsilon_{n'\mathbf{k}+\mathbf{q}}} + \frac{n_B(\omega_\nu(\mathbf{q})) + 1 - \frac{1}{2} f_{n'\mathbf{k}+\mathbf{q}}}{\omega + i\delta - \omega_\nu(\mathbf{q}) - \epsilon_{n'\mathbf{k}+\mathbf{q}}} \right] \tag{4.7}$$

for electrons, and

$$\Pi_\mu(\mathbf{q},\omega) = \frac{1}{N_\mathbf{k}} \sum_{nn'} \sum_{\mathbf{k}}^{1BZ} |g^\mu_{n'\mathbf{k}+\mathbf{q},n\mathbf{k}}|^2 \frac{f_{n\mathbf{k}} - f_{n'\mathbf{k}+\mathbf{q}}}{\epsilon_{n\mathbf{k}} - \epsilon_{n'\mathbf{k}+\mathbf{q}} + \omega + i\delta} \tag{4.8}$$

for phonons. In Eq. (4.7), the sum over phonon wavevectors is performed on a mesh of $N_\mathbf{q}$ $\mathbf{q}$-points within the corresponding first Brillouin zone. This value of $N_\mathbf{q}$ may differ from $N_\mathbf{k}$, which denotes the number of $\mathbf{k}$-points used in the sum over electron wavevectors in Eq. (4.8). These self-energies capture the effects of electron-phonon interactions on the respective quasiparticles, providing a detailed account of how this coupling modifies their intrinsic characteristics from their bare, non-interacting states. Specifically, the real part of the self-energies corresponds to the renormalization of the quasiparticle energy, while the imaginary part is linked to the linewidth of the respective electron or phonon band.

The renormalization of the phonon frequencies due to the electron-phonon interaction is inherently included in DFPT harmonic phonon calculations through the static limit of the corresponding electron-phonon self-energy, $\Pi_\mu(\mathbf{q},\omega = 0)$. This inclusion arises because calculating the second derivatives of the ionic potential within DFPT, in Eq. (3.18), involves the linear response of the electron density to static ionic displacements, which is an effect captured in $\Pi_\mu(\mathbf{q},\omega = 0)$. In fact, the electron-phonon self-energy $\Pi_\mu(\mathbf{q},w)$ closely resembles the Lindhard function shown in Fig. 2 [12, 83], which characterizes the linear response of a free electron gas to external perturbations, but in this case incorporating the square of the electron-phonon matrix elements. Since the real part of the Lindhard function is negatively defined, the electron-phonon interaction will always soften phonon frequencies, potentially leading to instabilities. Moreover, the softening of phonon modes can result in increased ionic displacements, especially if the system is near a structural phase transition, thereby increasing the anharmonicity of the system. Consequently, a strong electron-phonon interaction is generally linked to significant anharmonic effects, which further enhance the renormalization of phonon frequencies, as explained in the previous chapter.

On the other hand, the electron-phonon contribution to the linewidth of a phonon mode $\gamma_\mu(\mathbf{q})$ is related to the imaginary part of the phonon self-energy:

$$\gamma_\mu(\mathbf{q}) = -\mathrm{Im}\,\Pi_\mu(\mathbf{q}, w_\mu(\mathbf{q}))\ , \tag{4.9}$$

where $\gamma_\mu(\mathbf{q})$ represents the half width at half maximum (HWHM) of the phonon mode. Consequently, the full width at half maximum (FWHM) is given by: $2\gamma_\mu(\mathbf{q})$.

For temperatures well below the Fermi temperature, the occupation factor can be approximated as $f_{n\mathbf{k}} \approx 2\theta(\epsilon_F - \epsilon_{n\mathbf{k}})$. Additionally, given that the phonon frequencies (on the order of meV) are much smaller than the electronic energy scales (on the order of eV), the linewidth formula can be simplified to:

$$\gamma_\mu(\mathbf{q}) = \frac{2\pi w_\mu(\mathbf{q})}{N_\mathbf{k}} \sum_{nn'} \sum_{\mathbf{k}}^{1BZ} |g^\mu_{n'\mathbf{k}+\mathbf{q},n\mathbf{k}}|^2 \delta(\epsilon_{n'\mathbf{k}+\mathbf{q}} - \epsilon_F)\delta(\epsilon_{n\mathbf{k}} - \epsilon_F) \; . \tag{4.10}$$

This formula indicates that the electron-phonon contribution to the phonon linewidth depends solely on excitations occurring at the Fermi surface. Notably, the electron-phonon linewidth $\gamma_\mu(\mathbf{q})$ is independent of the phonon frequency $w_\mu(\mathbf{q})$ since the electron-phonon matrix elements scale as $w_\mu(\mathbf{q})^{-1/2}$. This property allows us to calculate $\gamma_\mu(\mathbf{q})$ at the harmonic level using DFPT even if the system is dynamically unstable at this level of approximation.

Indeed, the strength of the electron-phonon interaction can be characterized by analysing the phonon linewidth, which can be measured experimentally using techniques such as inelastic x-ray or neutron scattering. However, it is essential to note that the linewidth expression in Eq. (4.10) considers only the contribution from electron-phonon interactions. Experimental linewidths may also include additional contributions, such as those arising from anharmonic effects, as previously discussed.

4.1 The electron-phonon interaction with the SSCHA

In strongly anharmonic systems, the SSCHA significantly renormalizes the harmonic phonon spectrum, and the average atomic positions are given by the centroid positions at the minimum of the SSCHA free energy. To account for electron-phonon interactions in such systems, one combines the electron-phonon matrix elements, as expressed in Eq. (4.4), with the renormalized quantities obtained from the SSCHA. In particular, the variation of the Kohn-Sham Hamiltonian with respect to the ionic displacements is no longer evaluated at the ionic configuration that minimizes the BOES, but rather at the average ionic positions in the SSCHA free energy minimum. This is expressed as $\left[\frac{\partial \hat{\mathrm{H}}_{KS}}{\partial u_s^\alpha(\mathbf{T}_m)}\right]_{\mathbf{R}^0} \rightarrow \left[\frac{\partial \hat{\mathrm{H}}_{KS}}{\partial u_s^\alpha(\mathbf{T}_m)}\right]_{\boldsymbol{\mathcal{R}}_{eq}}$ in Eq. (4.4). Furthermore, the harmonic polarization vectors and frequencies are substituted with those derived from the SSCHA. In this sense, the results obtained using the SSCHA auxiliary dynamical matrices are similar to those derived from the dynamical matrices based on the free energy Hessian. Although the differences between these two approaches are usually small, in certain cases they can be significant. In such instances, the most accurate method is to calculate the electron-phonon properties using the full spectral function, which is in fact the most exact theoretical solution [84].

Part II

Charge density wave transitions in transition metal dichalcogenides

Transition Metal Dichalcogenides

The family of layered two-dimensional transition metal dichalcogenides (TMDs) is formed by compounds with the general chemical formula MX_2, where M is a transition metal and X a chalcogen: an element of the group 16 in the periodic table, such as S, Se or Te. The position of transition metals and chalcogens in the periodic table is indicated with red boxes in Fig. 4.1, with shaded areas specifying those elements forming TMDs.

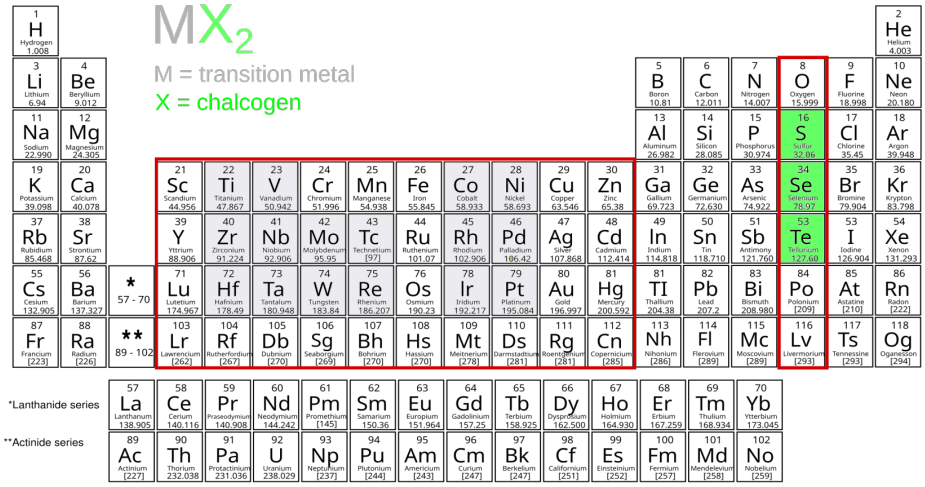

Figure 4.1: Periodic table highlighting transition metals and chalcogens, outlined with red boxes. Shaded regions highlight specific transition metals (M) and chalcogens (X) known to form MX_2 compounds, that is to say, TMDs.

TMDs are known to display a quasi-2D layered structure, in which electrical and thermal transport phenomena take relevance along the layers. Each layer is formed by a set of transition metal atoms sandwiched between two layers of chalcogen atoms. The atoms within each layer are held together through strong covalent bonds, while the chalcogen atoms between adjacent layers interact through weak van der Waals forces. This bonding structure makes these materials easy to exfoliate into thin 2D layers [17]. Notably, monolayer TMDs can also be directly grown by chemical means [85].

The arrangement of the covalently bonded chalcogen atoms around the central transition metal atom, along with the stacking patterns of these layers, defines the different crystalline structures of TMDs, known as polytypes. The most commonly observed ones include the one-layer *trigonal* form ($1T$), two-layer *hexagonal* form ($2H$) and three-layer *rhombohedral* form ($3R$). That is, the number indicates the layers found within the unit cell, while the italicized letter denotes the symmetry of the unit cell.

In TMDs, the interplay between strong electron-electron correlations arising from the d electrons of transition metals and the significant electron-phonon interactions results in rich phase diagrams, exhibiting a wide range of ground states such as CDWs [2], superconductivity [86] and excitonic instabilities [87, 88]. Among the collective electronic orderings, CDWs are particularly relevant because they compete/coexist with superconductivity [89–92] in a similar fashion as in high-temperature superconductors [4–8]. While the exact mechanism behind both CDW and superconducting instabilities in TMDs is linked to electron-phonon interactions, it is not yet fully understood [93–95]. In this sense, the relatively simple crystalline structure of TMDs, with a small number of atoms per unit cell, makes these materials excellent candidates to study the origin of CDW phases and eventually, their interaction with superconductivity. Precisely, the main objective of this chapter is to analyse comprehensively the CDW transition in members of the TMD family. By understanding the fundamental mechanisms in such straightforward systems we aim to provide insights that are relevant for exploring more complex strongly correlated materials.

Regarding CDW phases in TMDs, previous works using high-resolution inelastic x-ray scattering (IXS) experiments have provided evidence that the corresponding transition in prototypical members like $2H$-$NbSe_2$ [96] and $1T$-$TiSe_2$ [97] is triggered by the softening of a low energy phonon mode with the CDW wavevector $\mathbf{q}_{\mathrm{CDW}}$, together with an eventual collapse at the critical temperature T_{CDW}. However, the correct theoretical characterization of this phenomenon based on *ab initio* calculations is limited for all these TMDs undergoing CDW transitions due to the breakdown of the standard harmonic approximation for ionic dynamics, which cannot explain the stability of the high-temperature undistorted phases [94]. This hinders the study of both the origin and the melting of the charge modulated

state[1], complicating the comprehensive understanding of the CDW formation. Recent studies have shown that in order to suppress the CDW phases in TMDs and understand their phase diagrams large anharmonic effects are required, both in the bulk and in the monolayer limit [76–78, 94]. Moreover, in the paradigmatic case of $2H$-$NbSe_2$ ionic fluctuations play a more dominant role than electronic ones in the melting of the CDW order [77]. In Chapter 5 we present a comprehensive study of the anharmonic lattice dynamics and the CDW transition of $1T$-VSe2, which is a metallic member of the TMD family subject to strong debate.

Undoubtedly, the key factor that rekindled interest in layered TMDs at the start of the century was the opportunity to explore how reducing dimensionality [17] affects various physical phenomena. In this sense, there is an open debate on how the dimension reduction affects CDWs. As a system shifts from 3D to 2D, Fermi surfaces are more likely to exhibit parallel regions that enhance nesting. What is more, the electronic confinement in 2D systems limits their capacity to screen Coulomb interactions, enhancing electron-phonon interactions. These 2 factors favour the emergence of CDW orders. On the contrary, stronger thermal fluctuations in monolayers tend to destroy long-range orders. These competing effects lead to a great variability of behaviours. For instance, in $NbSe_2$, the CDW temperature hardly changes between the bulk and monolayer forms [77, 91]. On the contrary, the CDW is enhanced in the monolayer limit of the isoelectronic and isostructural NbS_2, whereas its bulk form does not exhibit charge ordering at all [76]. In monolayer $TiSe_2$ the critical temperature is also enhanced with respect to that in the bulk single crystal [98] and strongly depends on the substrate material [99].

In summary, there is no clear trend so far that, in general, allows the CDW order in the single-layer limit to be deduced from its bulk counterpart. What is clear is that experimental results in monolayers may be strongly conditioned by environmental factors or the different substrates on which they are deposited [76–78, 99]. Regarding the single-layer limit of VSe_2, there is a big debate in literature on which the CDW reconstruction is, as unrelated experiments have reported different orders with varying transition temperatures [100–105]. In Chapter 6 a purely theoretical analysis of the CDW transition in monolayer VSe_2 is performed by means of the SSCHA with the aim at clarifying the picture.

[1]The term "melting" is used here as a synonym for the transition to a phase with greater entropy. Hence, "CDW melting" describes the transition from the CDW state to a more uniform and symmetric high-temperature phase [78, 94].

5

Bulk VSe_2

5.1 Introduction

$1T$-VSe_2, shown in Fig. 5.1, belongs to the series of layered TMDs that develop a three-dimensional charge modulated state as a function of temperature. In particular, a complex incommensurate 3D-CDW with a propagation vector[1] $\mathbf{q}_{\mathrm{CDW}}$ = (0, 1/4, 0.3) emerges below T_{CDW} = 110 K [106]. This onset temperature is not only the lowest among the $1T$-polytypes, e.g. $T_{\mathrm{CDW}}[1T\text{-}TiSe_2] \approx 200$ K, and $T_{\mathrm{CDW}}[1T\text{-}TaS_2]$ = 550 K [3], but also resembles more closely those of selenium-based $2H$-polytypes: e.g. $T_{\mathrm{CDW}}[2H\text{-}NbSe_2]$ = 33 K and $T_{\mathrm{CDW}}[2H\text{-}TaSe_2]$ = 122 K. This stark contrast in transition temperatures raises intriguing questions about the underlying mechanisms, suggesting that substantial fluctuation effects could significantly influence the reduction of the mean-field transition temperature [107], while the out-of-plane coupling between VSe_2 layers, affected by weak van der Waals interactions, may also play a role in this phenomenon [108]. Additionally, in clear contrast to the pressure induced CDW suppression in similar TMDs such as $1T$-$TiSe_2$ [90, 109] and $2H$-$NbSe_2$ [94], an enhancement of the charge modulated state has been reported in bulk VSe_2 up to almost room temperature at $\sim$ 13 GPa [92]. Overall, $1T$-VSe_2 represents a unique and intriguing case within TMDs in general and the family of $1T$ polytypes in particular. However, while the electronic structure of bulk VSe_2 and its interplay with the CDW formation has been exhaustively analysed in the literature [110–113], the role of the lattice dynamics in this context has not been explored in detail.

[1] In this chapter and the following one, wavevectors are expressed in reciprocal lattice units, defined as: $\mathbf{q} = (h, k, l) = h\mathbf{b}_1 + k\mathbf{b}_2 + l\mathbf{b}_3$, where $\mathbf{b}_1$, $\mathbf{b}_2$, and $\mathbf{b}_3$ are the reciprocal lattice vectors.

This chapter of the thesis provides a comprehensive characterization of the lattice dynamics in $1T$-VSe_2, with special focus on the effects associated to the CDW transition. In particular, we examine whether phonon softening effects occur as the temperature decreases towards the transition, using *ab initio* non-perturbative anharmonic phonon calculations, complemented by inelastic x-ray scattering experimental results from Dr. Santiago Blanco-Canosa's group. We then analyse and compare the potential mechanisms that could lead to the emergence of the charge modulated state. Finally, we explore the pressure dependence of the CDW transition and the anomalous enhancement of the charge modulated state with increasing pressure. This comprehensive study aims to provide a clearer insight into key processes driving the CDW formation in this material, which may also be relevant in other members of the TMD family.

5.2 Crystal structure

At room temperature bulk VSe_2 crystallizes in a $1T$-phase (space group $P\bar{3}m1$) shown in Fig. 5.1. This trigonal (T) crystal system has an hexagonal crystal lattice defined by the following set of primitive vectors in Cartesian coordinates:

$$\mathbf{a}_1 = a\,(1,0,0)\,, \quad \mathbf{a}_2 = a\left(-\frac{1}{2}, \frac{\sqrt{3}}{2}, 0\right), \text{ and } \quad \mathbf{a}_3 = c\,(0,0,1)\,.$$

The lattice vectors $\mathbf{a}_1$ and $\mathbf{a}_2$ define an in-plane hexagonal basis with a lattice constant a, while the perpendicular lattice vector $\mathbf{a}_3$ determines the height c of the unit cell. The experimental values of the lattice parameters at room temperature are $a = 3.35$ Å and $c = 6.09$ Å.

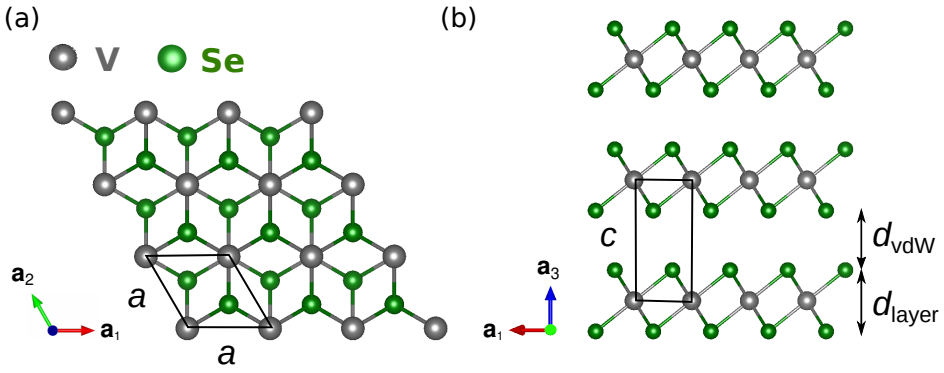

Figure 5.1: (a) Top and (b) side views of the crystal structure of $1T$-VSe_2. The unit cell is indicated with black lines, being a the in-plane lattice constant and c its height. Vanadium and selenium atoms are represented by grey and green spheres, respectively. In total there are 3 atoms per unit cell.

Regarding atomic positions, the $1T$ polytype of TMDs is characterized by hexagonal layers of transition metal atoms with chalcogen atoms covalently bonded to them with an octahedral coordination. The described atomic arrangement is shown in Fig. 5.1 and implies the equilibrium atomic positions listed in Table 5.1. Therefore, the position of vanadium atoms is fixed by symmetry at the origin of the primitive cells. Otherwise, the in-plane position of selenium atoms is as well fixed by symmetry[2], and they are only free to move along the $\hat{z}$ axis. Particularly, the classical relaxation of atomic coordinates with the cell parameters fixed to experimental values yields a relative distance of $z \simeq 0.256$ from the vanadium plane to each covalently bonded selenium layer, which corresponds to a vertical distance of $d_{\text{V-Se\_vert}} \simeq 1.559$ Å. The total thickness of a single VSe_2 layer is thus about $d_{\text{layer}} \simeq 3.118$ Å. The remaining space between adjacent layers constitutes the van der Waals gap, measuring around $d_{\text{vdW}} \simeq 2.972$ Å.

Atom	Wyckoff Position	Crystal Coordinates
Vanadium (V)	$1a$	$(0, 0, 0)$
Selenium (Se)	$2d$	$\left(\frac{1}{3}, \frac{2}{3}, z\right)$, $\left(\frac{2}{3}, \frac{1}{3}, -z\right)$

Table 5.1: Wyckoff positions and crystal coordinates of the three atoms in the unit cell of $1T$-VSe_2.

The reciprocal lattice is determined by the following vectors:

$$\mathbf{b}_1 = \frac{2\pi}{a}\left(1, \frac{1}{\sqrt{3}}, 0\right), \quad \mathbf{b}_2 = \frac{2\pi}{a}\left(0, \frac{2}{\sqrt{3}}, 0\right), \text{ and } \quad \mathbf{b}_3 = \frac{2\pi}{c}(0, 0, 1).$$

Figure 5.2 shows the first Brillouin zone that corresponds to the defined reciprocal lattice together with the high-symmetry points. Table 5.2 lists the reciprocal coordinates of the high-symmetry points that will be used in upcoming phonon dispersion analyses.

The reciprocal coordinates of the CDW wavevector are $\mathbf{q}_{\text{CDW}} = (0,\ 1/4,\ 0.3)$. The inelastic x-ray scattering (IXS) energy-loss experiments performed by Dr. Blanco-Canosa and his group scanned the low energy acoustic phonon branches dispersion around the point $(2.25,\ 0,\ 0.7)$. The symmetries of the space group $P\bar{3}m1$ (164) establish that both points are equivalent to the critical wavevector. This equivalence is derived from the following sequence of symmetry operations: translation by $-2\mathbf{b}_1$, inversion symmetry, C_3 rotational symmetry and translation by $+\mathbf{b}_3$. On the contrary, for instance, the critical point $\mathbf{q}_{\text{CDW}} = (0,\ 1/4,\ 0.3)$ and $(1/4,\ 0,\ 0.3)$ are not equivalent, which is a consequence of the fact that the above mentioned space group does not have the sixfold rotational symmetry C_6.

[2]The octahedral coordination implies that selenium atoms in the same unit cell are not aligned in the top view as illustrated in Fig. 5.1(a), which is the reason why this structure does not have 6 fold rotational symmetry.

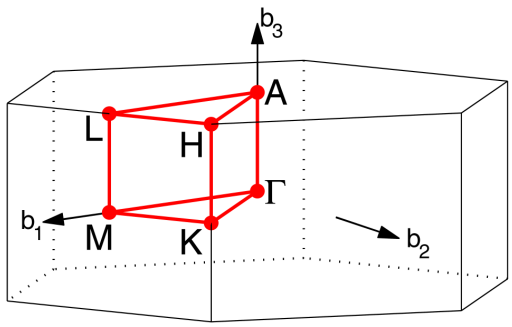

Figure 5.2: First Brillouin zone and the high-symmetry points of the space group $P\bar{3}m1$ (164). Figure taken from Ref. [114].

High-symmetry point	Reciprocal Coordinates
Γ	$(0, 0, 0)$
M	$\left(\frac{1}{2}, 0, 0\right)$
K	$\left(\frac{1}{3}, \frac{1}{3}, 0\right)$
A	$\left(0, 0, \frac{1}{2}\right)$

Table 5.2: High-symmetry points of space group $P\bar{3}m1$ (164) and their coordinates with respect to the reciprocal lattice vectors.

5.3 Computational details

5.3.1 Anharmonic lattice dynamics: The SSCHA method

The SSCHA theory was applied to the normal state phase of 1 T-VSe_2 ($P\bar{3}m1$), with the experimental lattice parameters at room temperature: $a = b = 3.35$ Å and $c = 6.09$ Å. The Born-Oppenheimer energies and forces required for the SSCHA variational minimization were calculated in 4×4×3 sized supercells (almost commensurate with $\mathbf{q}_{\mathrm{CDW}}$) using plane-wave based DFT within the PBE approximation [46] of the exchange-correlation functional, making use of the Quantum Espresso package [61, 62]. We also performed calculations by including van der Waals interactions using Grimme's semiempirical approach [47] and within the non-local functional developed by Dion et al. [48]. To avoid highly oscillating wave functions near the nucleus, we used an ultrasoft pseudopotential that includes $4s^2$ $3d^3$ valence electrons for V and a norm-conserving one with $4s^2$ $4p^4$ electrons in the valence for Se. We used a plane-wave energy cutoff of 40 Ry for the wave functions and 450 Ry for the charge density. The BZ integrals were performed in a 3×3×3 **k**-point grid in the supercell with a Methfessel-Paxton smearing [52] of 0.01 Ry.

Both static and dynamical SSCHA calculations were performed in the so-called bubble approximation [41], setting $\overset{(4)}{\mathbf{\Phi}} = 0$ in Eqs. (3.46) and (3.56). The static anharmonic spectra were obtained by interpolating the difference between anharmonic and harmonic dynamical matrices along the corresponding **q**-point path (see Appendix A for more details). The SSCHA dynamical self-energy was obtained following the equation based on Fourier interpolation described in Eq. (3.67), with a broadening of $\delta_{\text{se}} = 0.5$ cm^{-1} and a 48×48×32 **q**-point grid. The phonon frequencies and third-order force constants at these points were indeed determined through Fourier interpolation from the 4×4×3 grid. The spectral function was calculated within the "no mode-mixing" approximation, i.e. directly from Eqs. (3.69) and (3.70), as well as in the "one-shot" approximation (Eqs. (3.74)), and in the perturbative case (Eqs. (3.75)).

5.3.2 Harmonic phonons and the electron-phonon interaction: DFPT calculations

Harmonic phonon frequencies and electron-phonon matrix elements of the normal state phase of 1T-VSe_2 were calculated within density functional perturbation theory (DFPT) [115] as implemented in Quantum Espresso [61, 62]. DFPT calculations were performed with the ions in the relaxed positions that maintain the original symmetry of the structure, and with the same electronic calculation parameters as in the SSCHA, but with a 24×24×16 **k**-point grid and a Methfessel-Paxton smearing of 0.005 Ry for the BZ integrals. The election of these parameters ensures that the frequency of the phonon mode driving the CDW transition (which is expected to be one of the most pathological ones in terms of the Fermi surface sampling) is converged, as shown in Fig. 5.3. In this figure, convergence is determined by observing a *plateau* in the phonon frequency as the **k**-point grid density increases and the smearing decreases. This *plateau* indicates that further refinement no longer affects the result, meaning the calculation has reached the **k**-grid infinite and vanishing smearing limit, where the phonon frequency is well-sampled across the Fermi surface. Harmonic phonon calculations were carried out both in 4×4×3 and 8×8×6 **q**-point grids. The electron-phonon linewidth is given by Eq. (4.10), in which we use a 48×48×32 **k**-point grid and a Gaussian broadening of 0.003 Ry for the Dirac deltas. These parameters are chosen to ensure the convergence of the linewidth of the CDW driving mode, following a convergence criterion similar to that used in the harmonic phonon calculations.

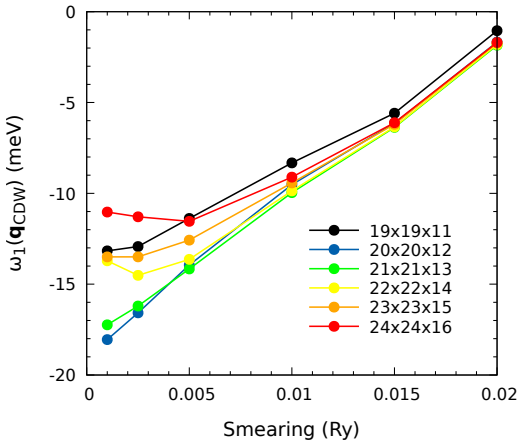

Figure 5.3: **k**-point grid and smearing optimization curve of the CDW driving mode. For a 24×24×16 **k**-point grid, a *plateau* shape appears at the smallest smearing values, so that harmonic phonon calculations are considered converged with a smearing width of 0.005 Ry.

5.4 Electronic properties

In this section, we summarize the current understanding of the electronic structure of the high-symmetry phase of 1 T-VSe_2. We focus on analysing the Fermi surface, as it will be crucial when determining whether nesting is the driving mechanism behind the CDW transition. First, we summarize the angle-resolved photoemission (ARPES) experimental findings on the Fermi surface, and then we compare these results with those from our theoretical calculations. Finally, we review experiments in the literature that explore how the CDW modifies the Fermi surface.

From the electronic point of view, ARPES experiments report that the Fermi surface of 1 T-VSe_2 consists of an intense feature at Γ and ellipsoidal electron pockets centered at M(L) points that extend along the k_z direction of the BZ exhibiting a warped dispersion [110]. These large ellipsoids, which come from the 3d orbitals of vanadium atoms, present in-plane parallel sections that theoretically should be susceptible to electronic instabilities [111]. Indeed, $\mathbf{q}_{\mathrm{CDW}}$ connects these portions of the Fermi surface, so that photoemission experiments usually infer that the CDW in 1 T-VSe_2 follows the nesting scenario. The 3D nature of the CDW is consequently attributed to the 3D warping of the Fermi surface [112].

Figure 5.4 displays the theoretically calculated Fermi surface. The top view in panel (a) illustrates that the Fermi surface contains pockets centered around both the K and M points. The side view in panel (b) emphasizes the three-dimensional warping of the Fermi surface along the k_z direction. In the top view of the $k_z = 0$ plane displayed in panel (c), the surface reveals a single Fermi pocket at the K point. Additionally, the features observed in ARPES experiments, specifically the intense peak at Γ and the ellipsoidal electron pockets located near the M(L) points,

are more accurately reproduced at -200 meV below the Fermi level, as shown in panel (d).

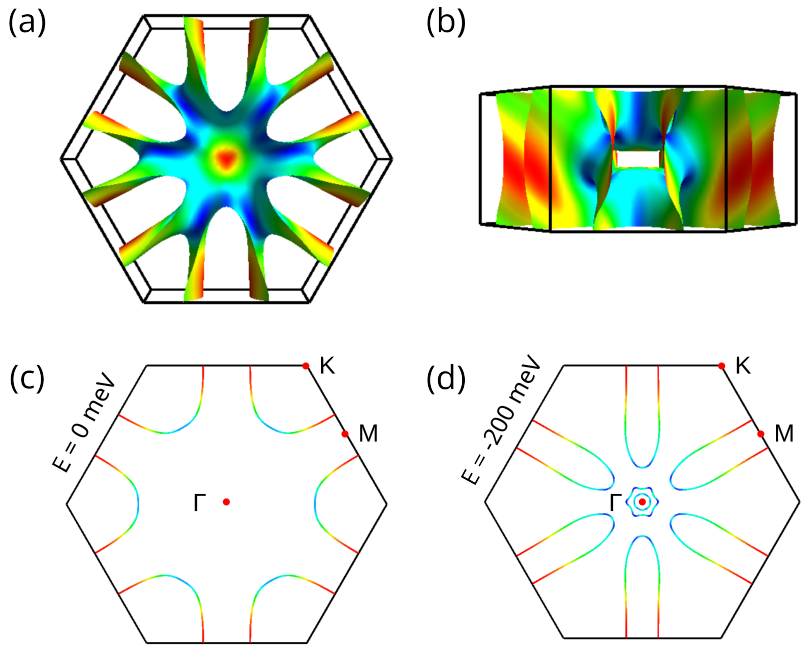

Figure 5.4: (a) Top and (b) side view of the Fermi surface of 1 T-VSe_2. Fermi surface in the $k_z = 0$ plane at (c) the Fermi energy and (d) a constant energy cut at -200 meV. The colour scale indicates the relative Fermi velocity, ranging from blue (lower velocity) to red (higher velocity).

Electronic transport experiments performed by Dr. Blanco-Canosa shown in Fig. 5.5 provide an experimental evidence that VSe_2 remains metallic after the CDW transition. The transition to the CDW state can be identified by a slight increase in the resistance (a tiny hump) at the critical temperature 110 K. This little loss of carriers can be better appreciated as a kink in the temperature derivative. In the same vein, photoemission experiments report that the CDW transition in 1 T-VSe_2 causes the depletion of electronic states near the Fermi level below the critical temperature, but with no traces of total gap openings [110, 111]. Remarkably, this partial suppression of the electronic density of states at the Fermi Energy level, known as pseudogap opening, suffices to prevent the emergence of ferromagnetism in this itinerant electron system [116]. Definitely, from an electronic point of view, the transition from 1 T-VSe_2 to the charge modulated state is not the prototypical Peierls transition from the metallic high-temperature state to the low temperature insulating one.

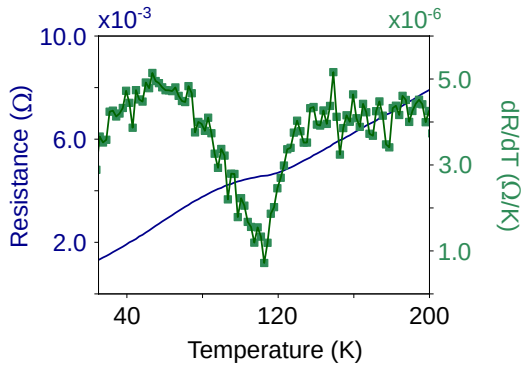

Figure 5.5: Electronic transport experiments in the VSe_2 single crystals, showing the CDW transition at 110 K from the resistance as a function of temperature.

5.5 Characterization of the CDW transition

This section analyses theoretically the response of the lattice to the CDW formation by calculating the phonon spectrum of 1 T-VSe2, the high-symmetry phase, as the temperature lowers towards the transition. First, the temperature-independent harmonic approximation is considered to find unstable modes in the phonon spectrum that could indicate potential structural instabilities towards the formation of a low-symmetry phase. However, as the temperature dependence of phonons is a purely anharmonic effect, this method will inevitably fail describing the lattice's response to the CDW emergence. Therefore, in the second part of this section, non-perturbative anharmonic phonon calculations are performed to accurately capture the temperature-dependent behaviour of the CDW mode. The latter theoretical calculations are supported by experimental measurements performed by Dr. Santiago Blanco-Canosa by means of high-resolution x-ray scattering in the Argonne National Laboratory (University of Chicago).

5.5.1 Harmonic phonon spectra

Harmonic dynamical matrices have been calculated within DFPT in a $\mathbf{q}$-point grid of $4 \times 4 \times 3$. This grid includes the point $\mathbf{q} = (0,\ 1/4,\ 1/3)$, which is almost commensurate with the CDW wavevector $\mathbf{q}_{\mathrm{CDW}} = (0,\ 1/4,\ 0.3)$. Therefore, to optimize our computational calculations, we have considered that the propagation vector of the CDW is commensurate: $\mathbf{q}_{\mathrm{CDW}} \equiv (0,\ 1/4,\ 1/3)$ instead of the exact one. Throughout the rest of the chapter it will be proven that this simplification does not affect significantly the accuracy of the theoretical results when compared to experimental data.

Fig. 5.6 shows the harmonic phonon curves obtained by the Fourier interpolation of the calculated dynamical matrices along two relevant **q**-point paths. The first path, shown in the left panel, covers the $\Gamma - \mathrm{M}$ direction at a height of $q_z = c/3$; that is: $(0,\ k,\ 1/3)$ with $0 < k < 1/2$. In this way it goes through the considered $\mathbf{q}_{\mathrm{CDW}}$ halfway. The second path, in the right panel, goes through the high-symmetry points $\Gamma - \mathrm{M} - \mathrm{K} - \Gamma - \mathrm{A}$.

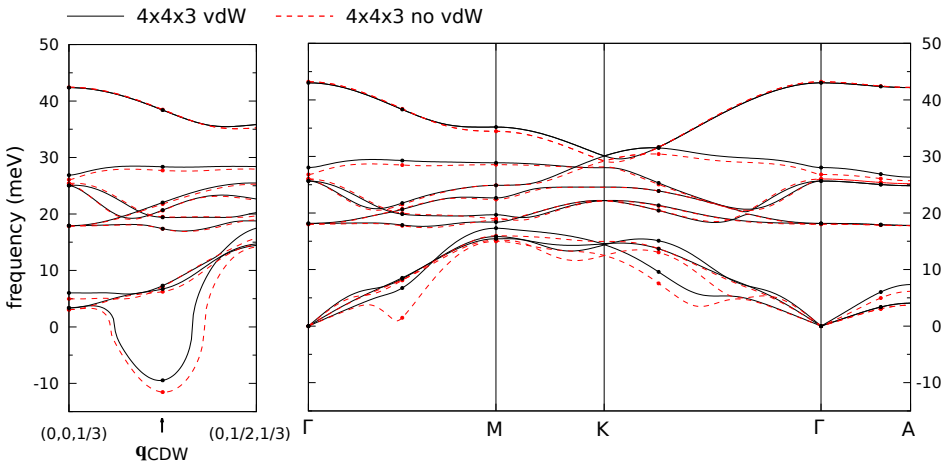

Figure 5.6: Harmonic phonon spectra along $(0,\ k,\ 1/3)$ and $\Gamma - \mathrm{M} - \mathrm{K} - \Gamma - \mathrm{A}$ paths. The black lines correspond to calculations including vdW interactions through Grimme's semiempirical approach, while red dashed lines indicate calculations that do not consider vdW interactions. The points on the curves are part of the $4 \times 4 \times 3$ **q**-point grid and therefore, exact DFPT calculations.

Harmonic phonon calculations in Fig. 5.6 show a sharp instability at $\mathbf{q}_{\mathrm{CDW}}$ regardless of whether van der Waals (vdW) interactions have been included. That is, the standard harmonic approximation is not able to explain the dynamical stability of 1*T*-VSe_2, as it concludes that this high-temperature phase is dynamically unstable towards a $4 \times 4 \times 3$ CDW reconstruction in any case. Yet, the harmonic spectra are affected by the inclusion of vdW interactions. Without vdW interactions (red dashed lines) the lowest energy acoustic branch shows also phonon softening effects towards an eventual collapse in the $\Gamma - \mathrm{M}$ and $\Gamma - \mathrm{K}$ paths. The inclusion of van der Waals dispersion forces with the DFT-D2 method of Grimme [47] (black lines) tends to stabilize the high-temperature phase. Specifically, while the instability at $\mathbf{q}_{\mathrm{CDW}}$ still exists, the corresponding softening it is not as pronounced. What is more, the softening of the lowest energy acoustic branch in the $\Gamma - \mathrm{M}$ and $\Gamma - \mathrm{K}$ paths is not so evident.

By performing DFPT calculations in a denser $8 \times 8 \times 6$ **q**-point grid it can be checked whether the hints of phonon softening effects in the $\Gamma - \mathrm{M}$ and $\Gamma - \mathrm{K}$ paths are real results within the harmonic approximation or just numerical artefacts of the Fourier interpolation. Fig. 5.7 shows the harmonic phonon spectra

interpolated from the DFPT calculations in the $8 \times 8 \times 6$ **q**-point grid compared to the previous results in a $4 \times 4 \times 3$. The denser **q**-point grid corrects previous interpolation errors by localizing in momentum space the instability at the CDW wavevector. Moreover, if vdW interactions are not considered in denser grid calculations (grey dashed lines), the system shows two additional instabilities at $\mathbf{q}_1 \simeq 1/2\overline{\Gamma M}$ and $\mathbf{q}_2 \simeq 3/5\overline{\Gamma K}$. The inclusion of van der Waals dispersion forces (blue lines) stabilizes both of them, but corroborates that phonon softening effects in the $\Gamma - M$ and $\Gamma - K$ paths reported in the calculation in $4 \times 4 \times 3$ **q**-point grid are not interpolation errors. In the analysis of the CDW transition in bulk VSe_2, the softening of the latter phonon modes is not relevant according to experimental evidence. However, we will revisit this point in the next chapter when we analyse the monolayer limit.

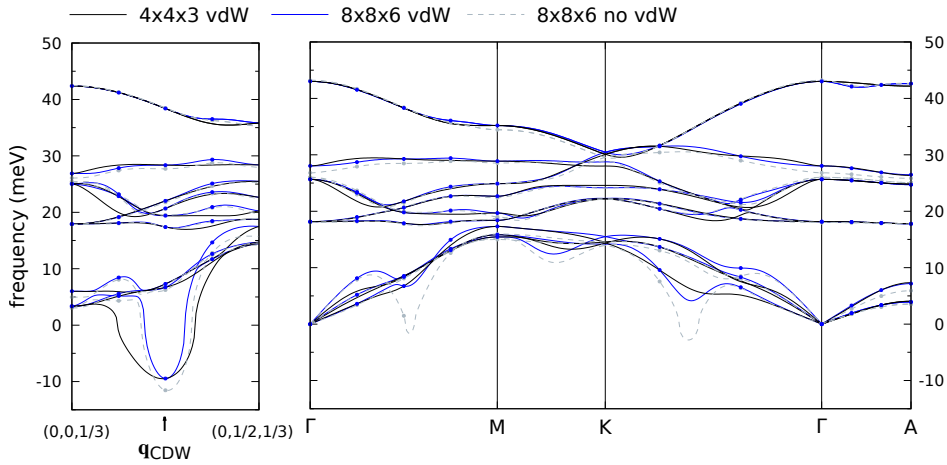

Figure 5.7: Harmonic phonon spectra along (0, k, 1/3) and $\Gamma - M - K - \Gamma - A$ paths for different **q**-point grids. Black ($4 \times 4 \times 3$) and blue ($8 \times 8 \times 6$) continuous lines correspond to calculations including vdW interactions through Grimme's semiempirical approach, while grey dashed lines indicate $8 \times 8 \times 6$ calculations that do not consider vdW interactions. The points on the curves are part of the $8 \times 8 \times 6$ **q**-point grid and therefore, exact DFPT calculations.

All in all, harmonic phonon calculations in this section do not agree with the experimental evidence above the CDW transition temperature, as they cannot explain the stability of the high-temperature undistorted phase. These findings highlight the need of incorporating non-perturbative anharmonic effects to accurately understand the phase diagrams of TMDs undergoing CDW transitions. Nevertheless, the harmonic calculations have brought into focus that weak van der Waals interactions between neighbouring VSe_2 layers seem to play an important role in this compound. As we will see in the next section, it will be essential to consider them in the anharmonic calculations.

5.5.2 Anharmonic phonon spectra

The transition to the charge modulated state can be correctly characterized theoretically through the temperature dependent anharmonic phonons in the static limit. These are obtained by diagonalizing the free energy Hessian at the minimum of the free energy. This minimum was reached within the SSCHA *ab initio* with and without considering vdW corrections at all the temperatures at which the IXS experiments were carried out.

We first center the analysis on the study of the temperature dependence of the frequency of the softest acoustic mode $\omega_1(\mathbf{q}_{\mathrm{CDW}})$. Figure 5.8 compares the experimental data with the SSCHA calculations using different exchange-correlation functionals for the vdW interactions. Experimental results (black squares) indicate that the CDW transition in 1T-VSe_2 is characterized by the softening of this phonon mode, which eventually collapses exactly at the critical temperature. The experimental data for the phonon collapse fits well with the square-root power law predicted by mean-field theory [117], just like in 2H-$NbSe_2$ [96], so that fluctuation corrections are unnecessary to explain the low critical temperature observed in 1T-VSe_2 [107]. Regarding theoretical results, when the SSCHA anharmonic calculation is performed without including the van der Waals corrections (green squares), the softest acoustic mode at $\mathbf{q}_{\mathrm{CDW}}$ remains unstable in all the temperature range where the experiments were carried out, even at room temperature. Remarkably, the inclusion of vdW forces in the SSCHA variational minimization melts the CDW below room temperature.

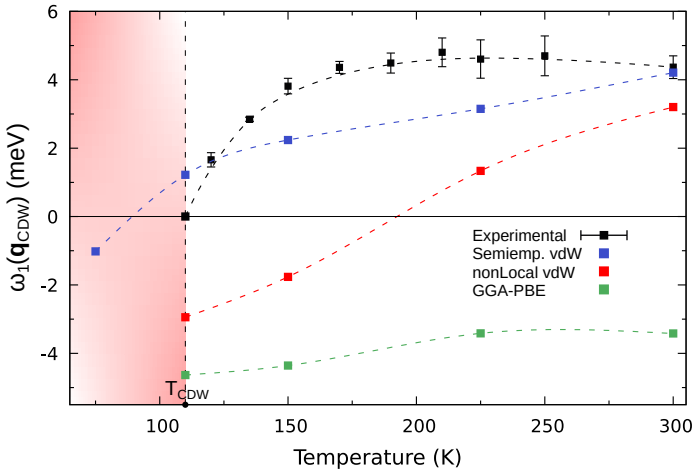

Figure 5.8: Experimental temperature dependence of the frequency of the softest mode, $\omega_1(\mathbf{q}_{\mathrm{CDW}})$, together with the theoretical anharmonic frequencies obtained with and without vdW corrections. The shaded area defines the experimental CDW region. Dashed lines are guides to the eye.

The physical reason behind the CDW melting with increasing temperature is the enhancement of thermal ionic fluctuations, which sample the anharmonic part of the potential. Accurately describing the anharmonic free energy landscape in the case of 1 T-VSe_2 involves including the weak vdW interactions (around $\sim$1 mRy/a_0 for a typical SSCHA supercell calculation), in stark contrast with the rest of the TMDs previously studied through the SSCHA [76–78]. This particular requirement can be related to the three-dimensional nature of the CDW, as the soft phonon mode driving the transition exhibits out-of-plane displacements of selenium atoms that modulate the interlayer distance. Definitely, anharmonicity stabilizes the 1T structure of VSe_2 at high temperatures thanks to the crucial role played by the weak van der Waals forces.

The calculated CDW critical temperature strongly depends on how vdW interactions are included in the *ab initio* calculation of energies and forces. The best agreement with the experimental result is obtained with the DFT-D2 method of Grimme [47], plotted with blue squares in Fig. 5.8, which simply adds a semiempirical dispersion correction on top of a converged Kohn-Sham energy. This theoretical result predicts that the soft mode frequency vanishes between 75 and 110 K, in good agreement with the experimental value of $T_{CDW} = 110$ K. The, *a priori*, more sophisticated vdW-DF functional proposed by Dion et al. [48], which is truly non-local, is plotted with red squares and succeeds in melting the CDW, but overestimates the critical temperature by approximately 80 K.

Figure 5.9 displays the experimental IXS spectra of the low-energy acoustic phonons at 300 K and 150 K, together with anharmonic calculations that include vdW interactions through Grimme's semiempirical approach. The scanned direction (2+h, 0, 0.7) is practically equivalent by space-group symmetry to the previously analysed (0, k, 1/3). Optical phonons, which will be analysed in the next section, appear above 17 meV and do not overlap with the acoustic branches. At both temperatures the spectrum consists of 2 phonon branches, labeled as ω_1 and ω_2, which belong to the same irreducible representation and, thus, do not cross. The third acoustic branch (plotted with grey lines) is silent in this direction of the reciprocal space in IXS experiments since the corresponding polarization vectors are perpendicular to the scanned wavevectors.

The theoretical dispersions nicely match the experimental data from the zone center to the border of the BZ. Namely, at room temperature anharmonic phonon calculations confirm the experimental evidence that both ω_1 and ω_2 branches develop a dip at $h \approx 0.25$ as shown in Fig. 5.9 (a). When lowering the temperature to 150 K, the dispersion of the branch ω_2 barely changes. Contrarily, the branch ω_1 lowers its energy specially around $\mathbf{q}_{CDW}$, softening from room temperature down to 110 K as previously reported in Fig. 5.8. At 150 K the softening extends over a wide region of momentum space $0.2 < h < 0.3$ (0.2 Å^{-1}), which is also well captured in the anharmonic phonon calculations. The sizeable momentum space range of the phonon softening is considered an experimental indicator for electron-phonon interaction driven CDW transitions [96, 97], given that it contrasts with

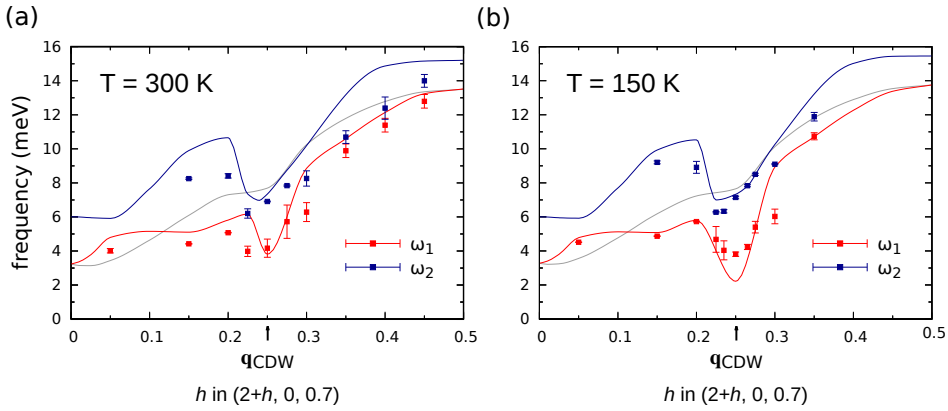

Figure 5.9: Experimental (points) and calculated (solid lines) dispersions of the low-energy acoustic phonons along the (2+h, 0, 0.7) direction at (a) 300 K and (b) 150 K.

the sharp dips associated with the electronic instabilities induced by Fermi surface nesting [118]. The momentum space spread of the phonon softening in ω_1 branch is revisited and thoroughly analysed in Section 5.7, which is devoted to analyse the origin of the CDW transition.

5.6 Lattice dynamical properties

While anharmonic phonon frequencies in the last section have been obtained from the diagonalization of the free energy Hessian, actual physical phonons measured in experiments are related to peaks in the spectral function that includes anharmonic effects. The positions of the phonon peaks coincide with the eigenvalues of the free energy Hessian when the spectral function is calculated using the static value of the full dynamical SSCHA self-energy, $\mathbf{\Pi}(\omega = 0)$, as described in Eqs. (3.65)–(3.66). This approximation of neglecting the dynamic effects in the anharmonic self-energy is valid for low-energy modes (where $\omega \to 0$), such as the CDW driving mode, because the corresponding value $\mathbf{\Pi}(\omega \to 0)$ is practically equal to the static one $\mathbf{\Pi}(\omega = 0)$. Therefore, the static analysis based on the free energy Hessian performed in the last section accurately characterizes the CDW transition. For high-energy phonon modes, the static limit fails due to significant dynamic effects, making it mandatory to calculate the anharmonic spectral function to capture them accurately.

In this section we present a theoretical analysis of the anharmonic spectral functions $\sigma(\mathbf{q}, \omega)$ at two relevant temperatures: the experimental critical temperature (110 K) and room temperature. In these calculations we include vdW interactions within Grimme's semiempirical approach, since the static calculations of the previous section have shown that it is the functional that best reproduces the physics of 1T-VSe_2.

First, we check the adequacy of the approximations introduced in Section 3.3.5 by calculating the anharmonic phonon spectral function at the critical wavevector $\sigma(\mathbf{q}_{CDW}, \omega)$ and 110 K. As shown in Fig. 5.10 (a), not all modes have a Lorentzian profile. For instance, the highest energy mode has a clear satellite peak, indicating that anharmonicity makes the quasiparticle picture questionable for this mode and, consequently, the Lorentzian approximations do not work well. This result emphasizes that anharmonicity is not only crucial to stabilize the lowest energy mode at $\mathbf{q}_{\mathrm{CDW}}$ as seen in the previous section, it also impacts high-energy optical modes considerably in their spectral properties. Nevertheless, the spectrum obtained within the Lorentzian "one-shot" approximation, plotted with blue solid lines, yields a reasonable result for most modes. In particular, for the lowest energy branch, the one driving the CDW transition, the result is not identical to the non-Lorentzian "no-mode mixing" approximation, but in both cases the positions coincide. The spectrum obtained in the perturbative limit, plotted with dashed yellow lines, is generally in agreement with the "one-shot" calculation. However, the frequency attributed to the phonon that drives the CDW transition is blue shifted in the latter case. This means the SSCHA self-energy cannot be considered small for the softened mode, and the perturbative approach fails.

Fig. 5.10 (c) still shows the spectral function at the critical wavevector, albeit now at room temperature. Increasing temperature flattens and broadens all phonon peaks due to enhanced scattering between phonons, hindering their experimental detection. Interestingly, the soft mode is strongly blue shifted with temperature up to ~ 5 meV at 300 K as expected from the static calculations presented in the previous section, while the other two acoustic modes become quasi-degenerate.

In Fig. 5.10 (b) and (d) the anharmonic phonon spectral function is presented at the Γ point for both 110 K and 300 K. For low-energy excitations the phonon quasiparticle picture is rather well defined. However, the huge phonon satellite ascribed to the highest-energy optical mode confirms this mode is strongly anharmonic throughout the whole BZ despite its high energy and that anharmonicity removes its quasiparticle nature. In fact, the splitting of this peak in two can lead to confusions during experiments. The highest energy mode is infrared (IR) and not Raman active, so that it might be difficult to observe the peak splitting with either of these techniques due to the large reflectivity of metals in the IR.

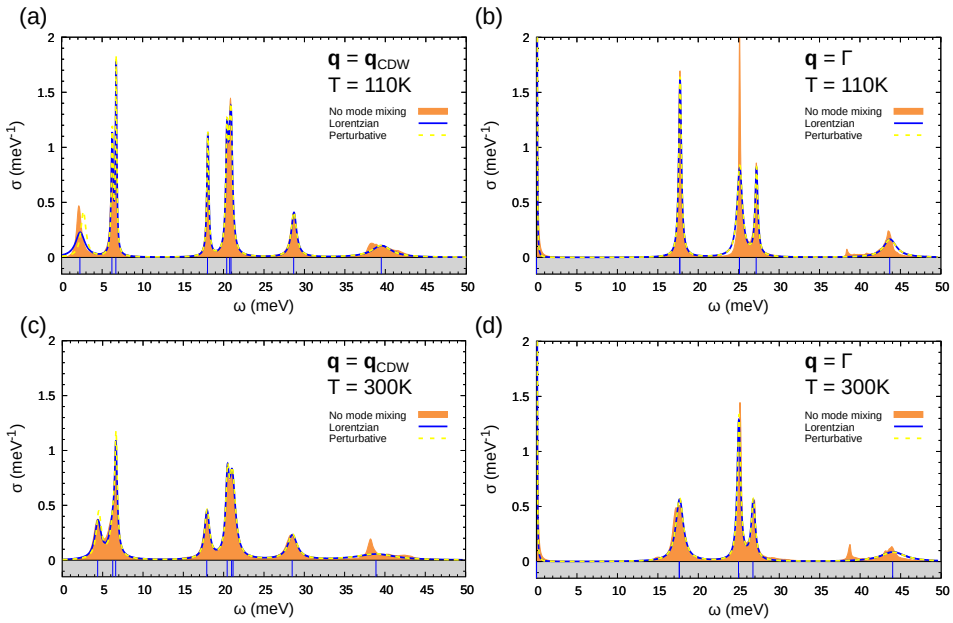

Figure 5.10: Anharmonic phonon spectral functions at 110 K at (a) $\mathbf{q}_{\mathrm{CDW}} = (0, 1/4, 1/3)$ and (b) Γ points, and at room temperature at (c) $\mathbf{q}_{\mathrm{CDW}}$ and (d) Γ points. The orange filled area indicates the result obtained with the "no mode-mixing" approximation in Eq. (3.69). The blue solid line is the spectrum calculated in the "one-shot" Lorentzian approximation in Eqs. (3.74). The center of these Lorentzians, specified with vertical blue lines in the grey shaded area below, indicate the anharmonic phonon frequencies in the quasiparticle picture. The dashed yellow line is the spectrum in the perturbative limit (see Eqs. (3.75)).

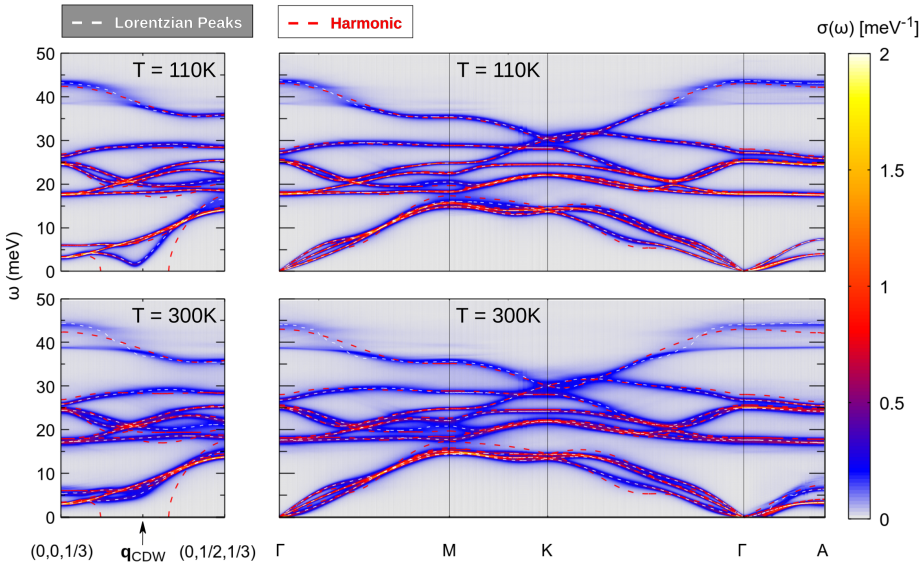

Figure 5.11: Anharmonic phonon spectral functions at 110 K and 300 K along (0, k, 1/3) and $\Gamma - M - K - \Gamma - A$ paths. The dashed white lines are the anharmonic phonon frequencies extracted from the center of the Lorentzians in the "one-shot" approximation, while red dashed lines are the harmonic phonon spectra interpolated from DFPT calculations in a $4 \times 4 \times 3$ **q**-point grid.

In Fig. 5.11 the full anharmonic phonon spectrum is plotted both at 110 K and 300 K and is compared to calculations using the harmonic approximation. The figure clearly illustrates that the main anharmonic renormalization of the phonon frequency concentrates around $\mathbf{q}_{\mathrm{CDW}}$. The frequency of the CDW driving ω_1 mode, unstable in the harmonic approximation, is strongly temperature dependent as reflected by the spectral function. It is interesting to remark that the lowest energy acoustic modes halfway between Γ-M and Γ-K, which display softening effects in the harmonic approximation, are slightly stabilized by anharmonic effects, but with a weak temperature dependence. The full spectral function reveals that the highest energy optical mode shows a clear double peak structure in most of the BZ at low and high temperatures and the highest energy longitudinal acoustic mode exhibits a satellite peak close to A at 300 K.

5.7 Origin of the CDW

Having established that the CDW formation is characterized by the collapse of a low-energy acoustic phonon mode, in this section we analyse which is the mechanism causing the phonon softening of the CDW mode $\omega_1(\mathbf{q}_{\mathrm{CDW}})$. Being TMDs systems with dimensions higher than 1D or quasi-1D, Peierls' initial proposal of the Fermi surface nesting as the CDW driving mechanism probably does not hold [16]. In fact, IXS and theoretical calculations already highlighted the importance of a highly momentum dependent electron-phonon interaction in the formation of the CDW in similar compounds of the TMD family, such as $2H$-$NbSe_2$ [96, 119] and $1T$-$TiSe_2$ [93, 97]. Regarding $1T$-VSe_2, the critical role of the momentum dependence of the electron-phonon interaction was already pointed out in Ref. [120] by means of quantitative models. However, ARPES experiments have endorsed to a pure electronic mechanism the formation of the charge modulated state, considering that $\mathbf{q}_{\mathrm{CDW}}$ connects many portions of the Fermi surface [112].

In this section we analyse in detail the role of the Fermi surface nesting and the electron-phonon interaction in the formation of the charge modulated state in $1T$-VSe_2. Since the momentum localization of the soft phonon mode is a presumed hint of the nesting mechanism easily accessible in IXS experiments [96, 97, 118], we first analyse experimentally and theoretically the momentum spread of the phonon softening and the electron-phonon interaction linewidth around $\mathbf{q}_{\mathrm{CDW}}$. We then corroborate our results by comparing the nesting and the electron-phonon interaction scenarios in a purely theoretical, yet more rigorous, analysis.

5.7.1 Anisotropic electron-phonon interaction

Since inelastic x-ray phonon measurements trying to elucidate the CDW origin base their conclusions on the width of the BZ range in which the phonon branch is damped [96, 97, 118], we consider useful to provide a deeper analysis by extending both the experimental and theoretical results to the perpendicular directions (h, k, l) around $\mathbf{q}_{\mathrm{CDW}}$.

In Fig. 5.12, we compare the frequencies and total linewidths of the soft phonon branch at 150 K, probing the perpendicular directions around $\mathbf{q}_{\mathrm{CDW}}$. The total linewidths include electron-phonon and anharmonic contributions. Figures 5.12 (a-c) display the momentum dependence of the phonon softening along the three directions. Once again, theoretical calculations considering anharmonicity within the SSCHA, represented by blue lines, nicely match the experimental data. The softening of the phonon modes is accompanied by an enhancement in their linewidth as shown in Figures 5.12 (d-f). The experimental phonon broadening reported in the latter Figures is also well captured by the total linewidth obtained theoretically, drawn with black lines.

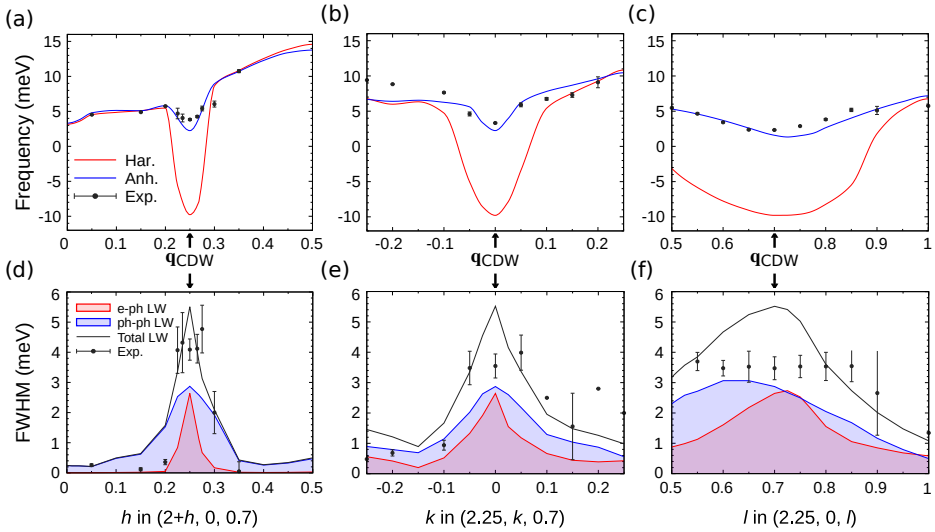

Figure 5.12: (a-c) Experimental (points) and calculated (solid lines) dispersions of the soft mode at 150 K around $\mathbf{q}_{CDW}$; probing the perpendicular directions (h, k, l). (d-f) Experimental (points) and theoretical (solid lines) linewidth in the same momentum range. The calculated linewidth (black line) includes the contribution of the electron-phonon interaction (red shaded line) and anharmonicity (blue shaded line).

In finer detail, we find that the region of momenta that undergoes a phonon softening (linewidth broadening) is anisotropic in momentum space, both experimentally and theoretically. This anisotropic behaviour is also present at the harmonic level (red lines in Fig. 5.12 (a-c)) and in the electron-phonon linewidths (red shaded lines in Fig. 5.12 (d-f)). In both of the latter cases the observed anisotropies are strongly correlated through the static limit of the electron-phonon self-energy for phonons, as described in Eq. (4.8). This correlation arises because the real part of the self-energy affects the harmonic phonon behaviour, while the imaginary part determines the electron-phonon linewidth. Since the electron-phonon matrix elements influence the mentioned phonon self-energy, these calculations capture effectively the anisotropy of the electron-phonon matrix elements in momentum space, and nesting in a lower extent.

In fact, considering the Fermi surface nesting scenario as the driving force of the CDW formation, naively one would expect a narrow and therefore isotropic softening (broadening) in momentum space. This is in clear contrast with the data reported in Fig. 5.12. Moreover, the anisotropic behaviour we report highlights the weakness of relying on the width of the BZ range where the phonon branch is damped to propose nesting as the origin of the CDW. Precisely, this kind of arguments may be conditioned by the direction in which the scan is performed, at least in the case of 1T-VSe_2. Still, the fact that the anisotropy is accentuated in the out-of-plane l direction, suggests that it may be related to the quasi-2D na-

ture of the compound and, thus, it is reasonable to think that the electron-phonon interaction and anharmonic effects are also anisotropic in other compounds of the TMD family and in other strongly correlated electron systems. Regardless of any potential generality, our results allow us to indicate that a pure nesting scenario for $1T$-VSe_2 cannot solely act as the driving force, and clearly support previous claims that point to the electron-phonon coupling as the trigger for the CDW formation.

5.7.2 Role of FSN and electron-phonon interaction

In this subsection, we move beyond the heuristic argument of electron-phonon anisotropy as the primary reason for discarding the nesting scenario. For this purpose, we conduct a detailed theoretical analysis to compare how the nesting and electron-phonon mechanisms influence the CDW formation. As a first step, we calculate the nesting function $\zeta(\mathbf{q})$ to better understand the electronic structure of VSe_2 and its impact on lattice dynamics:

$$\zeta(\mathbf{q}) = \frac{1}{N_{\mathbf{k}}} \sum_{nn'} \sum_{\mathbf{k}}^{1BZ} \delta(\epsilon_{n'\mathbf{k}+\mathbf{q}}) \delta(\epsilon_{n\mathbf{k}}) \ . \tag{5.1}$$

The nesting function probes the Fermi surface by peaking at nesting $\mathbf{q}$ wavevectors, revealing whether the CDW could emerge from an electronic instability. In Fig. 5.13 (a-c) we plot the nesting function around the perpendicular directions (h, k, l) of $\mathbf{q}_{\mathrm{CDW}}$. The nesting function peaks just at the CDW vector for h and k in-plane scans, and nearby for the out-of-plane l scan, so that $\mathbf{q}_{\mathrm{CDW}}$ coincides with a nested region of the Fermi surface, in agreement with ARPES experiments in Ref. [112]. However, it must be remarked that a peak at $\mathbf{q}_{\mathrm{CDW}}$ in the nesting function is not sufficient condition to determine whether the origin of the CDW is purely electronic. In order to reach a firm conclusion, the nesting function results have to be compared with the electron-phonon interaction scenario.

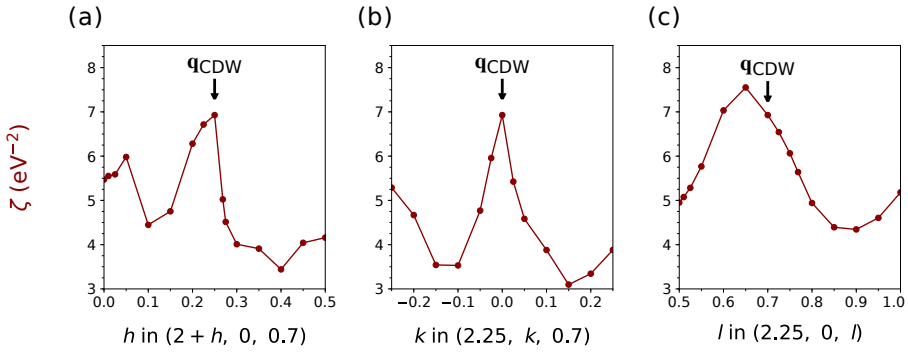

Figure 5.13: Nesting function around the perpendicular directions (h, k, l) of $\mathbf{q}_{\mathrm{CDW}}$.

To evaluate their respective impacts on the CDW formation, we plot in Fig. 5.14 the ratio between the electron-phonon linewidth contribution to the total linewidth and the nesting function for each acoustic phonon branch. In this way we assess directly the momentum and mode dependence of the electron–phonon coupling matrix elements following Eq. (4.4): if the electron-phonon matrix elements were constant, the ratio should be flat. Clearly this is not the case in Fig. 5.14, since the ratios suggest that the electron-phonon matrix elements are strongly mode and momentum dependent. In fact, each ratio for the softest branch ω_1 has a very similar shape to the electron-phonon linewidth itself, which was plotted in red shaded lines in Fig. 5.12 (d-f). This is a signature that the electron-phonon matrix elements depend more strongly on momentum than the nesting function itself. Remarkably, the scan alongside the out-of-plane direction shows that while the nesting function favours a commensurate $4\times4\times3$ CDW reconstruction, it is the electron-phonon mechanism that leads to the incommensurate CDW reconstruction reported in our experiments with $l \simeq 0.7$. In conclusion, the electron-phonon coupling is the main driving force of the CDW transition in $1\,T$-VSe_2 despite the presence of nesting at $\mathbf{q}_{\mathrm{CDW}}$, whose role is rather to be a factor enhancing the electron-phonon interaction than the main mechanism itself.

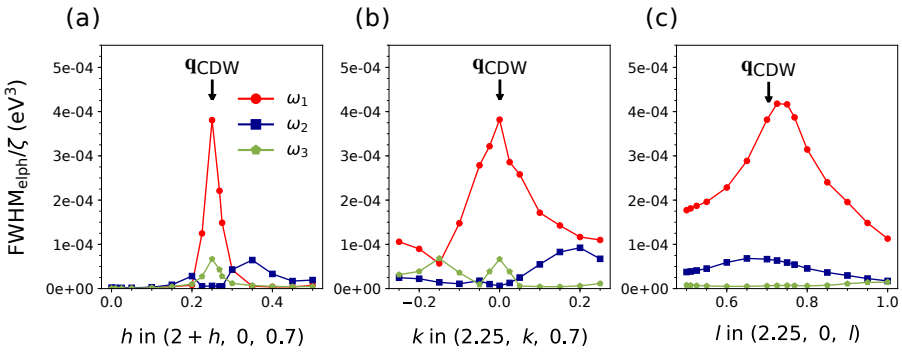

Figure 5.14: Ratio between the electron-phonon linewidth (full width at half maximum) and the nesting function around the perpendicular directions (h, k, l) of $\mathbf{q}_{\mathrm{CDW}}$.

Last but not least, it is important to highlight that the theoretical analysis of this section has focused on the imaginary parts of both the electronic susceptibility (the nesting function) and the electron-phonon self-energy. However, if the CDW instability is driven by any of these mechanisms, it is the real part of these quantities that must diverge, as this relates directly to the renormalization of phonon frequencies. In any case, calculating the ratio between the imaginary parts has allowed us to confirm the anisotropic behaviour of the electron-phonon matrix elements. And in fact, this anisotropy is also evident in the harmonic phonons, which are influenced by the real part of the static limit of the electron-phonon self-energy, as discussed in the previous subsection. This correlation confirms that the divergence observed in the imaginary part of the electron-phonon self-energy also manifests in the corresponding real part, further emphasizing the critical role of electron-phonon interactions in driving the CDW transition.

5.8 Effect of pressure on the CDW

Having comprehensively described the lattice dynamics and CDW transition of 1 T-VSe_2, we finally analyse the effect of pressure on the charge modulated state. The trend observed so far in other members of the TMD family is that pressure causes the suppression of the CDW. 2H-$NbSe_2$ is a paradigmatic case of this behaviour, in which the CDW suppression is related to the strong anharmonic character of the lattice potential, which stabilizes the high temperature phase under pressure [94]. TMDs apart, pressure induced CDW destructions have also been reported in correlated materials such as high-T_c cuprates [121] and kagome metals [122, 123].

In clear contrast to the typical behaviour observed in systems hosting CDWs, an enhancement of the CDW order in bulk VSe_2 up to $\sim$ 290 K (almost room temperature) at $\sim$ 13 GPa has been recently observed in transport experiments [92]. At this pressure VSe_2 undergoes a first order phase transition to a new $C2/m$ phase, which destroys the charge order and allows superconductivity to emerge below a critical temperature of $T_c \sim 4$ K. High-pressure Raman [124], x-ray diffraction, and spectroscopic experiments [125] confirmed that the transition to the $C2/m$ phase starts at room temperature. The $P-T$ phase diagram of 1 T-VSe_2 is shown in Fig. 5.15, which is a figure adapted from Ref. [92] with the aim of clarifying the scenario. All in all, seen the anomalous behaviour shown by the CDW phase of 1T-VSe_2 under pressure, in this section we finish our survey by studying both experimentally and theoretically the evolution of the soft mode with pressure at room temperature. The difficulties encountered in lowering the temperature during the experiments forced us to operate at this temperature, even tough it is actually slightly above the range where the CDW enhancement is observed.

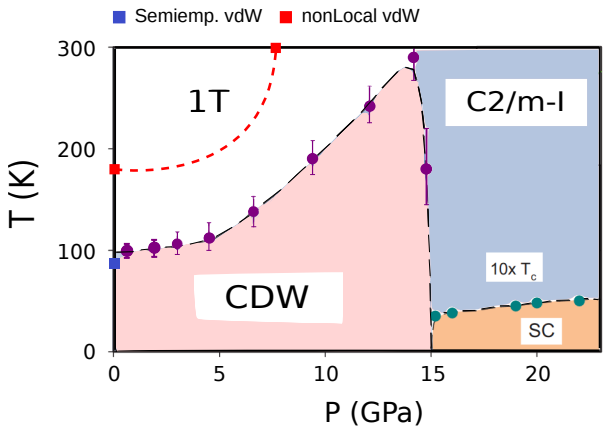

Figure 5.15: Experimental $P-T$ phase diagram of 1 T-VSe_2. Theoretical critical temperatures and pressures, obtained considering anharmonicity within the SSCHA using different vdW corrections, are included as squares. Dashed lines are guides to the eye. Figure adapted from Ref. [92].

For this purpose, SSCHA anharmonic calculations have been performed at room temperature for some pressure values inside the experimental range, making use of the experimental lattice parameters obtained through high-pressure x-ray powder diffraction experiments [110] and shown in Fig. 5.16. The application of pressure leads to a decrease of the lattice parameters. It is noteworthy that the reduction of the interlayer distance c lowers the out-of-plane vdW interactions, which have proven to be essential for melting the CDW state under temperature. Consequently the choice of exchange-correlation functional in the SSCHA calculations under pressure has to be performed carefully.

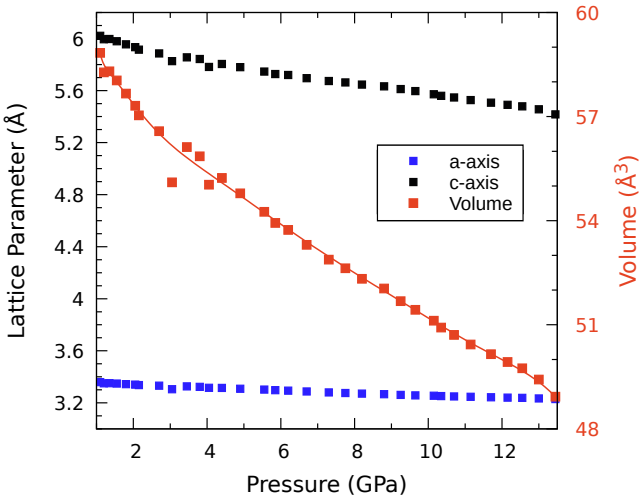

Figure 5.16: Experimental pressure dependence of the lattice parameters a and c, along with the unit cell volume, at room temperature.

Before entering into the debate about which functional best resembles our system under pressure, let us analyse the experimental phonon results obtained by means of high-pressure IXS. These are shown in Fig. 5.17 with black symbols. In this case the pressure dependence of the two visible branches ω_1 and ω_2 at $\mathbf{q}_{\mathrm{CDW}}$ is shown. The frequency of the $\omega_2(\mathbf{q}_{\mathrm{CDW}})$ mode in the upper panel has the expected behaviour under pressure, exhibiting an increase attributed to the stiffening of the lattice. Specifically, the frequency shows a linear grow ($\sim$ 0.3 meV/GPa) up to 13 GPa. In contrast, the experimental frequency of the soft mode $\omega_1(\mathbf{q}_{\mathrm{CDW}})$ remains pressure independent up to 10 GPa as shown in the bottom panel of Fig. 5.17, without collapsing on approaching the high-pressure phase, but softens $\sim$10% between 10 and 13 GPa. The distinct behaviour of the CDW driving phonon mode $\omega_1(\mathbf{q}_{\mathrm{CDW}})$ with temperature and pressure demonstrates that the measured phase transitions are fundamentally different.

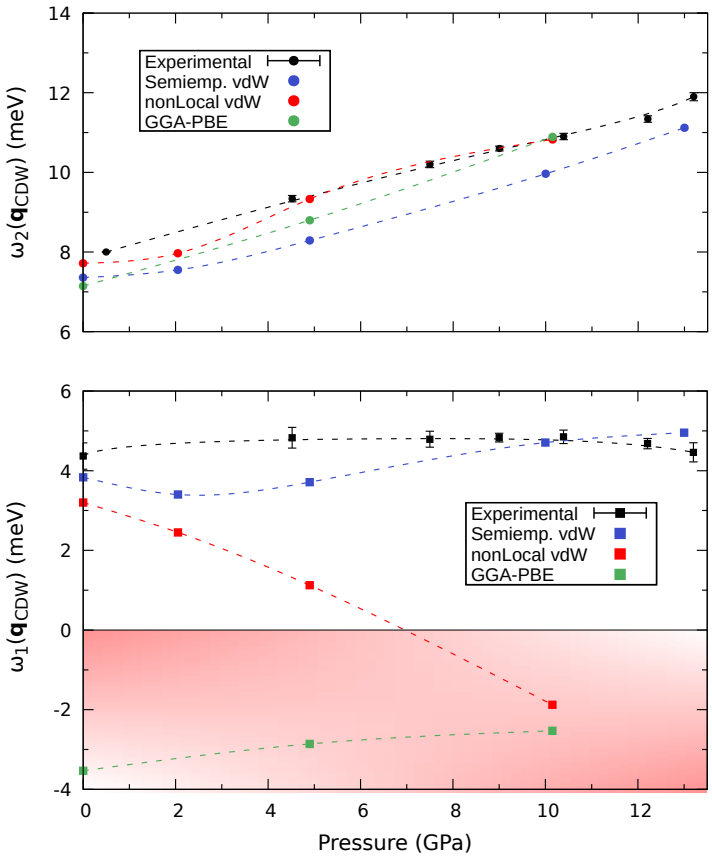

Figure 5.17: Experimental pressure dependence of ω_1 (bottom panel) and ω_2 (top panel) branches at $\mathbf{q}_{CDW}$ at room temperature, together with the theoretical anharmonic frequencies obtained with and without vdW corrections. The shaded area defines the CDW region. Dashed lines are guides to the eye.

The theoretical phonon frequencies calculated with different exchange-correlation functionals are also presented in Fig. 5.17. While all functionals yield accurate trends and frequencies for the ω_2 phonon branch, that is not the case regarding the soft mode $\omega_1(\mathbf{q}_{CDW})$. GGA-PBE wrongly predicts that, at 300 K, the system stays in the CDW phase for all pressures. Therefore, out-of-plane vdW interactions are still relevant when melting the charge modulated phase, even though they are expected to be quenched with increasing pressure. In fact, the non-local vdW exchange-correlation functional captures the CDW transition under pressure as the ω_1 phonon at $\mathbf{q}_{CDW}$ softens with increasing pressure, indicating that this functional correctly describes the increase of the CDW critical temperature with pressure. However, it underestimates the transition pressure to the new phase, in agreement with the fact that it overestimates at 0 GPa the CDW critical temperature, as indicated by red dashed lines in Fig 5.15. The semiempirical approach yields a phonon frequency ω_1 that increases with pressure, the opposite to the expected behaviour and the experimentally observed trend, even if the absolute

values obtained with this approach yield the closest frequencies to the experimental ones.

The behaviour of the frequency of the soft mode with respect the choice of functionals resembles the situation in the monolayer limit analysed in the next chapter [126], in which the inclusion of the non-local vdW interactions in the exchange-correlation functional will be mandatory to obtain a good description of the transition to the CDW phase. The reason is that, in the bulk case without pressure, although Grimme's semiempirical approach yields the best results, it introduces spurious intralayer interactions by applying a similar correction for vdW interactions between chalcogen atoms in adjacent layers and within the same layer. This oversimplifies the treatment of intralayer interactions as the screening effects from the transition metal are neglected. Thus, under pressure, these undesirable intralayer effects begin to dominate compared to the interlayer effects, which are increasingly quenched. Therefore, to accurately describe the transition to the CDW phase under pressure, it is crucial to adopt an approach that properly accounts for non-local interactions, as Grimme's method is insufficient in this context.

To sum up, high-pressure IXS experiments at room temperature show that the soft mode $\omega_1(\mathbf{q}_{\mathrm{CDW}})$ remains nearly constant under pressure up to 13 GPa, with only a slight softening before the transition to the high-pressure monoclinic *C2/m* phase. Regarding the corresponding theoretical calculations, the results obtained with the non-local vdW exchange-correlation functional show the increase of the CDW critical temperature with pressure reported in previous experiments, despite the fact that the simulated CDW transition differs from the one reported in the experiments. In conclusion, theoretical results indicate that the complexity of lowering the temperature in the experiments has prevented us from observing experimentally how the CDW phase emerged under pressure.

5.9 Conclusions and outlook

In this chapter the CDW transition of $1\,T$-VSe_2 has been comprehensively analysed. Non-perturbative anharmonic phonon calculations in conjunction with high-resolution IXS experiments have provided the first direct evidence that the CDW transition in this compound is driven by the collapse of a low-energy acoustic phonon mode with $\mathbf{q}_{\mathrm{CDW}} = (0,\ 1/4,\ 0.3)$ at $\mathrm{T_{CDW}} = 110$ K. This softening behaviour has also been reported in some similar TMD compounds like $2H$-$NbSe_2$ [96] and $1\,T$-$TiSe_2$ [97].

The theoretical analysis has highlighted that anharmonic effects play a crucial role in the collapse of the phonon mode driving the CDW transition. Phonon spectra show substantial changes when anharmonicity is considered, and, in fact, these anharmonic effects are responsible for stabilizing the high-symmetry phase of VSe_2 at high temperatures. In the same way as in other TMDs like $2H$-$NbSe_2$ [77], it is not necessary to consider the electronic entropy in the formalism to

achieve anharmonic results comparable to experimental findings. However, in notable contrast to other TMDs previously investigated using the SSCHA [76–78], the inclusion of weak vdW interactions between neighbouring VSe_2 layers is vital to melt the CDW. In fact, anharmonic calculations are only comparable to experimental results if vdW corrections are considered. The particular importance of vdW forces on $1\,T$-VSe_2 could be understood through the out-of-plane nature of the CDW. In fact, this explains in some way why the CDW critical temperature is enhanced in monolayer VSe_2 [100–105], in which evidently interlayer interactions are absent. Following the same logic, for the cases in which the CDW has an in-plane nature, it is expected the bulk and monolayer critical temperatures to be rather similar. Precisely, this is what happens in the paradigmatic member of TMDs family $2H$-$NbSe_2$ [77, 91]. The controversial CDW transition in monolayer VSe_2 deserves its own research line so that the next chapter is entirely devoted to its analysis.

The CDW transition in $1\,T$-VSe2 is primarily driven by the electron-phonon interaction, rather than pure Fermi surface nesting. While our nesting function calculations reveal a Fermi surface nested by $\mathbf{q}_{\mathrm{CDW}}$, consistent with ARPES experiments, further calculations indicate that nesting alone cannot explain the CDW formation [112]. The wide and anisotropic phonon softening in momentum space, the strong momentum and mode-dependent electron-phonon linewidth peaking at the CDW wavevector, and the weaker wavevector dependence of the nesting function all point to electron-phonon coupling as the dominant mechanism. Recent ARPES experiments have observed kinks in the dispersion of electronic bands near the Fermi energy, providing additional experimental confirmation of a strong electron-phonon coupling in this compound [113]. In conclusion, the electron-phonon interaction is the main driving force of the CDW transition in $1\,T$-VSe_2 despite the presence of nesting at the CDW wavevector, whose role is rather to be a factor intensifying the electron-phonon matrix elements rather than being the principal mechanism itself.

Finally, the effect of pressure on the charge modulated state has been analysed. Unlike the suppression of CDWs under pressure observed in similar TMDs, transport experiments on bulk VSe_2 report that the charge modulated phase actually enhances up to nearly room temperature. Our theoretical anharmonic results obtained with non-local vdW exchange-correlation functional support the enhancement of the CDW phase with pressure. This suggests that accounting for long-range vdW interactions remains essential for melting the CDW and accurately describing the transition, even when the interlayer distance is reduced. On the contrary, the high-pressure transition observed in the IXS experiments at room temperature is better described by a first-order phase transition. The $P-T$ phase diagram in Fig. 5.15 shows that the enhancement of the CDW phase in bulk VSe_2 is up to ~ 290 K, close to room temperature but still slightly below it. This suggests that the complexity of lowering the temperature in the experiments may have prevented the observation of the CDW phase's emergence under pressure, while the first-order phase transition to the $C2/m$ phase was probably measured instead.

6

Monolayer VSe_2

6.1 Introduction

In Chapter 5 both inelastic x-ray scattering experiments and non-perturbative anharmonic phonon calculations have provided evidence that the CDW transition in bulk VSe_2 is driven by the collapse of a low-energy acoustic mode. In the monolayer limit the CDW transition may also be characterized by similar phonon softening effects, but a less significant influence of van der Waals interactions can be expected.

The main problem in the monolayer of VSe_2 is the lack of consensus on which the CDW reconstruction is, as unrelated experiments have reported distinct orders with varying transition temperatures. A 4×4 order was observed in VSe_2 films grown on bilayer graphene on top of SiC and on highly oriented pyrolytic graphite (HOPG), with a T_{CDW} of $\sim 140 \pm 5$ K and a lattice parameter of $a = 3.31 \pm 0.05$ Å[100]. On the contrary, a $\sqrt{3} \times \sqrt{7}$ modulation has been observed in VSe_2 samples grown on several substrates by molecular beam epitaxy by different groups, with a consistent $T_{CDW} = 220$ K [101, 103]. Some other orders have also been reported: a combination of $2 \times \sqrt{3}$ and $\sqrt{3} \times \sqrt{7}$ with a $T_{CDW} \sim 135$ K [102, 105], and a 4×1 modulation with $T_{CDW} \sim 350$ K [102, 104]. These experimental contradictions point to the presence of different competing CDW orders, which can lead to different low-temperature phases depending on the substrate.

In fact, theoretical studies in the literature have already remarked the critical role of the substrate strain in the phase diagram of monolayer VSe_2. In particular, harmonic phonon calculations in the high temperature state have described the competition of different CDW orders as a function of strain [127]. However the

range of the simulated strain values[1] is not an entirely realistic representation of the experimentally reported lattice parameter $a = 3.31 \pm 0.05$ Å. Moreover, harmonic calculations cannot explain that above T_{CDW} the $1T$ phase is the ground state, just like analysed in Chapter 5 for bulk $1T$-VSe_2. Once again, only non-perturbative anharmonic calculations can provide a reliable analysis of the dynamical stability of this compound, as they predict correctly the transition temperature for each lattice parameter.

In this chapter, we analyse the strain effects on the CDW orders in monolayer VSe_2 by means of non-perturbative anharmonic phonon calculations. Since samples of at least 60μm thickness are needed to perform IXS experiments, our study is purely theoretical in this case.

6.2 Crystal structure

Similar to its bulk counterpart, monolayer VSe_2 crystallizes in a $1T$-phase with a space group $P\bar{3}m1$ at room temperature, but it naturally consists of only a single layer, as shown in Fig. 6.1. The corresponding 2D hexagonal crystal lattice is defined by the following set of primitive vectors in Cartesian coordinates:

$$\mathbf{a}_1 = a\,(1,0,0)\,, \text{ and } \quad \mathbf{a}_2 = a\left(-\frac{1}{2}, \frac{\sqrt{3}}{2}, 0\right).$$

The lattice structure is therefore fully determined by the lattice parameter a. The value of the experimentally reported lattice parameter $a = 3.31 \pm 0.05$ Å [100] shows reasonable agreement with the theoretical one of 3.35 Å obtained at the Perdew-Burke-Ernzerhof [46] level without considering the zero-point motion [101].

The usual way of defining 2D structures in simulation softwares based on 3D periodic boundary conditions, as it is the case of Quantum Espresso, is to increase hugely the cell size in the direction perpendicular to the layer. In this way, the large vacuum gap between two adjacent layers effectively prevents any interlayer interaction. In case of our simulations in monolayer VSe_2, the distance between vanadium atoms of adjacent layers was set equal to 4 $c_{bulk} = 24.36$ Å, which is enough to avoid any interplay between adjacent layers. The atomic positions for the $1T$ polytype, as listed in Table 5.1, are still valid for the monolayer structure shown in Fig. 6.1. In this case the classical relaxation of atomic coordinates with the in-plane lattice parameter fixed at 3.35 Å yields a vertical distance of $d_{\text{V-Se\_vert}} \simeq 1.598$ Å from the vanadium plane to each covalently bonded selenium layer, which corresponds to a total thickness of a single VSe_2 layer of about $d_{layer} \simeq 3.196$ Å.

[1] The magnitude of the strain is defined as $\epsilon = \frac{a-a_0}{a_0} \times 100\%$, where $a_0 = 3.356$ Å is the lattice parameter theoretically obtained at the PBE level. The range of the applied strain covers values of $\epsilon \in [-4, 4]\%$, which in terms of lattice parameter means that $a \in [3.22, 3.49]$ Å [127].

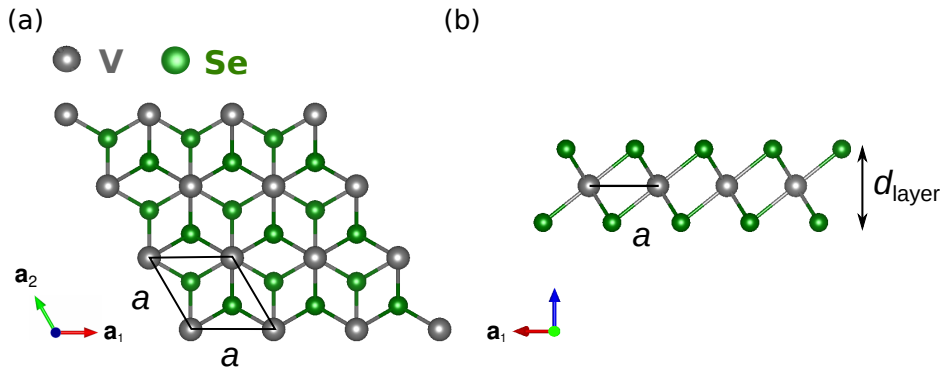

Figure 6.1: (a) Top and (b) side views of the crystal structure of monolayer 1 T-VSe_2. The unit cell is indicated with black lines, being a the lattice constant. Vanadium and selenium atoms are represented by grey and green spheres, respectively. In total there are 3 atoms per unit cell.

The 2D reciprocal lattice of the monolayer is determined by the following vectors:

$$\mathbf{b}_1 = \frac{2\pi}{a}\left(1, \frac{1}{\sqrt{3}}, 0\right), \text{ and } \quad \mathbf{b}_2 = \frac{2\pi}{a}\left(0, \frac{2}{\sqrt{3}}, 0\right),$$

which represent the in-plane projection of the 3D reciprocal lattice of the bulk. Figure 6.2 shows the first Brillouin zone that corresponds to the defined reciprocal lattice together with the high-symmetry points. Table 6.1 lists the reciprocal coordinates of the high-symmetry points that will be used in upcoming phonon dispersion analyses.

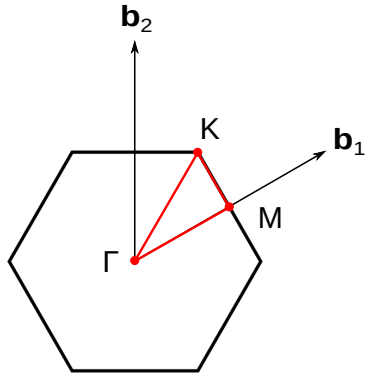

Figure 6.2: In-plane first Brillouin zone and the high-symmetry points of the space group $P\bar{3}m1$ (164).

High-symmetry point	Reciprocal Coordinates
Γ	$(0, 0, 0)$
M	$\left(\frac{1}{2}, 0, 0\right)$
K	$\left(\frac{1}{3}, \frac{1}{3}, 0\right)$

Table 6.1: In-plane high-symmetry points of space group $P\bar{3}m1$ (164) and their coordinates with respect to the reciprocal lattice vectors.

6.3 Computational details

6.3.1 Anharmonic lattice dynamics: The SSCHA method

The SSCHA theory was applied to the normal state phase of monolayer 1 T-VSe_2 for two lattice parameters that provide a good representation of the experimental range: $a_1 = 3.35$ Å and $a_2 = 3.30$ Å. The free energy minimization was performed by calculating forces on 4×4×1 supercells making use of DFT as implemented in Quantum Espresso package [61, 62]. These force calculations include vdW interactions through a non-local exchange-correlation functional [48]. We employed the same pseudopotentials as in the bulk analysis: an ultrasoft pseudopotential for vanadium, accounting for its $4s^2$ $3d^3$ valence electrons, and a norm-conserving pseudopotential for selenium, including its $4s^2$ $4p^4$ valence electrons. We used a plane-wave energy cutoff of 50 Ry for the wavefunctions and 550 Ry for the charge density. The Brillouin zone integrals were performed in a 4×4×1 **k**-point grid with a Methfessel-Paxton smearing [52] of 0.01 Ry. All the theoretical anharmonic phonon spectra were calculated in the static limit of the SSCHA theory, based on the free energy Hessian formalism. The difference between anharmonic and harmonic dynamical matrices was interpolated to a finer **q**-grid of size 8×8×1 in order to obtain other anharmonic phonon frequencies in more **q**-points (see Appendix A for more details).

6.3.2 Harmonic phonons and the electron-phonon interaction: DFPT calculations

Harmonic phonon frequencies and electron-phonon matrix elements of the normal state phase of monolayer 1 T-VSe_2 were calculated within density functional perturbation theory (DFPT) [115] as implemented in Quantum Espresso. DFPT calculations were performed for the same two lattice parameters, $a_1 = 3.35$ Å and $a_2 = 3.30$ Å , with the ions in the corresponding relaxed positions that keep the original symmetry of the structure. We used the same non-local van der Waals exchange-correlation functional, pseudopotentials and parameters described in the previous section, but with a 32×32×1 grid in the unit cell for the Brillouin zone integrals. Harmonic phonon calculations were carried out in a 8×8×1 **q**-point grid. The nesting function and the electron-phonon linewidth were calculated using a

48×48×1 **k**-point grid and a Gaussian broadening of 0.003 Ry for the Dirac deltas, which were enough to converge their values at the wavevectors associated with the CDW instabilities.

6.4 Characterization of the CDW transition

This section analyses theoretically the response of the lattice to the CDW formation by calculating the temperature dependence of the phonon spectrum of monolayer 1*T*-VSe2, the high-symmetry phase, for two lattice parameters that provide a good representation of the experimental range: $a_1 = 3.35$ Å and $a_2 = 3.30$ Å. However, the temperature-independent harmonic approximation is considered in first place to find unstable modes in the phonon spectrum that could indicate potential structural instabilities towards the formation of a low-symmetry phase. In the second part of this section, non-perturbative anharmonic phonon calculations are performed to accurately capture the temperature-dependent behaviour of the CDW driving phonon modes.

In both approaches the analysis about the stability of the different CDW orders is performed with a non-local van der Waals density exchange-correlation functional [48]. The previous chapter demonstrated that the inclusion of vdW interactions is vital to melt the CDW phase in the bulk form of this compound. In that case, Grimme's semiempirical approach provides the best match with experimental results because it effectively captures the weak vdW interactions between layers through its dispersion corrections. However, the semiempirical approach introduces some spurious intralayer interactions in the calculations, as it applies a similar correction for the vdW interactions between chalcogen atoms in adjacent layers and within the same one. That is, this practice oversimplifies the treatment of intralayer interactions by not accounting for the screening effects from the transition metal. This issue is particularly critical in single-layer cases, where Grimme's approach can lead to significant errors by introducing mostly unrealistic intralayer interactions. In such scenario, vdW interactions must be accounted for using the non-local method [126].

6.4.1 Harmonic phonon spectra

Harmonic dynamical matrices have been calculated within DFPT in a **q**-point grid of $8 \times 8 \times 1$ for two lattice parameters that reflect the experimental range: $a_1 = 3.35$ Å and $a_2 = 3.30$ Å. Fig. 6.3 shows the harmonic phonon curves obtained by the Fourier interpolation of the calculated dynamical matrices along a **q**-point path covering the high-symmetry points $\mathrm{K} - \Gamma - \mathrm{M} - \mathrm{K}$.

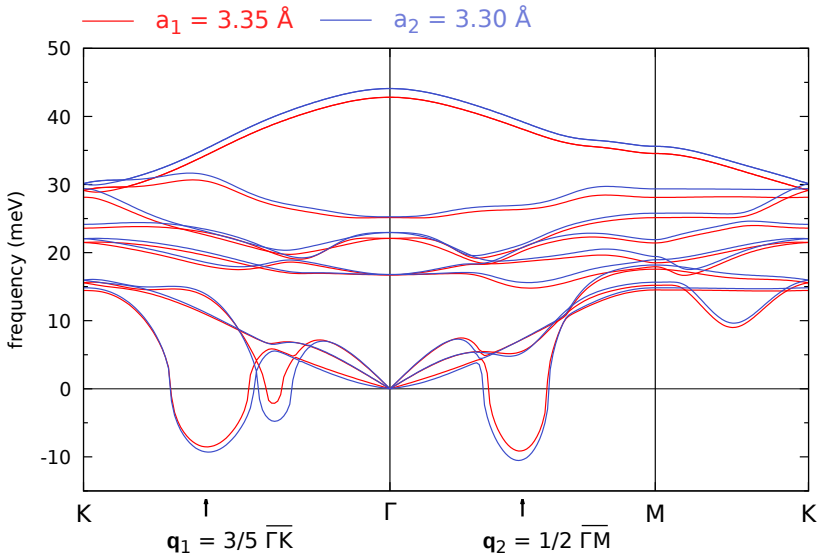

Figure 6.3: Harmonic phonon spectra along the $\mathrm{K}-\Gamma-\mathrm{M}-\mathrm{K}$ path for two lattice parameters that reflect the experimental range: $a_1 = 3.35$ Å (red lines) and $a_2 = 3.30$ Å (blue lines).

For both lattice parameters, harmonic phonon spectra show two principal instabilities at $\mathbf{q}_1 = 3/5\overline{\Gamma\mathrm{K}}$ and $\mathbf{q}_2 = 1/2\overline{\Gamma\mathrm{M}}$. The latter instability corresponds to the in-plane projection of the CDW wavevector $\mathbf{q}_{\mathrm{CDW}}$ in the bulk. The instability at $\mathbf{q}_1$ is associated with a $\sqrt{3} \times \sqrt{7}$ reconstruction, while the one at $\mathbf{q}_2$ leads to a 4×4 modulation, as shown in Fig. 6.4. An interesting aspect to highlight is that both softened phonon modes exhibit out-of-plane displacements of selenium atoms, as it was the case in the CDW transition in the bulk. This detail indicates that intralayer van der Waals interactions may also play a role in this transition, justifying the inclusion of vdW interactions in the calculations, though by no means as significant as their function in the bulk case. On the other hand, it is worth noting that phonon softening effects at $\mathbf{q}_1$ and $\mathbf{q}_2$ were already present in the harmonic phonon calculations for bulk 1T-VSe_2, as analysed in Section 5.5.1. However, in that case these effects were totally overshadowed by the principal instability.

In spite of providing the two intrinsic CDW orders, harmonic calculations do not suffice to predict neither which of these CDW orders prevails nor the associated transition temperature for each lattice parameter. In fact, a realistic change in the lattice parameter does not have a significant impact on the result at the harmonic level, as shown in Fig. 6.3. In the same way as in bulk $1T$-VSe_2, only non-perturbative anharmonic calculations can provide a reliable analysis of the dynamical stability of this compound.

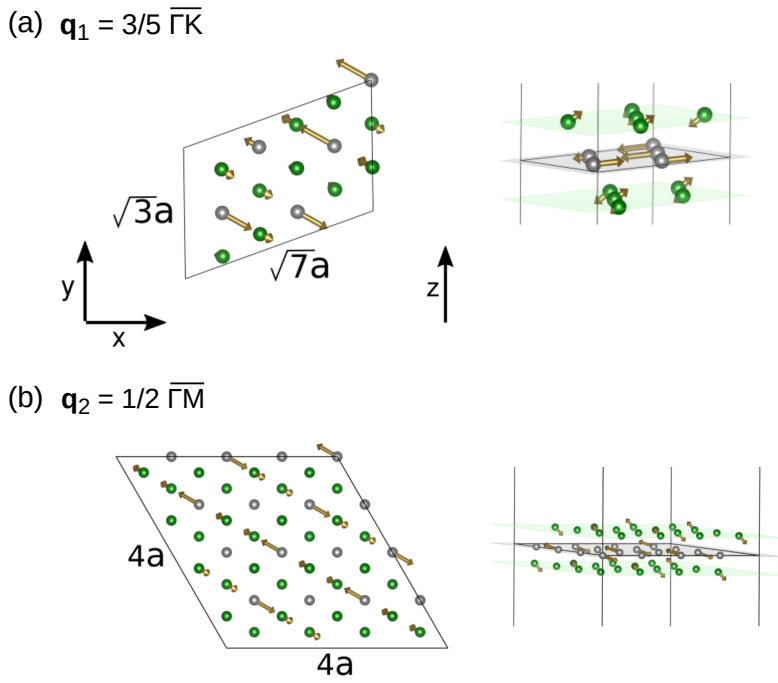

Figure 6.4: Intrinsic CDW orders with $\sqrt{3} \times \sqrt{7}$ and 4×4 modulations associated to the instabilities at $\mathbf{q}_1$ and $\mathbf{q}_2$, respectively. The displacement vectors associated to each CDW order are plotted as brown arrows. Planes perpendicular to the z-direction for V (Se) are plotted in gray (green) for a better characterization of the displacement vectors.

6.4.2 Anharmonic phonon spectra

In this section we present non-perturbative anharmonic phonon calculations in the high-symme-try phase of monolayer VSe_2, with the aim of capturing the temperature dependence of the CDW driving phonon modes. Figure 6.5 shows the temperature evolution of the anharmonic phonon spectra, obtained in the static limit of the SSCHA method, for the two lattice parameters $a_1 = 3.35$ Å (in red in the top panels of Fig. 6.5) and $a_2 = 3.30$ Å (in blue in the lower panels of Fig. 6.5). At high enough temperature, 250 K, the $1\,T$ phase is dynamically stable for both lattice parameters as shown in Figs. 6.5(a) and 6.5 (d). Therefore, anharmonicity melts the CDW phases in monolayer VSe_2, as it happens in the bulk form of this compound and other TMDs [76–78].

As the temperature decreases, the phonon modes associated with the CDW instabilities at $\mathbf{q}_1$ and $\mathbf{q}_2$ soften. In particular, for $a_1 = 3.35$ Å at 200 K (shown in Fig. 6.5(b)) we can observe that the mode at $q_1 = 3/5\overline{\Gamma K}$ becomes unstable, even if the one at $\mathbf{q}_2$ remains stable. This result indicates that for the bigger lattice

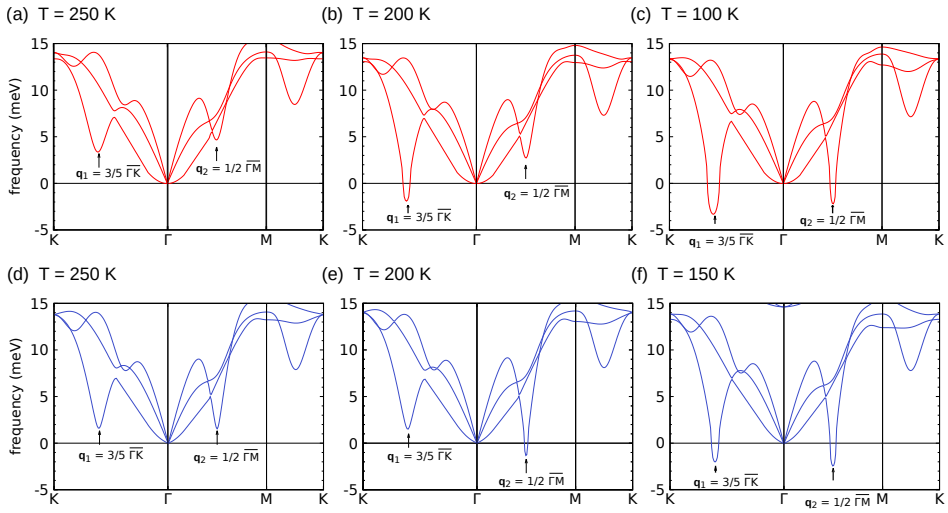

Figure 6.5: Anharmonic phonon spectra along the $K - \Gamma - M - K$ path for two different lattice parameters: $a_1 = 3.35$ Å (top panels with red lines) and $a_2 = 3.30$ Å (bottom panels with blue lines). Panels (a-c) correspond to temperatures of 250 K, 200 K, and 100 K, respectively, for a_1. Panels (d-f) display data for temperatures of 250 K, 200 K, and 150 K, respectively, for a_2.

parameter the $\sqrt{3} \times \sqrt{7}$ CDW order dominates. However, for $a_2 = 3.30$ Å at 200 K (illustrated in Fig. 6.5(e)), the phonon mode at $q_2 = 1/2\overline{\Gamma M}$ is the unstable one, while the phonon mode at $\mathbf{q}_1$ is stable this time. Therefore, for the smaller lattice parameter, the 4×4 CDW order is the dominant one. At low enough temperatures both $\mathbf{q}$-vectors show unstable modes, as depicted in Figs. 6.5(c) and 6.5(f). However, note that this situation is not indicating that at low temperatures both CDW orders coexist. Once one of the CDW orders gets stable when decreasing the temperature, the system collapses to it, and the analysis in terms of the anharmonic phonons of the high-symmetry phase is no longer useful to describe the evolution of each of the CDW phases at low temperatures. Nevertheless, the anharmonic phonons at low temperature shown in Figs. 6.5(c) and 6.5(f) confirm that both $\mathbf{q}_1$ and $\mathbf{q}_2$ are the intrinsic CDW orders of VSe_2 that can be accessed through a transition from the high-symmetry phase.

To further analyse the competition between the two CDW orders as a function of the lattice parameter, Fig. 6.6 shows the temperature-dependence of the frequency of the phonon mode that softens at $\mathbf{q}_1$ and $\mathbf{q}_2$. As shown in red in Fig. 6.6 (a), for the larger lattice parameter $a_1 = 3.35$ Å, the phonon frequency at $\mathbf{q}_1$ becomes negative (imaginary) at higher temperature than at $\mathbf{q}_2$ and hence the $\sqrt{3} \times \sqrt{7}$ CDW order is the dominant one. The opposite behaviour is observed for the small lattice parameter $a_2 = 3.30$ Å. As shown in blue in Fig. 6.6 (b), the

phonon frequency at $\mathbf{q}_2$ becomes negative at higher temperature that at $\mathbf{q}_1$, indicating that the 4×4 CDW order is dominant. From Fig. 6.6 we can obtain the transition temperature for each lattice parameter: for $a_1 = 3.35$ Å the $\sqrt{3} \times \sqrt{7}$ order emerges at $T_{CDW} = 217$ K, while for $a_2 = 3.30$ Å the 4×4 order arises at $T_{CDW} = 223$ K.

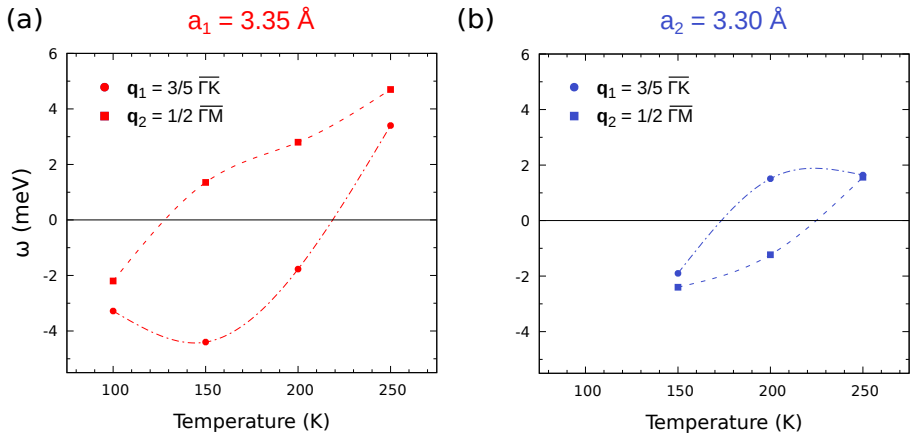

Figure 6.6: Temperature dependence of the theoretical anharmonic frequencies of the soft modes at $\mathbf{q}_1$ and $\mathbf{q}_2$ for (a) $a_1 = 3.35$ Å and (b) $a_2 = 3.30$ Å. Lines are guides to the eye.

The calculation of the anharmonic strain tensor through Eq. (3.43), which includes both the ionic zero-point motion and thermal fluctuations, yields an associated in-plane pressure of 0.7 GPa for the lattice parameter of $a_1 = 3.35$ Å and 1.3 GPa for $a_2 = 3.30$ Å. Given the lower in-plane pressure, these results point out that the natural CDW order in monolayer VSe_2 is $\sqrt{3} \times \sqrt{7}$ with a $T_{CDW} = 217$ K, which is in perfect agreement with the experiments on Refs. [101, 103]. Besides, the 4×4 order, which is the in-plane projection of the bulk $4 \times 4 \times 3$ CDW order, appears only under strain conditions. These results provide an explanation for the different CDW orders observed for small variations (∼1.5%) of the lattice parameter [100, 101]. Note that, eventually, other modulations could appear in monolayer VSe_2 as experimentally reported [102, 104, 105]. However, anharmonic calculations confirm that the $\sqrt{3} \times \sqrt{7}$ and 4×4 modulations are the intrinsic CDW orders in monolayer VSe_2, and point out that those different modulations are a consequence of the interplay between the highly dynamically-unstable high-symmetry phase and the particular substrate.

6.5 Origin of the CDWs

In the last chapter we established that in bulk $1\,T$-VSe_2 the electron-phonon interaction is the main driving force of the CDW transition. Yet, the three-dimensional critical wavevector $\mathbf{q}_{\mathrm{CDW}}$ connects many portions of the Fermi surface due to its warped dispersion in the k_z direction, but all in all the role of nesting in the CDW formation mainly serves to enhance the electron-phonon interaction. As the system shifts from bulk to monolayer, both Fermi surface nesting and electron-phonon interactions are expected to become more pronounced. In this part, we will examine the origin of the competing intrinsic CDW orders in monolayer VSe_2 by comparing these two scenarios for both lattice parameters.

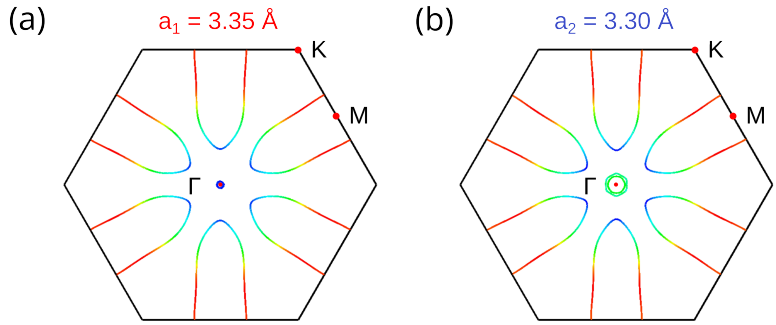

Figure 6.7: Fermi surface of the high-symmetry phase of monolayer VSe_2 for two different lattice parameters: $a_1 = 3.35$ Å (left panel) and $a_2 = 3.30$ Å (right panel). The colour scale indicates the relative Fermi velocity, ranging from blue (lower velocity) to red (higher velocity).

In order to do so, we perform a similar analysis to the one detailed in Section 5.7 for bulk $1\,T$-VSe_2, that is, we compute both the nesting function and the electron-phonon linewidth by means of DFPT. First, we present the calculated Fermi surfaces of the high-symmetry phase for both lattice parameters in Fig. 6.7. These Fermi surfaces exhibit ellipsoidal electron pockets centered at the M point that present parallel sections that should be prone to electronic instabilities, but in this case with no warping in the out-of-plane direction. However, in Figs. 6.8 (a-b) it can be seen that, for both lattice parameters, the nesting function does not show any strong peak at the CDW vectors despite the existence of small shoulders near $\mathbf{q}_1$ and $\mathbf{q}_2$. Therefore, the two critical wavevectors connect certain regions of the Fermi surface, but they are not particularly distinctive. This is in stark contrast with the clear peaks found in the nesting function for the corresponding critical wavevector in the bulk. In the bulk case, the three-dimensional CDW wavevector $\mathbf{q}_{\mathrm{CDW}}$ connects multiple sections of the warped Fermi surface. However, in the monolayer limit, the lack of k_z dispersion leads to a different scenario. The absence of a wavevector clearly nesting the Fermi surface suggests that the electron-phonon matrix elements play a crucial role inducing the phonon softening at both critical wavevectors.

In fact, Figs. 6.8 (c-d) show that the electron-phonon contribution to the linewidth of the soft phonon mode abruptly peaks at both $\mathbf{q}_1$ and $\mathbf{q}_2$ for both lattice parameters. Therefore, in all cases, the linewidth enhancement (as well as the phonon softening) comes from the mode and momentum dependence of the electron-phonon matrix elements. Therefore, the two intrinsic CDW orders developed by monolayer VSe_2 are exclusively driven by the electron-phonon coupling, in agreement with the theoretical predictions for 2D systems [16].

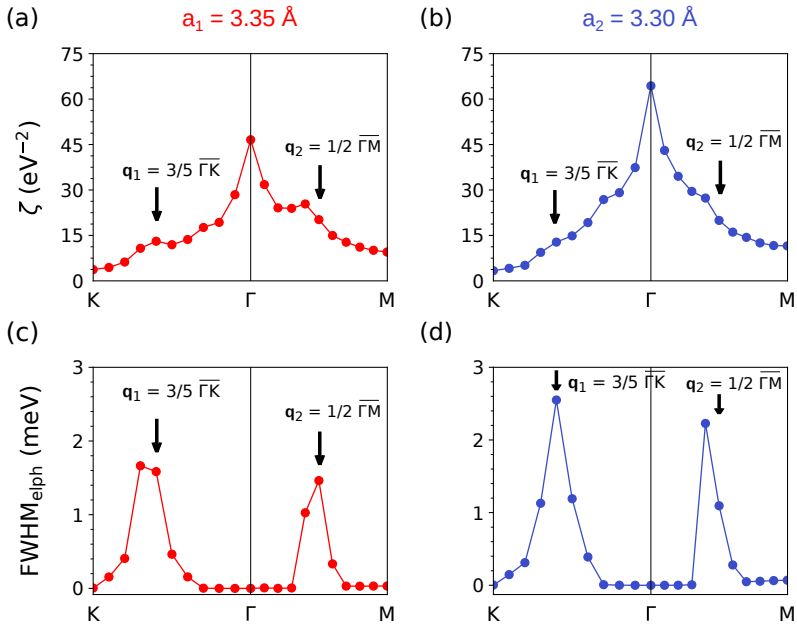

Figure 6.8: (a-b) Nesting function and (c-d) electron-phonon linewidth of the soft phonon mode along the $\mathrm{K}-\Gamma-\mathrm{M}$ path for two different lattice parameters: $a_1 = 3.35$ Å (left panels with red lines) and $a_2 = 3.30$ Å (right panels with blue lines).

6.6 Conclusions and outlook

In this chapter we have analysed theoretically the strain dependence of the CDW orders of monolayer 1T-VSe_2 with the aim of solving previous experimental contradictions. Our non-perturbative anharmonic phonon calculations reveal that monolayer VSe_2 develops two independent CDW orders that compete as a function of strain. Since variations of only 1.5% in the lattice parameter are enough to stabilize one order or the other, these results provide an explanation for the different modulations observed in experiments performed in different substrates [100–105].

In particular, our results show the natural CDW order in monolayer VSe_2 is $\sqrt{3} \times \sqrt{7}$, while the 4×4 order, which is the in-plane projection of the bulk $4 \times 4 \times 3$ CDW order, appears only under strain conditions. This behaviour contrasts with the usual behaviour reported in TMDs such as 2H-$NbSe_2$ [91] and 1T-$TiSe_2$ [78], where the monolayer CDW orders are the in-plane projection of the bulk one. The unexpected change of order when reducing dimensionality, together with the role played by vdW interactions in the bulk, remarks the importance of interlayer interactions in VSe_2. On the other side, the calculated CDW critical temperatures, as well as those reported in experiments, are enhanced in the monolayer with respect the one in the bulk. Since considering vdW interactions have turned out to be indispensable to melt the charge modulated phase in the bulk form of this compound, it seems logical that the absence of interlayer interactions leads to more robust CDW orders.

The intrinsic CDW orders reported for monoloyer VSe_2 are exclusively driven by the electron-phonon coupling, with no particular signatures of nesting at the CDW wavevectors. The lack of clear peaks in the nesting function contrasts with the ones found in the bulk. This absence of peaks is notable because both our theoretical calculations and ARPES experiments in monolayer 1T-VSe_2 report a similar Fermi surface to that of the bulk at the $k_z = 0$ plane [100, 101]. The Fermi surface of the high-symmetry phase exhibits then ellipsoidal electron pockets centered at the M point that present parallel sections that should be prone to electronic instabilities, but in this case with no warping in the out-of-plane direction. However, ARPES measurements find that both the critical wavevectors $\mathbf{q}_1$ [101] and $\mathbf{q}_2$ [100] satisfy the nesting condition, because the analysis is focused on one or the other depending on the reported order. Definitely, as our theoretical results show, there is nothing special about the critical wavevectors $\mathbf{q}_1$ and $\mathbf{q}_2$ in terms of Fermi surface nesting.

While our analysis based on the strain of the substate provides the theoretical support to understand the huge variability of CDW orders and transition temperatures reported by independent experiments in monolayer VSe_2, it does not account for other substrate-related effects. A clear example is the potential charge transfer between monolayer VSe_2 and the substrate, which has been shown to significantly impact CDW orders in other TMDs, such as 1T-$TiSe_2$ [78]. Analysing this aspect would require a detailed VSe_2-substrate sample study, which goes beyond the capabilities and scope of this work. However, this could be an interesting proposal for future research.

Part III

Mechanical properties of 2D systems

7

2D systems: Graphene

7.1 Introduction

For a long time, the possibility of having 2D crystalline order was considered unlikely. Nearly a century ago, Peierls [18] and Landau [19] argued that thermal fluctuations in 2D systems are so strong that they would destroy long-range order, preventing the atoms to maintain a periodic structure over long distances. Mermin formalized this argument with a rigorous mathematical proof [20], showing that for a 2D crystal with pairwise interactions the Fourier components of the one-particle density $\rho(\mathbf{r})$ must vanish for all non-zero reciprocal lattice vectors in the thermodynamic limit, thereby impeding true long-range order. The discovery of graphene in 2004 [17, 21, 22], a single layer of carbon atoms arranged in the honeycomb lattice shown in Fig. 7.1 (a), challenged these longstanding theoretical predictions. Still today the exact mechanism behind the stability of these materials is under strong debate.

The strong thermal fluctuations predicted for 2D systems are directly related to the quadratic dispersion of the out-of-plane acoustic (ZA) mode obtained within the harmonic approximation. In contrast, in-plane longitudinal (LA) and transverse (TA) acoustic modes exhibit a linear dispersion close to the zone centre, which is the typical behaviour of all acoustic modes in 3D crystals. The harmonic phonon dispersion of graphene, the prototypical 2D crystal, is shown in Fig. 7.2, where the different dispersions of the out-of-plane and in-plane acoustic modes in the long-wavelength limit are clearly visible. Indeed, such a low-energy quadratic dispersion leads the mean square out-of-plane displacement of the particles to diverge with the system size L, following the relation $\langle h^2 \rangle \sim L^2$.

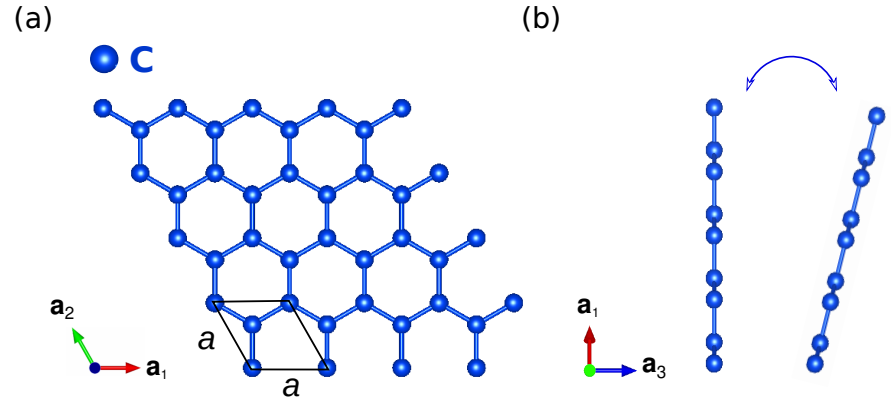

Figure 7.1: (a) Top view of the crystal structure of graphene. The unit cell is indicated with black lines, being a the lattice constant. Carbon atoms are represented by blue spheres, with each unit cell containing a total of two atoms. (b) Side view of graphene, highlighting the invariance of energies and atomic forces under any rotation of the whole system.

The anomalous dispersion expected for the ZA mode in the harmonic approximation is imposed by the combination of symmetry properties intrinsic to pure 2D systems. In first place, by the fact that the potential energy has to remain unchanged under a complete rotation of the system, as shown in Fig. 7.1 (b). This rotational invariance, together with the fact that the mirror symmetry in a strictly 2D system decouples in-plane and out-of-plane components of the second order force constants, makes the ZA mode acquire the mentioned quadratic dispersion close to zone center [26]. The explicit mathematical proof is included in Appendix B.

The theoretical debate on the stability of 2D crystalline systems resembles strongly the discussion regarding the stability of elastic membranes, which are low-dimensional flexible systems embedded in a space of higher dimension. Studies of 2D elastic membranes within a 3D space have shown that their flat phase tends to crumple due to strong thermal fluctuations [31, 34], similar to how such fluctuations can disrupt long-range positional order in 2D crystalline systems [20]. In the case of membranes, it has long been assumed that incorporating anharmonic interactions resolves this crumpling issue by introducing a linear term at small wavevectors in the out-of-plane vibrational frequency [31]. The reason is that the linearization of the ZA mode affects macroscopic properties of the material. In particular, it renormalizes its bending rigidity κ, which quantifies how much energy is required to bend the material to a unit curvature, and it is related to the dispersion relation of the ZA mode as:

$$\omega_{ZA}(q) = \sqrt{\frac{\kappa(q)}{\rho}} q^2, \tag{7.1}$$

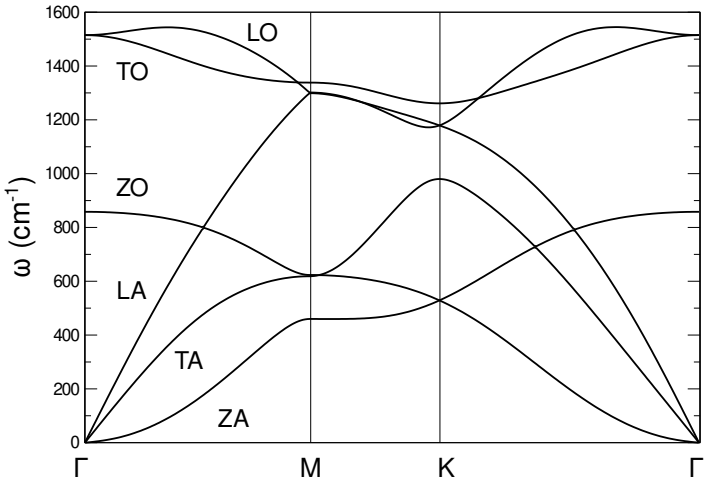

Figure 7.2: Harmonic phonon spectrum of graphene along high-symmetry directions of the Brillouin zone. The acoustic modes are illustrated, with the out-of-plane acoustic (ZA) mode showing a quadratic dispersion near the Γ point, while the transverse acoustic (TA) and longitudinal acoustic (LA) modes exhibit a linear dispersion. The optical modes, including the out-of-plane optical (ZO), transverse optical (TO), and longitudinal optical (LO) branches, are also indicated. Figure taken from Ref. [128].

where $\omega_{ZA}(q)$ is the frequency of the ZA mode, q is the wavevector, and ρ is the mass density of the membrane. As the ZA mode is linearized, the bending rigidity is renormalized from constant κ to a momentum-dependent effective bending rigidity $\kappa \sim q^{-\eta}$, where η is a positive exponent. Attempts to obtain the value of the exponent η by means of analytical calculations, including the Self-Consistent Screening Approximation (SCSA) [32] and renormalization group (NPRG) calculations [33], result in: $\eta \sim [0.80 - 0.85]$. In any case, a diverging bending rigidity in the long-wavelength limit yields the interpretation that the larger the membrane, the stiffer it becomes. The stiffening of the membrane partially suppresses the amplitude of its height-fluctuations, which is usually studied from the height correlation function in momentum space, $\langle |h(\mathbf{q})|^2 \rangle$. In particular, while in the classical harmonic approximation it scales as $\langle |h(\mathbf{q})|^2 \rangle \sim \omega_{ZA}(\mathbf{q})^{-2} \sim q^{-4}$, it is corrected to $q^{-4+\eta}$ when the ZA modes are linearized, which in real space translates to $\langle h^2 \rangle \sim L^{2-\eta}$ [31, 32, 34]. The quenching of height fluctuations is interpreted as the stabilization of a long-range orientational order, so that the flat phase for the membrane is stable, but not perfectly flat as it might exhibit significant height fluctuations.

The discovery of graphene provided a real-world context to these theoretical debates. In particular, the observation of ripples and fluctuations in suspended graphene [22] resembled strongly to the long-range orientational order predicted by anharmonic models of elastic membranes. At that point it became clear that graphene was the ideal playground to prove the old phenomenological theories of thermal fluctuations in elastic membranes [129]. The fact that classical Monte Carlo [24, 130] and molecular dynamics [131] simulations in graphene obtain similar values for the exponent η to the analytical calculations within the membrane model, strongly supports the idea that continuous models of polymerized membranes are suitable for describing the elastic properties of graphene [26]. In this sense, it is considered that the anharmonic coupling between in-plane and out-of-plane phonon modes renormalizes the dispersion of the ZA phonon modes also in graphene [23–30], providing it with a linear term at small momenta that cures the pathologies, as it happens in phenomenological models for membranes.

All of the above has established a standard theory on the stability of graphene, and in general of 2D materials, so far. Even tough, the experimental confirmation of these ideas is challenging due to both the difficulties in measuring the bending rigidity of graphene [35, 36] and the substrate effects on the dispersion of the ZA modes measured with helium diffraction [37–40]. At this point it has to be brought into focus that the out-of-plane displacements in real space predicted by the harmonic theory are of the order of the length of the graphene flake, with $\langle h^2 \rangle \sim L^2$. In contrast, the standard anharmonic treatment predicts that out-of-plane fluctuations scale as $\langle h^2 \rangle \sim L^{2-\eta}$, resulting in fluctuations that are much smaller than the sample size but potentially still larger than the interatomic distance. Given the significant height fluctuations predicted by both approaches, it is more sensible to tackle the problem of the mechanical stability in graphene through a non-perturbative inclusion of anharmonicity. As it has been demonstrated already in this manuscript, the SCHA method is an ideal way to carry out this task. Moreover, the quantum character of the method allows to consider ionic quantum fluctuations, otherwise neglected in classical approaches [24, 31–34, 129, 130]. In fact, a straightforward estimation of graphene's Debye temperature based on the harmonic dispersion yields $\mathrm{T}_D \sim 1000$ K, a higher value than room temperature, highlighting the importance of accounting for these quantum effects in the calculations [132].

This chapter is devoted to offer a new perspective to this longstanding puzzle by combining non-perturbative anharmonic effects with the intrinsic symmetries of strictly 2D systems, which are factors known to be relevant to this problem. Namely, physical phonons measured in experiments are related to peaks in the spectral function associated to the phonon Green's function including anharmonic effects. For low-energy modes such as the ZA mode in question, the static limit can be taken, such that their phonon peaks coincide with the eigenvalues of the free energy Hessian [41]. It is worth pointing out that physical phonons at the static limit coinciding with the eigenvalues of the free energy Hessian is not a particular result of the SCHA formalism; it is exact for any static theory, as proven

in Ref. [133]. Then, being both F and V thermodynamic quantities, they have to obey the same symmetry properties and in conclusion, the ZA mode should still be quadratic once anharmonic interactions are included, just as was the case in the harmonic approach. This result is compatible with a non diverging bending rigidity in the long-wavelength limit. These hypotheses were proven for graphene in Unai Aseginolaza's doctoral thesis by means of both atomistic simulations and the membrane model [128]. Since these statements are based on symmetry arguments, they can be generalized to any strictly 2D material, not only graphene.

This new perspective clearly contradicts the claims of the standard theory regarding the mechanical stability of graphene, which, as described, has been validated through various analytical and computational methods. Therefore, it is crucial to be as rigorous as possible when presenting such an innovative hypothesis. A critical limitation in the previous calculations presented in Ref. [128] is that some results do not reach the order of magnitude of wavevectors where the linearization in the ZA mode dispersion due to anharmonic effects should be observed. Specifically, for graphene at ambient temperatures, the anharmonic renormalization is expected to manifest at a wavevector magnitude on the order of $q \sim 0.01\text{Å}^{-1}$ [34]. Importantly, the work presented here reaches these small orders of magnitude, allowing us to explore anharmonic effects that were previously inaccessible. Moreover, this advancement allows us to perform meaningful comparisons with the literature data, highlighting in this way the contributions of our findings to the understanding of the mechanical stability of 2D materials.

This chapter begins with the presentation of the theoretical foundations of the membrane model and its implementation within the SCHA. The general expression for the equal time displacement-displacement correlation function is then derived using the SCHA formalism, with a focus on the height-height correlation function within the membrane model. Employing an interacting picture in this mathematical derivation enables a precise comparison with previously published results. Following this, we present results reinforcing the hypotheses concerning the quadratic out-of-plane mode dispersion and the non-diverging bending rigidity of graphene. Finally, the Fourier transform of the height-height correlation function is computed, allowing for a thorough comparison of our hypothesis with existing results in the literature.

7.2 The membrane model

The membrane model is widely used in the literature to describe crystals as elastic 2D continuum systems, overlooking in this way the microscopic atomic structure of the solid. Such a continuum approach is particularly well-suited for characterizing long-wavelength acoustic phonons, as these low-energy vibrational phenomena occur over length scales that are significantly larger than atomic distances.

Specifically, the model assumes an average flat configuration where the equilibrium positions are represented by the continuous vector $\mathbf{x} = (x_0,\ y_0,\ 0)$. Deviations from these equilibrium positions are captured by a continuous displacement field, which can be separated into in-plane displacements $\mathbf{u}(\mathbf{x}) = (u_x(\mathbf{x}),\ u_y(\mathbf{x})) \equiv \mathbf{u}$ and out-of-plane fluctuations $h(\mathbf{x}) \equiv h$.

Up to second-order on phonon fields, the most general rotationally invariant membrane potential that accounts for the coupling between in-plane and out-of-plane acoustic modes is given by [134]:

$$V = \frac{1}{2}\int_\Omega d^2x \left(\kappa(\nabla^2 h)^2 + C^{ijkl}u_{ij}u_{il}\right). \tag{7.2}$$

The sum over identical indexes $ijkl = x, y$ is implicit in the previous equation. Here, Ω is the area of the membrane in equilibrium, κ is the bending rigidity and h is the out-of-plane component of the displacement field. The first term in the potential describes then the bending energy, accounting for the energy penalty due to deviations from a flat configuration. The second term represents the stretching energy, which considers the energy cost associated with changes in the in-plane distances and bond angles between atoms. The elastic constants tensor C^{ijkl} is affected by the symmetry constraints of the underlying crystalline structure. In the case of an isotropic solid, it is determined by just 2 elastic constants, λ and μ, known as the Lamé coefficients: $C^{ijkl} = \lambda\delta^{ij}\delta^{kl} + \mu(\delta^{ik}\delta^{jl} + \delta^{il}\delta^{jk})$, where δ^{ij} is the Kronecker delta. On the other hand, the rotationally invariant strain tensor u_{ij} is defined using the in-plane displacement field u_i:

$$u_{ij} = \frac{1}{2}(\partial_i u_j + \partial_j u_i + \partial_i \boldsymbol{u}\cdot\partial_j \boldsymbol{u} + \partial_i h\partial_j h). \tag{7.3}$$

By inserting this strain tensor in Eq. (7.2), the potential can be rewritten as

$$\begin{aligned} V = \frac{1}{2}\int_\Omega d^2x[\kappa(\nabla^2 h)^2 &+ C^{ijkl}\partial_i u_j\partial_k u_l + C^{ijkl}\partial_i u_j\partial_k h\partial_l h + \\ &+ \frac{C^{ijkl}}{4}\partial_i h\partial_j h\partial_k h\partial_l h + \frac{C^{ijkl}}{2}\partial_i \boldsymbol{u}\cdot\partial_j \boldsymbol{u}\partial_k h\partial_l h + \\ &+ C^{ijkl}\partial_i u_j\partial_k \boldsymbol{u}\cdot\partial_l \boldsymbol{u} + \frac{C^{ijkl}}{4}\partial_i \boldsymbol{u}\cdot\partial_j \boldsymbol{u}\partial_k \boldsymbol{u}\cdot\partial_l \boldsymbol{u}]. \end{aligned} \tag{7.4}$$

In the harmonic approximation, by neglecting the high-order non-linear terms in the strain tensor in Eq. (7.3), the out-of-plane and in-plane modes are decoupled. Neglecting these anharmonic terms results in two in-plane acoustic phonons with linear dispersion relations: the longitudinal mode $\omega_{LA}(q) = \sqrt{(\lambda + 2\mu)/\rho}q$ and the transverse mode $\omega_{TA}(q) = \sqrt{\mu/\rho}q$, where ρ is the mass density of the membrane. On the contrary, the out-of-plane acoustic phonon mode displays a quadratic dispersion: $\omega_{ZA}(q) = \sqrt{\kappa/\rho}q^2$. In the case of graphene, fitting the parameters to the atomistic potential in Ref. [135] yields the values [128]: $\lambda = 4.3$ eVÅ^{-2}, $\mu = 9.3$ eVÅ^{-2}, $\kappa = 1.5$ eV and, $\rho/\hbar^2 = 1097$ eV^{-1}Å^{-4}.

At this point, it is important to emphasize that the hypotheses we aim to validate are restricted to membranes that exhibit rotational invariance. In this sense, it is crucial to note that a strained membrane loses its rotational symmetry due to the strain causing an uneven deformation. To ensure that the system remains strainless at each temperature, it is necessary to account for the relaxation of the lattice parameter a in the free energy minimization. The thermal expansion is included in this formalism by modifying the in-plane derivatives as $\partial_i u_j \to \partial_i u_j + \delta^{ij}\delta a$, with $\delta a = (a - a_0)/a_0$, and a_0 the lattice parameter that minimizes V.

By taking the Fourier transform of the potential and minimizing the SCHA free energy with respect to both the lattice constant and the auxiliary force constants, we derive the SCHA equations in the membrane model (we use $\hbar = k_B = 1$):

$$\begin{aligned}\frac{\partial \mathcal{F}(\mathcal{V})}{\partial \delta a} = 0 = 2\Omega\left(2\delta a + 3\delta a^2 + \delta a^3\right)(\lambda+\mu) \\ + \frac{1}{2}\sum_{\boldsymbol{q}} g[\omega^{(ZA)}_{SCHA}(\boldsymbol{q})]\left[2(1+\delta a)(\lambda+\mu)|\boldsymbol{q}|^2\right] \\ + \frac{1}{2}\sum_{\boldsymbol{q}} g[\omega^{(LA)}_{SCHA}(\boldsymbol{q})]\left[2(1+\delta a)(\lambda+2\mu)|\boldsymbol{q}|^2 + 2(1+\delta a)(\lambda+\mu)|\boldsymbol{q}|^2\right] \\ + \frac{1}{2}\sum_{\boldsymbol{q}} g[\omega^{(TA)}_{SCHA}(\boldsymbol{q})]\left[2(1+\delta a)\mu|\boldsymbol{q}|^2 + 2(1+\delta a)(\lambda+\mu)|\boldsymbol{q}|^2\right] \quad (7.5)\end{aligned}$$

$$\begin{aligned}\Phi^{(ZA)}_{SCHA}(\boldsymbol{q}) = \kappa|\boldsymbol{q}|^4 + 2(1+\delta a/2)\delta a(\lambda+\mu)|\boldsymbol{q}|^2 \\ + \frac{\lambda+2\mu}{2\Omega}\sum_{\boldsymbol{k}} g[\omega^{(ZA)}_{SCHA}(\boldsymbol{k})]\left[|\boldsymbol{q}|^2|\boldsymbol{k}|^2 + 2(\boldsymbol{q}\cdot\boldsymbol{k})^2\right] \\ + \frac{1}{2\Omega}\sum_{\boldsymbol{k}}\left\{g[\omega^{(LA)}_{SCHA}(\boldsymbol{k})] + g[\omega^{(TA)}_{SCHA}(\boldsymbol{k})]\right\}\left[\lambda|\boldsymbol{q}|^2|\boldsymbol{k}|^2 + 2\mu(\boldsymbol{q}\cdot\boldsymbol{k})^2\right] \quad (7.6)\end{aligned}$$

$$\begin{aligned}\Phi^{(LA)}_{SCHA}(\boldsymbol{q}) = &(\lambda+2\mu)|\boldsymbol{q}|^2 + 2(1+\delta a/2)\delta a(\lambda+2\mu)|\boldsymbol{q}|^2 \\ &+ 2(1+\delta a/2)\delta a(\lambda+\mu)|\boldsymbol{q}|^2 \\ &+ \frac{1}{2\Omega}\sum_{\boldsymbol{k}} g[\omega^{(ZA)}_{SCHA}(\boldsymbol{k})]\left[\lambda|\boldsymbol{q}|^2|\boldsymbol{k}|^2 + 2\mu(\boldsymbol{q}\cdot\boldsymbol{k})^2\right] \\ &+ \frac{1}{4\Omega}\sum_{\boldsymbol{k}}\Big\{ 4g[\omega^{(TA)}_{SCHA}(\boldsymbol{k})]\left[\lambda(\boldsymbol{q}\cdot\boldsymbol{k})^2 + \mu|\boldsymbol{q}|^2|\boldsymbol{k}|^2 + \mu(\boldsymbol{q}\cdot\boldsymbol{k})^2\right](\hat{\boldsymbol{q}_\perp}\cdot\hat{\boldsymbol{k}_\perp}) \\ &+ 2g[\omega^{(TA)}_{SCHA}(\boldsymbol{k})]\left[\lambda|\boldsymbol{q}|^2|\boldsymbol{k}|^2 + 2\mu(\boldsymbol{q}\cdot\boldsymbol{k})^2\right] \\ &+ 2g[\omega^{(LA)}_{SCHA}(\boldsymbol{k})]\left[\lambda|\boldsymbol{q}|^2|\boldsymbol{k}|^2 + 2\mu(\boldsymbol{q}\cdot\boldsymbol{k})^2\right] \\ &+ 4g[\omega^{(LA)}_{SCHA}(\boldsymbol{k})]\left[\lambda(\boldsymbol{q}\cdot\boldsymbol{k})^2 + \mu|\boldsymbol{q}|^2|\boldsymbol{k}|^2 + \mu(\boldsymbol{q}\cdot\boldsymbol{k})^2\right](\hat{\boldsymbol{q}}\cdot\hat{\boldsymbol{k}})\Big\} \end{aligned} \tag{7.7}$$

$$\begin{aligned}\Phi^{(TA)}_{SCHA}(\boldsymbol{q}) = &\mu|\boldsymbol{q}|^2 + 2(1+\delta a/2)\delta a\mu|\boldsymbol{q}|^2 \\ &+ 2(1+\delta a/2)\delta a(\lambda+\mu)|\boldsymbol{q}|^2 \\ &+ \frac{1}{2\Omega}\sum_{\boldsymbol{k}} g[\omega^{(ZA)}_{SCHA}(\boldsymbol{k})]\left[\lambda|\boldsymbol{q}|^2|\boldsymbol{k}|^2 + 2\mu(\boldsymbol{q}\cdot\boldsymbol{k})^2\right] \\ &+ \frac{1}{4\Omega}\sum_{\boldsymbol{k}}\Big\{ 4g[\omega^{(TA)}_{SCHA}(\boldsymbol{k})]\left[\lambda(\boldsymbol{q}\cdot\boldsymbol{k})^2 + \mu|\boldsymbol{q}|^2|\boldsymbol{k}|^2 + \mu(\boldsymbol{q}\cdot\boldsymbol{k})^2\right](\hat{\boldsymbol{q}_\perp}\cdot\hat{\boldsymbol{k}_\perp}) \\ &+ 4g[\omega^{(LA)}_{SCHA}(\boldsymbol{k})]\left[\lambda(\boldsymbol{q}\cdot\boldsymbol{k})^2 + \mu|\boldsymbol{q}|^2|\boldsymbol{k}|^2 + \mu(\boldsymbol{q}\cdot\boldsymbol{k})^2\right](\hat{\boldsymbol{q}_\perp}\cdot\hat{\boldsymbol{k}}) \\ &+ 2g[\omega^{(TA)}_{SCHA}(\boldsymbol{k})]\left[\lambda|\boldsymbol{q}|^2|\boldsymbol{k}|^2 + 2\mu(\boldsymbol{q}\cdot\boldsymbol{k})^2\right]\Big\} \end{aligned} \tag{7.8}$$

where $\Phi^{(\alpha)}_{SCHA}$ ($\alpha = ZA, LA, TA$) are the SCHA force constants, and $\omega^{\alpha}_{SCHA}(\boldsymbol{q}) = \sqrt{\frac{\Phi^{(\alpha)}_{SCHA}(\boldsymbol{q})}{\rho}}$ the corresponding SCHA auxiliary frequencies. The function $g(\omega)$, which was previously introduced in real space for periodic crystals in Eq. (3.30), now appears in its Fourier-transformed form for the membrane model. Indeed, it represents the Fourier transform of the displacement-displacement correlation function calculated using the SCHA density $\rho_{\mathcal{H}}$, and is given by $g(\omega_\alpha(\mathbf{q})) = \langle u_\alpha(\mathbf{q})u_\alpha(\mathbf{-q})\rangle_{\rho_{\mathcal{H}}} = \frac{1+2n_B(\omega_\alpha(\mathbf{q}))}{2\rho\omega_\alpha(\mathbf{q})}$, where ρ is the mass density of the membrane.

When solving this set of coupled equations, it has been taken into account that the assumed periodic boundary conditions make the reciprocal space discrete. In order to reach wavevectors an order of magnitude smaller than in the atomistic calculations in Ref. [128], we have worked with a squared membrane of size $L_x = L_y = \frac{2\pi}{0.01}$Å. On the other side, the implicit continuity of the membrane Hamiltonian makes Fourier transforms to be non-periodic. Then, as displacement fields $\mathbf{u}(\mathbf{x})$ and $\mathrm{h}(\mathbf{x})$ are smooth functions in real space, their discrete and non-

periodic Fourier transforms $\mathbf{u}(\mathbf{q})$ and $\mathrm{h}(\mathbf{q})$ (and related magnitudes) are expected to decay rapidly in reciprocal space. Therefore, we can converge our results with respect to a cut-off radius in momentum space, defining in this way a circular grid. The value of this cut-off radius is temperature dependent, because modes with greater wavevector values are thermally excited when increasing the temperature. We have found that with a value of $\mathrm{R}_{cut} = 0.8$ Å^{-1} convergence is achieved for temperatures close to 0 K. This radius encloses 20080 $\mathbf{q}$-points, which yields a total of $3\mathrm{n}_{\mathbf{q}}+1 = 60241$ coupled equations that we have solved by applying the Newton-Raphson method [136].

To deal with such a complex scenario efficiently, the code implementing the SCHA minimization for the membrane model has been substantially improved during this thesis. Key enhancements include the use of analytical derivatives instead of finite differences for computing the Jacobian matrix in the Newton-Raphson method, and the integration of the LAPACK package [137] to optimize matrix-vector operations. These changes successfully reduce the complexity of the algorithm, resulting in faster execution times and the ability to handle the required larger $\mathbf{q}$-point grids optimally.

Regarding the second derivative of the free energy, the exact correction to the SCHA auxiliary force constant matrix of the out-of-plane mode is given by:

$$\Phi^{(ZA)}_{corr}(\boldsymbol{q}) = \sum_{\gamma\delta\epsilon\zeta}\sum_{\boldsymbol{pk}} \overset{(3)}{\Phi}_{h\gamma\delta}(-\boldsymbol{q},\boldsymbol{p},\boldsymbol{q}-\boldsymbol{p})\times \\ \times [1 - \overset{(4)}{\Phi}_{\gamma\delta\epsilon\zeta}(-\boldsymbol{p},\boldsymbol{p}-\boldsymbol{q},\boldsymbol{k},\boldsymbol{q}-\boldsymbol{k})]^{-1}\overset{(3)}{\Phi}_{\epsilon\zeta h}(-\boldsymbol{k},\boldsymbol{k}-\boldsymbol{q},\boldsymbol{q}). \quad (7.9)$$

where the subindexes run on the normal coordinates $\alpha,\beta,\gamma,\delta,\epsilon,\zeta = h, u_{LA}, u_{TA}$ and the third and fourth-order SCHA force constant tensors are defined as:

$$\overset{(3)}{\Phi}_{\alpha\beta\gamma}(\boldsymbol{q},\boldsymbol{k},\boldsymbol{p}) = \left\langle \frac{\partial^3 V}{\partial\alpha(\boldsymbol{q})\partial\beta(\boldsymbol{k})\partial\gamma(\boldsymbol{p})} \right\rangle_{\rho_{\mathcal{H}}} \sqrt{G_{\beta\gamma}(\boldsymbol{k},\boldsymbol{p})}, \quad (7.10)$$

$$\overset{(4)}{\Phi}_{\alpha\beta\gamma\epsilon}(\boldsymbol{q},\boldsymbol{q}',\boldsymbol{k},\boldsymbol{k}') = \left\langle \frac{\partial^4 V}{\partial\alpha(\boldsymbol{q})\partial\beta(\boldsymbol{q}')\partial\gamma(\boldsymbol{k})\partial\epsilon(\boldsymbol{k}')} \right\rangle_{\rho_{\mathcal{H}}} \sqrt{G_{\alpha\beta}(\boldsymbol{q},\boldsymbol{k})G_{\gamma\epsilon}(\boldsymbol{q}',\boldsymbol{k}')}. \quad (7.11)$$

The matrix $G_{\alpha\beta}(\boldsymbol{q},\boldsymbol{k})$ is defined as:

$$G_{\alpha\beta}(\boldsymbol{q},\boldsymbol{k}) = \frac{F(0,\omega^{\alpha}_{SCHA}(\boldsymbol{q}),\omega^{\beta}_{SCHA}(\boldsymbol{k}))}{\omega^{\alpha}_{SCHA}(\boldsymbol{q})\omega^{\beta}_{SCHA}(\boldsymbol{k})}, \quad (7.12)$$

$F(0,\omega^{\alpha}_{SCHA}(\boldsymbol{q}),\omega^{\beta}_{SCHA}(\boldsymbol{k}))$ being the static limit of the function defined in Eq. (3.48).

The correction formula can be simplified by noting that the only terms in the potential that will contribute to the statistical average in the third-order SCHA

force constant tensor in Eq. (7.10) are those of the type $\int_\Omega d^2x C^{ijkl}\partial_i u_j \partial_k h \partial_l h$. Then, Eq. (7.9) can be rewritten as:

$$\Phi^{(ZA)}_{corr}(\boldsymbol{q}) = 4\sum_{\alpha\beta}\sum_{\boldsymbol{pk}} \overset{(3)}{\Phi}_{hh\alpha}(-\boldsymbol{q},\boldsymbol{p},\boldsymbol{q}-\boldsymbol{p})\times \\ \times [1 - \overset{(4)}{\Phi}_{h\alpha h\beta}(-\boldsymbol{p},\boldsymbol{p}-\boldsymbol{q},\boldsymbol{k},\boldsymbol{q}-\boldsymbol{k})]^{-1}\overset{(3)}{\Phi}_{h\beta h}(-\boldsymbol{k},\boldsymbol{k}-\boldsymbol{q},\boldsymbol{q}), \quad (7.13)$$

where now the subindexes only run over the in-plane normal coordinates: $\alpha,\beta = u_{LA}, u_{TA}$. The required statistical averages are given by:

$$\left\langle \frac{\partial^3 V}{\partial h(\boldsymbol{k}_1)\partial h(\boldsymbol{k}_2)\partial u_{LA}(\boldsymbol{k}_3)} \right\rangle_{\rho_{\mathcal{H}}} = \frac{1+\delta a}{\sqrt{\Omega}}\delta_{\boldsymbol{k}_1+\boldsymbol{k}_2+\boldsymbol{k}_3,0}\times \\ \times \left[\lambda|\boldsymbol{k}_3|\boldsymbol{k}_1\cdot\boldsymbol{k}_2 + 2\mu\frac{(\boldsymbol{k}_3\cdot\boldsymbol{k}_1)(\boldsymbol{k}_3\cdot\boldsymbol{k}_2)}{|\boldsymbol{k}_3|}\right], \quad (7.14)$$

$$\left\langle \frac{\partial^3 V}{\partial h(\boldsymbol{k}_1)\partial h(\boldsymbol{k}_2)\partial u_{TA}(\boldsymbol{k}_3)} \right\rangle_{\rho_{\mathcal{H}}} = \frac{\mu(1+\delta a)}{\sqrt{\Omega}}\delta_{\boldsymbol{k}_1+\boldsymbol{k}_2+\boldsymbol{k}_3,0}\times \\ \times \left[\frac{(\boldsymbol{k}_3\cdot\boldsymbol{k}_1)(\boldsymbol{k}_{3\perp}\cdot\boldsymbol{k}_2) + (\boldsymbol{k}_3\cdot\boldsymbol{k}_2)(\boldsymbol{k}_{3\perp}\cdot\boldsymbol{k}_1)}{|\boldsymbol{k}_3|}\right], \quad (7.15)$$

$$\left\langle \frac{\partial^4 V}{\partial h(\boldsymbol{k}_1)\partial h(\boldsymbol{k}_2)\partial u_{LA}(\boldsymbol{k}_3)\partial u_{LA}(\boldsymbol{k}_4)} \right\rangle_{\rho_{\mathcal{H}}} = \\ \frac{1}{\Omega}\delta_{\boldsymbol{k}_1+\boldsymbol{k}_2+\boldsymbol{k}_3+\boldsymbol{k}_4,0}\frac{\boldsymbol{k}_3\cdot\boldsymbol{k}_4}{|\boldsymbol{k}_3||\boldsymbol{k}_4|}[\lambda(\boldsymbol{k}_3\cdot\boldsymbol{k}_4)(\boldsymbol{k}_1\cdot\boldsymbol{k}_2)+ \\ + \mu(\boldsymbol{k}_3\cdot\boldsymbol{k}_1)(\boldsymbol{k}_4\cdot\boldsymbol{k}_2) + \mu(\boldsymbol{k}_3\cdot\boldsymbol{k}_2)(\boldsymbol{k}_4\cdot\boldsymbol{k}_1)], \quad (7.16)$$

$$\left\langle \frac{\partial^4 V}{\partial h(\boldsymbol{k}_1)\partial h(\boldsymbol{k}_2)\partial u_{TA}(\boldsymbol{k}_3)\partial u_{TA}(\boldsymbol{k}_4)} \right\rangle_{\rho_{\mathcal{H}}} = \\ \frac{1}{\Omega}\delta_{\boldsymbol{k}_1+\boldsymbol{k}_2+\boldsymbol{k}_3+\boldsymbol{k}_4,0}\frac{\boldsymbol{k}_{3\perp}\cdot\boldsymbol{k}_{4\perp}}{|\boldsymbol{k}_3||\boldsymbol{k}_4|}[\lambda(\boldsymbol{k}_3\cdot\boldsymbol{k}_4)(\boldsymbol{k}_1\cdot\boldsymbol{k}_2)+ \\ + \mu(\boldsymbol{k}_3\cdot\boldsymbol{k}_1)(\boldsymbol{k}_4\cdot\boldsymbol{k}_2) + \mu(\boldsymbol{k}_3\cdot\boldsymbol{k}_2)(\boldsymbol{k}_4\cdot\boldsymbol{k}_1)], \quad (7.17)$$

and

$$\left\langle \frac{\partial^4 V}{\partial h(\boldsymbol{k}_1)\partial h(\boldsymbol{k}_2)\partial u_{LA}(\boldsymbol{k}_3)\partial u_{TA}(\boldsymbol{k}_4)} \right\rangle_{\rho_{\mathcal{H}}} = \\ \frac{1}{\Omega}\delta_{\boldsymbol{k}_1+\boldsymbol{k}_2+\boldsymbol{k}_3+\boldsymbol{k}_4,0}\frac{\boldsymbol{k}_3\cdot\boldsymbol{k}_{4\perp}}{|\boldsymbol{k}_3||\boldsymbol{k}_4|}[\lambda(\boldsymbol{k}_3\cdot\boldsymbol{k}_4)(\boldsymbol{k}_1\cdot\boldsymbol{k}_2)+ \\ + \mu(\boldsymbol{k}_3\cdot\boldsymbol{k}_1)(\boldsymbol{k}_4\cdot\boldsymbol{k}_2) + \mu(\boldsymbol{k}_3\cdot\boldsymbol{k}_2)(\boldsymbol{k}_4\cdot\boldsymbol{k}_1)]. \quad (7.18)$$

The equations cannot be simplified further, but we have all the elements needed to calculate them numerically. We have checked numerically that the contribution of the fourth-order SCHA force constants tensor $\overset{(4)}{\mathbf{\Phi}}$ is practically negligible even at the smallest wavevectors, as shown in Fig. 7.3. The red crosses in the figure represent the first term of the Taylor expansion of the inverse matrix $[1 - \overset{(4)}{\mathbf{\Phi}}]^{-1} \approx 1 + \overset{(4)}{\mathbf{\Phi}}$ in Eq. (7.13), while blue dots correspond to the sum of these 2 terms. The results are identical for both cases across all wavevectors, which is consistent with the atomistic calculations of Refs. [128, 133].

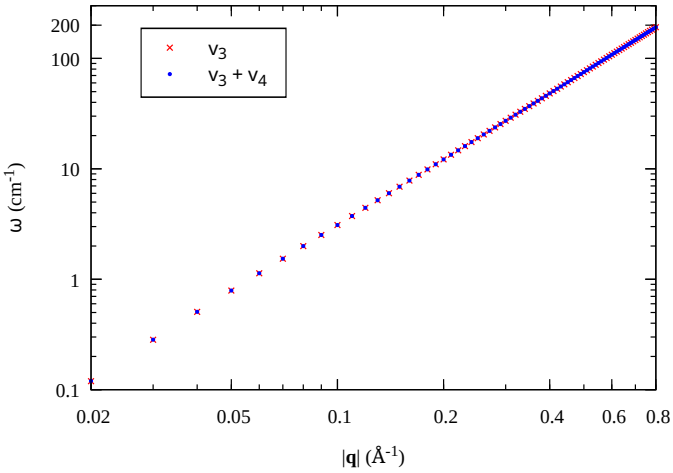

Figure 7.3: ZA physical phonons in the static approach within the membrane model at 12.5 K, neglecting and including $\overset{(4)}{\mathbf{\Phi}}$ in Eq. (7.13), and presented on a logarithmic scale.

7.2.1 The non-rotationally invariant membrane

Given that out-of-plane fluctuations are significantly larger than in-plane ones at the harmonic level, anharmonic terms involving out-of-plane displacement fields are expected to be dominant compared to those including only in-plane displacement fields. Consequently, most analytical works in the literature [23, 25, 27, 31–34, 130] neglect the $\partial_i \boldsymbol{u} \cdot \partial_j \boldsymbol{u}$ term in the strain tensor:

$$u_{ij} \approx \frac{1}{2}(\partial_i u_j + \partial_j u_i + \partial_i h \partial_j h). \tag{7.19}$$

This corresponds to neglecting the fourth-order terms containing in-plane displacement fields in the membrane potential:

$$V \approx \frac{1}{2}\int_\Omega d^2x[\kappa(\nabla^2 h)^2 + C^{ijkl}\partial_i u_j \partial_k u_l + C^{ijkl}\partial_i u_j \partial_k h \partial_l h + \frac{C^{ijkl}}{4}\partial_i h \partial_j h \partial_k h \partial_l h]. \tag{7.20}$$

In the SCHA framework, where averages are computed using a harmonic Gaussian distribution, the average of the odd terms is zero. Since fourth-order terms involving in-plane displacement fields are neglected at this level of approximation, the SCHA equations simplify significantly. In particular, the in-plane and out-of-plane components become decoupled. In-plane phonons are not renormalized and retain their harmonic values. The SCHA equations for out-of-plane phonons, including thermal expansion as previously described, are given by:

$$\delta a = -\frac{1}{4\Omega}\sum_{\boldsymbol{q}} |\boldsymbol{q}|^2 g[\omega^{(ZA)}_{SCHA}(\boldsymbol{q})], \tag{7.21}$$

$$\Phi^{(ZA)}_{SCHA}(\boldsymbol{q}) = \kappa|\boldsymbol{q}|^4 + 2\delta a(\lambda+\mu)|\boldsymbol{q}|^2 + \frac{\lambda+2\mu}{2\Omega}\sum_{\boldsymbol{k}} g[\omega^{(ZA)}_{SCHA}(\boldsymbol{k})][|\boldsymbol{q}|^2|\boldsymbol{k}|^2 + 2(\boldsymbol{q}\cdot\boldsymbol{k})^2]. \tag{7.22}$$

As a result, the number of coupled equations is reduced from the previous $3n_{\mathbf{q}}+1$ to $n_{\mathbf{q}}+1$, significantly simplifying the numerical implementation of the problem. Even more, this approach enables the analytical solution of the corresponding SCHA equations by inserting Eq. (7.21) in Eq. (7.22) and considering the infinite volume limit ($\Omega \to \infty$):

$$\Phi^{(ZA)}_{SCHA}(\boldsymbol{q}) = \kappa|\boldsymbol{q}|^4 + \gamma|\boldsymbol{q}|^2, \tag{7.23}$$

where γ is given by the solution of

$$\begin{aligned}\gamma &= \frac{\lambda+3\mu}{4\pi}\int_0^{\Lambda} dp p^3 g[\omega^{(ZA)}_{SCHA}(p)] \\ &= \gamma\frac{\lambda+3\mu}{16\pi\kappa\sqrt{\rho\kappa}}\int_0^{\Lambda\sqrt{\kappa/\gamma}} ds \frac{s^2 coth[\gamma s\sqrt{1+s^2}/(2T\sqrt{\rho\kappa})]}{\sqrt{1+s^2}}.\end{aligned} \tag{7.24}$$

Here, Λ is an ultraviolet cutoff used to avoid divergences. Eqs. (7.23) and (7.24) indicate that the dispersion of the SCHA auxiliary ZA modes is linear at long-wavelengths due to the presence of the coefficient γ: $\omega^{(ZA)}_{SCHA}(\boldsymbol{q}) \sim \sqrt{\frac{\gamma}{\rho}}|\boldsymbol{q}|$. When calculating the correction needed to obtain physical phonons in the static approach in Eq. (7.13) (with the fourth-order tensor being zero in this case), the result is

$$\Phi^{(ZA)}_{F}(\boldsymbol{q}) = \kappa|\boldsymbol{q}|^4 + (\gamma-\sigma)|\boldsymbol{q}|^2 + O(|\boldsymbol{q}|^4), \tag{7.25}$$

where at $T = 0$ K

$$\sigma = \frac{\rho\sqrt{\gamma}}{8\pi\kappa^{3/2}}\sum_{\alpha=LA,TA} v_\alpha f(\Lambda\sqrt{\kappa/\gamma}, v_\alpha\sqrt{\rho/\gamma}), \tag{7.26}$$

with

$$f(x,y) = \int_0^x ds \frac{s^2}{\sqrt{1+s^2}[\sqrt{1+s^2}+y]}. \tag{7.27}$$

Eq. (7.25) shows that the dispersion of the physical ZA phonon modes remains linear at long-wavelengths, due to the coefficient $\gamma - \sigma$ in this case. To compare the linear terms of the auxiliary and physical phonons, we estimate the ratio $\frac{\gamma-\sigma}{\gamma}$. Setting the ultraviolet cutoff to the Debye momentum, $\Lambda = \sqrt{\frac{8\pi}{3^{1/2}a_0^2}} = 1.55$ Å^{-1}, we find that $1-\sigma/\gamma = 20\%$. This means that the linear component of the physical frequencies is approximately 40% smaller than that of the SCHA auxiliary frequency. The presence of a non-zero linear term in the physical frequencies results from the fact that neglecting the fourth-order terms involving in-plane displacements breaks the rotational invariance of the potential, as proved in Appendix C.

7.3 The height-height correlation function

The ripples observed in graphene arise due to out-of-plane fluctuations of carbon atoms and they have a significant impact on its overall roughness and texture. The roughness of a crystalline membrane, and therefore its degree of corrugation, can be quantified by the height-height correlation function $h^2(\mathbf{r})$. This function measures how the height fluctuations of the membrane are correlated at a fixed in-plane distance $\mathbf{r}$ and it is defined as:

$$h^2(\mathbf{r}) = \frac{1}{\Omega}\int_\Omega d^2x\; h(\mathbf{x})h(\mathbf{x}+\mathbf{r}). \tag{7.28}$$

The height-height correlation function can be transformed into reciprocal space to obtain information about how the amplitude of the corrugations is distributed across different wavelengths. Inserting the Fourier transform of the height displacement field and applying the closure relation for periodic systems, one obtains:

$$h^2(\mathbf{r}) = \sum_{\mathbf{q}} h(\mathbf{q})h(\mathbf{-q})e^{-i\mathbf{q}\cdot\mathbf{r}} = \sum_{\mathbf{q}} |h(\mathbf{q})|^2 e^{-i\mathbf{q}\cdot\mathbf{r}} \tag{7.29}$$

The Fourier transform of the height-height correlation function, $|h(\mathbf{q})|^2$, represents the power spectrum of the height fluctuations, which shows how the amplitude of fluctuations varies with the wavevector. As the displacement field h($\mathbf{x}$) is a smooth function, its discrete and non-periodic Fourier transform h($\mathbf{q}$) and related magnitudes are expected to decay in reciprocal space. In particular, the smoother h($\mathbf{x}$) is, the faster h($\mathbf{q}$) decays. Therefore, for rougher surfaces, which are characterized by shorter wavelength ripples, the power spectrum $|h(\mathbf{q})|^2$ will have significant contributions at higher wavevector values.

In practice, the average of the Fourier transform of the height-height correlation function, $\langle|h(\mathbf{q})|^2\rangle$, serves as a measure to characterize the corrugation of membranes in most studies in the literature. This average can be obtained either by time averaging or ensemble averaging. Both approaches will yield equivalent results provided that the system is ergodic.

In the next section, we will derive the formula for the ensemble average of this correlation function within the SCHA formalism. We will begin by deriving the general expression for equal-time displacement-displacement correlation functions within the SCHA framework, using an interacting picture for the first time. Following this, we will specifically address the height-height correlation function within the membrane model.

7.3.1 The equal time height-height correlation function within SCHA

As a mean-field theory, SCHA has traditionally used a non-interacting picture for ensemble averages, relying on the harmonic density matrix derived from the mean-field solution of the SCHA free energy minimization [41]. However, in a similar way to the anharmonic renormalization of the frequencies, an interacting picture is necessary to go beyond mean-field and obtain correlation functions comparable to those in the literature. In this section we will obtain for the first time the general expression of the equal time displacement-displacement correlation function within the SCHA formalism using an interacting picture. Subsequently, we will focus specifically on the height-height correlation function in the framework of the membrane model.

Within an interacting picture, the ensemble average of any displacement-displacement correlation function is given by the following equal time Green function (we still use $\hbar = k_B = 1$):

$$\sqrt{M_a M_b}\langle u_a u_b\rangle = G^{ab}(\tau = \delta^+) = -T\sum_n G^{ab}(i\Omega_n), \tag{7.30}$$

where a and b represent both atom and Cartesian indices, M_a is the mass of the atom a and u_a the corresponding displacement component. $G^{ab}(i\Omega_n)$ is the SCHA Green function in the frequency domain for the variable $\sqrt{M_a}(R^a - \mathcal{R}^a_{eq})$, as defined in Eq. (3.55). Here, $\Omega_n = 2\pi T n$ represents the bosonic Matsubara frequencies and $\mathcal{R}^a_{eq}$ are the centroid positions that minimize the SCHA free energy.

The summation in Equation (7.30) is performed by expressing the Green's function in its Lehmann representation and then applying standard techniques for Matsubara frequency summations [138], resulting in:

$$\sqrt{M_a M_b}\langle u_a u_b\rangle = -T\sum_n G^{ab}(i\Omega_n) = \int_{-\infty}^{\infty}\frac{d\omega}{2\pi}\,\sigma^{ab}(\omega)n_B(\omega), \tag{7.31}$$

being $n_B(\omega)$ the Bose-Einstein distribution function and $\sigma^{ab}(\omega)$ the spectral function of the interacting Green function, defined in this case as:

$$\sigma^{ab}(\omega) = -2\mathrm{Im}\,[G^{ab}(\omega + i\delta^+)]. \tag{7.32}$$

In order to avoid divergences in the integral, the sum is redefined as:

$$\sqrt{M_a M_b}\langle u_a u_b\rangle = -TG^{ab}(0) + \int_{-\infty}^{\infty} \frac{d\omega}{2\pi}\, \sigma^{ab}(\omega) \left[n_B(\omega) - \frac{T}{\omega}\right]. \tag{7.33}$$

Regarding the first term in the sum, according to Eq. (3.58), the static limit of the Green function corresponds to the inverse of the free energy dynamical matrix:

$$G^{ab}(i\Omega_n = 0) = -[\mathrm{D}^{(\mathrm{F})}]^{-1}_{ab} = \sum_{\mu} \epsilon^a_\mu \epsilon^b_\mu \left(-\frac{1}{\Omega^2_\mu}\right), \tag{7.34}$$

where Ω_μ are the phonon frequencies and ϵ^a_μ the polarization vectors obtained by diagonalizing the free energy Hessian.

Retaining only the first term of the dynamical SCHA self energy $\mathbf{\Pi}(i\Omega_n)$ and neglecting the mode-mixing, the spectral function $\sigma^{ab}(\omega)$ resembles a superposition of Lorentzians, but with frequency dependent shifts and widths. When the quasiparticle picture is valid after the inclusion of anharmonicity, the spectral function can actually be expressed as a superposition of Lorentzians:

$$\sigma^{ab}(\omega) = \sum_{\mu} \epsilon^a_\mu \epsilon^b_\mu \left(\frac{1}{\omega}\left[\frac{\Gamma_\mu}{(\omega - \Theta_\mu)^2 + (\Gamma_\mu)^2} + \frac{\Gamma_\mu}{(\omega + \Theta_\mu)^2 + (\Gamma_\mu)^2}\right]\right), \tag{7.35}$$

where Θ_μ is the frequency of the SCHA quasiparticle in the Lorentzian approximation, and Γ_μ represents the half-width at half maximum (HWHM) of the anharmonic linewidth.

Inserting Eqs. (7.34) and (7.35) in Eq. (7.33) we get:

$$\sqrt{M_a M_b}\langle u_a u_b\rangle = \sum_{\mu} \epsilon^a_\mu \epsilon^b_\mu \left(\frac{T}{\Omega^2_\mu} + \int_{-\infty}^{\infty} \frac{d\omega}{2\pi} \left(\frac{1}{\omega}\left[\frac{\Gamma_\mu}{(\omega - \Theta_\mu)^2 + (\Gamma_\mu)^2} + \right.\right.\right.$$
$$\left.\left.\left. + \frac{\Gamma_\mu}{(\omega + \Theta_\mu)^2 + (\Gamma_\mu)^2}\right]\right) \left[n_B(\omega) - \frac{T}{\omega}\right]\right). \tag{7.36}$$

This integral can be simplified when the phonon-phonon linewidth tends to zero. For those cases, the Lorentzian representation of the Dirac delta function can be used:

$$\delta(x) = \frac{1}{\pi} \lim_{\epsilon \to \delta^+} \frac{\epsilon}{x^2 + \epsilon^2}. \tag{7.37}$$

Then,

$$\sqrt{M_a M_b}\langle u_a u_b\rangle = \sum_{\mu} \epsilon^a_\mu \epsilon^b_\mu \left(\frac{T}{\Omega^2_\mu} + \frac{1}{2}\int_{-\infty}^{\infty} d\omega \times \right.$$
$$\left. \times \left(\frac{1}{\omega}\left[\delta(\omega - \Theta_\mu) + \delta(\omega + \Theta_\mu)\right]\right) \left[n_B(\omega) - \frac{T}{\omega}\right]\right). \tag{7.38}$$

And

$$\langle u_a u_b \rangle = \frac{1}{\sqrt{M_a M_b}} \sum_\mu \epsilon_\mu^a \epsilon_\mu^b \left(\frac{T}{\Omega_\mu^2} + \frac{-n_B(-\Theta_\mu) + n_B(\Theta_\mu)}{2\Theta_\mu} - \frac{T}{\Theta_\mu^2} \right). \tag{7.39}$$

Finally, when the static phonons coming from the free energy Hessian and the ones extracted from the Lorentzian shaped spectral function are nearly identical ($\Omega_\mu^2 \approx \Theta_\mu^2$), we recover the formula of the non-interacting case but evaluated with the physical phonons in the static approach:

$$\begin{aligned} \langle u_a u_b \rangle &= \frac{1}{\sqrt{M_a M_b}} \sum_\mu \epsilon_\mu^a \epsilon_\mu^b \left[\frac{(n_B[\Omega_\mu] - n_B[-\Omega_\mu])}{2\Omega_\mu} \right] \\ &= \frac{1}{\sqrt{M_a M_b}} \sum_\mu \epsilon_\mu^a \epsilon_\mu^b \left[\frac{(1 + 2n_B[\Omega_\mu])}{2\Omega_\mu} \right]. \end{aligned} \tag{7.40}$$

In the continuous case of the membrane model, the displacement-displacement correlation function is:

$$\langle u_a(\mathbf{x}) u_b(\mathbf{x}') \rangle = \frac{1}{\rho} \sum_\mu \epsilon_\mu^a(\mathbf{x}) \epsilon_\mu^b(\mathbf{x}') \left[\frac{(1 + 2n_B[\Omega_\mu])}{2\Omega_\mu} \right], \tag{7.41}$$

where a and b are just the Cartesian indexes and $\mu = ZA, LA, TA$ in this case. Essentially, discrete magnitudes are now continuous, while the individual atomic masses M_a and M_b are replaced by the mass density of the membrane ρ. The corresponding Fourier transform is given by

$$\langle u_a(\mathbf{q}) u_b(\mathbf{-q}) \rangle = \sum_\mu \epsilon_\mu^a(\mathbf{q}) \epsilon_\mu^b(-\mathbf{q}) \left[\frac{(1 + 2n_B[\Omega_\mu(\mathbf{q})])}{2\rho\Omega_\mu(\mathbf{q})} \right]. \tag{7.42}$$

We are particularly interested in the Fourier transform of the out-of-plane correlation function. As in the membrane model ZA is the only mode with an out-of-plane component, we finally obtain:

$$\langle |h(\mathbf{q})|^2 \rangle = \frac{(1 + 2n_B[\Omega_{ZA}(\mathbf{q})])}{2\rho\Omega_{ZA}(\mathbf{q})}, \tag{7.43}$$

which is the formula that will be implemented to obtain the Fourier transform of the height-height correlation function.

Nearly all the approximations taken in this mathematical derivation were proved for the ZA mode of graphene in the atomistic calculations in Refs. [128, 133]. In summary, dynamic effects have no impact on frequencies as low as those of the quadratic mode. Therefore, the frequencies obtained from the dynamical spectral function are the same as those in the static limit, that is, by diagonalizing the free energy Hessian, as shown for different temperatures in Fig. 7.4 (a-b). The only task left was showing that anharmonicity does not remove the quasiparticle picture of ZA modes, which is indeed the case, as depicted in Fig. 7.4 (c).

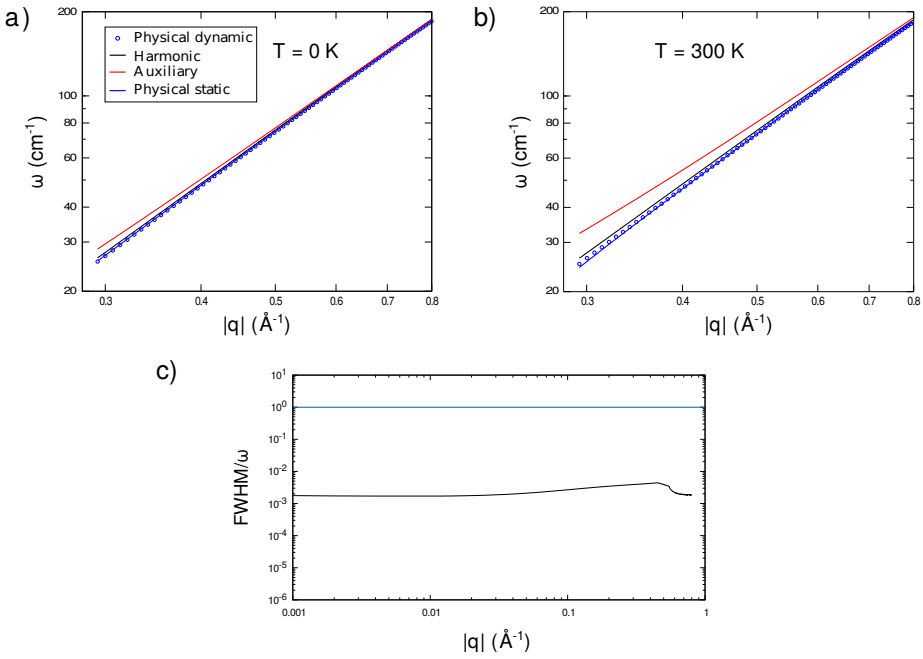

Figure 7.4: Harmonic, and SCHA auxiliary and physical phonons (static and dynamic) calculated at 0 K (a) and 300 K (b) with the atomistic potential for the ZA mode. These calculations showing the negligible dynamic effects in the ZA mode frequencies are taken from Refs. [128, 133]. (c) Linewidth (full width at half maximum) of the ZA phonon mode divided by its frequency at 300 K calculated within the membrane model. The ratio never exceeds 1 (marked by the horizontal blue line), indicating that anharmonicity does not remove the quasiparticle picture for this mode.

7.4 Results

All the results presented in this chapter were obtained using the membrane potential described earlier. In first place, we examine the validity of the membrane model in accounting for the negative thermal expansion observed in graphene. This paves the way for a deep analysis of the dispersion of the ZA mode in the long-wavelength limit and its implications on the bending rigidity of graphene. By doing so, we aim to confirm and solidify the conclusions drawn in previous studies [128]. The performed code refinement allows to reach wavevector values an order of magnitude smaller than those in earlier calculations, enabling the observation of relevant physical phenomena such as the potential anharmonic linearization of the ZA phonon modes predicted by other works. In the second part, we focus on the nature of the ripples by analysing the scaling of the equal time out-of-plane correlation function, a well-explored quantity in the literature. Throughout the chapter, the results for the rotationally invariant membrane are compared with those for the non-invariant counterpart, as the latter is a commonly used approximation in

most analytical studies in the literature. In this way, we perform a comprehensive comparison between our results and those in the existing literature, explaining how our novel hypothesis fits within the established knowledge.

7.4.1 Thermal expansion in graphene

Solving numerically the coupled set of SCHA equations (7.5)–(7.8) reveals that the membrane model accurately captures phenomena such as the negative thermal expansion of graphene, as shown by the black connected dots in Fig. 7.5. This behaviour originates from the low-energy dispersion of the out-of-plane bending modes, which generate an effective contraction of the material's area. The contribution of the in-plane acoustic modes to the obtained thermal expansion is minimal due to their low thermal occupation at the temperatures considered in this study, particularly in view of the much higher thermal population of the out-of-plane modes.

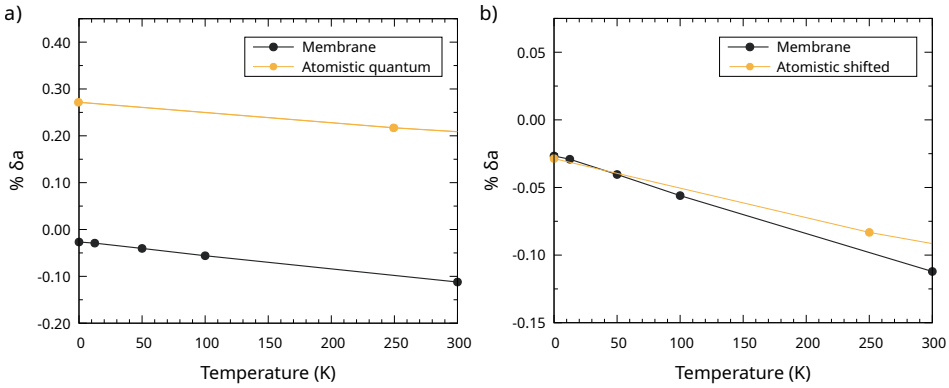

Figure 7.5: Graphene's negative thermal expansion. (a) Percentage of the relative change in the lattice parameter, δa, as a function of temperature in the membrane model (black connected dots), compared to the quantum atomistic calculations of Refs. [128, 133] (orange connected dots). (b) The same data, but with a constant shift applied to the quantum atomistic calculations, neglecting the effect of the zero-point motion of the optical modes.

The atomistic quantum calculations in Refs. [128, 133] have been included with orange connected dots in Fig. 7.5 to evaluate the validity of the thermal expansion results predicted by the membrane model. In Fig. 7.5 (a), the atomistic calculations show a consistent shift from the membrane model results at each temperature, attributed to the zero-point energy of the optical modes, which the membrane model does not account for. In panel (b) the effect of the zero-point motion of the optical modes is virtually neglected by applying a constant shift to the quantum atomistic calculations. The close alignment of both results suggests that the membrane model effectively captures the impact of the acoustic modes on the thermal expansion.

Definitely, while the membrane model successfully addresses the competition among various acoustic modes, it fails to consider the contributions of optical modes at both low and high temperatures. In fact, at higher temperatures than those considered, the thermal occupation of the optical modes drives a transition towards positive thermal expansion [139]. This observation underscores the need for a more comprehensive model to fully capture graphene's complex thermal response, particularly at elevated temperatures.

7.4.2 The dispersion of the ZA mode and the bending rigidity

Aiming at identifying quadratic dispersions, Fig. 7.6 presents the frequency of the ZA mode over the squared momentum at two temperatures: 0 K and 300 K. In particular, we compare the constant ratio obtained with the quadratic harmonic phonon dispersion with the one obtained with the SCHA auxiliary dynamical matrix based on Eq. (7.6) (light blue dots) and the static physical phonons coming from the free energy Hessian (green dots). Due to the low frequencies of the ZA modes, taking this static limit for the physical phonons is perfectly valid, as demonstrated in the atomistic calculations of Fig. 7.4 (a-b). Then, while the ratio calculated with the auxiliary phonons represents the mean-field approximation, the truly renormalized anharmonic phonons, which are the only ones with physical significance, are those derived from the free energy Hessian.

The results obtained for the rotationally invariant membrane are displayed with filled dots in both panels. The ratio calculated with ZA phonons obtained from the auxiliary SCHA force constants, plotted with light blue filled dots, diverges in the long-wavelength limit as a consequence of the linearization of the ZA phonons at small momenta. In contrast, the ratio calculated with the physical ZA phonons derived from the free energy Hessian, shown with green filled dots, remains independent of the wavevector. This indicates that, indeed, the ZA anharmonic phonons exhibit a quadratic dispersion in the long-wavelength limit in an unstrained membrane once high-order interactions are considered, as expected by symmetry. In fact, the ratio gets practically on top of the harmonic values even at the smallest wavevectors at any temperature. Therefore, the bending rigidity, which is proportional to this ratio, is barely affected by anharmonic interactions, in contradiction to the broadly assumed result that it diverges at small momentum in membranes due to thermal fluctuations [31]. In particular, the bending rigidity that we obtain is around the harmonic value of 1.5 eV, in good agreement with the experiments by Al Taleb et al. [38] and Tømterud et al. [40].

Empty symbols in Fig. 7.6 show the results obtained by breaking rotational invariance of the membrane model through different mechanisms. In particular, empty dots in Fig. 7.6 (a) show the result obtained when neglecting the high-order $\partial_i \boldsymbol{u} \cdot \partial_j \boldsymbol{u}$ term in the membrane potential of Eq. (7.4). In this case the bending rigidity shows a divergent tendency in the long-wavelength limit due to

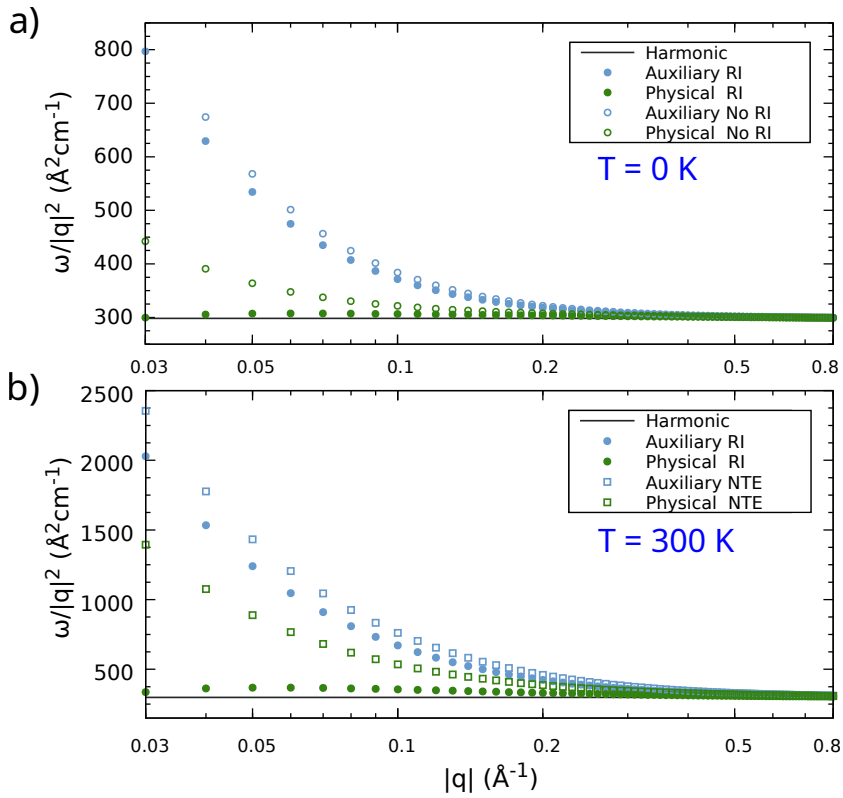

Figure 7.6: (a) Frequency of the ZA mode divided by the squared momentum, calculated within the harmonic approximation and within the SCHA auxiliary and physical cases at 0 K in the membrane model. We name rotationally invariant (RI) the results considering the full potential in Eq. (7.4). We name no rotationally invariant (No RI) the results neglecting the $\partial_i \boldsymbol{u} \cdot \partial_j \boldsymbol{u}$ term in Eq. (7.3). (b) Same results at 300 K with the full membrane potential in the rotationally invariant case. The results without considering thermal expansion (NTE) are also shown.

the linearization of the ZA dispersion predicted in our analytical calculation in Eq. (7.25). The departure from the results obtained in the rotationally invariant model highlights the importance of including these high-order terms in the potential to accurately estimate the mechanical properties of membranes, even though they tend to be neglected in the literature [23, 25, 27, 31–34, 130]. On the other side, a similar effect occurs in the anharmonic calculation when the lattice parameter is not relaxed to the minimum of the free energy, as shown with empty squares in Fig. 7.6 (b). In this case the bending rigidity also diverges in the long-wavelength limit due to the ZA mode linearization caused by the strain, although the exponent is different. Definitely, a strained membrane is no longer rotationally invariant, which emphasizes that properly accounting for thermal expansion is essential to recover the quadratic dispersion of the flexural modes.

In conclusion, our results upturn the conventional wisdom of 2D membranes [23, 25, 27, 31–34, 130]: interactions do not linearize the dispersion of the ZA mode and the bending rigidity does not diverge at small momentum. The main reason behind the observation of these phenomena in previous analytical works is that the $\partial_i \boldsymbol{u} \cdot \partial_j \boldsymbol{u}$ term in the strain tensor, which guarantees the rotational invariance of the potential (see Appendix C), is neglected. This omission unavoidably lowers the power of the ZA phonon frequency to $\sim q^d$, as shown in Fig. 7.6 (a). In particular, in the range of wave numbers studied, we obtain that $d \sim 1.6$, even if in the ultimate $q \to 0$ limit we expect a linear dispersion from our quantum calculation in Eq. (7.25), as suggested also in Ref. [27].

7.4.3 The height-height correlation function

In practice, the anharmonic stiffening of the membrane is usually studied from the height-height correlation function in momentum space, $\langle |h(\mathbf{q})|^2 \rangle$, both in analytical calculations and numerical simulations. While in the harmonic approximation it scales as $\langle |h(\mathbf{q})|^2 \rangle \sim q^{-4}$, the amplitude of the height-fluctuations is partially suppressed to $q^{-4+\eta}$ when the ZA modes are linearized. Different analytical calculations [23, 25, 27, 31–34, 130] yield consistent values of $\eta \sim 0.80 - 0.85$. Our hypothesis suggests that the amplitude of height fluctuations, or ripples, in the long-wavelength limit would reflect the lack of rotational symmetry in these calculations. However, classical Monte Carlo [24, 130] and molecular dynamics [131] simulations of graphene, which inherently respect the rotational invariance, obtain similar values for the exponent η. In this section we compute the Fourier transform of the height-height correlation function, allowing for a thorough comparison of our hypothesis with existing results in the literature.

As explained in Section 7.3.1, the ensemble average of the out-of-plane displacement correlation function $\langle |h(\mathbf{q})|^2 \rangle$ in our membrane model can be computed within the SCHA, which in the static limit results in the simplified expression given by Eq. (7.43). In this equation, $n_B(\omega)$ is the bosonic occupation factor and $\Omega_{ZA}(\mathbf{q})$ the interacting physical flexural phonon frequency coming from the free energy Hessian. The presence of the bosonic occupation completely determines the dependence on $\mathbf{q}$ of the correlation function. Specifically, in the classical limit, when temperature is larger than the frequency of the ZA mode, the correlation function scales as $\langle |h(\mathbf{q})|^2 \rangle \sim \Omega_{ZA}(\mathbf{q})^{-2}$. On the contrary, in the quantum limit, when the ZA mode is not thermally occupied but exhibits zero-point motion, it scales as $\langle |h(\mathbf{q})|^2 \rangle \sim \Omega_{ZA}(\mathbf{q})^{-1}$. Therefore, this crossover occurs at different wave numbers depending on the temperature, basically when the energy of the ZA phonon mode is of the order of the thermal energy: $\hbar \Omega_{ZA}(\mathbf{q}) \sim k_B T$.

In Fig. 7.7 we show the Fourier transform of the height-height correlation function at 12.5 K, evaluating Eq. (7.43) with frequencies at different levels of approximation. As predicted, there is a clear crossover between the regimes in which thermal (orange shaded) and quantum (purple shaded) fluctuations determine the ripples, separated with the dashed vertical line. In both regimes, the correlation

function decays with increasing wavevectors. In the case of the classical regime, the decaying behaviour arises from the decreasing of the thermal occupation of the flexural phonon modes according to Bose-Einstein statistics. The fact that the correlation function depends inversely on phonon frequencies enhances this decaying behaviour, explaining why this function still decays in the quantum regime, but with a different exponent.

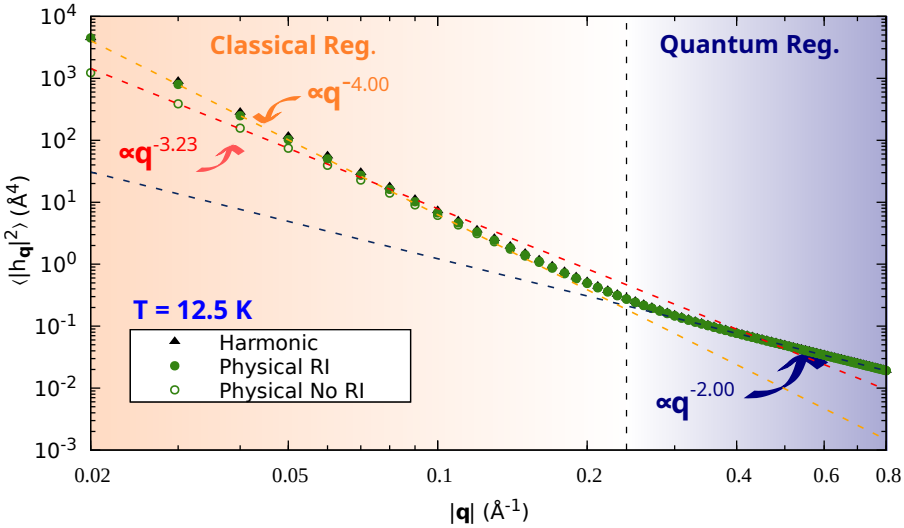

Figure 7.7: Fourier transform of the height-height correlation function at 12.5 K in the membrane model evaluated at different levels of approximation: harmonic (black dots), anharmonic RI result (green filled dots) and anharmonic No RI result (green empty dots). The dashed vertical line specifies the wavevector at which the crossover from classical (orange background) to quantum correlations (violet background) occurs at this temperature. The dashed lines correspond to linear fits with different exponents.

Since the exponent of the correlation function in each regime depends on the ZA phonon dispersion, it changes depending on the approximation level. At 12.5 K, the exponent does not change in the quantum regime even if a non rotationally invariant potential is considered: $\langle|h(\mathbf{q})|^2\rangle \sim \Omega_{ZA}(\mathbf{q})^{-1} \sim q^{-2}$. The common exponent arises from the fact that the linearization of the ZA phonon affects only small wavevectors, as shown in Fig. 7.6. In the classical regime, we recover the $\langle|h(\mathbf{q})|^2\rangle \sim q^{-3.2}$ behaviour when we neglect $\partial_i \boldsymbol{u} \cdot \partial_j \boldsymbol{u}$, as shown with empty dots, showing that our result is consistent with previous calculations within SCSA and NPRG methods in the wave number range studied [23, 25, 27, 31–34, 130]. However, when we keep full rotational invariance, the ZA modes acquires a quadratic dispersion and thus $\langle|h(\mathbf{q})|^2\rangle \sim q^{-4}$, which is the result obtained in the harmonic case. Consequently, anharmonicity does not suppress the amplitude of the ripples in the long-wavelength limit, upturning the previous consensus [23, 25, 27, 31–34, 130]. It is worth noting, however, that in the renormalization group calculations presented in Ref. [132] a q^{-4} behaviour was not recovered even if the Hamiltonian

contained the $\partial_i \boldsymbol{u} \cdot \partial_j \boldsymbol{u}$ term and was, thus, rotationally invariant. At this point, it should be stressed that accounting correctly for the thermal expansion and not using a fix lattice parameter a_0 is crucial to recover the quadratic dispersion of the ZA mode as well as the consequent q^{-4} power law of the height correlation function. As shown in Fig. 7.6 (b) with light blue empty squares, a strained membrane results equally in a divergent bending rigidity.

Finally, we compare our results from the membrane model with the atomistic calculations on graphene available in the literature, which employ empirical potentials that theoretically maintain rotational symmetry. Path-integral Monte Carlo (PIMC) simulations of freestanding graphene have reported a similar crossover between the regimes where thermal and quantum fluctuations dominate the ripples [140]. However, atomistic classical Monte Carlo and molecular dynamics simulations have estimated $\langle |h(\mathbf{q})|^2 \rangle$ for small wave numbers in the order of $q \sim 0.01 \text{Å}^{-1}$, finding a scaling law not far from the $q^{-3.2}$ obtained in the membrane model when rotational symmetry is broken [24, 130, 131, 140]. Even if this contradicts our results since such atomistic calculations respect in principle rotational symmetry, an uncontrolled small strain in these calculations could influence the exponent of the height-height correlation function.

To assess the significance of small strains on the behaviour of the height-height correlation function, we formulate a simple harmonic model that describes the relationship between the ZA frequency and the biaxial strain δa. Biaxial strain is incorporated in the strain tensor of Eq. (7.3) in a similar fashion to thermal expansion, by modifying $\partial_i u_j \to \partial_i u_j + \delta^{ij} \delta a$, but here δa is treated as a constant external strain rather than a variable to be relaxed. In any case the only second-order term involving out-of-plane fluctuations is $\delta a(\lambda + \mu) \int_\Omega d^2x \; \partial_k h \partial_k h$. Consequently, the modified harmonic potential energy for h due to strain can be expressed as

$$V_{\delta a} = \frac{1}{2} \Big[\int_\Omega d^2x \; \kappa (\nabla^2 h)^2 + 2\delta a(\lambda + \mu) \int_\Omega d^2x \; \partial_k h \partial_k h \Big], \tag{7.44}$$

whose diagonalization leads to

$$\omega_{ZA}(q) = \sqrt{\frac{2(\lambda + \mu)\delta a q^2 + \kappa q^4}{\rho}} \; . \tag{7.45}$$

In Fig. 7.8, we present the explicit calculation of $\langle |h(\mathbf{q})|^2 \rangle$ as a function of biaxial strain at $T = 12.5$ K, obtained by substituting Eq. (7.45) into the equation for the height-height correlation function. The figure demonstrates that even the application of a minimal tensile strain is enough to suppress out-of-plane fluctuations, making it an effective mechanism for stabilizing long-range orientational order [130]. In fact, the results suggest that an uncontrollable strain in the numerical simulations as small as $\delta a = 10^{-5}$ can lower the ripples amplitude from the q^{-4} law expected for the unstrained membrane (black dashed lines) to $q^{-3.23}$ (red dashed lines) in the wavevector window of the order of $q \sim 0.01 \text{Å}^{-1}$. This specific wavevector range is precisely the one classical atomistic simulations can

effectively probe [24, 130, 131, 140]. Actually, the exponent for a strained membrane is expected to approach q^{-2} for the smaller wavevectors, as predicted by Eq. (7.45), which implies that probing the longest wavelengths, we would find that the exponent is not -3.23 but rather -2. This indicates that the supposed anharmonic exponent observed in atomistic simulations can arise from a combination of the presence of such small, uncontrollable strains and the limited wavevector range accessible to these techniques. In short, even though our model predicts an asymptotic value of q^{-2} under strain, the figure underscores how sensitive the exponent is to factors that extend beyond the precision of current atomistic simulation methods.

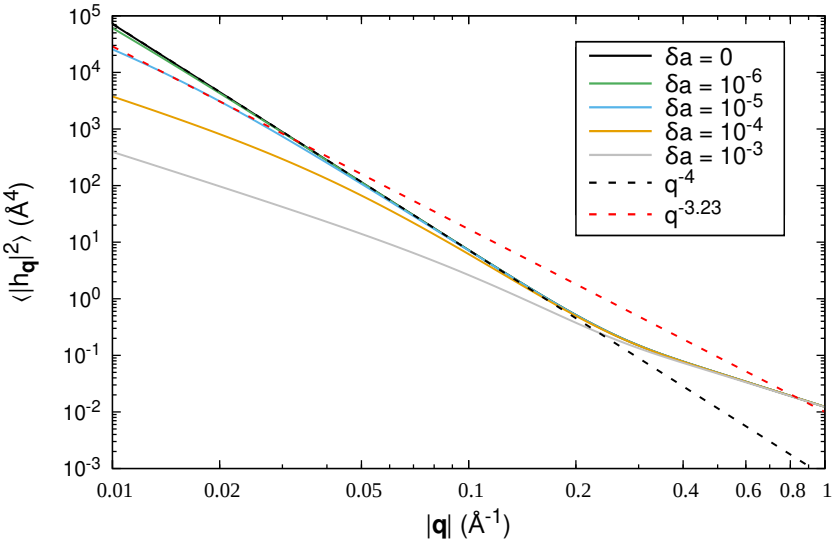

Figure 7.8: Fourier transform of the height-height correlation function at 12.5 K in the membrane model as a function of the biaxial strain δa. The dashed lines correspond to linear fits with the exponents found in the previous figure for the rotationally invariant membrane (black dashed line) and for the non-rotationally invariant membrane (red dashed line). In the long-wavelength limit, the behaviour deviates from the q^{-4} law even for very small strains, such as $\delta a = 10^{-5}$.

In addition to the impact of external strain on the stability of 2D materials, other factors can also influence the exponent derived from atomistic simulations. In fact, considering that the ZA mode with $q \sim 0.01$Å^{-1} requires about 1 nanosecond to complete one period, very long simulation times are needed to describe a thermodynamically flat phase of graphene. As a result, these Monte Carlo and molecular dynamics numerical simulations may be affected by non-ergodic conditions, impacting the determination of the height correlation function in the long-wavelength limit. On the contrary, in our SCHA simulations the ionic equilibrium positions are always in the plane. The positive phonon frequencies observed in all our calculations confirm that this flat configuration is indeed a minimum of the free energy at the studied temperatures and therefore, at least, a metastable state.

7.4.4 Temperature effects on the height-height correlation function

Finally, this subsection examines how temperature affects the nature of graphene's out-of-plane fluctuations, or ripples. To understand their shift from classical to quantum behaviour, we compare the height-height correlation function at room temperature (300 K) with that at absolute zero (0 K). Analysing the correlation functions at these temperatures enables us to clarify how thermal and quantum fluctuations influence the surface texture of graphene.

Even if graphene's Debye temperature has a higher value than room temperature, at 300 K all the out-of-plane modes are substantially thermally occupied in the wavevector range in which we have focused our analysis on. As shown in Fig. 7.9, thermal fluctuations dominate, and the height-height correlation function shows a classical behaviour. Again, the quadratic dispersion of both harmonic (black dots) and anharmonic rotationally invariant results (green filled dots) leads to an exponent of $\langle |h(\mathbf{q})|^2 \rangle \sim q^{-4}$, consistent with classical statistics. The linearization of anharmonic phonons in the long-wavelength limit when the rotational invariance is broken makes us recover the exponent obtained in the classical counterparts in the literature once more.

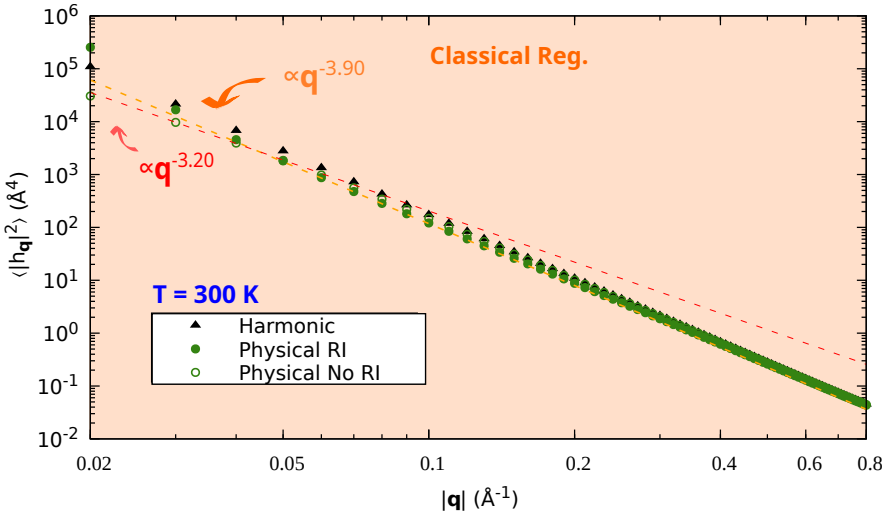

Figure 7.9: Fourier transform of the height-height correlation function at 300 K in the membrane model evaluated at different levels of approximation: harmonic (black dots), anharmonic RI result (green filled dots) and anharmonic No RI result (green empty dots). The dashed lines correspond to the linear fitting in each case.

At 0 K there is no phonon mode thermally occupied, but all of them fluctuate due to quantum zero-point motion. The height-height correlation function shows a fully quantum behaviour, with no crossover to a classical regime, as illustrated in Fig. 7.10. The harmonic (black dots) and anharmonic rotationally invariant result (green filled dots) yield the same exponents due to their quadratic dispersion: $\langle|h(\mathbf{q})|^2\rangle \sim q^{-2}$. When the membrane lacks rotational invariance due to neglecting the $\partial_i \boldsymbol{u} \cdot \partial_j \boldsymbol{u}$ term in the strain tensor, anharmonic phonons (green empty dots) are quadratic in the short-wavelength limit, consistent with Eq. (7.25). However, in the long-wavelength limit, they exhibit a linearized behaviour with $\langle|h(\mathbf{q})|^2\rangle \sim \Omega_{ZA}(\mathbf{q})^{-1} \sim q^{-1.62}$. This exponent reminds of the phonons in the SCSA, which scale as q^{ν} with $\nu \sim 1.6$ [32].

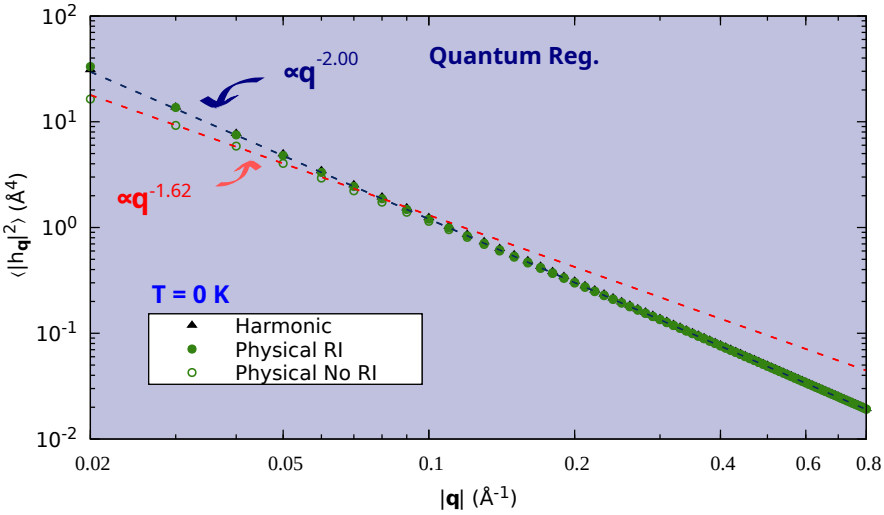

Figure 7.10: Fourier transform of the height-height correlation function at 0 K in the membrane model evaluated at different levels of approximation: harmonic (black dots), anharmonic RI result (green filled dots) and anharmonic No RI result (green empty dots). The dashed lines correspond to the linear fitting in each case.

Therefore, even at absolute zero, graphene exhibits some degree of corrugation, which corresponds to the macroscopic manifestation of the atomic zero-point motion. However, quantum ripples differ significantly from their classical counterparts [140]. Specifically, quantum zero-point motion results in weaker long-wavelength flexural fluctuations compared to thermal fluctuations, which means that quantum ripples tend to make graphene globally flatter, without crumpling the system. However, the slower decay of the height-height correlation function reflects how quantum zero-point motion leads to relatively more pronounced short-wavelength fluctuations, making the surface locally rougher compared to classical graphene.

7.5 Conclusions and outlook

In this chapter we have analysed theoretically the mechanical properties of graphene by means of a non-perturbative treatment of anharmonicity. Based on the consideration that the anharmonic free energy fulfills the same symmetry properties as the harmonic potential, we have proved using a membrane model that the quadratic dispersion for the ZA mode persists even when anharmonic interactions are considered. Remarkably, even if in the harmonic case a quadratic dispersion implies non-propagating sound, within our anharmonic theory in-plane phonons can propagate sound even if the flexural modes have a quadratic dispersion [128, 133]. Due to this quadratic dispersion, we find that, contrary to previous assumptions, graphene's bending rigidity does not diverge in the long-wavelength limit.

In order to compare our hypothesis with results from the literature, we have computed the height-height correlation function and examined how sensitive the results are to factors that break rotational invariance. Specifically, our findings suggest that literature results often show deviations from rotational invariance, primarily due to the omission of high-order in-plane terms in the membrane Hamiltonian in analytical calculations, and the influence of strain in numerical simulations. In summary, our results demonstrate that the temperature dependence of membrane height fluctuations is indeed governed by thermal or quantum fluctuations. However, contrary to previous assumptions, there is no anharmonic suppression of their amplitude when a rotationally invariant model is used. All the conclusions exposed so far are universal and can be extrapolated to any strictly 2D material or membrane.

These results and their implications are, however, limited to intrinsic 2D systems without any external perturbation that breaks rotational symmetry and to situations in which the average positions of the atoms in the 2D material are strictly confined to the plane. In practice, however, 2D materials are usually grown on substrates that apply some degree of strain, even if minimal, which breaks rotational symmetry. The repercussions of our findings under these conditions remain to be determined. Nevertheless, the simple harmonic model used to describe the effect of biaxial strain indicates that even a minimal tensile strain can effectively suppress out-of-plane fluctuations and stabilize long-range orientational order [130].

On the other hand, it is still unclear whether 2D materials are truly flat as assumed or whether they exhibit static ripples. We have demonstrated that the flat configuration is dynamically stable, given the absence of unstable phonons in our calculations. However, these findings alone are not enough to establish that the flat phase is energetically favourable, as the rippled configuration might represent the global minimum of the free energy landscape. Therefore, to further validate our interpretation of the mechanical properties of 2D materials, the next step would be to analyse whether static ripples can form in unstrained graphene, and to evaluate if such potential formation is energetically favourable with respect to the flat configuration within the theoretical framework of this study.

Despite the sensitivity of the results to strain and the flatness of the sample, these findings are highly relevant as they describe the intrinsic mechanical properties of graphene and other flat membranes. For instance, considering that phonons are at the core of heat transport, our ideas could impact the understanding of thermal conductivity in 2D systems. In particular, a quadratic dispersion of ZA phonons would lead to a lower group velocity compared to linearly dispersing modes.

Part IV

Conclusions and outlook

Conclusions and outlook

This thesis has systematically explored the significance of anharmonic effects in the behaviour of various physical systems, particularly in reduced dimensionality scenarios involving 2D and quasi-2D materials. By employing non-perturbative approaches, we have proved that anharmonicity plays a crucial role in determining the properties and stability of systems such as bulk and monolayer $1\,T$-VSe_2 as well as graphene.

In the first chapter we have examined the CDW transition in $1\,T$-VSe_2, revealing that it is driven by the collapse of a low-energy acoustic phonon mode at $\mathbf{q}_{\mathrm{CDW}} = (0,\ 1/4,\ 0.3)$ and $\mathrm{T_{CDW}} = 110$ K, similar to behaviours observed in other TMDs like $2H$-$NbSe_2$ and $1\,T$-$TiSe_2$. Anharmonic effects play a crucial role in stabilizing the high-symmetry phase at high temperatures, while weak van der Waals interactions between VSe_2 layers are essential for melting the CDW. The electron-phonon interaction is the main driving force of the CDW transition in $1\,T$-VSe_2 despite the presence of nesting at the CDW wavevector, whose role is rather to be a factor enhancing the electron-phonon matrix elements rather than being the principal mechanism itself. Interestingly, unlike other TMDs where the CDW is typically quenched under pressure, bulk VSe_2 shows an enhancement of the charge modulated phase, potentially reaching around 290 K. We suggest that the long-range vdW interactions are also crucial for understanding this behaviour. Under pressure, the layers are brought closer together, effectively quenching the interlayer vdW interactions and thereby enhancing the stability of the CDW phase.

Next, we have analysed theoretically the strain dependence of the CDW orders in monolayer $1\,T$-VSe_2 to resolve previous experimental contradictions. Our non-perturbative anharmonic phonon calculations have revealed that monolayer VSe_2 can develop two independent CDW orders that compete as a function of strain. Variations as small as 1.5% in the lattice parameter are sufficient to stabilize one order or the other. We have found that the natural CDW order is $\sqrt{3}\times\sqrt{7}$, while the 4×4 order, which is the in-plane projection of the $4 \times 4 \times 3$ order in the bulk, appears only under strain. The change in order with reduced dimensionality emphasizes the significance of interlayer interactions in VSe_2. Besides, critical temperatures in the monolayer are enhanced compared to the bulk, due to the absence of interlayer interactions, resulting in more robust CDW orders. Our findings also indicate that intrinsic the CDW orders in monolayer VSe_2 are primarily driven by the electron-phonon coupling, without significant nesting sig-

natures at the CDW wavevectors. While our analysis explains the variability of CDW orders and transition temperatures in monolayer VSe_2, it does not address substrate-related effects, such as potential charge transfer that could impact CDW orders, suggesting future research opportunities in this area.

In line with the discussion in the preceding paragraphs, the evidence gathered in this thesis suggests that strong vdW interactions tend to suppress CDW phases [126]. It is important to note that in all the TMDs studied prior to VSe_2 using the SSCHA method [76–78], it has not been necessary to include vdW interactions in the exchange-correlation functional to melt the charge modulated phase and achieve transition temperatures consistent with experimental values. This does not mean that theoretical estimates could not be refined by considering these interactions, but it is evident that vdW interactions play a unique role in both bulk VSe_2 and its monolayer, possibly due to their 3D nature. Definitely, a more detailed analysis of when vdW effects influence CDWs in TMDs could represent a highly interesting research avenue for the future. In this sense, an interesting compound to analyse to gain a better understanding on the influence of vdW interactions is the isostructural and isoelectronic 1 T-VTe_2. Similar to 1 T-VSe_2, the CDW in 1 T-VTe_2 is also 3D; however, the corresponding transition temperature is relatively high at 475 K [141]. That is, despite the structural, electronic and 3D CDW nature similarities with 1T-VSe_2, the stronger CDW phase reported in experiments indicates that vdW effects do not play a significant role in this compound. Undoubtedly, studying the CDW transition in 1 T-VTe_2 would provide deeper insights into the impact of vdW interactions in TMDs.

Finally, we have studied the mechanical properties of graphene employing the same non-perturbative approach to include anharmonic effects. We have established that the anharmonic free energy retains the same symmetry properties as the Born-Oppenheimer potential, demonstrating through a membrane model that the quadratic dispersion of the ZA mode persists despite anharmonic interactions. Notably, our findings indicate that the bending rigidity does not diverge in the long-wavelength limit. We have computed the height-height correlation function and highlighted that literature results often deviate from rotational invariance due to neglecting high-order in-plane terms and strain effects. While the temperature dependence of membrane height fluctuations is influenced by thermal or quantum fluctuations, we found no anharmonic suppression of these fluctuations under a rotationally invariant model. All these conclusions are universal and applicable to any strictly 2D material or membrane, as they are founded on symmetry properties.

Still, the fact that anharmonicity does not suppress out-of-plane fluctuations in reciprocal space implies that these fluctuations remain significant in real space, on the order of the graphene flake. Given that the membrane model is primarily designed for small fluctuations, this result raises questions about its effectiveness in describing the physics of this problem, particularly in the long-wavelength limit. The limitations of the membrane model might not only apply to our specific case but could also be relevant for standard anharmonic treatments in the literature. In any case, these potential limitations do no invalidate the hypothesis that the

quadratic behaviour should be recovered within a non-perturbative treatment of anharmonicity, since it is rooted in symmetry arguments. Rather, they suggest that the membrane model may not be the most suitable framework for fully capturing the complexities of the longstanding problem surrounding the mechanical stability of 2D crystals. On the other hand, our results are limited to intrinsic 2D systems without external perturbations that break rotational symmetry. In practice, 2D materials typically experience minimal strain from substrates, which may affect our findings, as even slight tensile strain can suppress out-of-plane fluctuations and stabilize long-range order. Nevertheless, we have established that the flat configuration of graphene is dynamically stable, although it is still uncertain if this state is energetically favourable compared to a potential rippled configuration. Future research should investigate the energetics of static ripples in unstrained graphene to further validate our findings.

The findings in this thesis underscore the importance of considering anharmonic effects in the study of 2D materials, as they significantly impact both their dynamical properties and mechanical stability. In particular, our results have introduced a novel perspective on the necessity of incorporating van der Waals interactions to accurately characterize materials that host charge density waves. Consequently, it is now common practice to include vdW interactions when analysing CDW transitions using the SSCHA method, even in systems that are not purely 2D, such as the kagome metals. In this regard, it is important to emphasize that Grimme's method, which works well for layered systems like graphite, likely introduces non-pure vdW interactions in other systems, potentially leading to a misleading stabilization of their CDWs. Therefore, it is not advisable to apply this correction indiscriminately without some physical intuition. In conclusion, this thesis contributes to a deeper understanding of how anharmonicity and reduced dimensionality interact to shape the physical properties of low-dimensional systems, paving the way for future research in this area.

Appendices

Appendix A

Interpolation of the SSCHA anharmonic dynamical matrices

The stochastic implementation of the SCHA method involves the evaluation of energies and forces in supercells, which results in obtaining the anharmonic dynamical matrices on a commensurate grid of **q**-points. Therefore, calculating dynamical matrices on a dense grid of **q**-points requires large supercells, which significantly increases the computational cost and makes the calculations exceedingly time-consuming. Such high computational demands represent a major drawback of the method. To address this issue and obtain the free energy Hessian dynamical matrix at any desired **q**-point in the reciprocal space, we have employed the following interpolation scheme.

We begin by defining the anharmonic dynamical matrices obtained from the SSCHA calculation on a coarse **q**-point grid as $\mathbf{D}^{(\mathrm{F})}_{coarse}(\mathbf{q})$, which corresponds to employing a small supercell. The harmonic dynamical matrices calculated on the same **q**-point grid are denoted as $\mathbf{D}^{(h)}_{coarse}(\mathbf{q})$. The difference between the SSCHA anharmonic and the harmonic force constant matrices is then given by:

$$\tilde{\mathbf{D}}_{coarse}(\mathbf{q}) = \mathbf{D}^{(\mathrm{F})}_{coarse}(\mathbf{q}) - \mathbf{D}^{(h)}_{coarse}(\mathbf{q}). \tag{A.1}$$

This difference is assumed to vary smoothly in the reciprocal space, indicating that it is more localized in real space than either the harmonic or anharmonic force constant matrices individually. Based on this assumption, the difference $\tilde{\mathbf{D}}_{coarse}(\mathbf{q})$ can be interpolated using Fourier methods to any **q**-point in the Brillouin zone, resulting in $\tilde{\mathbf{D}}_{target}(\mathbf{q})$.

Finally, by calculating the harmonic dynamical matrices at specific **q**-points, which is significantly faster than computing the anharmonic ones, we can estimate the anharmonic dynamical matrices at any arbitrary **q**-point not commensurate with the supercell. This estimation is achieved through the following expression:

$$\mathbf{D}^{(\mathrm{F})}_{target}(\mathbf{q}) = \mathbf{D}^{(h)}_{target}(\mathbf{q}) + \tilde{\mathbf{D}}_{target}(\mathbf{q}). \tag{A.2}$$

This interpolation scheme allows us to efficiently obtain anharmonic dynamical matrices along a specific **q**-point path in reciprocal space, or on a finer **q**-point grid. From this finer grid, we can then Fourier interpolate to extract the phonon dispersion, significantly improving computational efficiency and accuracy in the calculation of anharmonic phonon properties.

Appendix B

Quadratic dispersion of the ZA mode in the harmonic approximation

In this appendix, we present a mathematical proof demonstrating that the dispersion relation of the ZA phonon mode in 2D materials exhibits a quadratic behaviour in the long-wavelength limit, $\mathbf{q} \to 0$, within the harmonic approximation.

To proceed, it is important to recall that in the harmonic approximation introduced in Section 3.1, lattice vibrations are described as a superposition of independent modes, known as phonons. Each phonon is characterized by a wavevector $\mathbf{q}$ and a branch index $\mu = 1, \ldots, 3p$, where p represents the number of atoms per unit cell. The squared phonon frequencies $\omega_\mu^2(\mathbf{q})$ are obtained as the eigenvalues of the $3p \times 3p$ dynamical matrix:

$$D_{ss'}^{\alpha\alpha'}(\mathbf{q}) = \sum_n \frac{\Phi_{ss'}^{\alpha\alpha'}(\mathbf{T}_n, 0)}{\sqrt{M_s M_{s'}}} e^{-i\mathbf{q}\cdot\mathbf{T}_n}. \tag{B.1}$$

In the particular case of graphene, there are $p = 2$ atoms per unit cell. Furthermore, since both atoms in the unit cell are carbon atoms, we have $M_s = M_{s'} = M_C$, where M_C is the mass of the carbon atom.

The elements of the force constant matrix $\Phi_{ss'}^{\alpha\alpha'}(\mathbf{T}_n, 0)$, and consequently those of the dynamical matrix $D_{ss'}^{\alpha\alpha'}(\mathbf{q})$, are constrained and interconnected by the symmetries of the underlying lattice. In strictly 2D materials, where equilibrium positions are confined to the $z = 0$ plane, the following constraints arise:

1. **Mirror Symmetry**: The mirror symmetry with respect to the $z = 0$ plane leads to the vanishing of the following second-order force constant compo-

nents:

$$\phi_{ss'}^{xz}(\mathbf{T}_n, 0) = \phi_{ss'}^{yz}(\mathbf{T}_n, 0) = 0. \tag{B.2}$$

This constraint implies that the dynamical matrix is block diagonal:

$$D_{ss'}^{xz}(\mathbf{q}) = D_{ss'}^{yz}(\mathbf{q}) = 0, \tag{B.3}$$

allowing us to analyse the in-plane and out-of-plane vibrational modes independently.

2. **Inversion Symmetry**: The symmetry of inversion implies that the system remains unchanged when all spatial coordinates are reversed, so that:

$$\phi_{ss'}^{\alpha\alpha'}(\mathbf{T}_n, 0) = \phi_{ss'}^{\alpha\alpha'}(-\mathbf{T}_n, 0). \tag{B.4}$$

In the case of the dynamical matrix, it behaves the same if we replace **q** with **-q**:

$$D_{ss'}^{\alpha\alpha'}(\mathbf{q}) = D_{ss'}^{\alpha\alpha'}(-\mathbf{q}). \tag{B.5}$$

Additionally, in the case of graphene, the inversion symmetry with respect to the center of the hexagon results in the relationship:

$$\phi_{11}^{\alpha\alpha'}(\mathbf{T}_n, 0) = \phi_{22}^{\alpha\alpha'}(\mathbf{T}_n, 0). \tag{B.6}$$

This translates to the dynamical matrices in Equation (B.1) as follows:

$$D_{11}^{\alpha\alpha'}(\mathbf{q}) = D_{22}^{\alpha\alpha'}(\mathbf{q}). \tag{B.7}$$

3. **Translational Invariance**: The principle of translational invariance dictates that displacing the entire crystal without causing any internal distortion results in no net forces. This condition leads to the acoustic sum rule (ASR):

$$\sum_{ns} \phi_{ss'}^{\alpha\alpha'}(\mathbf{T}_n, 0) = 0. \tag{B.8}$$

As a direct consequence of the ASR, we obtain the following relation for the dynamical matrices at the Γ point:

$$D_{12}^{\alpha\alpha'}(\mathbf{q} = 0) + D_{11}^{\alpha\alpha'}(\mathbf{q} = 0) = 0. \tag{B.9}$$

4. **Rotational Invariance**: The principle of rotational invariance states that rotating a 2D crystal as a whole in 3D space should not alter its energy or generate any forces on the atoms. This property ensures that the physical characteristics of the crystal remain unchanged regardless of its orientation, and it is expressed as:

$$\sum_{ns} \phi_{ss'}^{zz}(\mathbf{T}_n, 0) T_n^{\alpha} T_n^{\beta} = 0. \tag{B.10}$$

As a consequence of the rotational invariance, we obtain the following relation for the dynamical matrices at the Γ point:

$$\left[\frac{\partial^2 D_{11}^{zz}(\mathbf{q})}{\partial q_\alpha \partial q_\beta} + \frac{\partial^2 D_{12}^{zz}(\mathbf{q})}{\partial q_\alpha \partial q_\beta} \right]_{\mathbf{q}=0} = 0. \tag{B.11}$$

Now, considering Eq. (B.3) in conjunction with Eq. (B.7), and using the commutativity of partial derivatives, we can deduce that the squared frequencies associated with the acoustic flexural mode of interest are given by:

$$\omega_{ZA}^2(\mathbf{q}) = D_{11}^{zz}(\mathbf{q}) + D_{12}^{zz}(\mathbf{q}). \tag{B.12}$$

To prove that this mode exhibits quadratic dispersion in the long-wavelength limit, we perform a Taylor expansion of $\omega_{ZA}^2(\mathbf{q})$ around the Γ point:

$$\omega_{ZA}^2(\mathbf{q}) \approx \omega_{ZA}^2(\mathbf{q}=0) + \sum_{\alpha} \left.\frac{\partial \omega_{ZA}^2}{\partial q_\alpha}\right|_{\mathbf{q}=0} q_\alpha + \frac{1}{2}\sum_{\alpha,\beta} \left.\frac{\partial^2 \omega_{ZA}^2}{\partial q_\alpha \partial q_\beta}\right|_{\mathbf{q}=0} q_\alpha q_\beta + \dots \tag{B.13}$$

where α, β are the Cartesian components. The squared phonon frequency at the Γ point is 0, $\omega_{ZA}^2(\mathbf{q}=0) = 0$, due to Eq. (B.9), that is, as a consequence of the translational invariance. Additionally, due to the inversion symmetry constrain in Eq. (B.5), $\omega_{ZA}^2(\mathbf{q})$ is an even function of the wavevector $\mathbf{q}$, so that all the odd-order terms in the Taylor expansion must vanish. Finally, the constraint imposed by rotational invariance in Eq. (B.11) implies that the Taylor expansion begins with the fourth-order terms. As a result, in the long-wavelength limit, we find that:

$$\omega_{ZA}(\mathbf{q}) \propto q^2. \tag{B.14}$$

Proving in this way that the dispersion relation of the ZA phonon mode in 2D materials exhibits a quadratic behaviour within the harmonic approximation.

It is worth emphasizing that, while rotational invariance is a crucial factor that ultimately leads to the quadratic dispersion of the ZA mode, this symmetry can also be present in 3D crystals. In contrast, strictly 2D systems present a different scenario. Here, the rotational invariance combines with the inherent mirror symmetry of the system, which effectively decouples the in-plane and out-of-plane components of the second-order force constants. It is this unique combination what enables the ZA mode of 2D systems to exhibit the mentioned quadratic dispersion near the zone center within the harmonic approximation.

Appendix C

Rotational invariance of the membrane potential

In this appendix we prove explicitly that the membrane potential in Eq. (7.4) is rotationally invariant, and that neglecting the high-order in-plane terms $\partial_i \mathbf{u} \cdot \partial_j \mathbf{u}$ results in a breaking of this invariance. Let us remember the model for a continuous elastic membrane embedded in 3D space. Without loss of generality, we assume that the flat membrane lies in the xy plane in the equilibrium configuration. We introduce the local deformations of the membrane from the flat geometry by means of the vector:

$$\delta\mathbf{R}(\mathbf{x}) = u_x(\mathbf{x})\mathbf{i} + u_y(\mathbf{x})\mathbf{j} + h(\mathbf{x})\mathbf{k}, \tag{C.1}$$

where $\mathbf{x} = x\mathbf{i} + y\mathbf{j}$ is the coordinate relative to the flat membrane, u_x, u_y are the in-plane displacements and h is the out-of-plane displacement. The strain tensor corresponding to the deformation in Eq. (C.1) is defined as:

$$u_{ij} = \frac{1}{2}\left(\partial_i u_j + \partial_j u_i + \partial_i \mathbf{u} \cdot \partial_j \mathbf{u} + \partial_i h \partial_j h\right), \tag{C.2}$$

where we omit the explicit dependence on $\mathbf{x}$ for simplicity. The energy cost for the deformation is given by:

$$\delta E = \frac{1}{2}\int_\Omega d^2x \left(\kappa(\nabla^2 h)^2 + C^{ijkl} u_{ij} u_{il}\right). \tag{C.3}$$

The sum over identical indexes $ijkl = x, y$ is implicit in the previous equation. As defined in the main text, κ is the bending rigidity and $C^{ijkl} = \lambda\delta^{ij}\delta^{kl} + \mu\left(\delta^{ik}\delta^{jl} + \delta^{il}\delta^{jk}\right)$ the elastic moduli tensor, with λ and μ the Lamé coefficients.

In what follows we show that the potential of Eq. (C.3) is invariant under any rigid rotation about the plane of the membrane. To this purpose, we first define the rotation axis in the xy plane as $\mathbf{n} = n_x\mathbf{i} + n_y\mathbf{j}$, where $|\mathbf{n}| = 1$ ensures that $\mathbf{n}$ is

a unit vector. The rigid rotation of the membrane around the axis $\mathbf{n}$ by an angle θ is characterized by the following linear transformation:

$$\mathbf{x} \to \mathbf{x}' = \exp\left[\theta \mathbf{n}\times\right] \mathbf{x}. \tag{C.4}$$

In this case the local deformation of the membrane is expressed as:

$$\delta\mathbf{R}(\mathbf{x}) = \left[\exp\left(\theta\mathbf{n}\times\right) - 1\right]\mathbf{x} = \sum_{k\geq 1} \frac{\theta^k}{k!} \left(\mathbf{n}\times\right)^k \mathbf{x}. \tag{C.5}$$

And the following identities can be derived:

$$\begin{aligned}
\mathbf{n}\times\mathbf{x} &= (n_x y - n_y x)\mathbf{k}, && \text{(C.6a)}\\
\left(\mathbf{n}\times\right)^2 \mathbf{x} &= (n_x y - n_y x)(n_y \mathbf{i} - n_x \mathbf{j}), && \text{(C.6b)}\\
\left(\mathbf{n}\times\right)^{2k+1} \mathbf{x} &= (-)^k \mathbf{n}\times\mathbf{x} && \text{(C.6c)}\\
\left(\mathbf{n}\times\right)^{2k} \mathbf{x} &= (-)^{k-1} \left(\mathbf{n}\times\right)^2 \mathbf{x}. && \text{(C.6d)}
\end{aligned}$$

So that the local deformation of the membrane after a rotation by angle θ around the axis $\mathbf{n}$ is finally written as:

$$\delta\mathbf{R}(\mathbf{x}) = \sin\theta\,(\mathbf{n}\times\mathbf{x}) + (1-\cos\theta)\left[\left(\mathbf{n}\times\right)^2\mathbf{x}\right]. \tag{C.7}$$

Identifying the latter equation with the general deformation in Eq. (C.1), and using (C.6) yields:

$$u_x(\mathbf{x}) = u_x^0 f(\mathbf{x}), \quad u_y(\mathbf{x}) = u_y^0 f(\mathbf{x}), \quad h(\mathbf{x}) = h^0 f(\mathbf{x}), \tag{C.8a}$$

where the coefficients, which depend only on the rotation parameters, are:

$$(u_x^0, u_y^0, h^0) = \left[n_y(1-\cos\theta), -n_x(1-\cos\theta), \sin\theta\right], \tag{C.8b}$$

and the deformation field depends linearly on the function:

$$f(\mathbf{x}) = n_x y - n_y x. \tag{C.8c}$$

The strain tensor of Eq. (C.2) can then be written as:

$$u_{ij} = \frac{1}{2}\left\{u_j^0 \partial_i f + u_i^0 \partial_j f + \left[\left(u_x^0\right)^2 + \left(u_y^0\right)^2 + \left(h^0\right)^2\right]\partial_i f \partial_j f\right\}. \tag{C.9}$$

A straightforward calculation using Eqs. (C.8) reveals that each component of the strain tensor vanishes: $u_{ij} = 0\ \forall ij$. Concerning the bending energy term $\kappa\left(\nabla^2 h\right)^2$ in Eq. (C.3), it is trivially zero as h is a linear function of $\mathbf{x}$ in the rigid rotation that we are considering. This finally shows that there is no change in energy, $\delta E = 0$, for any rigid rotation about the membrane's plane. Note that the $\partial_i \mathbf{u}\cdot\partial_j\mathbf{u}$ term in the potential is needed to keep $\delta E = 0$. When it is neglected, $\delta E \neq 0$ for a rigid rotation, and the model lacks rotational invariance.

List of publications

List of publications

Most of the results discussed in this manuscript have been published in the following references:

1. "van der Waals driven anharmonic melting of the 3D charge density wave in VSe_2",
   Josu Diego, A. H. Said, S. K. Mahatha, Raffaello Bianco, Lorenzo Monacelli, Matteo Calandra, Francesco Mauri, K. Rossnagel, Ion Errea, and S. Blanco-Canosa.
   Nature Communications 12, 598 (2021).

2. "Anharmonicity Reveals the Tunability of the Charge Density Wave Orders in Monolayer VSe_2",
   Adolfo Otero Fumega, **Josu Diego**, Víctor Pardo, S. Blanco-Canosa, and Ion Errea.
   Nano Letters 23, 1794 (2023).

3. "Electronic structure and lattice dynamics of $1T$-VSe_2: Origin of the three dimensional charge density wave",
   Josu Diego, David Subires, A. H. Said, D. A. Chaney, A. Korshunov, G. Garbarino, F. Diekmann, S. K. Mahatha, V. Pardo, J. M. Wilkinson, J. S. Lord, J. Strempfer, Pablo J. Bereciartua Perez, S. Francoual, C. Popescu, M. Tallarida, J. Dai, Raffaello Bianco, Lorenzo Monacelli, Matteo Calandra, A. Bosak, Francesco Mauri, K. Rossnagel, Adolfo O. Fumega, Ion Errea, and S. Blanco-Canosa.
   Physical Review B 109, 035133 (2024).

4. "Bending rigidity, sound propagation and ripples in flat graphene",
   Unai Aseginolaza*, **Josu Diego***, Tommaso Cea, Raffaello Bianco, Lorenzo Monacelli, Francesco Libbi, Matteo Calandra, Aitor Bergara, Francesco Mauri, and Ion Errea.
   Nature Physics 20, 1288 (2024).
   *U.A. and J.D. contributed equally to this work.

Summary in Basque

Laburpena

Materialak osatzen dituzten atomoek euren oreka posizioaren inguruan fluktuatzen eta oszilatzen dute edozein tenperaturatan, baita zero absolutuan ere, euren zero-puntuko mugimendu kuantikoaren ondorioz. Bibrazio hauek materialen propietate fisiko eta kimiko ugari zehazten dituzte, hala nola euren ezaugarri termodinamikoak zein garraio propietateak. Esaterako, bibrazio atomikoek materialen propietate termodinamikoen tenperaturarekiko dependentzia zehazten dute, bibrazio hauek elektroiak baino askoz tenperatura baxuagoetan kitzikatzen baitira. Ondorioz, fluktuazio atomikoek eragin handia dute fase-trantsizio, bero espezifiko eta espantsio termiko bezalako fenomenoetan. Bestalde, materialen garraio elektriko eta termikoa ezin da ulertu elektroien eta bibrazio atomikoen kuantuen, fonoien, arteko elkarrekintza kontuan hartu gabe, ezta fonoien arteko elkarrekintza alde batera utzita. Supereroankortasuna bera ere, materialetan azaleratzen den fenomeno intrigagarrienetako bat, elektroi-fonoi elkarrekintzaren emaitza izaten da askotan. Honetaz gain, dinamika bibrazionalak sinadura espektroskopiko ezberdinak uzten ditu, infragorri, Raman, eta x-izpi edo neutroi bidezko sakabanaketa esperimentuetan ikus daitezkeenak.

Gaur egun, materialen propietate bibrazionalak lehen-printzipio metodoen bidez kalkulatzen dira hurbilketa harmonikoa prozedura estandar gisa aplikatuz. Esparru honetan, atomoen dinamika deskribatzen duen Born-Oppenheimer potentziala bigarren ordenara arte garatzen da desplazamendu atomikoen funtzio bezala. Alabaina, hurbilketa honek fonoiak ongi definituriko kuasipartikulak direla iragartzen du, euren bizidenbora infinitua eta energia tenperaturarekiko independente direlarik. Benetan, fonoiek bizidenbora finitua dute hainbat faktore direla medio, elkarrekintza anharmonikoak, esaterako. Hala erakusten dute sakabanaketa inelastiko esperimentuetan neurtzen diren fonoi gailurren zabalerek. Areago, fonoi energiek tenperaturarekiko menpekotasuna dute, bigarren ordenako fase trantsizioetatik gertu dauden moduen biguntze eta kolapsoak adierazten duen bezala. Bigarren ordenako fase trantsizioei dagokienez, hurbilketa harmonikoak tenperatura altuko fase ez-distortsionatuen egonkortasun dinamikoa azaltzeko orduan arazoak ditu baita. Hala adierazten dute simetria altuko fasearen fonoi espektro harmonikoetan ageri diren maiztasun irudikariek. Fonoi maiztasun hauek atomoen zenbait desplazamenduk distortsio espontaneoak eragin ditzaketela iradokitzen dute, hain zuzen. Fenomeno hauek guztiak atzemateko, hurbilketa harmoniko estandarretik harago joan behar da, termino anharmonikoak sartuz deskribapen teorikoan.

Efektu anharmonikoak barne hartzeko modu bat emaitza harmonikoei perturbazio teoria aplikatzea da. Hurbilketa hau fonoien tenperaturarekiko dependentzia eta bizidenbora finitua bezalako fenomeno garrantzitsuak harrapatzeko gai da. Alabaina, hurbiltze perturbatiboak guztiz kolapsatzen du baldin eta fluktuazio ionikoen anplitudearen ondorioz garapen harmonikoak ez badu potentzial erreala hurbiltzen. Kolapso hau maiz gertatzen da desplazamendu atomiko esanguratsuak dituzten sistemetan. Esaterako ioi arinak dituzten horietan, baita karga dentsitate uhinak (ingelesez, *charge density wave*, CDW) bezalako fase trantsizio displaziboetara hurbiltzen diren materialetan ere, edota dimentsio baxuko sistemetan, non atomoek fluktuatzeko askatasun handiagoa duten. Kasu horietan guztietan, efektu anharmonikoak dira nagusi sistemaren portaeran eta propietateetan, eta beraz, hurbiltze metodo ez-perturbatiboak beharrezkoak dira analisi zehatz bat gauzatzeko.

Hain zuzen ere, tesi honek efektu anharmoniko ez-perturbatiboen eragina aztertzen du zenbait sistema fisikoren dinamika ionikoan. Egun, hurbilketa harmoniko autobateragarria (ingelesez, *self-consistent harmonic approximation*, SCHA) [1] da anharmonikotasunaren tratamendu ez-perturbatiboa eskaintzen duen metodorik eraginkorrena, bibrazio atomikoetan eragin termikoak eta kuantikoak kontuan hartzen dituelarik. Ondorioz, SCHA da lan honetan erabilitako oinarrizko *ab initio* metodoa. Tesi honek material oso anharmonikoak aztertzen dituen arren, gai komun batek lotzen ditu sistema hauek guztiak: dimentsio baxuko konposatuak direla. Zehazki, sistema bidimentsional eta quasi-bidimentsionalak aztertu ditugu.

Tesi honen **lehenengo helburua** karga dentsitate uhin ezegonkortasunak *ab initio* kalkuluen bidez ikertzean eta ulertzean datza. Gaur egun, lehenengoprintzipioetan oinarritutako kalkuluen bidez fenomeno hau teorikoki ezaugarritzea ez da tribiala, izan ere, aipatu bezala, ohiko hurbilketa harmonikoak ezin du tenperatura altuko distortsiorik gabeko fasearen egonkortasun dinamikoa azaldu. Muga honek karga dentsitate uhinen jatorriaren eta urtzearen atzean dauden mekanismoak ulertzea ekiditen du. Lan honetan arazo hauei aurre egiten diegu geure kalkuluetan efektu anharmoniko ez-perturbatiboak kontsideratuz.

Karga dentsitate uhinak dituzten solidoen artean, trantsizio-metalen dikalkogenuroak (ingelesez, *transition metal dichalcogenides*, TMDs) dira bereziki interesgarri. Izan ere, egitura geruzadun quasi-bidimentsionala duten material hauen fase diagrama [89–92] tenperatura altuko supereroaleen diagramaren antzekoa da [4–8], zeinetan supereroankortasuna eragiten duen akoplamendu mekanismoa ezezaguna den. Izatez, TMD-ak kristal-egitura sinplea duten materialak izanik, karga dentsitate uhinen jatorria eta fase honek supereroankortasunarekin duen harremana aztertzeko hautagai bikainak dira. Areago, euren egitura kristalino quasi-bidimentsionala dela eta, material hauek geruza meheetan erraz esfoliatu daitezke [17] eta ondorioz, CDW-ak dimentsio murrizketarekiko duten menpekotasuna aztertzeko plataforma paregabea eskaintzen dute. Gauzak horrela, II. atalaren helburua TMD familiako kideetan CDW trantsizioak aztertzea da. Sistema sinple hauetan jazotzen diren oinarrizko mekanismoak ulertuz, korrelazio handiko material

konplexuetan garrantzitsu izan daitezkeen ikuspegiak azalera ekartzeko helburua dugu. Bereziki, TMD familiako kide metaliko batean zentratzen gara atal horretan, 1T-VSe_2-n.

5. kapituluan 1T-VSe_2-ren sare dinamika modu sakon batean ezaugarritzen da, CDW trantsizioari dagozkion efektuei arreta berezia jartzen zaielarik. Geure fonoi anharmoniko kalkulu ez-perturbatiboek, x-izpi sakabanaketa inelastiko esperimentuen datuekin batera, konposatu honen CDW trantsizioa energia baxuko fonoi modu akustiko baten kolapsoak bultzatzen duela agerira ekarri dute. Fonoi moduaren uhin-bektore kritikoa $\mathbf{q}_{\mathrm{CDW}} = (0,\ 1/4,\ 0{,}3)$ da eta $\mathrm{T}_{\mathrm{CDW}} = 110$ K. Biguntze portaera hau TMD familiako antzeko konposatuetan hauteman da baita, hala nola 2H-$NbSe_2$-n [96] eta 1T-TiSe2-n [97]. Geure analisi teorikoak azpimarratzen du efektu anharmonikoak erabakigarriak direla tenperatura altuetan VSe_2-ren simetria altuko fasea egonkortzeko. Alabaina, aldez aurretik SSCHA baliatuz ikerturiko beste TMD-tan ez bezala [76–78], kasu honetan geruzen arteko van der Waals (vdW) elkarrekintza ahulak kontsideratzea funtsezkoa da CDW-a urtzeko. Bestalde, elektroi-fonoi elkarrekintza da CDW trantsizioaren indar eragile nagusia 1T-VSe_2-n, nahiz eta uhin-bektore kritikoetan Fermi gainazalaren habiaketa baden. Hala ere, egindako kalkulu gehigarriek adierazten dute habiaketa hau ez dela trantsizioaren atzean dagoen mekanismo nagusia, baizik eta elektroi-fonoi matrize elementuak hobetzen dituen faktore bat. Bitxia bada ere, beste TMD batzuetan ez bezala [94], VSe_2-ren egitura masiboak CDW fasearen hobekuntza erakusten du presiopean, potentzialki 290 K ingurura iritsiz [92]. Distantzia luzeetan ematen diren vdW elkarrekintzak portaera hau ulertzeko erabakigarriak direla iradokitzen dugu. Hain zuzen ere, presioak geruzak gerturatzen dituenez, euren arteko vdW interakzioak arintzen ditu eta ondorioz, CDW fasea sendoagoa da.

6. kapituluan, 1T-VSe_2 monogeruzaren CDW ordenek deformazioekiko duten mendekotasuna aztertu dugu teorikoki, literaturan dauden kontraesan esperimentalak argitze aldera [100–105]. Geure kalkulu ez-perturbatibo anharmonikoek agerian utzi dute VSe_2 monogeruzak deformazioaren arabera lehiatzen diren bi CDW ordena independente garatzen dituela. Sare parametroan %1,5 baino txikiagoak diren aldaketak nahikoak dira ordena bat edo bestea egonkortzeko. Beraz, emaitza honek substratu desberdinetan egindako esperimentuetan behatutako modulazio desberdinentzat azalpena ematen du. Zehazki, CDW ordena naturala $\sqrt{3} \times \sqrt{7}$ dela aurkitu dugu, 4×4 ordena (egitura masiboaren $4 \times 4 \times 3$ ordenaren planoko proiekzioa) soilik tentsiopean agertzen delarik. Bestalde, geruza bakarrarentzat kalkulaturiko zein esperimentuetan behaturiko tenperatura kritikoak altuagoak dira egitura masiboarenarekin alderatuta, joera hau geruzen arteko vdW interakzio ezagatik dela iradokitzen dugu. Azkenik, geure kalkuluek adierazten dute elektroi-fonoi elkarrekintza dela VSe_2 monogeruzako CDW trantsizioen eragile, eta uhin-bektore kritikoetan Fermi gainazalaren habiaketaren sinadura esanguratsurik ez dagoela. Gure analisiak VSe_2 monogeruzentzat literaturan iragarritako CDW ordenen eta trantsizio tenperaturen aldagarritasuna azaltzen duen arren, ez ditu substratuaren efektuak kontuan hartzen. Esaterako, substratu baten karga transferentziak CDW ordenetan eragina izan lezake [78]. Honakoa abiapuntu interesgarria izan daiteke etorkizuneko ikerketei begira.

Tesi honetan aztertu dugun **bigarren problemak** izaera historikoa du, bi dimentsioko materialen egonkortasun mekanikoa baitu hizpide. Nahiz eta aurreko paragrafoan material bidimentsionalen existitzeari buruzko ebidentziak aurkeztu, historikoki, bi dimentsiotan kristal-ordena existitzeko aukera ezinezkotzat jotzen zen [18–20]. Grafenoaren aurkikuntzak 2004. urtean [17, 21, 22] aspaldiko iragarpen teoriko hauei aurre egin zien. Material hauen egonkortasunaren atzean dauden mekanismo zehatzen inguruko eztabaida gaur egun dirau.

Problema honek duen zailtasun teoriko handiena 2D sistementzat aurreikusitako fluktuazio termiko handietatik dator, izan ere, dimentsio murrizketak atomoei planotik kanpo fluktuatzeko aukera ematen die. Fluktuazio garai hauek lotura estua dute hurbilketa harmonikoaren barruan plano-kanpoko fonoi modu akustikoentzat (ZA moduentzat) lortzen den dispertsio erlazio koadratikoarekin. Izan ere, energia baxuko fonoi-modu hauek azkar okupatzen dira tenperatura igo ahala. Izatez, teoria harmonikoak plano-kanpoko espazio errealeko desplazamenduak materialaren tamainarekin konparagarriak direla iragartzen du, modu honetan edozein ordena kristalino eragotziz. Teoria estandarren arabera, plano-barneko eta plano-kanpoko fonoi moduen arteko akoplamendu anharmonikoak ZA fonoi moduen dispertsioa linealizatzen du, patologiak sendatuz [23–30]. Antzera batean, luzaroan onartu izan da edozein membrana jarraituren plano-kanpoko bibrazio frekuentziek termino lineal bat eskuratzen dutela uhin-bektore txikietan interakzio anharmonikoen ondorioz [31]. Termino lineal honek membrana gogortzen du eta, ondorioz, honek gainazalean ematen diren uhinen (ingelesez, *ripples*) anplitudea murrizten du. Eskuarki, espazio erreziprokoko altuera-korrelazio funtziotik aztertzen da uhinen anplitudea, $\langle |h(\mathbf{q})|^2 \rangle$. Hurbilketa harmonikoan, korrelazio funtzio honek $\langle |h(\mathbf{q})|^2 \rangle \sim q^{-4}$ bezala eskalatzen du, eta ZA moduak linealizatzean $q^{-4+\eta}$-ra zuzentzen da, non $\eta \sim 0.80 - 0.85$ den [32, 33]. Materialaren flexioarekiko zurruntasunak (ingelesez, *bending rigidity*) limite klasikoan $\langle |h(\mathbf{q})|^2 \rangle q^4$ gisa eskalatzen duenez [31, 32, 34], interpretazio honen arabera, membrana guztien eta oro har 2D materialen flexioarekiko zurruntasunak uhin-luzera luzearen limitean dibergitzen du. Honek zalantzazko interpretazio bat sortzen du, alegia, zenbat eta handiagoa izan membrana, orduan eta zurrunago bihurtzen dela. Ideia hauek esperimentuen bidez baieztatzea ez da erraza, alde batetik zaila delako grafenoaren flexioarekiko zurruntasuna neurtzea [35, 36], eta bestalde, ZA moduen dispertsioa helio difrakzioz neurtzean substratuaren efektuak nabariak direlako [37–40].

ZA moduarentzat hurbilketa harmonikoan espero den dispertsio koadratikoa hertsiki 2D diren sistemen berezko simetriek ezartzen dute. Kasu honetan fonoi frekuentziak $\phi_{ab}/\sqrt{M_a M_b}$ matrize dinamikoa diagonalizatuz lortzen dira, non a eta b indizeek aldi berean indize atomiko eta kartesiarrak biltzen dituzten. Orduan, M_a a atomoaren masa da, eta $\phi_{ab} = \left[\frac{\partial V}{\partial R_a \partial R_b}\right]_{\mathbf{R}_0}$ bigarren ordenako indar konstante harmonikoak, zeinak Born-Oppenheimer potentzialaren bigarren deribatua $\boldsymbol{R}$ posizio atomikoekiko hartuz eta V-ren minimoan ebaluatuz lortzen diren. Hain zuzen, hurbilketa harmoniko honetan, ZA moduak dispertsio koadratikoa hartzen du Brillouin-en eskualdearen mugan simetria errotazionalaren eta planoarekiko

ispilu simetriaren arteko konbinazioaren ondorioz [26]. Alabaina, esperimentuetan neurtzen diren fonoiak efektu anharmonikoak kontsideratzen dituen fonoi Green-en funtzioaren zati irudikaritik kalkulatu beharko lirateke [41]. Energia baxuko moduentzat, efektu dinamikoak alde batera utz daitezke segurtasunez. Limite honetan, fonoi gailurrak bat datoz $[\frac{\partial F}{\partial \mathcal{R}_a \partial \mathcal{R}_b}]_{\boldsymbol{\mathcal{R}}_{eq}}/\sqrt{M_a M_b}$ energia askearen Hessiarretik lortutako autobalioekin, non F energia aske anharmonikoa den, $\mathcal{R}_a$ bataz besteko posizio atomikoak, eta deribatua F minimizatzen duten posizioetan ebaluatzen den [41]. Horrek ondorio harrigarri bat dakar, orain arte oharkabean geratu dena: F-k eta V-k simetria propietate berdinak betetzen dituztenez, ZA moduaren dispertsioak koadratiko izaten jarraitu behar du elkarrekintza anharmonikoak sartu ostean.

Nolanahi ere, 2D sistementzat aurreikusitako fluktuazio garaiek iradokitzen dute problema honetan potentzialeko termino anharmonikoek harmonikoek bezalako garrantzia, edo handiagoa, dutela. Beraz, 2D sistemen egonkortasun mekanikoaren problemari aurre egiteko ikuspegirik egokiena efektu anharmoniko ez-perturbatiboak erabiltzea da. Hala izanik, tesi honen 7. kapituluan, hurbilketa harmoniko autobateragarria aplikatzen diogu grafenoari membrana eredu bat erabiliz. Horrela, deformaziorik gabeko grafenoan eta beste edozein 2D membranan ZA moduaren dispertsio koadratikoa espero dela frogatzen dugu modu sinesgarri batean. Halaber, fonoi-fonoi elkarrekintzek grafenoaren flexioarekiko zurruntasunean eraginik ez dutela egiaztatzen dugu. Gure emaitzak ez datoz bat aurrez onartutako membranen portaerarekin errotazio-inbariantza erabat mantentzen dugulako. Hain zuzen ere, gure hipotesia egungo teoria estandarrarekin alderatu eta lerrokatzeko, altuera-altuera korrelazio funtzioaren Fourier-en transformatua kalkulatzen dugu, $\langle |h(\mathbf{q})|^2 \rangle$. Membranaren altuera fluktuazioek izaera termikoa edo kuantikoa dutela ikusten dugu, baina errotazionalki inbariantea den eredu bat izanik, ez dugu fluktuazio hauen murrizketa anharmonikorik aurkitu. Hau da, $\langle |h(\mathbf{q})|^2 \rangle \sim q^{-4}$ baita efektu anharmonikoak kontuan hartzen direnean ere. Modu honetan azpimarratzen dugu literaturan dauden emaitzak gehienak, ZA moduaren linealizazioa eta $\langle |h(\mathbf{q})|^2 \rangle \sim q^{-4+\eta}$ proposatzen duten horiek, ez direla errotazionalki inbariante. Inbariantza apurketa hau barne-planoko ordena altuko terminoak edota deformazio-efektuak alde batera uzteagatik gerta daiteke.

Zentzu honetan, geure emaitzak kanpo perturbaziorik gabeko (simetria errotazionala apurtu ez dadin) eta hertsiki 2D diren sistemetara mugatuta daude. Praktikan ordea, 2D materialek substratuak eragindako deformazio txikia izan ohi dute, eta horrek eragina izan dezake gure aurkikuntzetan. Izatez, trakzio-deformazio txiki batek ere plano-kanpoko fluktuazioak ezaba ditzake eta irismen luzeko ordena egonkortu [130]. Dena den, grafenoaren konfigurazio laua dinamikoki egonkorra dela ezarri dugu, nahiz eta oraindik zalantzazkoa den egoera hau ondulatua den konfigurazio baten aldean energetikoki aldekoa den. Etorkizuneko ikerketek deformaziorik gabeko grafenoan uhin estatikoen energetika ikertu beharko lukete gure aurkikuntzak are gehiago baliozkotzeko.

Tesi honetako aurkikuntzek material bidimentsionalen azterketan efektu anharmonikoak kontuan hartzearen garrantzia nabarmentzen dute, haien propietate dinamikoetan zein egonkortasun mekanikoan nabarmen eragiten baitute. Funtsean, tesi honi esker sakonago ulertu dugu nola efektu anharmonikoek eta dimentsionaltasunaren murrizketak elkarri eragiten dioten dimentsio baxuko sistemen propietate fisikoak moldatzeko, etorkizunean arlo honetan egin daitezkeen ikerketetarako bidea erraztuz.

Acknowledgements

Acknowledgements

¿Qué es más importante, el viaje o el destino?
La compañía.

Cuatro años de doctorado dan para mucho. Durante este tiempo, he sentido que he progresado tanto como científico como persona. Ahora que ha llegado el momento de cerrar esta etapa de mi vida, no puedo evitar mirar hacia atrás y agradecer a todas las personas que me han acompañado en este viaje. Diría que esta es la parte de la tesis que menos me ha costado escribir y la que más me gusta releer. Por lo tanto, para mí al menos, éste es el capítulo más importante.

Ion, zure gidaritzapean lan egin dudan urte hauetan guztietan oso zorioneko sentitu naiz. Kosta egiten zait zugandik dudan miresmena adierazten duten hitzak aurkitzea. Baina funtsean, niretzat erreferente bat zara, zientzialari zein pertsona gisa. Eskerrik asko, hain lanpetuta egon arren, nitaz benetan arduratzen zinela egunero erakusteagatik. Niretzako denbora beti aurkitzeagatik. Neure zalantza guztiak argitzeko prest egoteagatik. Nire artikulu bakoitza eta eskuizkribu hau xehetasun osoz irakurri izanagatik. Irakatsitako zientzia guztiagatik. Eta batez ere, erakutsitako gizatasunagatik. Denagatik, bihotz-bihotzez, mila esker, Ion.

Raffaello, despite being physically far away, I have felt that you have never stopped caring about how I was doing in my PhD and about trying to understand all the projects I have been involved in. I greatly admire your ability to do physics with just a pen and paper; I remember it was a great help for the graphene paper. Thank you also for the warm welcome in Modena, I felt that you made sure I was comfortable at all times. I sincerely feel that we were understanding each other very well in the project on the symmetry reduction of the force constants, and that it was progressing at a very good pace. If I have one regret about this thesis, it is that the lack of time has not allowed me to conclude that project and include it on the manuscript. Thank you once again for everything!

Entre los colaboradores, tengo que resaltar a Santi. Él ha sido el mayor responsable de que la interminable trilogía del VSe_2 saliese adelante. Con Santi he compartido muchas comidas en las que hemos hablado de ciencia (un poco), ciclismo (algo más) y fútbol (sobre todo). Aunque claro, siendo del Barcelona, ha tenido motivos de sobra estos últimos años para estar preocupado. Gracias por todo, Santi! Gracias también a David, el mago del Inkscape. Si las figuras de la tesis os parecen buenas, en gran medida es gracias a él. Ánimo con lo que te queda, Subirés. Lo tienes ya hecho. Gracias también a Adolfo, como diría Santi, el Messi de la ciencia, pero sobre todo un muy buen tío. Como dijo Jan el día que le conocí, el paper de la monolayer fue todo un pelotazo. I would also like to express my gratitude to Lorenzo Monacelli, Francesco Libbi and Tomasso Cea. Thanks a lot for your ideas and contributions to the graphene paper, I sincerely believe that they were really helpful for understanding much better the problem. Grazie mile! Special thanks as well to Matteo Calandra and Lorenzo Monacelli (again) for taking the time to thoroughly review my thesis and provide the required reports.

I would also like to thank the people I have shared group with. Mila esker Unairi, asko lagundu zenidan neure lehenengo kalkuluekin. Sekulako lana egin zenuen grafenoarekin gainera. I remember the time when the office was full of Italians. Francesco, with his Spanish that made him sound almost English (?), answered many of my questions, specially about LaH_4. Antonella, with her perfect Spanish, kept trying to poison me with coffee that was incredibly strong ;) Grazie! Con Martín he compartido oficina durante prácticamente todo el doctorado. Tiempo en el que he alucinado con que haya sabido responder a todas las preguntas que le he planteado, por lo que le estoy muy agradecido. I want also to thank the more experienced postdocs in the group, Djordje, Yue-Wen and Diego, who have always been there to help me. Azken fitxajeei dagokienez, Manex eta Francesc, seguru nago izugarrizko tesia egingo duzuela, zorte on!

Mil gracias a la gente del grupo "Vamos al Etna"[1]. Ondarruko Josebari, milesker taldeko ateak irekitzearren eta zeure euskera arraro hori irakasten saiatzeagatik. Oraindik ez zaitut ulertzen, txo. A Alvariño que siempre venía a buscarnos para la genial costumbre del café (+pintxo casi siempre) de las 11 con algo interesante que contar. Más tarde Bruno le cogió el relevo y además tuvo la buena idea de organizar las pachangas con menos calidad futbolística que recuerde. El bueno de Johnny siempre venía a buscarme para comer con toda su buena onda y sus hueás. O si no era Adri, con ganas de comentar el último capítulo del Conquis. Iker ha sido el único aliado athleticzale en esta ciudad hostil; tantos sinsabores después todavía no me creo que ganasemos La Copa! Aupa Athletic! El Doctor Babaze es de la Real, pero hay que reconocer que sabe cómo organizar un tesi eguna. Un crack dentro y fuera de la clase. He hablado mucho de fútbol también con el Rober, o de cualquier tema de actualidad que surgiese. Jon Laser solía entrar al trapo en casi todos. Martín es realmente una de las personas más buenas que conozco, siempre preocupándose por los demás. Arru denetarako balio duen tipo bat da; zientzia egitea, musika konposatzea edo Minneapolisera kongresu

[1]Una cafetería de Donosti. Casi nunca fuimos.

batera laguntzea, dena egiten du ondo. De Carlos me llevé los mejores consejos. Alberto, cuando quieras echamos ese futbolín. No sé qué sería de nosotros si no estuviera María, la verdadera dinamizadora del grupo, menos mal que está ella para proponer alguna actividad que no sea jugar a las Magics. Y gracias igualmente a mucha otra gente: Benji (vaya fichaje!), Jorge (el talismán athleticzale), Raulillo, Cris, Isa, Mikel (tenemos pendiente un trail), Nikos (the Greek Alcaraz), Aurelian, Txemikel, Asier, Rubén, Xabi, Sebas...

Me alegra que los del máster que nos quedamos haciendo el doctorado hayamos sabido mantener el contacto. Han dado mucho de sí los psicos semanales con Andrea y el Nathaniel, quien no ha dejado de quejarse todos estos años ;) Tampoco he perdido el contacto con Los Hombres de Arka-san, el mejor grupo de análisis. Un agradecimiento especial a Jon, que siempre está ahí para responder a mis preguntas por muy locas que sean, especialmente las burocráticas de los últimos 4 años. Gracias también a Jan, que ha sido un gran compañero de doctorado y de congresos. Una de las principales conclusiones que me llevo del doctorado es que los gallegos son rabudos, pero muy buenos paisanos. He compartido muchos congresos también con la gente topológica del DIPC. Lejos de casa o cerca, los he disfrutado igual, bien lo saben Irián y David. No me quiero olvidar de mis compañeros de piso del 9B de la calle Mikeletes 12: Urko, mi gymbro Miguel, Valdi y Hao.

Guardo un recuerdo muy grato de mi estancia en Módena. Llegué a la ciudad sin muchas expectativas, y todo lo que vino fue un regalo. Mil gracias a Aguayo por abrirme las puertas de su casa desde el primer día en que nos conocimos, de Italia me llevé un colega para toda la vida. Por muy lejos que quede Córdoba de Euskadi, ojalá seamos capaces de mantener el contacto siempre. Muchas gracias también a Guille, por ayudarme a integrarme tanto dentro del Collegio como fuera de él. Eres un tío genial, me alegro que hayas encontrado tu sitio en esta ciudad que tanto nos ha dado. Sin duda alguna mi sitio favorito de Módena es La Ratonera de Sant'Eufemia 66, donde pasé muchas horas con mi cordobés favorito, Olguita, Mery Ibiza y Charlie. Gracias por todos los buenos momentos vividos juntos. E igualmente gracias al resto de los chavales del ESN Módena: Joan Petit, Sergio, Javi Gil, Lupa, Lidia, María, Inma, Ana, Isa, Carol, Ale, Piero, Elena-Nerea, Pavarotti, Luis... En definitiva, toda la peña con la que compartí tantas noches de Duomo, Giardinis y Qubos. Gracias por hacerme sentirme (más) joven durante unos pocos meses y experimentar el Erasmus que nunca tuve.

Grazie alle persone del gruppo "Coca Butonisti, braulini e basaltisti" per tutti i pasti e le uscite sugli Appennini che abbiamo condiviso. Infine, non voglio dimenticare tutti gli studenti dell Collegio San Carlo. Se devo essere onesto, avevo dei dubbi sul venire al Collegio. Ma presto ho capito che era stato una magnifica decisione, perchè ho incontrato persone che sono sempre state gentili con me. Grazie mile al mio compagno di stanza Ludovico, ai miei vicini Gabriele e Matti, Alan, Marisa, a ogniuno di ragazzi di palestra, Valerio e a tutte le persone che hanno incrociato una parola con me per aiutarmi a imparare un pochino di italiano. Penso di essere moderatamente fluente grazie a tutti voi!

Insomma, grazie a tutti, io porto Modena nel mio cuore!

No querría dejar pasar la oportunidad de agradecer a la kuadrilla. Gracias a los chavales de La Mosca Gao: Bully, YDG, Vivenk, Borjio, Mansik, DuHier, Tintx, Chris, Kevin, Santi, Hernán y Braniff (Perreoman?). Por ayudarme a desconectar todos los findes que he vuelto a Artzi. He perdido la cuenta de todos los partidos de pádel, pachangas, tarde-noches de Arteko, cenas de Kobá, partidos del Athletic en La Encina y demás historias que hemos compartido estos últimos años. Os voy a echar mucho de menos este tiempo que esté fuera. Un día que me puse sentimental dije que éramos la mejor kuadrilla de Artzi, y me sobran razones para seguirlo creyendo.

Gracias también a los chavales de Gautxoris y demás Drink Team, habéis estado en muchos de esos momentos. Eskerrik asko a mi tía Txaro por el bonito diseño de la portada. También a Inés, la prima más guay del mundo. Eskerrik asko a Maider, por preocuparte siempre por qué tal iba todo y por interesarte en lo que hacía en el doctorado. Suerte entendiendo los papers ;) A Zior, por ser la mejor referente y compañera. Por ser la mejor en realidad. Muchas gracias también al tío Fer, por seguir de cerca mi doctorado. Pero sobre todo, por todo lo que se preocupa por todos nosotros, sus sobrinos.

Por último, gracias a los de casa. A mi hermano Ander, que lleva unos años fuera y a quien echo de menos. Pero con quien me sigo entendiendo tan bien como siempre. Muchas veces pienso que aprendo yo más de ti, que tú de mi. Y a mis aitas. Que siempre se han preocupado de que a Ander y mi nunca nos faltase de nada. De educarnos, de enseñarnos y de cuidarnos. Por tanto, la persona que soy y esta tesis en concreto es la consecuencia de vuestro buen hacer. Así que va dedicada a vosotros. Sé que no lo suelo decir pero os quiero mucho.

Artziniega-Donostia, Octubre de 2024.

Josu Diego

Bibliography

Bibliography

[1] D. Hooton. "LI. A new treatment of anharmonicity in lattice thermodynamics: I". In: *The London, Edinburgh, and Dublin Philosophical Magazine and Journal of Science* 46 (1955), pp. 422–432.

[2] J. A. Wilson, F. J. Di Salvo, and S. Mahajan. "Charge-Density Waves in Metallic, Layered, Transition-Metal Dichalcogenides". In: *Physical Review Letters* 32 (1974), pp. 882–885.

[3] K. Rossnagel. "On the origin of charge-density waves in select layered transition-metal dichalcogenides". In: *Journal of Physics: Condensed Matter* 23 (2011), p. 213001.

[4] G. Ghiringhelli, M. L. Tacon, M. Minola, S. Blanco-Canosa, C. Mazzoli, N. B. Brookes, G. M. D. Luca, A. Frano, D. G. Hawthorn, F. He, T. Loew, M. M. Sala, D. C. Peets, M. Salluzzo, E. Schierle, R. Sutarto, G. A. Sawatzky, E. Weschke, B. Keimer, and L. Braicovich. "Long-Range Incommensurate Charge Fluctuations in (Y,Nd)$Ba_2Cu_3O_{(6+x)}$". In: *Science* 337 (2012), pp. 821–825.

[5] J. Chang, E. Blackburn, A. T. Holmes, N. B. Christensen, J. Larsen, J. Mesot, R. Liang, D. A. Bonn, W. N. Hardy, A. Watenphul, M. v. Zimmermann, E. M. Forgan, and S. M. Hayden. "Direct observation of competition between superconductivity and charge density wave order in $YBa_2Cu_3O_{6.67}$". In: *Nature Physics* 8 (2012), pp. 871–876.

[6] S. Blanco-Canosa, A. Frano, T. Loew, Y. Lu, J. Porras, G. Ghiringhelli, M. Minola, C. Mazzoli, L. Braicovich, E. Schierle, E. Weschke, M. Le Tacon, and B. Keimer. "Momentum-Dependent Charge Correlations in $YBa_2Cu_3O_{6+\delta}$ Superconductors Probed by Resonant X-Ray Scattering: Evidence for Three Competing Phases". In: *Physical Review Letters* 110 (2013), p. 187001.

[7] S. Blanco-Canosa, A. Frano, E. Schierle, J. Porras, T. Loew, M. Minola, M. Bluschke, E. Weschke, B. Keimer, and M. Le Tacon. "Resonant x-ray scattering study of charge-density wave correlations in $YBa_2Cu_3O_{6+x}$". In: *Physical Review B* 90 (2014), p. 054513.

[8] M. Le Tacon, A. Bosak, S. M. Souliou, G. Dellea, T. Loew, R. Heid, K.-P. Bohnen, G. Ghiringhelli, M. Krisch, and B. Keimer. "Inelastic X-ray scattering in $YBa_2Cu_3O_{6.6}$ reveals giant phonon anomalies and elastic central peak due to charge-density-wave formation". In: *Nature Physics* 10 (2013), pp. 52–58.

[9] R. E. Peierls. *Quantum Theory of Solids*. Oxford University Press, 1955.

[10] W. Wen, C. Dang, and L. Xie. "Photoinduced phase transitions in two-dimensional charge-density-wave 1T-TaS_2". In: *Chinese Physics B* 28 (2019), p. 058504.

[11] G. Grüner. "The dynamics of charge-density waves". In: *Reviews of Modern Physics* 60 (1988), pp. 1129–1181.

[12] G. Grüner. *Charge Density Waves in Solids*. Addison-Wesley, 1994.

[13] W. Kohn. "Image of the Fermi Surface in the Vibration Spectrum of a Metal". In: *Physical Review Letters* 2 (1959), pp. 393–394.

[14] D. Lamago, M. Hoesch, M. Krisch, R. Heid, K.-P. Bohnen, P. Böni, and D. Reznik. "Measurement of strong phonon softening in Cr with and without Fermi-surface nesting by inelastic x-ray scattering". In: *Physical Review B* 82 (2010), p. 195121.

[15] H. Miao, R. Fumagalli, M. Rossi, J. Lorenzana, G. Seibold, F. Yakhou-Harris, K. Kummer, N. B. Brookes, G. D. Gu, L. Braicovich, G. Ghiringhelli, and M. P. M. Dean. "Formation of Incommensurate Charge Density Waves in Cuprates". In: *Physical Review X* 9 (2019), p. 031042.

[16] M. D. Johannes and I. I. Mazin. "Fermi surface nesting and the origin of charge density waves in metals". In: *Physical Review B* 77 (2008), p. 165135.

[17] K. S. Novoselov, D. Jiang, F. Schedin, T. J. Booth, V. V. Khotkevich, S. V. Morozov, and A. K. Geim. "Two-dimensional atomic crystals". In: *Proceedings of the National Academy of Sciences* 102 (2005), pp. 10451–10453.

[18] R. Peierls. "Bemerkungen über Umwandlungstemperaturen". In: *Helvetica Physica Acta* 7 (1934), pp. 81–83.

[19] L. D. Landau. "Zur Theorie der Phasenumwandlungen II". In: *Physikalische Zeitschrift der Sowjetunion* 11 (1937), pp. 26–35.

[20] N. D. Mermin. "Crystalline order in two dimensions". In: *Physical Review* 176 (1968), p. 250.

[21] K. S. Novoselov, A. K. Geim, S. V. Morozov, D. Jiang, Y. Zhang, S. V. Dubonos, I. V. Grigorieva, and A. A. Firsov. "Electric field effect in atomically thin carbon films". In: *Science* 306 (2004), pp. 666–669.

[22] J. C. Meyer, A. K. Geim, M. I. Katsnelson, K. S. Novoselov, T. J. Booth, and S. Roth. "The structure of suspended graphene sheets". In: *Nature* 446 (2007), pp. 60–63.

[23] E. Mariani and F. Von Oppen. "Flexural phonons in free-standing graphene". In: *Physical Review Letters* 100 (2008), p. 076801.

[24] J. Los, M. I. Katsnelson, O. Yazyev, K. Zakharchenko, and A. Fasolino. "Scaling properties of flexible membranes from atomistic simulations: application to graphene". In: *Physical Review B* 80 (2009), p. 121405.

[25] P. De Andres, F. Guinea, and M. Katsnelson. "Bending modes, anharmonic effects, and thermal expansion coefficient in single-layer and multilayer graphene". In: *Physical Review B* 86 (2012), p. 144103.

[26] M. I. Katsnelson and A. Fasolino. "Graphene as a prototype crystalline membrane". In: *Accounts of chemical research* 46 (2013), pp. 97–105.

[27] B. Amorim, R. Roldán, E. Cappelluti, A. Fasolino, F. Guinea, and M. Katsnelson. "Thermodynamics of quantum crystalline membranes". In: *Physical Review B* 89 (2014), p. 224307.

[28] H. Wang and M. S. Daw. "Anharmonic renormalization of the dispersion of flexural modes in graphene using atomistic calculations". In: *Physical Review B* 94 (2016), p. 155434.

[29] K. H. Michel, S. Costamagna, and F. M. Peeters. "Theory of anharmonic phonons in two-dimensional crystals". In: *Physical Review B* 91 (2015), p. 134302.

[30] K. H. Michel, P. Scuracchio, and F. M. Peeters. "Sound waves and flexural mode dynamics in two-dimensional crystals". In: *Physical Review B* 96 (2017), p. 094302.

[31] D. Nelson and L. Peliti. "Fluctuations in membranes with crystalline and hexatic order". In: *Journal de Physique France* 48 (1987), pp. 1085–1092.

[32] P. Le Doussal and L. Radzihovsky. "Self-consistent theory of polymerized membranes". In: *Physical Review Letters* 69 (1992), pp. 1209–1212.

[33] J.-P. Kownacki and D. Mouhanna. "Crumpling transition and flat phase of polymerized phantom membranes". In: *Physical Review E* 79 (2009), p. 040101.

[34] D. Nelson, T. Piran, and S. Weinberg. *Statistical Mechanics of Membranes and Surfaces*. World Scientific, 2004.

[35] M. K. Blees, A. W. Barnard, P. A. Rose, S. P. Roberts, K. L. McGill, P. Y. Huang, A. R. Ruyack, J. W. Kevek, B. Kobrin, D. A. Muller, and P. L. McEuen. "Graphene kirigami". In: *Nature* 524 (2015), pp. 204–207.

[36] N. Lindahl, D. Midtvedt, J. Svensson, O. A. Nerushev, N. Lindvall, A. Isacsson, and E. E. B. Campbell. "Determination of the Bending Rigidity of Graphene via Electrostatic Actuation of Buckled Membranes". In: *Nano Letters* 12 (2012), pp. 3526–3531.

[37] A. Al Taleb, G. Anemone, D. Farías, and R. Miranda. "Acoustic surface phonons of graphene on Ni (111)". In: *Carbon* 99 (2016), pp. 416–422.

[38] A. Al Taleb, H. K. Yu, G. Anemone, D. Farías, and A. M. Wodtke. "Helium diffraction and acoustic phonons of graphene grown on copper foil". In: *Carbon* 95 (2015), pp. 731–737.

[39] A. Al Taleb, G. Anemone, D. Farías, and R. Miranda. "Resolving localized phonon modes on graphene/Ir (111) by inelastic atom scattering". In: *Carbon* 133 (2018), pp. 31–38.

[40] M. Tømterud, S. K. Hellner, S. D. Eder, S. Forti, J. R. Manson, C. Colletti, and B. Holst. "Temperature Dependent Bending Rigidity of Graphene". In: *arXiv preprint* arXiv: 2210.17250 (2022).

[41] R. Bianco, I. Errea, L. Paulatto, M. Calandra, and F. Mauri. "Second-order structural phase transitions, free energy curvature, and temperature-dependent anharmonic phonons in the self-consistent harmonic approximation: Theory and stochastic implementation". In: *Physical Review B* 96 (2017), p. 014111.

[42] P. Hohenberg and W. Kohn. "Inhomogeneous Electron Gas". In: *Physical Review* 136 (1964), B864–B871.

[43] D. M. Ceperley and B. J. Alder. "Ground State of the Electron Gas by a Stochastic Method". In: *Physical Review Letters* 45 (1980), pp. 566–569.

[44] J. P. Perdew and A. Zunger. "Self-interaction correction to density-functional approximations for many-electron systems". In: *Physical Review B* 23 (1981), pp. 5048–5079.

[45] K. Capelle. "A bird's-eye view of density-functional theory". In: *Brazilian Journal of Physics* 36 (2002).

[46] J. P. Perdew, K. Burke, and M. Ernzerhof. "Generalized Gradient Approximation Made Simple". In: *Physical Review Letters* 77 (1996), pp. 3865–3868.

[47] S. Grimme. "Semiempirical GGA-type density functional constructed with a long-range dispersion correction". In: *Journal of Computational Chemistry* 27 (2006), pp. 1787–1799.

[48] M. Dion, H. Rydberg, E. Schröder, D. C. Langreth, and B. I. Lundqvist. "Van der Waals Density Functional for General Geometries". In: *Physical Review Letters* 92 (2004), p. 246401.

[49] G. Román-Pérez and J. M. Soler. "Efficient Implementation of a van der Waals Density Functional: Application to Double-Wall Carbon Nanotubes". In: *Physical Review Letters* 103 (2009), p. 096102.

[50] N. W. Ashcroft and N. D. Mermin. *Solid State Physics*. Harcourt College Publishers, 1976.

[51] H. J. Monkhorst and J. D. Pack. "Special points for Brillouin-zone integrations". In: *Physical Review B* 13 (1976), pp. 5188–5192.

[52] M. Methfessel and A. T. Paxton. "High-precision sampling for Brillouin-zone integration in metals". In: *Physical Review B* 40 (1989), pp. 3616–3621.

[53] D. R. Hamann, M. Schlüter, and C. Chiang. "Norm-Conserving Pseudopotentials". In: *Physical Review Letters* 43 (1979), pp. 1494–1497.

[54] D. Vanderbilt. "Soft self-consistent pseudopotentials in a generalized eigenvalue formalism". In: *Physical Review B* 41 (1990), pp. 7892–7895.

[55] H. Hellmann. *Einfurung in die Quantumchemie*. Deuticke, 1939.

[56] R. P. Feynman. "Forces in Molecules". In: *Physical Review* 56 (1939), pp. 340–343.

[57] S. Baroni, P. Giannozzi, and A. Testa. "Green's-function approach to linear response in solids". In: *Physical Review Letters* 58 (1987), pp. 1861–1864.

[58] X. Gonze. "Adiabatic density-functional perturbation theory". In: *Physical Review A* 52 (1995), pp. 1096–1114.

[59] S. Baroni, S. de Gironcoli, A. Dal Corso, and P. Giannozzi. "Phonons and related crystal properties from density-functional perturbation theory". In: *Reviews of Modern Physics* 73 (2001), pp. 515–562.

[60] R. M. Sternheimer. "Electronic Polarizabilities of Ions from the Hartree-Fock Wave Functions". In: *Physical Review* 96 (1954), pp. 951–968.

[61] P. Giannozzi, S. Baroni, N. Bonini, M. Calandra, R. Car, C. Cavazzoni, D. Ceresoli, G. L. Chiarotti, M. Cococcioni, I. Dabo, A. Dal Corso, S. de Gironcoli, S. Fabris, G. Fratesi, R. Gebauer, U. Gerstmann, C. Gougoussis, A. Kokalj, M. Lazzeri, L. Martin-Samos, N. Marzari, F. Mauri, R. Mazzarello, S. Paolini, A. Pasquarello, L. Paulatto, C. Sbraccia, S. Scandolo, G. Sclauzero, A. P. Seitsonen, A. Smogunov, P. Umari, and R. M. Wentzcovitch. "QUANTUM ESPRESSO: a modular and open-source software project for quantum simulations of materials". In: *Journal of Physics: Condensed Matter* 21 (2009), p. 395502.

[62] P. Giannozzi, O. Andreussi, T. Brumme, O. Bunau, M. Buongiorno Nardelli, M. Calandra, R. Car, C. Cavazzoni, D. Ceresoli, M. Cococcioni, N. Colonna,

I. Carnimeo, A. Dal Corso, S. de Gironcoli, P. Delugas, R. A. DiStasio, A. Ferretti, A. Floris, G. Fratesi, G. Fugallo, R. Gebauer, U. Gerstmann, F. Giustino, T. Gorni, J. Jia, M. Kawamura, H.-Y. Ko, A. Kokalj, E. Küçükbenli, M. Lazzeri, M. Marsili, N. Marzari, F. Mauri, N. L. Nguyen, H.-V. Nguyen, A. Otero-de-la-Roza, L. Paulatto, S. Poncé, D. Rocca, R. Sabatini, B. Santra, M. Schlipf, A. P. Seitsonen, A. Smogunov, I. Timrov, T. Thonhauser, P. Umari, N. Vast, X. Wu, and S. Baroni. "Advanced capabilities for materials modelling with Quantum ESPRESSO". In: *Journal of Physics: Condensed Matter* 29 (2017), p. 465901.

[63] R. Car and M. Parrinello. "Unified Approach for Molecular Dynamics and Density-Functional Theory". In: *Physical Review Letters* 55 (1985), pp. 2471–2474.

[64] D. M. Ceperley. "Path integrals in the theory of condensed helium". In: *Reviews of Modern Physics* 67 (1995), pp. 279–355.

[65] I. Errea, B. Rousseau, and A. Bergara. "Anharmonic Stabilization of the High-Pressure Simple Cubic Phase of Calcium". In: *Physical Review Letters* 106 (2011), p. 165501.

[66] I. Errea, M. Calandra, and F. Mauri. "Anharmonic free energies and phonon dispersions from the stochastic self-consistent harmonic approximation: Application to platinum and palladium hydrides". In: *Physical Review B* 89 (2014), p. 064302.

[67] L. Monacelli, I. Errea, M. Calandra, and F. Mauri. "Pressure and stress tensor of complex anharmonic crystals within the stochastic self-consistent harmonic approximation". In: *Physical Review B* 98 (2018), p. 024106.

[68] P. Ehrenfest. "Phasenumwandlungen im ueblichen und erweiterten Sinn, classifiziert nach den entsprechenden Singularitaeten des thermodynamischen Potentiales". In: *Proceedings of the Royal Academy of Amsterdam* 36 (1933), pp. 153–157.

[69] L. D. Landau and E. M. Lifshitz. *Statistical Physics, Part 1*. 3rd ed. Vol. 5. Course of Theoretical Physics. Butterworth-Heinemann, 1980.

[70] D. Subires, A. Korshunov, A. H. Said, L. Sánchez, B. R. Ortiz, S. D. Wilson, A. Bosak, and S. Blanco-Canosa. "Order-disorder charge density wave instability in the kagome metal (Cs, Rb)V_3Sb_5". In: *Nature Communications* 14 (2023).

[71] I. Errea, M. Calandra, C. J. Pickard, J. R. Nelson, R. J. Needs, Y. Li, H. Liu, Y. Zhang, Y. Ma, and F. Mauri. "Quantum hydrogen-bond symmetrization in the superconducting hydrogen sulfide system". In: *Nature* 532 (2016), pp. 81–84.

[72] R. Bianco, I. Errea, M. Calandra, and F. Mauri. "High-pressure phase diagram of hydrogen and deuterium sulfides from first principles: Structural and vibrational properties including quantum and anharmonic effects". In: *Physical Review B* 97 (2018), p. 214101.

[73] I. Errea, F. Belli, L. Monacelli, A. Sanna, T. Koretsune, T. Tadano, R. Bianco, M. Calandra, R. Arita, F. Mauri, and J. A. Flores-Livas. "Quantum crystal structure in the 250-kelvin superconducting lanthanum hydride". In: *Nature* 578 (2020), pp. 66–69.

[74] U. Aseginolaza, R. Bianco, L. Monacelli, L. Paulatto, M. Calandra, F. Mauri, A. Bergara, and I. Errea. "Phonon Collapse and Second-Order Phase Transition in Thermoelectric SnSe". In: *Physical Review Letters* 122 (2019), p. 075901.

[75] U. Aseginolaza, R. Bianco, L. Monacelli, L. Paulatto, M. Calandra, F. Mauri, A. Bergara, and I. Errea. "Strong anharmonicity and high thermoelectric efficiency in high-temperature SnS from first principles". In: *Physical Review B* 100 (2019), p. 214307.

[76] R. Bianco, I. Errea, L. Monacelli, M. Calandra, and F. Mauri. "Quantum Enhancement of Charge Density Wave in NbS_2 in the Two-Dimensional Limit". In: *Nano Letters* 19 (2019), pp. 3098–3103.

[77] R. Bianco, L. Monacelli, M. Calandra, F. Mauri, and I. Errea. "Weak Dimensionality Dependence and Dominant Role of Ionic Fluctuations in the Charge-Density-Wave Transition of $NbSe_2$". In: *Physical Review Letters* 125 (2020), p. 106101.

[78] J. S. Zhou, L. Monacelli, R. Bianco, I. Errea, F. Mauri, and M. Calandra. "Anharmonicity and Doping Melt the Charge Density Wave in Single-Layer $TiSe_2$". In: *Nano Letters* 20 (2020), pp. 4809–4815.

[79] H. Bruus and K. Flensberg. *Many-Body Quantum Theory in Condensed Matter Physics: An Introduction*. Oxford Graduate Texts. OUP Oxford, 2004.

[80] L. Monacelli and F. Mauri. "Time-dependent self-consistent harmonic approximation: Anharmonic nuclear quantum dynamics and time correlation functions". In: *Physical Review B* 103 (2021), p. 104305.

[81] J.-M. Lihm and C.-H. Park. "Gaussian time-dependent variational principle for the finite-temperature anharmonic lattice dynamics". In: *Physical Review Research* 3 (2021), p. L032017.

[82] A. B. Migdal. "Interactions between Nucleons in the Theory of Nuclear Matter". In: *Soviet Physics JETP* 7 (1958), pp. 996–1002.

[83] R. M. Martin. *Electronic Structure: Basic Theory and Practical Methods*. Cambridge University Press, 2004.

[84] D. Dangić, L. Monacelli, R. Bianco, F. Mauri, and I. Errea. "Large impact of phonon lineshapes on the superconductivity of solid hydrogen". In: *Communications Physics* 7 (2024).

[85] S. Manzeli, D. Ovchinnikov, D. Pasquier, O. V. Yazyev, and A. Kis. "2D transition metal dichalcogenides". In: *Nature Reviews Materials* 2 (2017).

[86] B. Clayman and R. Frindt. "The superconducting energy gap of $NbSe_2$". In: *Solid State Communications* 9 (1971), pp. 1881–1884.

[87] A. Kogar, M. S. Rak, S. Vig, A. A. Husain, F. Flicker, Y. I. Joe, L. Venema, G. J. MacDougall, T. C. Chiang, E. Fradkin, J. van Wezel, and P. Abbamonte. "Signatures of exciton condensation in a transition metal dichalcogenide". In: *Science* 358 (2017), pp. 1314–1317.

[88] T. Mueller and E. Malic. "Exciton physics and device application of two-dimensional transition metal dichalcogenide semiconductors". In: *npj 2D Materials and Applications* 2 (2018), p. 29.

[89] E. Morosan, H. W. Zandbergen, B. S. Dennis, J. W. G. Bos, Y. Onose, T. Klimczuk, A. P. Ramirez, N. P. Ong, and R. J. Cava. "Superconductivity in Cu_xTiSe_2". In: *Nature Physics* 2 (2006), pp. 544–550.

[90] A. F. Kusmartseva, B. Sipos, H. Berger, L. Forró, and E. Tuti š. "Pressure Induced Superconductivity in Pristine $1T-TiSe_2$". In: *Physical Review Letters* 103 (2009), p. 236401.

[91] M. M. Ugeda, A. J. Bradley, Y. Zhang, S. Onishi, Y. Chen, W. Ruan, C. Ojeda-Aristizabal, H. Ryu, M. T. Edmonds, H.-Z. Tsai, A. Riss, S.-K. Mo, D. Lee, A. Zettl, Z. Hussain, Z.-X. Shen, and M. F. Crommie. "Characterization of collective ground states in single-layer $NbSe_2$". In: *Nature Physics* 12 (2016), pp. 92–97.

[92] S. Sahoo, U. Dutta, L. Harnagea, A. K. Sood, and S. Karmakar. "Pressure-induced suppression of charge density wave and emergence of superconductivity in $1T - VSe_2$". In: *Physical Review B* 101 (2020), p. 014514.

[93] M. Calandra and F. Mauri. "Charge-Density Wave and Superconducting Dome in $TiSe_2$ from Electron-Phonon Interaction". In: *Physical Review Letters* 106 (2011), p. 196406.

[94] M. Leroux, I. Errea, M. Le Tacon, S.-M. Souliou, G. Garbarino, L. Cario, A. Bosak, F. Mauri, M. Calandra, and P. Rodière. "Strong anharmonicity induces quantum melting of charge density wave in $2H$-$NbSe_2$ under pressure". In: *Physical Review B* 92 (2015), p. 140303.

[95] F. Zheng and J. Feng. "Electron-phonon coupling and the coexistence of superconductivity and charge-density wave in monolayer $NbSe_2$". In: *Physical Review B* 99 (2019), p. 161119.

[96] F. Weber, S. Rosenkranz, J.-P. Castellan, R. Osborn, R. Hott, R. Heid, K.-P. Bohnen, T. Egami, A. H. Said, and D. Reznik. "Extended Phonon Collapse and the Origin of the Charge-Density Wave in $2H-NbSe_2$". In: *Physical Review Letters* 107 (2011), p. 107403.

[97] F. Weber, S. Rosenkranz, J.-P. Castellan, R. Osborn, G. Karapetrov, R. Hott, R. Heid, K.-P. Bohnen, and A. Alatas. "Electron-Phonon Coupling and the Soft Phonon Mode in $TiSe_2$". In: *Physical Review Letters* 107 (2011), p. 266401.

[98] P. Chen, Y.-H. Chan, X.-Y. Fang, Y. Zhang, M. Y. Chou, S.-K. Mo, Z. Hussain, A.-V. Fedorov, and T.-C. Chiang. "Charge density wave transition in single-layer titanium diselenide". In: *Nature Communications* 6 (2015), p. 8943.

[99] S. Kolekar, M. Bonilla, Y. Ma, H. C. Diaz, and M. Batzill. "Layer- and substrate-dependent charge density wave criticality in 1T–$TiSe_2$". In: *2D Materials* 5 (2017), p. 015006.

[100] J. Feng, D. Biswas, A. Rajan, M. D. Watson, F. Mazzola, O. J. Clark, K. Underwood, I. Marković, M. McLaren, A. Hunter, D. M. Burn, L. B. Duffy, S. Barua, G. Balakrishnan, F. Bertran, P. Le Fèvre, T. K. Kim, G. van der Laan, T. Hesjedal, P. Wahl, and P. D. C. King. "Electronic Structure and Enhanced Charge-Density Wave Order of Monolayer VSe_2". In: *Nano Letters* 18 (2018), pp. 4493–4499.

[101] P. Chen, W. W. Pai, Y.-H. Chan, V. Madhavan, M. Y. Chou, S.-K. Mo, A.-V. Fedorov, and T.-C. Chiang. "Unique Gap Structure and Symmetry of the Charge Density Wave in Single-Layer VSe_2". In: *Physical Review Letters* 121 (2018), p. 196402.

[102] G. Duvjir, B. K. Choi, I. Jang, S. Ulstrup, S. Kang, T. Thi Ly, S. Kim, Y. H. Choi, C. Jozwiak, A. Bostwick, E. Rotenberg, J.-G. Park, R. Sankar, K.-S. Kim, J. Kim, and Y. J. Chang. "Emergence of a Metal–Insulator Transition and High-Temperature Charge-Density Waves in VSe_2 at the Monolayer Limit". In: *Nano Letters* 18 (2018), pp. 5432–5438.

[103] P. M. Coelho, K. Nguyen Cong, M. Bonilla, S. Kolekar, M.-H. Phan, J. Avila, M. C. Asensio, I. I. Oleynik, and M. Batzill. "Charge Density Wave State Suppresses Ferromagnetic Ordering in VSe_2 Monolayers". In: *The Journal of Physical Chemistry C* 123 (2019), pp. 14089–14096.

[104] G. Duvjir, B. K. Choi, T. T. Ly, N. H. Lam, K. Jang, D. D. Dung, Y. J. Chang, and J. Kim. "Multiple charge density wave phases of monolayer VSe_2 manifested by graphene substrates". In: *Nanotechnology* 32 (2021), p. 364002.

[105] D. Biswas, A. J. H. Jones, P. Majchrzak, B. K. Choi, T.-H. Lee, K. Volckaert, J. Feng, I. Marković, F. Andreatta, C.-J. Kang, H. J. Kim, I. H. Lee,

C. Jozwiak, E. Rotenberg, A. Bostwick, C. E. Sanders, Y. Zhang, G. Karras, R. T. Chapman, A. S. Wyatt, E. Springate, J. A. Miwa, P. Hofmann, P. D. C. King, Y. J. Chang, N. Lanatà, and S. Ulstrup. "Ultrafast Triggering of Insulator–Metal Transition in Two-Dimensional VSe_2". In: *Nano Letters* 21 (2021), pp. 1968–1975.

[106] D. J. Eaglesham, R. L. Withers, and D. M. Bird. "Charge-density-wave transitions in 1T-VSe_2". In: *Journal of Physics C: Solid State Physics* 19 (1986), p. 359.

[107] P. A. Lee, T. M. Rice, and P. W. Anderson. "Fluctuation Effects at a Peierls Transition". In: *Physical Review Letters* 31 (1973), pp. 462–465.

[108] M.-L. Lin, Y. Zhou, J.-B. Wu, X. Cong, X.-L. Liu, J. Zhang, H. Li, W. Yao, and P.-H. Tan. "Cross-dimensional electron-phonon coupling in van der Waals heterostructures". In: *Nature Communications* 10 (2019), p. 2419.

[109] C. S. Snow, J. F. Karpus, S. L. Cooper, T. E. Kidd, and T.-C. Chiang. "Quantum Melting of the Charge-Density-Wave State in $1T-TiSe_2$". In: *Physical Review Letters* 91 (2003), p. 136402.

[110] J. Diego, D. Subires, A. H. Said, D. A. Chaney, A. Korshunov, G. Garbarino, F. Diekmann, S. K. Mahatha, V. Pardo, J. M. Wilkinson, J. S. Lord, J. Strempfer, P. J. B. Perez, S. Francoual, C. Popescu, M. Tallarida, J. Dai, R. Bianco, L. Monacelli, M. Calandra, A. Bosak, F. Mauri, K. Rossnagel, A. O. Fumega, I. Errea, and S. Blanco-Canosa. "Electronic structure and lattice dynamics of $1T-VSe_2$: Origin of the three-dimensional charge density wave". In: *Physical Review B* 109 (2024), p. 035133.

[111] K. Terashima, T. Sato, H. Komatsu, T. Takahashi, N. Maeda, and K. Hayashi. "Charge-density wave transition of $1T-VSe_2$ studied by angle-resolved photoemission spectroscopy". In: *Physical Review B* 68 (2003), p. 155108.

[112] V. N. Strocov, M. Shi, M. Kobayashi, C. Monney, X. Wang, J. Krempasky, T. Schmitt, L. Patthey, H. Berger, and P. Blaha. "Three-Dimensional Electron Realm in VSe_2 by Soft-X-Ray Photoelectron Spectroscopy: Origin of Charge-Density Waves". In: *Physical Review Letters* 109 (2012), p. 086401.

[113] Y. Falke, N. Ehlen, G. Marini, A. V. Fedorov, V. Y. Voroshnin, B. V. Senkovskiy, K. Nikonov, M. Hoesch, T. K. Kim, L. Petaccia, G. Di Santo, T. Szkopek, G. Profeta, and A. Grüneis. "Coupling to zone-center optical phonons in VSe_2 enhanced by charge density waves". In: *Physical Review B* 104 (2021), p. 235137.

[114] W. Setyawan and S. Curtarolo. "High-throughput electronic band structure calculations: Challenges and tools". In: *Computational Materials Science* 49 (2010), pp. 299–312.

[115] S. Baroni, S. de Gironcoli, A. Dal Corso, and P. Giannozzi. "Phonons and related crystal properties from density-functional perturbation theory". In: *Reviews of Modern Physics* 73 (2001), pp. 515–562.

[116] A. O. Fumega, M. Gobbi, P. Dreher, W. Wan, C. González-Orellana, M. Peña-Díaz, C. Rogero, J. Herrero-Martín, P. Gargiani, M. Ilyn, M. M. Ugeda, V. Pardo, and S. Blanco-Canosa. "Absence of Ferromagnetism in VSe_2 Caused by Its Charge Density Wave Phase". In: *The Journal of Physical Chemistry C* 123 (2019), pp. 27802–27810.

[117] J. Diego, A. H. Said, S. K. Mahatha, R. Bianco, L. Monacelli, M. Calandra, F. Mauri, K. Rossnagel, I. Errea, and S. Blanco-Canosa. "van der Waals driven anharmonic melting of the 3D charge density wave in VSe_2". In: *Nature Communications* 12 (2021), p. 598.

[118] M. Hoesch, A. Bosak, D. Chernyshov, H. Berger, and M. Krisch. "Giant Kohn Anomaly and the Phase Transition in Charge Density Wave $ZrTe_3$". In: *Physical Review Letters* 102 (2009), p. 086402.

[119] M. Calandra, I. I. Mazin, and F. Mauri. "Effect of dimensionality on the charge-density wave in few-layer $2H$-$NbSe_2$". In: *Physical Review B* 80 (2009), p. 241108.

[120] J. Henke, F. Flicker, J. Laverock, and J. van Wezel. "Charge order from structured coupling in VSe_2". In: *SciPost Physics* 9 (2020), p. 56.

[121] S. M. Souliou, A. Subedi, Y. T. Song, C. T. Lin, K. Syassen, B. Keimer, and M. Le Tacon. "Pressure-induced phase transition and superconductivity in $YBa_2Cu_4O_8$". In: *Physical Review B* 90 (2014), p. 140501.

[122] K. Y. Chen, N. N. Wang, Q. W. Yin, Y. H. Gu, K. Jiang, Z. J. Tu, C. S. Gong, Y. Uwatoko, J. P. Sun, H. C. Lei, J. P. Hu, and J.-G. Cheng. "Double Superconducting Dome and Triple Enhancement of T_c in the Kagome Superconductor CsV_3Sb_5 under High Pressure". In: *Physical Review Letters* 126 (2021), p. 247001.

[123] Q. Wang, P. Kong, W. Shi, C. Pei, C. Wen, L. Gao, Y. Zhao, Q. Yin, Y. Wu, G. Li, H. Lei, J. Li, Y. Chen, S. Yan, and Y. Qi. "Charge Density Wave Orders and Enhanced Superconductivity under Pressure in the Kagome Metal CsV_3Sb_5". In: *Advanced Materials* 33 (2021), p. 2102813.

[124] J. Feng, R. A. Susilo, B. Lin, W. Deng, Y. Wang, B. Li, K. Jiang, Z. Chen, X. Xing, Z. Shi, C. Wang, and B. Chen. "Achieving Room-Temperature Charge Density Wave in Transition Metal Dichalcogenide $1T$-VSe_2". In: *Advanced Electronic Materials* 6 (2020), p. 1901427.

[125] Z. Guo, X. Hao, J. Dong, H. Li, J. Liao, and D. Chen. "Observation of pressure induced charge density wave order and eightfold structure in bulk VSe_2". In: *Scientific Reports* 11 (2021), p. 18157.

[126] A. O. Fumega, J. Diego, V. Pardo, S. Blanco-Canosa, and I. Errea. "Anharmonicity Reveals the Tunability of the Charge Density Wave Orders in Monolayer VSe_2". In: *Nano Letters* 23 (2023), pp. 1794–1800.

[127] J. G. Si, W. J. Lu, H. Y. Wu, H. Y. Lv, X. Liang, Q. J. Li, and Y. P. Sun. "Origin of the multiple charge density wave order in $1T - VSe_2$". In: *Physical Review B* 101 (2020), p. 235405.

[128] U. Aseginolaza. "Anharmonic Effects in Thermoelectric and 2D Materials". PhD thesis. Universidad del País Vasco (UPV/EHU), 2020.

[129] A. Fasolino, J. H. Los, and M. I. Katsnelson. "Intrinsic ripples in graphene". In: *Nature Materials* 6 (2007), pp. 858–861.

[130] R. Roldán, A. Fasolino, K. V. Zakharchenko, and M. I. Katsnelson. "Suppression of anharmonicities in crystalline membranes by external strain". In: *Physical Review B* 83 (2011), p. 174104.

[131] D. Wei and F. Wang. "Graphene: A partially ordered non-periodic solid". In: *The Journal of Chemical Physics* 141 (2014).

[132] O. Coquand and D. Mouhanna. "Flat phase of quantum polymerized membranes". In: *Physical Review E* 94 (2016), p. 032125.

[133] U. Aseginolaza, J. Diego, T. Cea, R. Bianco, L. Monacelli, F. Libbi, M. Calandra, A. Bergara, F. Mauri, and I. Errea. "Bending rigidity, sound propagation and ripples in flat graphene". In: *Nature Physics* 20 (2024), pp. 1288–1293.

[134] L. D. Landau and E. M. Lifshitz. *Theory of Elasticity*. 1st ed. Vol. 7. Course of Theoretical Physics. Pergamon Press, 1959.

[135] P. Rowe, G. Csányi, D. Alfè, and A. Michaelides. "Development of a machine learning potential for graphene". In: *Physical Review B* 97 (2018), p. 054303.

[136] T. J. Ypma. "Historical development of the Newton–Raphson method". In: *SIAM review* 37 (1995), pp. 531–551.

[137] E. Anderson, Z. Bai, C. Bischof, S. Blackford, J. Demmel, J. Dongarra, J. Du Croz, A. Greenbaum, S. Hammarling, A. McKenney, and D. Sorensen. *LAPACK Users' Guide*. Third ed. Philadelphia, PA: Society for Industrial and Applied Mathematics, 1999.

[138] G. D. Mahan. *Many-Particle Physics*. Physics of Solids and Liquids. Springer, 2000.

[139] D. Yoon, Y.-W. Son, and H. Cheong. "Negative Thermal Expansion Coefficient of Graphene Measured by Raman Spectroscopy". In: *Nano Letters* 11 (2011), pp. 3227–3231.

[140] J. Hašík, E. Tosatti, and R. Martoňák. “Quantum and classical ripples in graphene”. In: *Physical Review B* 97 (2018), p. 140301.

[141] N. Mitsuishi, Y. Sugita, M. S. Bahramy, M. Kamitani, T. Sonobe, M. Sakano, T. Shimojima, H. Takahashi, H. Sakai, K. Horiba, H. Kumigashira, K. Taguchi, K. Miyamoto, T. Okuda, S. Ishiwata, Y. Motome, and K. Ishizaka. “Switching of band inversion and topological surface states by charge density wave”. In: *Nature Communications* 11 (2020), p. 2466.